Undersampling to accelerate time-resolved MRI velocity measurement of carotid blood flow

Yuehui Tao

PhD

The University of Edinburgh

2009

I declare that this thesis has been composed by myself, and that the work contained in it is my own. Where work has been published that has been done by other people associated with the research group, an appropriate acknowledgement is made. I also declare that the work has not been submitted for any other degree or professional qualification.

Yuehui Tao

March 2009

To my parents

Acknowledgements

It is really difficult to put into words my gratitude to Prof. Ian Marshall, the supervisor of this work. Without his encouragement, inspiration, guidance and advice, I would have been completely lost. I am also deeply grateful to my second supervisor, Dr. Mark Bastin, for his extremely thorough proofreading and constructive comments. I would like to thank Dr. Peter Hoskins for being a wonderful mentor, and Dr. Paul Armitage for many useful discussions.

I must thank all members of the SFC Brain Imaging Research Centre for their support throughout this study. Thanks to Nadine, Moira, and others for their office administration; thanks to Elaine, Iona, Andrew, Hazel, Angus and other radiographers for always being there to help when I was hacking the scanner and for their kind offers of volunteering my scans; thanks to Dr. Trevor Carpenter for his excellent maintenance of the file and processing servers, which is out of his duty; thanks to Dr. David McGonigle for teaching me how to use the A/D box and drinks after work; thanks to Dr. Andrew Farrall for sharing his knowledge of carotid arteries; thanks to David Perry and the DCN IT team for computing support; my thanks also to Katherine, Mike, Jon, Susana and other fantastic lab mates.

I must also thank all members of the Medical Physics department. I feel slightly sorry that my office and lab are miles away from the department and that I only made three of the weekly cake afternoons. Prof. Norman McDicken has been really kind to me, and I always receive prompt support from Irene. I have been very fortunate to hang out with James, Mairead, Michael, Kate, Steven, David, Ben, Dave, Adele, Antonios and other fellow Medical Physics postgraduate students. I will never forget the cake rating student group meetings all around Edinburgh and those trips to Firbush.

Many people outside the university helped a lot as well to make my study go this far. I would like to thank Dr. Paul Summers for encouraging me to stay in research; I thank Dr. Yuji Shen and Dr. Li Sun for sharing their research experience and showing me around during the British Chapter meetings; I thank Dr. Jeffery Tsao for inventing k-t BLAST and his comments on my work; I also want to thank Ameng and other best friends in Shanghai for making me feel not so far from China.

I received the Oversea Research Student Award and the Principal's Scholarship of the College of Medicine and Veterinary Medicine for the study in Edinburgh. I would like to thank Dr. Dorothy Watson and Paul McGuire for their assistance in securing and managing the funding.

I would like to thank GE Healthcare for providing the technical details of the scanner, which allowed me to carry out this work. It has not been easy to work with the old EPIC manual, so I would also like to thank all contributors to the EPIC mailing list for their tips and inputs.

Finally, congratulations to my parents. My acknowledgements to them could make another small book and it is better to show them rather than talk about it. My thanks also to other family members for their support during the days I was away.

Abstract

Time-resolved velocity information of carotid blood flow can be used to estimate haemodynamic conditions associated with carotid artery disease leading to stroke. MRI provides high-resolution measurement of such information but long scan time limits its clinical application in this area. In order to reduce scan time the MRI signal is often undersampled by skipping part of the signal during data acquisition. The aim of this work is to implement and evaluate different undersampling techniques for carotid velocity measurement on a 1.5 T clinical scanner.

Most recent undersampling techniques assume spatial and temporal redundancies of real time-resolved MRI signal. In these techniques different undersampling strategies were proposed. Prior information or different assumptions of the nature of true signal were used in signal reconstruction. A brief review of these techniques and details of a representative technique, known as k-t BLAST, are presented. Another undersampling scheme, termed ktVD, is proposed to use predesigned undersampling patterns with variable sampling densities in both temporal and spatial dimensions. It aims to collect enough signal content at the signal acquisition stage and simplify signal reconstruction.

Fidelity of the results from undersampled data is affected by many factors, such as signal dynamic content, degree of signal redundancy, noise level, degree of undersampling, undersampling patterns, and parameters of post-processing algorithms. Simulations and *in vivo* scans were conducted to investigate the effects of these factors in time-resolved 2D scans and time-resolved 3D scans. The results suggested velocity measurement became less reliable when they were obtained from less than 25% of the full signal. In time-resolved 3D scans the signal can be undersampled in either one or two spatial dimensions in addition to the temporal dimension. This allows more options in the design of undersampling patterns, which were tested *in vivo*. In order to test undersampling in three dimensions in high resolution 3D scans and measure velocity in three dimensions, a flow phantom was also scanned at high degrees of undersampling to test the proposed method.

Contents

List of Figures

List of Tables

Chapter 1

Introduction

1.1 Background

Stroke is the second most common cause of death and major cause of disability worldwide [1], and ischaemic strokes account for 88% of all strokes [2]. It is believed that carotid artery disease accounts for 20% of ischaemic strokes [3].

Haemodynamic quantities, such as Wall Shear Stress (WSS) estimated from blood flow velocities measured with non-invasive imaging techniques, can be used as potential risk indicators in the prediction and clinical management of carotid artery disease. Magnetic Resonance Imaging (MRI) is one of the most promising imaging techniques capable of *in vivo* velocity measurement, but the lengthy scan time has been its major limitation. In order to accelerate such MRI scans, skipping a certain part of the signal acquisition regarded as redundant has been a popular approach to save scan time.

1.1.1 Carotid arteries

The carotid arteries are major blood vessels between the heart and the brain in the front of the neck. They deliver blood to the arteries in the brain and supply nutrients and oxygen to the cerebral cortex, which is responsible for many important brain functions such as consciousness, memory and control of voluntary movements. The carotid arteries are paired structures, including the left and right carotid arteries. As shown in Figure (1.1), at the level close to the chin the right common carotid artery (RCCA) bifurcates into the right internal carotid artery (RICA) and the right external carotid artery (RECA). In the left half of the neck the left carotid arteries (LCCA, LICA, and

LECA) form a very similar structure, which is known as a carotid bifurcation. The slight dilation in the internal carotid artery is known as a carotid bulb. The internal carotid arteries (ICA) travel into the skull and supply the brain. The external carotid arteries (ECA) are more close to the surface, supplying the neck and face. Close to the bifurcations the external carotid arteries have many branches such as the superior thyroid arteries and the ascending pharyngeal arteries. At the same level the internal carotid arteries do not have any branches.

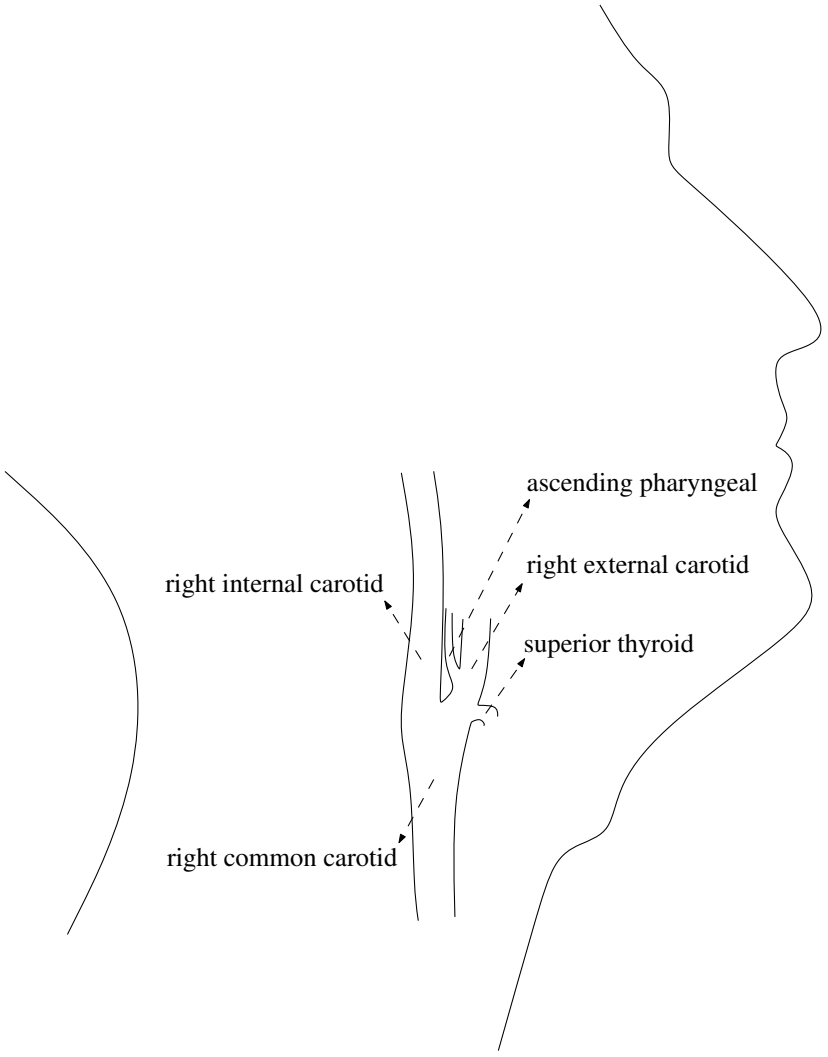

Figure 1.1: The right carotid arteries. Only two of the branches of the right external carotid artery close to the bifurcation are displayed.

There are age, sex and inter-subject differences in the carotid bifurcation geometries [4, 5]. The diameter of a common carotid artery (CCA) of a healthy subject is normally between 7 mm and 9 mm [4]. The ICA/CCA diameter ratio normally ranges from 0.77 to 0.81, and the ECA/CCA diameter ratio is normally between 0.75 and 0.81 [5].

The artery wall consists of three primary layers: the intima, media and adventia [6, 7], as shown in Figure (1.2). The intima consists of a monolayer of endothelial cells and an underlying basal lamina. The endothelium works as an interface between the blood and the content of the artery wall, and it actively responds to chemical and mechanical stimuli, which may lead to various changes in the vessel wall such as promoting cell replication or modifying blood-borne substance for transport into the wall. The media consists primarily of smooth muscle cells embedded in a plexus of elastin, various types of collagen, and proteoglycans. Smooth muscle allows the artery to constrict or dilate, modifying wall properties and regulating blood flow locally. The adventia consists primarily of fibroblasts, collagen, elastic fibres and nerves. It is believed to serve as a protective sheath that prevents acute overdistension of the media.

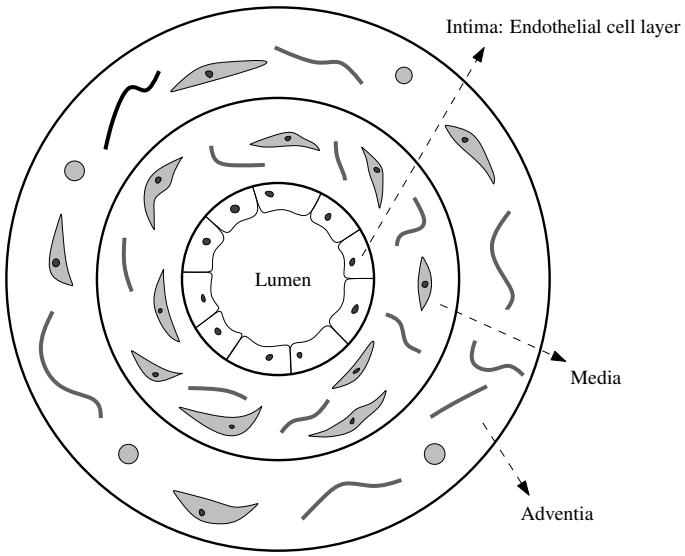

Figure 1.2: A schematic view of the layers of an artery wall cross-section

1.1.2 Carotid atherosclerosis and stroke

Carotid artery disease occurs if a carotid artery becomes narrowed or blocked, mostly due to atherosclerosis. Atherosclerosis is the process by which fatty deposits called plaque build up beneath the luminal surface in the innermost layer of arterial wall. As atherosclerosis progresses, enlarging plaque may gradually encroach into the lumen and cause abnormal narrowing of the artery, which is known as a stenosis. Serious stenosis can significantly reduce blood flow through the vessel. The luminal surface of a healthy artery is normally smooth. Some unstable plaque vulnerable to rupture may disrupt the luminal surface and form rough and irregular areas. As an inflammatory response, these areas are covered with blood-clotting cells. A blood clot can form and grow to block blood flow completely. This can lead to an ischaemic stroke if the decrease in blood and oxygen supply results in dysfunctions of certain part of the brain. A clot or a piece of plaque may break free, travel with the blood flow and block downstream smaller arteries. This can also cause an ischaemic stroke and is often more serious than an upstream blockage in which blood flow may take alternative routes to the brain.

Since in early stages carotid artery atherosclerosis may not cause any symptoms for many years, and a plaque rupture may lead to stroke in minutes, there is always intense interest in developing imaging techniques for early detection and monitoring of plaque progression.

1.1.3 Risk factors for atherosclerosis

Many risk factors are associated with atherosclerosis, such as hypertension [8], smoking [9], hyperlipidemia [10], diabetes mellitus [11], social stress [12], sedentary lifestyle [11], viral infection [13], and possibly chlamydial infection [14].

Haemodynamics are also believed to play an important role in the formation and progression of atherosclerotic plaque [15, 16, 17, 18]. Arterial walls are subjected to mechanical forces, in the form of axial stress due to blood pressure and wall shear stress (WSS) due to friction of blood against the wall [19, 20]. In studies comparing human post-mortem distributions of plaque to *in vitro* fluid dynamic models [21, 22], it was observed atherosclerosis developed largely in regions of relatively low WSS and disturbed blood flow. Different hypotheses have been proposed to explain the relationship between plaque location and abnormal WSS. High WSS, low WSS and oscillat-

ing WSS have each been suggested as initiating factors in atherosclerosis [23, 24, 16]. Most following studies [25, 21, 22] supported the low WSS hypothesis. The precise underlying biological mechanisms remain unknown. It has been reported that WSS can change the morphology and orientation of the endothelial cells in the intima. Endothelial cells subjected to high WSS tend to elongate and align in the direction of flow, whereas those experiencing low or oscillatory WSS remain more rounded and have no preferred alignment pattern [26, 27]. Exposure to a relatively low WSS may increase intercellular permeability and consequently increase the vulnerability of these regions of the vessel to atherosclerosis [28]. Levels of the vasoactive substances released by endothelial cells (prostacyclin, nitric oxide, and endothelin-1) are strongly influenced by shear stress [29, 30, 31, 32]. Nonpulsatile high WSS promotes release of factors from endothelial cells that inhibit coagulation, migration of leukocytes, and smooth muscle proliferation, while simultaneously promoting endothelial cell survival. Low and oscillating WSS leads to the opposite effects, thereby contributing to the development of atherosclerosis. In recent years numerous animal, molecular, and cellular studies have been carried out to investigate the arterial wall's response to WSS changes [17, 18]. It is widely accepted that the local wall shear stress is a major factor in atherosclerosis development.

1.1.4 Wall shear stress

Wall shear stress is defined as the tangential force per unit area that is exerted by the flowing fluid on the surface of the conduit tube, as illustrated in Figure (1.3). The magnitude of WSS τ_w is proportional to the velocity gradient $\frac{\delta v}{\delta r}$ near the tube wall [33], as shown in Equation (1.1).

$$\tau_w = \mu \frac{\delta v}{\delta r} \tag{1.1}$$

In Equation (1.1), μ is the fluid dynamic viscosity, v is the velocity along the tube axis, and r is the distance perpendicular to and away from the tube wall.

The velocity gradient $\frac{\delta v}{\delta r}$ near the wall, also known as wall shear rate, describes how fast the flow velocity increases when moving from a point at the wall to an immediately adjacent point in a direction perpendicular to the tube wall toward the centre of the tube, as shown in Figure (1.4). Since at the wall the flow velocity is zero, low wall shear rates are associated with low local velocities in the near-wall region.

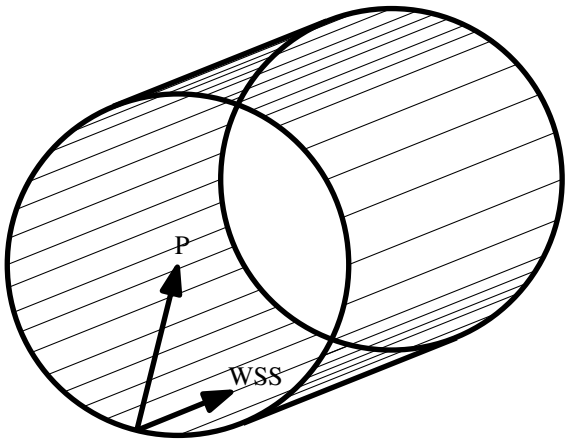

Figure 1.3: The directions of axial stress (P) due to blood pressure and wall shear stress (WSS).

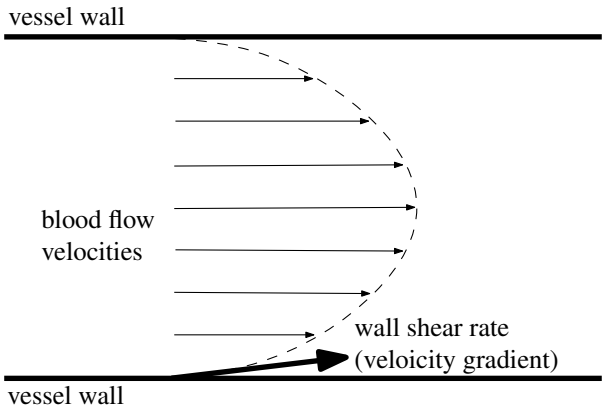

Figure 1.4: The wall shear rate (velocity gradient near vessel wall) of a parabolic velocity profile in a straight vessel.

Due to the complex shapes and curvatures of the carotid arteries, the velocity pattern of *in vivo* carotid blood flow is also complex. For example, when a vessel curves, blood flow is faster along the outer side wall of the curvature than along the inside wall. This leads to significantly different WSS along the length and around the circumference of the blood vessel. Pulsatile blood flow also makes WSS change with the cardiac cycle quasi-periodically.

In order to map WSS, local blood flow velocities in the near-wall region need to be measured. Accurate calculation of the wall shear rates requires high spatial resolution near the vessel wall, which is difficult for the imaging techniques because in this region blood flow is slow and the exact location of vessel wall is hard to determine. On the other hand, it is easier to obtain relatively more accurate velocity measurements near the centre of the artery where blood flow is often faster. This practical limitation leads to two approaches for WSS estimation. One approach uses curve fitting or interpolation algorithm [34] to build the velocity profile (the velocity distribution over a cross-section normal to the flow direction) from measurements at a discrete number of positions in the vessel. The other approach assumes the carotid blood flow can be treated as Poiseuille flow [33], so the wall shear rates can be calculated from volume flow rate or maximum velocity measured in a vessel cross-section.

When the wall shear rates are calculated through interpolation, the slope of the velocity profile is estimated from at least two, preferably three, velocity values measured near the vessel wall [35]. The accuracy of this method depends on how accurate the velocities can be measured at adjacent points and on the adopted interpolation algorithm [36]. The limited spatial resolution of the method used for velocity measurement affects the accuracy of the WSS estimation. It has been reported that extrapolation of the data on the wall shear rates assessed in venules as a function of vessel radius [37] indicates that shear rate determined 250 to 300 μm from the wall underestimates WSS by about 10%. If the wall shear rates are interpolated from measurements even further from the vessel wall (as in MRI scans), the errors can be larger. Various interpolation algorithms have been applied [34], such as linear extrapolation, quadratic extrapolation, and least-squares fitting. The interpolation is generally less robust if a higher order polynomial is used for the fitting of the velocity profile, and the results become more sensitive to background noise.

When the carotid blood flow is assumed Poiseuille flow [33], a parabolic velocity profile is expected, as shown in Figure (1.4). This assumption simplifies the flow as

a steady (nonpulsatile), fully developed flow of a Newtonian fluid (constant viscosity) in a rigid cylindrical tube. The WSS can be calculated analytically by the Hagen-Poiseuille formula [33], as shown in Equation (1.2).

$$\tau_w = \frac{4\mu Q}{\pi R^3} \tag{1.2}$$

In Equation (1.2), Q is the volume flow rate, μ is the fluid dynamic viscosity, and R is the inner radius of the conduit cylindrical tube.

Based on the same assumption of Poiseuille flow, the WSS can also be calculated from the highest velocity v_{max} (velocity at the centre of the tube) [33], as shown in Equation (1.3).

$$\tau_w = \frac{2\mu v_{max}}{R} \tag{1.3}$$

Similarly, average velocity v_{avg} (over a cross-section normal to the flow direction) can also be used to calculate the WSS, as shown in Equation (1.4).

$$\tau_w = \frac{4v_{avg}}{R} \tag{1.4}$$

Although the Poiseuille flow assumptions, such as steady flow and rigid vessel wall, are not valid in the context of real carotid blood flow, Equation (1.2), (1.3) and (1.4) are easy to use and can provide possibly useful approximations of WSS based on clinical measurements. For this reason, this approach has been adopted in many studies.

1.1.5 Imaging techniques for velocity measurement

As described previously, the estimation of the WSS requires the location of vessel wall and blood flow velocities in the near-wall region. Most imaging techniques can provide vessel geometries, with different levels of accuracy, and some of them can be used to measure blood flow velocities.

X-ray angiography

X-ray angiography involves the intra-arterial injection of an iodinated contrast agent, so the blood vessel lumen will be highlighted in the projection images. For the carotid artery, single or multiplane projections are typically acquired, both before and after

the injection of the contrast agent. Preinjection images are digitally subtracted from the corresponding images collected after the injection in order to remove background bone and tissue for higher contrast. Such images obtained through subtraction are known as digital subtraction angiograms (DSA). Reconstruction of three-dimensional (3D) geometries requires multiple projections in different directions. Advanced X-ray techniques can rapidly (4-6 s) collect multiple (about 200) projection images, which can be used to reconstruct 3D lumen structure at high (200-400 μm isotropic) spatial resolution [38].

Normally a catheter (fine tube) is placed into the artery in the groin and guided to the carotid artery, so the contrast agent can be released into blood at a location very close to or in the field of image acquisition. Alternatively the contrast agent can be injected intravenously, but this approach typically produces poorer contrast images of the lumen.

In principle, X-ray can be used to measure blood flow rates *in vivo* [39, 40]. Changes in the X-ray image intensity due to changes of the contrast agent concentration can be analysed to extract the mean flow rate and the waveform. Some techniques [41, 42, 43] are based on bolus tracking using time intensity curves at different sites along a vessel. The arrival of the contrast agent bolus is tracked along the vessel. Velocity estimates are determined from the difference of the arrival times at two sites of known distance. These methods are easy to implement, but they are known to give unreliable results in the case of pulsatile flow. It is not possible to extract a time dependent blood flow waveform using these methods. Some techniques [44, 45] determine the distance which the bolus has travelled between two consecutive frames by finding the shift which gives the best match between the distance intensity curves from both frames. If this is repeated for all frames of the sequence, a time dependent blood flow waveform can be determined. Optical flow methods [46, 47, 48] use the mass conservation law to numerically compute an estimate of the flow rate from temporal and spatial derivatives of iodine concentration. Optical flow methods can also be used to estimate a time dependent blood flow waveform, but noise can lead to errors in the computation of derivatives. Optical flow methods and those based on distance intensity curves may overestimate during the inflow and underestimate during the outflow phase [49]. The contrast agent in the centre of the vessel is transported faster, so it enters the region of interest first and it causes an overestimation of the velocity during the inflow phase. The contrast agent at the border of the vessel is transported more slowly, so it

leaves the region of interest last and it causes an underestimation of the velocity during the inflow phase.

X-ray angiography offers superior image contrast, temporal and spatial resolution over other imaging modalities. For example, micro-CT scanners can readily provide high (100-200 μm isotropic) resolution images [50, 51]. However, the risks associated with ionizing radiation and catheterization [52] limit its clinical implementation. It is difficult to carry out human studies of early atherosclerosis and local haemodynamics using X-ray angiography. It is also difficult to map time-resolved velocities with the X-ray methods described previously, which are largely experimental.

Laser Doppler flowmetry

Laser Doppler flowmetry (LDF) uses monochromatic laser light beams and the Doppler effect to measure blood flow velocity [53, 54, 55].

The Doppler effect or Doppler shift [56] describes the frequency change of a wave observed by a moving observer, as shown in Equation (1.5).

$$f_o = \frac{c - v_o}{c - v_s} f_s \tag{1.5}$$

In Equation (1.5) f_o is the apparent frequency perceived by the observer, f_s is the source frequency, c is the wave speed, v_o is the velocity of the observer, and v_s is the velocity of the source. Since the frequency change depends on the relative velocities of the source and the observer, the effect can be used to measure velocities.

When the source of a wave, such as sound or light, is moving relatively closer to an observer, the frequency of the wave observed by the observer is higher than the source frequency. When the source is moving away, the observed frequency is lower.

LDF is based on the fact that light beams scattered in moving red blood cells undergo a frequency shift according to the Doppler effect, while beams scattered in static tissue alone remain unshifted in frequency. The frequency shift is proportional to the velocity of the red blood cell. In practice the frequency shift is very small (10-1000 kHz) compared to the very high frequencies of light (100 THz), so it is difficult to measure directly. If the original light beam is interfered with the reflected beam, the high frequency part of the reflected beam is cancelled out, and the small frequency shift can be measured.

LDF is non-invasive, simple to use, and capable of measuring microcirculatory blood flow in tissue. It is widely used to measure the microcirculatory flux of the tissue and fast changes of perfusion during provocations [55]. The technique can also partially quantify perfusion in real time. The major limitation of LDF is the limited penetration depth of laser light. The penetration depth of light in tissue depends on its wavelength. Near infrared light (of wavelength about 1 μm) penetrates several mm, red light (about 650 nm) up to about 2 mm and green light (about 540 nm) hardly at all [57]. For this reason, LDF is mainly applied to measure blood flow of the skin. Carotid flow has been measured with LDF in phantom studies [58], but the technique can not be used for *in vivo* carotid flow non-invasively.

Ultrasound velocity measurement

Ultrasound scanners make use of sound waves reflected from tissues to collect structural information [59]. One or more transducers are used to transmit sound waves into the subject. When a sound wave encounters a tissue of a different density (acoustical impedance), part of the wave is reflected back and this can be detected as an echo with an ultrasound receiver. The distance between the location of reflection and the ultrasound probe can be calculated by recording the time interval between the transmission and the detection if the speed of sound in the subject is known. Since the acoustical impedance is different in different tissues, the structures along a line into the subject can be visualized as the changes of acoustical impedance at different depths along the transmitted sound beam. A two-dimensional (2D) image can be formed by sweeping the line or using a linear array of transducers. 3D images can be generated by acquiring many adjacent 2D images. For this purpose, the transducers used for 2D scans can either be moved mechanically, or 2D phased array transducers can be used, which can sweep the ultrasound beams electronically.

Typical diagnostic ultrasound scanners operate in the frequency range of 2 to 18 MHz, hence the name ultrasound (above human hearing). Higher frequencies correspond to smaller wavelengths, and can be used for scans of higher resolutions. However, the penetration depth decreases with frequency. For example, a frequency of around 3.5 MHz is generally used for a penetration of about 150 mm, and when it is increased to 10 MHz, the penetration is reduced to about 20 mm [60]. For this reason Ultrasound scans are more suitable for tissues close to surface. Since the difference in

acoustic impedance between soft tissue and bone or air is so great, most of the acoustic energy will be reflected back and it is difficult for an ultrasound beam to reach tissues behind bone or air. For example, carotid ultrasound imaging is much easier than non-invasive cardiac or transcranial ultrasound scans.

A miniaturized ultrasound probe can be attached to a fine catheter and guided to the inside of the artery of investigation to collect intravascular ultrasound (IVUS) images [61]. IVUS can be used in carotid artery to acquire detailed images of the vessel wall structure and early plaque [62], but it is highly invasive and is mostly used in interventional procedures for patients with severe stenosis. The inserted catheter and the probe will also disturb the blood flow and make it difficult to measure blood flow velocities in the original conditions.

Ultrasound can be used to measure blood flow velocity because the red blood cells act as ultrasonic scatters. Ultrasonic contrast agent [63], such as microbubbles [64], can also enhance backscattering from blood. The ultrasound techniques for blood flow measurement and visualization are generally known as Doppler ultrasound [65], including continuous-wave Doppler (CWD) and pulsed-wave Doppler (PWD) [66].

CWD works in a way similar to laser Doppler. Uninterrupted ultrasonic waves of constant frequency and amplitude are emitted into the subject by the transmitting transducer. The echoes detected by the receiving transducer have the same frequency as that of the transmitter if they are reflected by stationary structures. Those from flowing blood are shifted in frequency by the Doppler effect. Neglecting the effect of the moving medium in which the red blood cells are suspended, a moving scattering ensemble of the red blood cells acts both as a receiver of Doppler-shifted ultrasound as the distance between the ensemble and the transmitting transducer changes, and as a transmitter of this already Doppler-shifted ultrasound which is Doppler-shifted again as the distance between the ensemble and the receiving transducer also simultaneously changes. Effectively the path length of the ultrasound wave backscattered from blood changes at a velocity $2v_i$, where v_i is the velocity of the ensemble in the direction of the ultrasound beam. According to Equation (1.5) and considering ultrasound speed c is much higher than v_i, the Doppler frequency shift f_d can be calculated as in Equation (1.6).

$$f_d = \frac{2v_i}{c} f_e \tag{1.6}$$

In Equation (1.6) f_e is the frequency of the ultrasound waves emitted from the

transducer, and v_i is positive when an ensemble is moving toward the transducers.

When the ultrasound beam and the blood flow are not in the same direction, as shown in Figure (1.5), the velocity of an ensemble can be calculated as in Equation (1.7).

$$v = \frac{f_d}{2 f_e cos\theta} c \tag{1.7}$$

In Equation (1.7) θ is the angle between the ultrasound beam and the velocity of the ensemble.

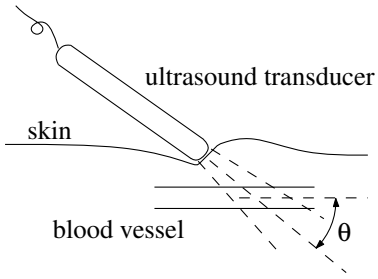

Figure 1.5: The ultrasound beam and the blood flow may not be in the same direction.

CWD is unable to measure the precise localization of the scatter since the ultrasound wave travel time is not available. Frequency spectrum analysis is applied to the acquired signal and velocities can be displayed in real time. CWD can be used to measure the peak velocity in a carotid artery.

PWD uses series of short ultrasound pulses instead of continuous waves used in CWD. Echoes from different pulses can be separated and distance information can be extracted from the recorded time interval between the reception of an echo and the transmission of the corresponding pulse. Velocities can be mapped with the location information. In practice, operators of a PWD system can set a delay so that only echoes in a short period following the delay after the transmission of each pulse are collected. This effectively limits the scan range in the subject.

The mechanism used in PWD for velocity measurement is different from that in CWD. Doppler shift of each pulse is ignored. Instead the relative phase shifts between echoes corresponding to two subsequent pulses are used to calculate the velocity. For example, if a scatter is moving toward a transducer, it will take longer time for a first pulse to cover the distance between the transducer and the scatter than the time for a second pulse. If the sound speed c is assumed to be constant, the travel time t of a

pulse can be calculated from the distance d between the scatter and the transducers, as shown in Equation (1.8).

$$t = \frac{2d}{c} \tag{1.8}$$

If the following pulse is transmitted after a delay of T_{pr} (pulse repetition time), the scatter has moved with the blood flow to a different location when the second pulse is reflected, as shown in Figure (1.6). The difference in pulse travel time can be calculated as in Equation (1.9).

$$t_2 - t_1 = \frac{2(d_2 - d_1)}{c} \tag{1.9}$$

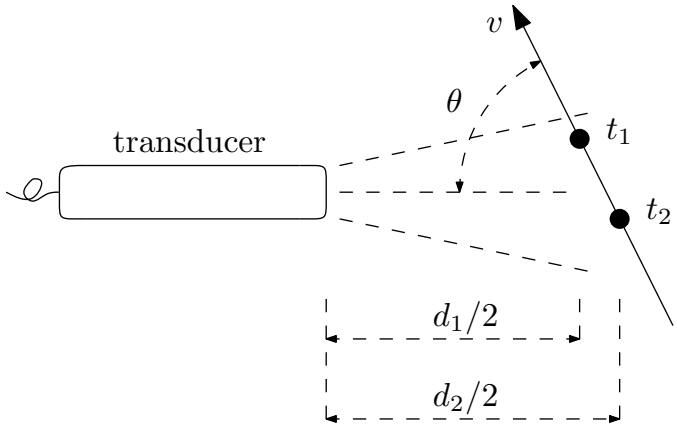

Figure 1.6: A schematic diagram of pulsed wave Doppler.

The difference in distance $d_2 - d_1$ can be calculated from the velocity of the scatter v, as shown in Equation (1.10).

$$d_2 - d_1 = vT_{pr}cos\theta \tag{1.10}$$

In Equation (1.10) θ is the angle between the ultrasound beam and the blood flow.

If the ultrasound frequency is f_e, the phase shift $\Delta\phi$ between the echoes from the two pulses can be calculated as in Equation (1.11).

$$\Delta\phi = 2\pi f_e(t_2 - t_1) \tag{1.11}$$

The scatter velocity can be calculated by combining Equation (1.9), (1.10), and

(1.11), as shown in Equation (1.12).

$$v = \frac{\Delta\phi}{4\pi f_e T_{pr} cos\theta} c = \frac{f_{pr}\Delta\phi}{4\pi f_e cos\theta} c \tag{1.12}$$

In Equation (1.12) f_{pr} is the pulse repetition frequency corresponding to T_{pr}. Since the measured value of a phase shift has a limited range, for a certain f_{pr} high velocities may lead to large phase shifts out of the range and cause aliasing [67]. This means the maximum velocity that can be measured without aliasing is limited by the pulse repetition frequency. In order to measure high velocities, a high pulse repetition frequency is needed. However, the pulse repetition time should be long enough to allow a pulse to complete the journey to and from a scatter before the next pulse is transmitted. The pulse repetition frequency is then limited by the sampling depth. This means PWD is more suitable to measure velocities in a limited range to avoid aliasing, while CWD does not have this limitation.

In addition to CWD and PWD, velocity information can also be extracted from ultrasound signal by means of time-domain processing [68, 69]. The method uses temporal tracking of the spatial position of individual coherent blood ensembles. Pattern matching is applied to signal patterns obtained in successive acquisitions [70, 71]. Since position tracking can be used in two or three dimensions, the velocity measurement is not limited in the direction of the ultrasound beam.

Peak velocity and vessel diameter measured with ultrasound have been used to estimate carotid wall shear stress by assuming parabolic velocity profiles across the arterial lumen [72, 73]. Systolic blood flow velocity was measured in a small sample volume (1 mm) placed in the centre of the vessel. It has been demonstrated that common carotid artery wall shear stress measurement *in vivo* with this method is reproducible [72]. The limitation of this approach is the assumption of Poiseuille flow and only the peak velocity is measured for the calculation of wall shear stress.

A direct method based on assessment of the radial derivative of the velocity distribution with a high-resolution multigate pulsed Doppler ultrasound system has also been used to assess in humans in a noninvasive way the instantaneous velocity distribution over time [74]. Appropriate processing of the received radio frequency signal enabled the high-precision assessment of low-blood-flow velocities close to the wall [75, 76]. The mean of the maximum of the radial derivatives of the velocity distributions at the anterior and posterior walls is used as an estimate for the local axial wall

shear rate. With this method it has been reported the observed mean shear rate is a factor of two lower than that reported in earlier studies based on the extrapolation from steady flow through a rigid tube to pulsatile flow through a distensible tube.

One of the disadvantages of PWD is its relatively poor spatial resolution [77, 78]. The nonnegligible dimensions of the measurement volume in Doppler velocimetry introduce the phenomenon of convolution, which alters the accuracy of profile determination in a proportion that depends both on the nature of the profile and the relative dimensions of the sample volume to the vascular diameter. An offline deconvolution process can be applied to improve spatial resolution. It has been demonstrated that corrected deconvoluted velocity profiles have allowed noticeable improvement in the estimation of wall shear rate when compared with the uncorrected Doppler profiles [79, 80].

Ultrasound is widely used in clinics since it is relatively inexpensive compared with other imaging modalities and noninvasive ultrasound scans have no known long-term side effects. Temporal resolution of ultrasound measurements is good and it is often used for real-time imaging. For structure imaging ultrasound scans are also fast. For example, 3D ultrasound images with high effective resolution ($0.2 \times 0.2 \times 0.6 mm^3$) can be collected in less than 10 s [81]. The major limitation of ultrasound techniques is that the method is often operator dependent. Unless the positions of the transducers are electronically tracked, the locations of the images in the subject are not available. In Doppler ultrasound scans, the angle between the ultrasound beam and the blood flow needs to be measured in order to calculate the velocities accurately. This is difficult when the ultrasound probe is operated manually. It has been reported that the Doppler methods are capable of good absolute accuracy in flow rate measurement when suitably designed equipment is used in appropriate situations, with systematic errors of 6% or less [67]. There may be considerable random errors due to errors in measuring the cross-sectional area and the angle of approach, which can be reduced to an acceptable level by repeating the scans and averaging the results. In a phantom study [82] of fully developed flow in a rigid and circular tube, the results suggested that steep velocity gradients and transit-time-effects from high velocities produced significantly larger errors in velocity measurement, wall shear rate estimates were most precise when calculated using the position of the wall and two velocity points, and the calculated wall shears were within 20%-30% of theoretically predicted values. In another study [83] a string phantom was used to assess the accuracy of maximum velocity estimates made using

six commercial Doppler ultrasound systems. Under standard conditions the maximum velocity was overestimated in all cases (0-29% error). For all measurements maximum velocity errors ranged from -4% to 47%. There was a large intraprobe variation in maximum velocity estimation (mean variation of 25%), a large interprobe variation (mean variation of 25%), and a large interprobe variation (mean variation of 18%). The error and variability that results from human factors in Doppler peak velocity measurement has also been studied [84]. The results suggested Doppler angle, sample volume placement, and the Doppler gain were the most significant sources of error and variability. The peak velocity error varied between 9% to 24%. The velocity profiles obtained with ultrasound are generally not known with sufficient accuracy as a result of numerous errors affecting both spatial and velocity measurements: error in positioning of the ultrasound probe and its sampling volume, alternation of the signal-to-noise ratio, echoes of the distal wall, and effects of the finite nonconstant sample volume [85, 78]. Maximum shear rate has been reported to be assessed at 250 to 300 μm from the vessel wall [86], which indicates that blood flow shear rates could not be determined accurately at the wall. Wall shear rates could only be determined reliably in relatively straight vessels [86]. In the common carotid artery, it has been reported that the intra-subject inter-session variability on different days varied between 13% and 15% for peak wall shear rate and between 10% and 12% for mean wall shear rate, while the inter-subject variability varied between 16% and 19% for peak wall shear rate and between 11% and 17% for mean wall shear rate [87].

MRI velocity measurement

MRI exploits differences in the nuclear physical properties of the various bodily tissues and fluids [88]. The subject is placed in a strong static magnetic field and the static magnetic field is modulated with high-frequency magnetic pulses to cause the hydrogen nuclei (protons) in a certain spatial range to produce a rotating magnetic field detectable by the scanner. This signal can be manipulated by additional magnetic fields (known as gradient magnetic fields) to make it position dependent. MRI signal is a vector quantity, with magnitude and phase. Normally for structural imaging only the signal intensities are displayed in MRI images. To measure velocity, the signal phases can also be made velocity dependent with a technique known as phase contrast (PC) [89, 90, 91]. In the technique's simplest form, two opposing gradient magnetic

pulses are added to a scan. A gradient magnetic pulse will cause a position dependent change in the phase of the signal. For static tissue, the effects of the two pulses will cancel. Protons in flowing blood will experience the two pulses at different locations and the effects can not cancel. This will lead to net phase shifts in the signal from these protons, which is proportional to the velocities. The phase shifts can be detected by carrying out two scans, with and without the pair of opposing gradient magnetic pulses. All three components of the velocity vector can be measured by applying the gradient magnetic field in different directions. The principles of MRI and the phase contrast technique will be described in detail in Chapter 2.

Typically in an MRI phase contrast scan, in-plane image voxel sizes vary from about 0.2 mm (peripheral and carotid vessels) to about 2-3 mm (deep vessels and heart chambers) at temporal resolutions (averaged over multiple cardiac cycles) 20-70 ms [91]. Velocity measurement represents an average value of the velocity over the entire voxel, including both moving and stationary structures. In carotid artery, this leads to two problems if the spatial resolution is limited for better signal-to-noise ratio. First, the position of the arterial wall inside an image voxel cannot be determined accurately. Second, wall shear rate cannot be directly measured when blood flow velocity changes considerably inside an image voxel. This means with spatial resolution at this level wall shear rate can not be measured directly. It has been reported that in aorta if the wall position in the edge voxel is not correctly estimated, an error of 34% in wall shear stress measurement could be made [35]. Several methods have been proposed to estimate wall shear stress from MRI measurements at limited spatial resolution. It has been suggested that the edge voxel can be ignored when determining the slope of the velocity profile from a polynomial fit to the velocity points [92]. Fourier velocity encoding has been used to determine the velocity distribution in a voxel that straddles the blood-vessel wall interface [93], and with this method the estimates of shear rate were obtained with a mean error of 15% compared with 73% obtained by extrapolation of the velocity profile over multiple voxels. A 3D paraboloid model has been used to fit the velocity measurements in order to determine vessel wall position, wall shear stress and volume blood flow at a subvoxel level [94]. *In vitro* lumen area was measured in a glass tube using MR velocimetry with a mean error of 0.6%, and the method is also applied to wall shear stress measurement in the common carotid artery in healthy human volunteers.

The temporal resolution of blood flow velocity mapping is determined by three

factors, being the number of cardiac beats for averaging, the measurement interval and the acquisition duration within the cardiac cycle [91]. Typically PC MRI provides less temporal resolution than pulsed Doppler ultrasound. Ultrasound measurements are often made about every 1 ms, where as MRI measurements are often made about every 30 ms or more [95]. Since the acquisition time of a full frame is often longer than the cardiac cycle, normally only several lines of raw data for each frame is collected in each cardiac cycle, and the data of multiple cardiac cycles are combined to generate a frame. The scan time for each frame is extended further for velocity mapping by the collection of reference and velocity-encoded data within the same cycle. Averaging over multiple cardiac cycles requires good periodicity of the flow velocity signal. *In vivo* blood flow are only quasiperiodic due to heart rate variability [96]. Breathing can also alter cardiac function and blood flow [97, 98]. Although breathholding is widely applied in cardiac scans to reduce respiratory artefacts, it is rarely used in carotid scans. Due to heart rate variability and breathing, averaging over multiple cardiac cycles leads to smoothing of measured velocity waveforms. It has been reported that accuracy was retained by cine frames less than 60-70 ms [99], longer if the flow is less pulsatile [100]. Smoothing might sometimes have less effect on mean flow measurements [101]. In the common carotid artery flow velocity maps over the cross-section of an artery can be obtained with a spatial resolution of 1-2 mm and a temporal resolution of 25 ms, while averaging over 10 heart beats [94, 102].

Despite relatively low temporal resolution, MRI can be used for almost any blood vessel in the body without regard to overlying bone or bowel gas. Furthermore, precise location information is readily available in velocity measurements and the velocity data can be matched with anatomic images. 3D PC scans can be conducted on most commercial MRI scanners without hardware or software modifications, while spatially resolved quantitative velocity measurement with Doppler ultrasound is still in development and mostly used in research. Like ultrasound, MRI does not require the use of ionizing radiation, and it has no known long-term side effects. Because of projectile and interference hazards in the strong magnetic field, MRI is difficult to use on patients with life-support apparatus. Patients with metal implant such as cardiac pacemaker cannot have MRI scan.

Many factors may affect the accuracy of PC velocity measurements. It has been reported in a study of steady flow with computer simulation and *in vitro* scans [103] that limited resolution is the major obstacle to accurate flow measurement for both laminar

and plug flow. The results showed that at least 16 voxels must cover the cross section of the vessel lumen to obtain a measurement accuracy within 10%, and measurement accuracy was better for laminar flow than plug flow. For unsteady flow the accuracy has also been quantitatively assessed *in vitro* [104]. The overall root-mean-square (RMS) difference between the measured and analytic velocities, calculated according to the Navier-Stokes equations governing fluid flow, was 1.6 cm/s for nominally sinusoidal flow waveforms with peak velocities ranging from 51.6 cm/s to 59.8 cm/s. This RMS difference corresponded to 7.5% of the mean fluid velocity, which is similar to the reported accuracy of approximately 5% for MR PC velocimetry for steady flows [105, 106, 107, 108]. In stenotic flow or highly turbulent flow, PC velocity measurements are less accurate because the assumption that velocity is constant over each measurement (typically around 10 ms) is not valid. It has been reported in a study [109] with a 90% reduction stenotic phantom that velocity measurements can be in error by over 100% immediately upstream and downstream of the stenosis throat and by 20% far downstream of the throat in comparison with laser Doppler anemometer measurements taken at the same location, and the errors can be reduced to under 30% at all measurement locations through the use of MR sequences with high signal-to-noise ratios, low echo times, and thick slices. A later study [110] of single harmonic sinusoidal flow in a rigid bypass graft model showed a spatially and temporally averaged RMS error in velocity between 7.8% and 11.5% could be achieved with the aid of phase angle dynamic range extension. Spin saturation primarily and phase dispersion secondarily in complex transient recirculation zones were found to be significant contributors to overall error. The repeatability of *in vivo* aortic PC velocity measurement was confirmed statistically with high precision [111].

1.1.6 Computational fluid dynamics simulation

In principle, both Doppler ultrasound and phase contrast MRI can be used to measure *in vivo* carotid blood flow velocities directly and noninvasively with good precision (around 10% of peak velocity), and the latter is most promising by providing anatomic images matching the velocity measurements. In practice, the implementation of these techniques for *in vivo* wall shear stress estimation is still difficult, due to limited spatiotemporal resolution of these techniques near the vessel wall and the complex nature of carotid blood flow. It is also not straightforward to evaluate the *in vivo* accuracy

of the direct velocity measurements obtained with the imaging techniques because of the absence of a validated clinical flow quantification technique. For these reasons, computational fluid dynamics (CFD) simulations [112] have been widely used to complement the imaging techniques.

CFD simulations seek the numerical solution of flow conditions (such as velocity and pressure) subject to the governing (Navier-Stokes) equations and certain boundary conditions for the flow variables. In order to carry out a CFD simulation, the 3D lumen geometry needs to be reconstructed from medical images. Then the complex lumen geometry (often obtained with imaging techniques) is discretized into a large number of smaller but regular elements or volumes (typically tetrahedral or hexahedral) forming a computational mesh. At the boundaries of the lumen, such as the inlet and outlet of a segment of a vessel, the flow conditions need to be measured with imaging techniques. The discretization (in space and time) of the governing differential equations results in a system of algebraic equations, whose numerical solution yields the unknown flow variables at the mesh points. In contrast to direct velocity measurement experiments, it is easy in CFD simulations to change model parameters, such as flow rates or wall properties, to study the relationship between flow conditions and atherosclerosis progression.

Early image-based CFD studies statistically confirmed the relationship between wall shear stress and atherosclerosis progression [113, 114]. Most ultrasound-based CFD studies of coronary artery haemodynamics have assumed steady flow, with the implicit assumption that these models provide a faithful representation of the time-averaged haemodynamics. A study [51] of pulsatile coronary artery haemodynamics, carried out in a model of human coronary artery reconstructed from high-resolution CT images, showed that relatively small amounts of out-of-plane curvature had a dramatic effect on the skewing of the axial velocity profiles and orientation of the secondary flow vortices along the length of the vessel, and the time-averaged WSS behaviour from pulsatile flow studies was similar to that from a corresponding steady flow study. Other studies [115, 116] also highlighted the sensitivity of coronary artery blood flow patterns to local geometric features and the importance of subject-specific geometry in CFD simulations. The relatively large size and superficial location of the carotid arteries, unlike the coronary artery, make the carotid bifurcation an ideal target for image-based CFD techniques. A study [117] of normal subject-specific carotid bifurcation haemodynamics demonstrated how averaged or idealized carotid bifurcation

models can mask interesting haemodynamic features that may be of importance in understanding the localization of individual lesions. 3D maps of both WSS and wall thickness have been reconstructed in a subject-specific manner [118]. Results obtained from a patient with early atherosclerosis and a normal volunteer showed a qualitative association between increased wall thickness at the carotid bulb and low and oscillating shear. Recent studies [119] demonstrated the feasibility of carrying out detailed fluid-structure interaction modelling studies of realistic carotid bifurcation.

A number of studies showed that CFD simulations could reliably model flow in complex, realistic artery geometries [120, 121, 51]. Physical and experimental models of a human artery were constructed, physiologically flow conditions were measured with imaging techniques, and the same flow conditions were imposed on 3D CFD models. Generally good qualitative agreement was observed between experimental and numerical results. In a study [121] where time-resolved 2D PC MRI was used with models of a human carotid artery bifurcation specimen, differences in axial peak flow velocities between the experimental and numerical results were less than 10%. It is, however, difficult to determine whether a reconstructed model is faithfully reproducing the *in vivo* haemodynamic environment due to the absence of a gold standard technique for measuring velocities *in vivo*. PC MRI is most promising, but it still suffers from a number of practical, but not fundamental, limitations. Good qualitative agreement between computed and PC MRI imaged *in vivo* velocity patterns has been reported in several studies [122, 123, 118]. Hardware and software improvements may eventually make PC MRI a viable gold standard for *in vivo* velocimetry.

Many sources of error, assumptions and trade offs are involved in image-based CFD simulations. Errors in reconstructed geometries can lead to marked differences in computed WSS and flow separation patterns, amounting to 15%-35% differences in mean WSS [124, 125]. Another potential source of error is the inadequate resolution of the finite element mesh. It has been demonstrated that extremely fine local mesh densities were required to resolve WSS to within 10% [126]. Many modelling assumptions are often used in CFD simulations. Most studies assumed rigid vessel wall, but wall distensibility can produce apparent mismatches in the inlet and outlet flow rate boundary conditions that can only be reconciled with a distensible CFD model [127]. Another assumption often used is fully developed steady flow, which is obviously different from *in vivo* pulsatile flow. Small side branches arising from the vessel of interest are often ignored, largely because they are often difficult to resolve using

in vivo imaging techniques. Given all these limitations, it is reasonable to consider image-based CFD models satisfactory if they can predict WSS patterns, rather than absolute WSS values, faithfully [125, 112]. As high-resolution imaging techniques become more robust, and more realistic models of the flow conditions are adopted, it can be anticipated that image-based CFD simulations will produce more reliable quantitative results.

1.1.7 Undersampling

As described previously, limited spatial and temporal resolution has been the major limitation for PC MRI. Either for direct velocity measurement or for providing boundary conditions in CFD simulations, a higher resolution is most desirable. To cover the same region of interest, a higher spatial resolution requires a larger scan matrix and longer scan time. Higher temporal resolution requires faster measurement. Due to signal to noise trade offs and hardware physical limitations, it is difficult to increase acquisition speed substantially. An alternative approach, known as undersampling, is to collect only a subset of the signal normally required to reconstruct the images. In reconstruction prior knowledge or assumptions are incorporated into the sampled signal to recover the skipped signal. If a large fraction of the signal can be skipped and correctly recovered, scan time will be significantly reduced. This is especially beneficial for velocity measurement of pulsatile carotid flow because a time-resolved 3D PC MRI scan at a reasonable resolution can take more than two hours, making it difficult for *in vivo* studies. Shorter PC MRI measurements also benefit from reduced errors induced by subject motion and heart beat variability. Since in average the acquisition time for each image is shorter, more time frames can be collected in a limited number of cardiac cycles. This improves temporal resolution for both 2D and 3D scans.

Many undersampling methods have been proposed, which will be briefly reviewed in Chapter 3. The performance of these undersampling techniques depends on the degree of redundancy of the signal and the prior knowledge or assumptions used in image reconstruction. For example, in a time-resolved scan, different time frames of the same slice may have some part in common. In carotid scans, dynamic signal is limited in blood vessels and a large fraction of each image remains unchanged over the cardiac cycle. Therefore the signal has a higher degree of redundancy and a larger portion of the signal can be skipped in contrast to cardiac scans, where the moving

heart usually occupies a much larger area in the time frames. The prior knowledge or assumptions may be consistent or inconsistent with the skipped signal, which will obviously have an influence on the accuracy of the results in reconstruction. Another issue of undersampling is to determine which part of the signal can be skipped. This depends on the prior knowledge or assumptions. For example, if the image is known to be smooth, it may give good performance by skipping some of the high frequency signals.

Early undersampling methods exploit spatial redundancies in structural images. Scan time reduction is not significant and often at the cost of spatial resolution. Recent techniques [128] often undersample in both the spatial and temporal dimensions of the signal to achieve further acceleration. The most widely used one of such techniques, known as k-t BLAST (k-t Broad-use Linear Acquisition Speed-up Technique) [129], uses a predesigned spatial temporal sampling pattern and recovers skipped signal by adaptively incorporating low resolution training data collected separately. The technique has been widely applied in dynamic cardiac studies [130, 131, 132, 133, 134, 135]. Scans were usually accelerated by a factor of 4 or 5 so as to enable single breathhold 3D acquisitions. In volumetric imaging of the heart for the assessment of ventricular volume and ejection fraction [130, 132, 133], the results derived from 3D k-t BLAST scans showed good agreement with those from fully sampled 2D scans or standard multiple breathhold cine scans, and the calculated bias was found to be minimal (0.4-4%). In a cardiac flow measurement study [131], simulations of undersampling with fully sampled 2D data showed the relative RMS error in velocity obtained with the k-t BLAST method was between 7% and 9% when the scans were accelerated by a factor less than 5. In a study of 3D aortic blood flow [134], the k-t BLAST scans accelerated by a factor of 6 underestimated peak velocity by around 15% compared the reference scans and temporal blurring was observed. In an comparison [135] between 2D k-t BLAST PC MRI and Doppler ultrasound scans of aortic flow, all k-t BLAST scans showed significant correlations for peak velocity with Doppler ultrasound, but the scans accelerated by a factor of 6 or 8 showed significant underestimation. Difference in peak velocity was around 20% and in the ascending aorta stroke volume showed significant differences from Doppler ultrasound results for all k-t BLAST scans. For 3D carotid flow, it has been reported in a phantom study [136] that flow waveforms estimated from k-t BLAST reconstructions undersampled by a factor of 4 were in good agreement with those measured from the full data set. RMS

error was better than 7% for individual time frames.

As described previously, in a fully sampled PC MRI scan, the reported errors in velocity measurements are above or close to 10% of the peak velocity. The undersampling errors, calculated as the differences between the results from an undersampled scan and those from a similar fully sampled scan, need to be smaller than the potential 10% absolute errors. For carotid studies, this level of accuracy in velocity needs to be achieved at a high spatial resolution, preferably with in-plane image voxel sizes smaller than 1 mm. Since the performance of undersampling techniques depends on the degree of redundancy of the signal, and little has been reported about undersampling performance for *in vivo* MRI measurements of time-resolved velocity field in carotid arteries, it is necessary to carry out further *in vivo* carotid studies to evaluate available undersampling methods and develop new undersampling techniques.

1.2 Aim

This study aims to implement and evaluate undersampling techniques for time-resolved MR velocity measurement of carotid blood flow in order to reduce acquisition time for such scans.

In order to achieve this aim, the following objectives need to be addressed:

- Optimal settings of the parameters for each undersampling technique need to be determined;
- The techniques need to be implemented on a clinical MRI scanner for scans of volunteers;
- Undersampled results need to be compared with fully sampled results;
- Results obtained with different undersampling techniques need to be compared;
- Comparisons need to be carried out in 2D and 3D scans;
- The relationship between undersampling errors and the degree of undersampling needs to be studied.

1.3 Outline of chapters

In Chapter 2 the concepts and principles of MRI and velocity measurement are introduced. A basic description is provided about the physics of MRI signal generation and detection, the methods of spatial encoding, the controls of an MRI scanner during the scan, the methods of making time-resolved measurements, and the methods of velocity encoding. Recent undersampling techniques are briefly reviewed in Chapter 3. The k-t BLAST method is described in detail, and a new undersampling scheme is proposed to improve sampling efficiency and simplify image reconstruction. The method of the implementation of the undersampling methods on a clinical scanner is also introduced. These two methods are then tested in simulations in Chapter 4. Realistic data sets acquired in a fully sampled 2D scan are used as source data sets for simulated undersampling. Different settings of control parameters of each undersampling method are tested. The differences between the reconstruction results obtained from the undersampled data and the source data sets are used to evaluate undersampling errors. Optimal settings of the control parameters are selected accordingly. These settings are used in Chapter 5 where the two methods are implemented on a clinical scanner and tested in 2D *in vivo* scans. A fully sampled scan is also carried out to produce reference data sets. The results obtained with different undersampling methods and different sampling patterns were compared with those from the fully sampled scan in both spatial and temporal dimensions. In Chapters 4 and 5 the signals are undersampled only in two dimensions, one spatial and one temporal. The method which produced the best results in the 2D scans in Chapter 5 is tested in 3D *in vivo* scans in Chapter 6. With one extra dimension available for undersampling in 3D scans, further undersampling is tested. Comparisons are carried out between scans undersampled in two dimensions and those undersampled in three dimensions. Due to scan time limit, the spatial resolution of the *in vivo* scans is not high, and in those scans velocity is measured in only one direction. In Chapter 7 a flow phantom is used to test undersampling methods for high resolution scans and velocity measurements in three directions. Results from the scans undersampled in three dimensions are compared with those from a fully sampled scan in the same way as in the *in vivo* tests. Velocity patterns are also compared. Chapter 8 summarises the results obtained in previous chapters and suggests future work.

Chapter 2

Introduction to MR Flow Measurement

2.1 Introduction

In a magnetic field, certain atomic nuclei will re-emit energy in the form of radio signals if they are stimulated by radio waves of a particular frequency. This phenomenon is known as nuclear magnetic resonance (NMR) [137, 138]. Since 1946 it has been applied in the study of the structure of chemicals and interactions between nuclei in various materials and biological systems. In 1973 it was reported that an image of the distribution of the nuclei in the sample could be obtained by spatially encoding the emitted signal [139, 140]. This process is known as Magnetic Resonance Imaging (MRI). Since then MRI has been widely used in many healthcare areas including carotid flow measurement.

In this chapter the principles of MRI and velocity measurement are introduced. A basic description is provided about the physics of MRI signal generation and detection, the methods of spatial encoding, the controls of an MRI scanner during the scan, the methods of making time-resolved measurements, and the methods of velocity encoding.

2.2 Principles of MRI

2.2.1 NMR signal and detection

A comprehensive explanation of the induction of the MR signal requires a background in quantum mechanics [141]. An alternative description through the principles of classical mechanics and magnetism is not as rigorous as that through quantum mechanics but is easier to understand. The simpler explanation will be used in following descriptions. More details of NMR principles can be found in standard texts [141, 142, 143].

Nucleons (protons or neutrons) in atomic nuclei have an intrinsic angular momentum or "spin". When protons or neutrons exist in pairs in a nucleus, their spins will cancel out. If a nucleus contains an unpaired proton, an unpaired neutron, or both, such as 1H, 13C, 19F, and 31P, the nucleus will show a net spin. With the associated electric charge distribution of each nucleon, the net spin or rotation of the nucleus produces a magnetic field and the nucleus can be considered to act as a minute magnetic dipole. Physically it is represented by a vector known as magnetic moment. In an object that contains a large number of such spins, the macroscopic magnetization of the object is the vector sum of all the microscopic magnetic moments. Without the influence of an external magnetic field, the orientations of the microscopic magnetic moments are random and the object shows no macroscopic magnetization. In the presence of an external static magnetic field, the spins tend to align themselves with the external field. In the object the spins whose magnetic moments are in the same direction as the external field will have a larger population than those in the opposite direction. This leads to a bulk magnetization $\vec{M}$ in the direction of the external field. At equilibrium the magnitude of this bulk magnetization is given by the Boltzmann distribution [88]. For proton (1H) the magnitude is given in Equation (2.1).

$$\|M\| = \frac{\gamma^2 \cdot \hbar^2 \cdot B_0 \cdot N_s}{4 \cdot K \cdot T} \tag{2.1}$$

In Equation (2.1) γ is the gyromagnetic ratio for the nucleus (proton), N_s is the number of spins in the sample, B_0 is the strength of the external field, T is the absolute temperature, $\hbar$ is the Plank constant, and K is the Boltzmann constant. Equation (2.1) suggests the magnitude of the bulk magnetization is proportional to the spin density and the external field strength. Lower temperature can also result in a larger magnitude.

The behaviour of the bulk magnetization in an external magnetic field is described by the Bloch equation [88], as shown in Equation (2.2).

$$\frac{\partial \vec{M}}{\partial t} = \gamma \cdot \vec{M} \otimes \vec{B} \tag{2.2}$$

In Equation (2.2) $\vec{B}$ is the applied external field and $\otimes$ means vector cross product. The Bloch equation shows the bulk magnetization $\vec{M}$ experiences a torque in the direction of the cross product of $\vec{M}$ and $\vec{B}$. If $\vec{M}$ and $\vec{B}$ are in the same or opposite direction, the cross product is zero and there will be no torque. $\vec{M}$ retains its direction, as shown in Figure (2.1).

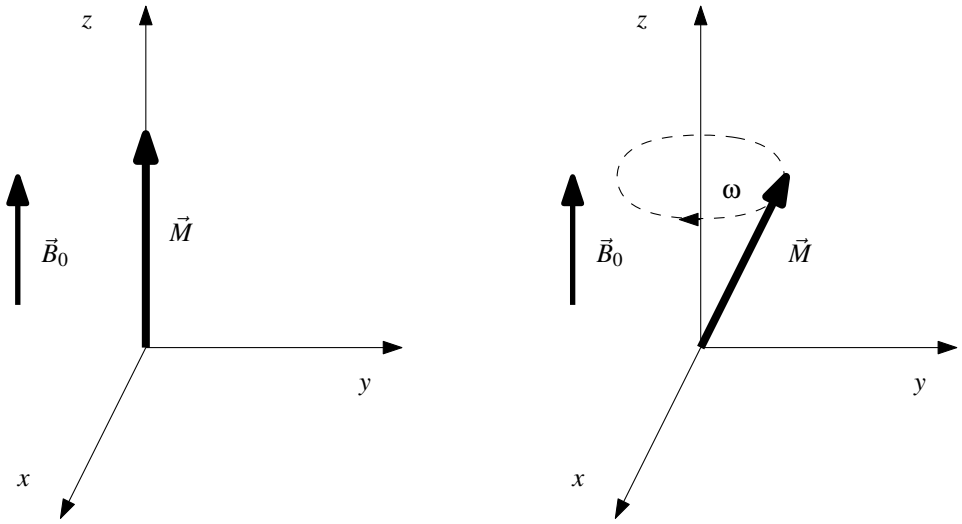

Figure 2.1: Bulk magnetization remains unchanged when it is in the same direction as the external field (left). It will rotate around the direction of the external field if not in that direction (right).

Conventionally in the description of an NMR experiment the z-axis is placed along the direction of the external static field. If only the static field $\vec{B}_0$ is present ($\vec{B}$ is time-independent), and $\vec{M}$ is not in the same or opposite direction of $\vec{B}$, the torque will make $\vec{M}$ rotate around $\vec{B}_0$ or z-axis. The angular velocity $\vec{\omega}$ of the rotation is given in Equation (2.3).

$$\vec{\omega} = -\gamma \cdot \vec{B}_0 \tag{2.3}$$

In Equation (2.3) $\vec{\omega}$ is known as the Larmor frequency. It should be noticed in this

case the projection of the bulk magnetization in the transverse plane (x-y plane) is not zero and also rotates at the Larmor frequency, as shown in Figure (2.2). This can be used to induce signal in a radio frequency (RF) coil placed perpendicular to the x-y plane, as shown in Figure (2.2).

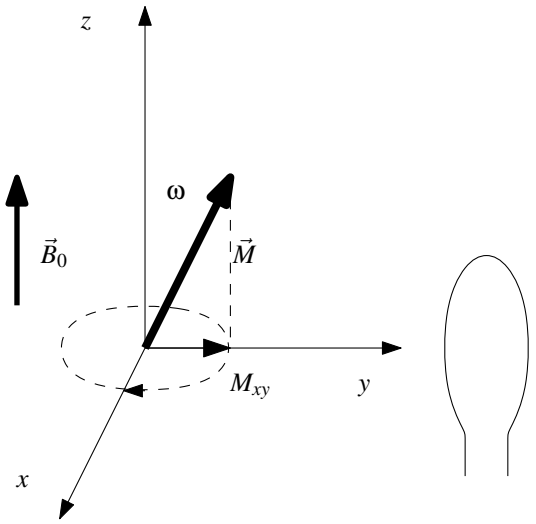

Figure 2.2: The transverse component of the bulk magnetization rotates around the direction of the external field and signals can be induced by this in a radio frequency coil perpendicular to the transverse plane.

As described before the bulk magnetization at equilibrium is in the same direction as $\vec{B}_0$. In order to detect the bulk magnetization it is necessary to "flip" $\vec{M}$ toward the x-y plane to generate the component perpendicular to $\vec{B}_0$. This can be achieved by applying an additional magnetic field $\vec{B}_1$ in the transverse plane via radio waves at appropriate frequencies (RF pulse), as shown in Figure (2.3).

It should be noted the frequency of the RF pulse has to match the Larmor frequency of the spins, which is proportional to the static field strength and the sample-related gyromagnetic ratio. According to the Bloch equation, $\vec{M}$ will experience an additional torque from $\vec{B}_1$ and rotate around $\vec{B}_1$. This will reorientate $\vec{M}$ and the transverse magnetization can be observed. The angle θ between $\vec{M}$ and $\vec{B}_0$ due to the application of the RF pulse is known as flip angle. If the flip angle is 90°, the magnitude of the transverse magnetization component equals the magnitude of the bulk magnetization and maximum signal can be detected with the coil. If the flip angle is 180°, $\vec{M}$ is still perpendicular to the transverse plane and no signal can be detected.

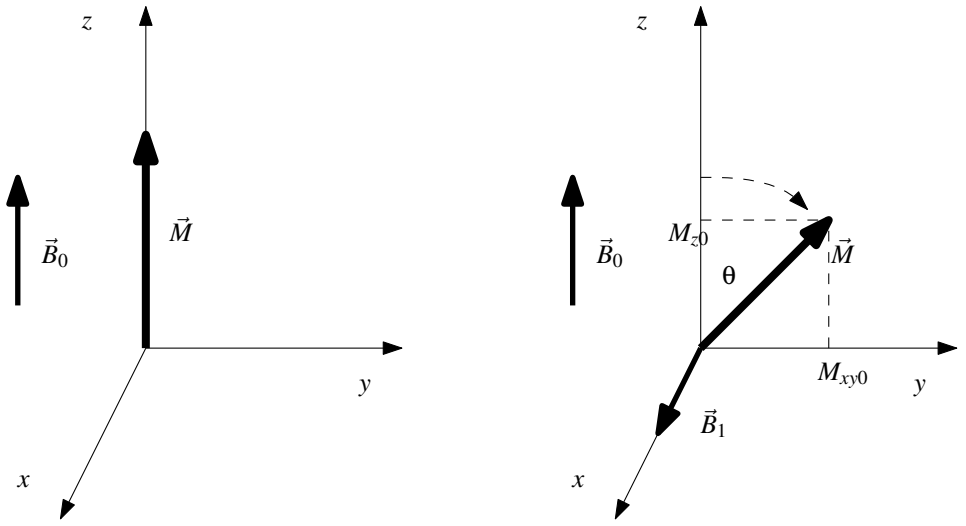

Figure 2.3: The direction of the bulk magnetization can be changed by applying an additional magnetic field in the transverse plane via radio waves at appropriate frequencies.

2.2.2 Relaxation

Usually in MRI experiments the RF pulse is very short and it is stopped after the desired flip angle is reached. The bulk magnetization then tends to return to its equilibrium state. This process is known as relaxation. It is characterized by two sample-related time constants: the longitudinal (spin-lattice) relaxation time (T_1) and the transverse (spin-spin) relaxation time (T_2). T_1 represents the time needed for the magnitude of the longitudinal component M_z of the bulk magnetization to return to 63% of its initial value after the RF pulse [144], as shown in Equation (2.4).

$$\frac{\partial M_z(t)}{\partial t} = \frac{M_z(t) - M_{z0}}{T_1} \tag{2.4}$$

In Equation (2.4), M_{z0} is the initial value of M_z at the start of relaxation. Physically this happens due to the nuclei losing energy to their environment or the surrounding lattice. When the longitudinal component of the bulk magnetization is restored, another RF pulse can be applied. T_2 reflects how fast the magnitude of the net transverse magnetization component M_{xy} diminishes exponentially because of the internuclear magnetic interactions and the energy exchange between spinning nuclei, as shown in

Equation (2.5).

$$\frac{\partial M_{xy}(t)}{\partial t} = \frac{M_{xy}(t)}{T_2} \tag{2.5}$$

In practice a shorter T_2^* is often used [145] to include the effects of magnetic field inhomogeneity and the application of the magnetic field gradients which will be described in later sections.

For example, a small packet of spins immersed in an external static magnetic field $\vec{B}_0$ has a bulk magnetization $\vec{M}$ in the same direction of $\vec{B}_0$ at equilibrium. Let $\vec{B}_0$ be along the z-axis, the bulk magnetization vector $\vec{M}$ will also be along the z-axis, too. If an additional magnetic field $\vec{B}_1$ (by an RF pulse in the appropriate frequency) is applied along the x-axis for a very short period and tips the magnetization vector $\vec{M}$ away from the z-axis by a flip angle θ, at the end of the RF pulse, the magnetization vector will end up with a longitudinal component M_{z0} on the z-axis and a transverse component M_{xy0} along the y-axis, as shown in Figure (2.3). If the initial magnitude of $\vec{M}$ is M_0, the magnitudes M_{z0} and M_{xy0} are given in Equation (2.6).

$$\begin{aligned} M_{z0} &= M_0 \cdot cos(\theta) \\ M_{xy0} &= M_0 \cdot sin(\theta) \end{aligned} \tag{2.6}$$

Since the time of the applied RF pulse is very short, relaxation during the RF pulse can be neglected. After the RF pulse, the relaxation applies while the bulk magnetization vector rotates around the static magnetic field $\vec{B}_0$ according to the Bloch equation, as shown in Equation (2.7).

$$\begin{aligned} \frac{\partial M_z(t)}{\partial t} &= \gamma \cdot M_{xy}(t) \cdot B_0 - \frac{M_z(t) - M_{z0}}{T_1} \\ \frac{\partial M_{xy}(t)}{\partial t} &= \gamma \cdot M_z(t) \cdot B_0 - \frac{M_{xy}(t)}{T_2} \end{aligned} \tag{2.7}$$

The longitudinal component and the transverse component of $\vec{M}$ will be time dependent, as shown in Equation (2.8).

$$\begin{aligned} M_z(t) &= M_0 \cdot (1 - exp(-t/T_1)) + M_{z0} \cdot exp(-t/T_1) \\ M_{xy}(t) &= M_{xy0} \cdot exp(-t/T_2) exp(-i \cdot \omega \cdot t) \\ \omega &= \gamma \cdot B_0 \end{aligned} \tag{2.8}$$

Since the transverse component rotates around $\vec{B}_0$ with the bulk magnetization vec-

tor at the angular velocity of the Larmor frequency, in Equation (2.8) M_{xy} is represented in the form of a complex number. Conventionally NMR or MRI signals induced by M_{xy} are also represented as complex numbers whose phases change at the Larmor frequencies of the spins in the sample.

If no magnetic fields other than $\vec{B}_0$ are applied afterwards the bulk magnetization vector will precess in this way until the transverse component is reduced to zero, as shown in Figure (2.4).

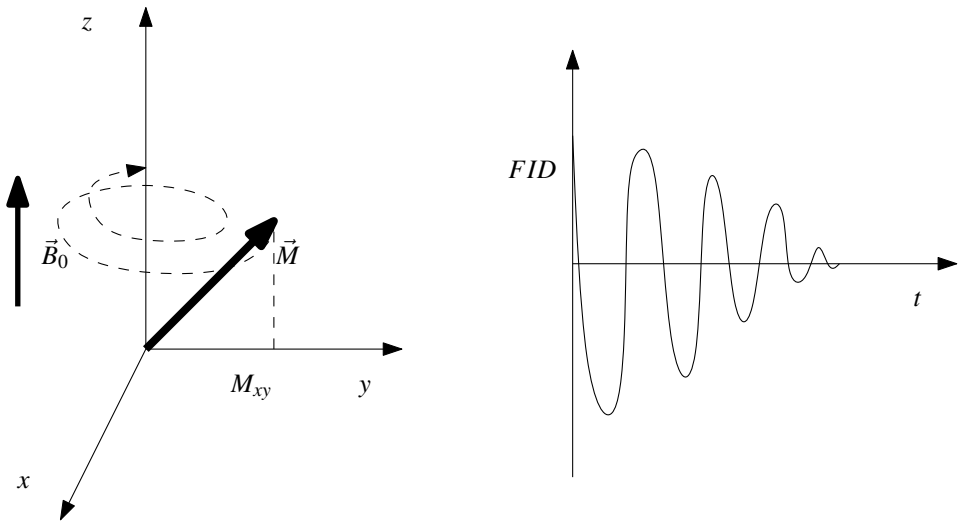

Figure 2.4: Free precession of the bulk magnetization (left) and the free induction decay signal (right).

The process is known as free precession and the signal decay detected with an RF coil from the transverse component of the bulk magnetization in free precession is known as Free Induction Decay (FID).

2.2.3 Spatial encoding

In an FID signal there is no information about the spatial locations of the spins. By manipulating the RF pulse or the external magnetic field spatial information can be encoded into the signal for imaging purposes. This process is known as spatial encoding.

As described previously, to induce an FID signal the frequency of the RF pulse has to match the Larmor frequency of the spins. Those spins whose Larmor frequencies are different from the frequency of the RF pulse will give no signal. This allows signal

to be selectively excited at different locations. The Larmor frequency is proportional to the strength of the static field. A magnetic field gradient can be applied to make the static field change linearly along one spatial dimension, as shown in Figure (2.5).

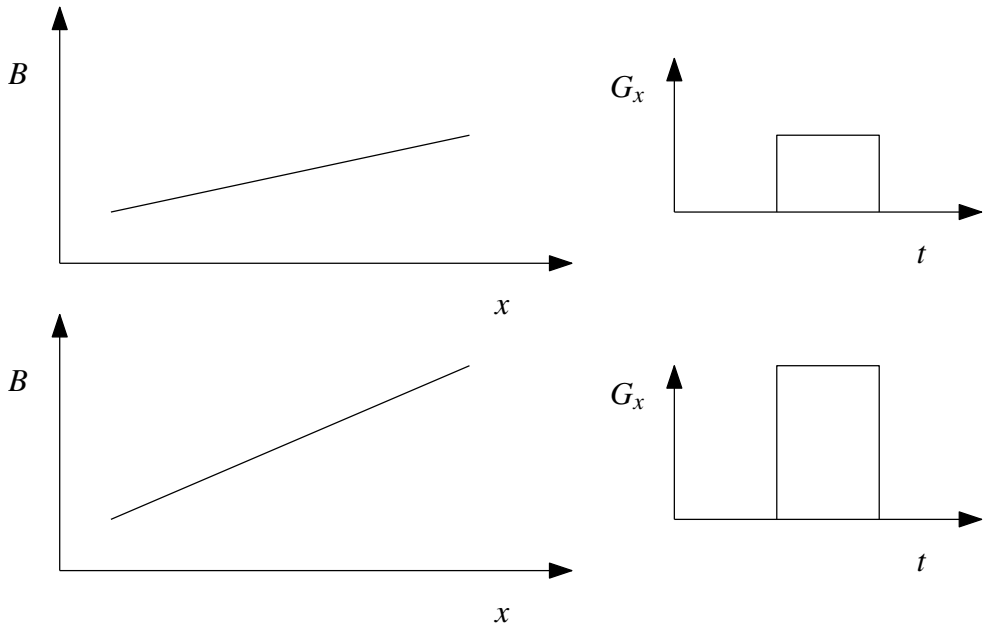

Figure 2.5: Two magnetic field gradients of different strengths (the top row and the bottom row). The controls of the gradients are shown on the right.

When the gradient is applied the Larmor frequency of the spins also vary linearly along the spatial dimension. If an RF pulse of a frequency band is applied together, only those spins in a slice of the scanned object corresponding to the frequency band will be excited, as shown in Figure (2.6). This is known as slice selection.

If different FID signals change at different frequencies, they can be separated in the Fourier domain as a frequency spectrum. This can be achieved by applying a gradient during signal acquisition. When the gradient is applied the spins will have Larmor frequencies that vary linearly along the direction of the gradient. The acquired signals from different locations in that direction will also have different frequencies. The frequency spectrum of the acquired data amounts to a one-dimensional projection of the scanned object, as shown in Figure (2.7). This is known as frequency encoding. The gradient applied for frequency encoding is usually known as a readout gradient.

With slice selection and frequency encoding, only two of the three spatial dimensions are resolved. Since NMR signals are complex numbers, the phases of the signals

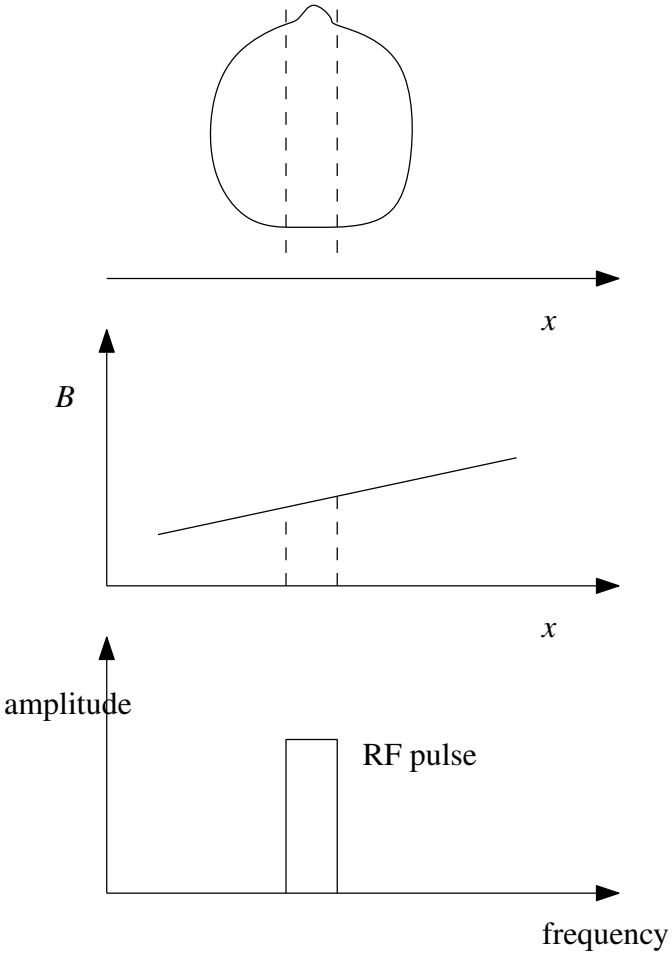

Figure 2.6: Slice selection with a linear gradient and an RF pulse of a frequency band.

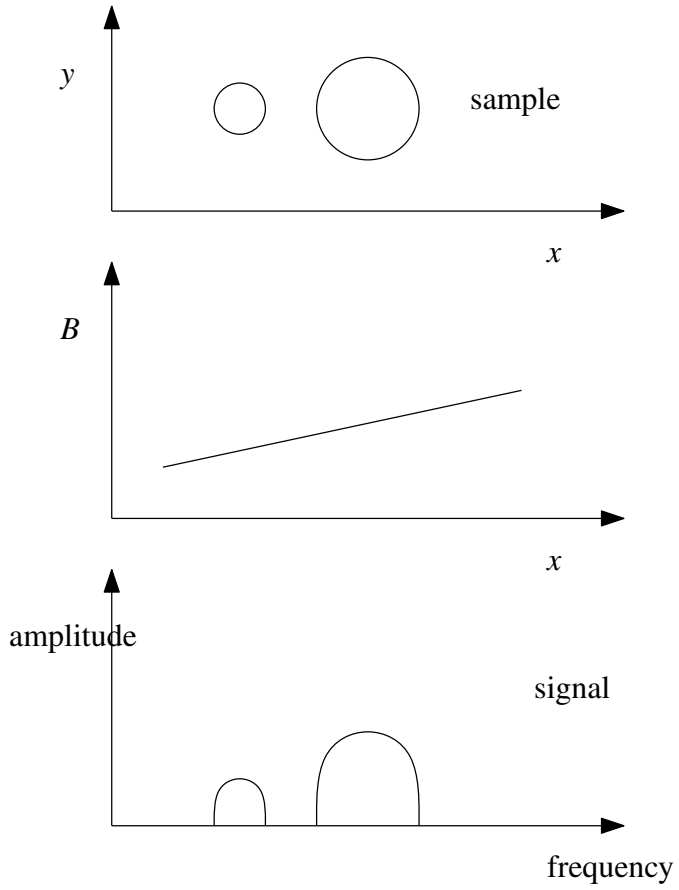

Figure 2.7: Frequency encoding with a linear gradient.

can also be used for spatial encoding, which is known as phase encoding. Similar to frequency encoding, a gradient is applied for a short duration along one direction after signal excitation, but before signal acquisition. When the gradient is switched on the angular velocities of the spins are different at different locations. After the gradient is switched off the angular velocities of all the spins return to their original values before the gradient. This leads to phase differences at different locations, as shown in Figure (2.8). In the Fourier domain the signals with different phases can be separated. In order to separate signals from many locations in one dimension, phase encoding has to be repeated many times with different settings of the phase encoding gradient.

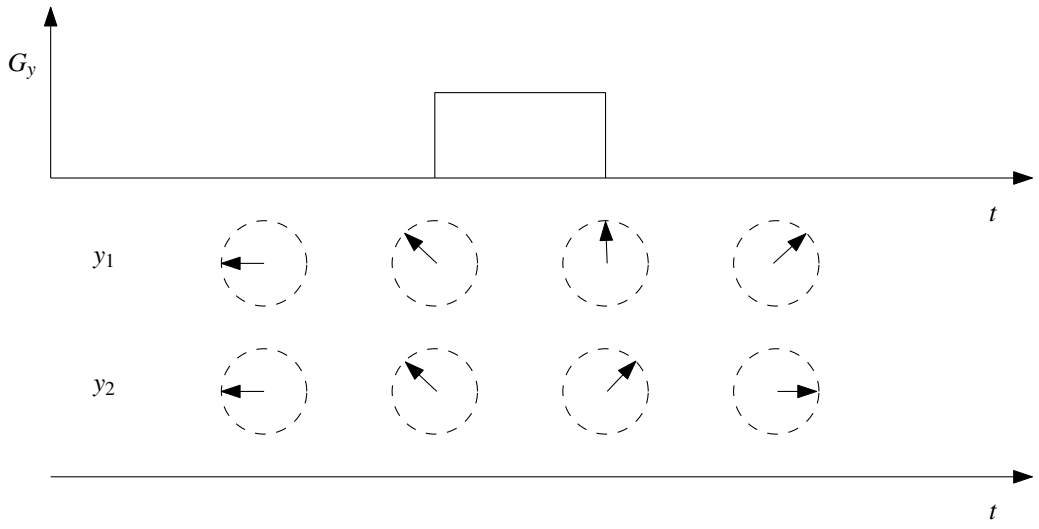

Figure 2.8: Phase encoding with a field gradient. Two spins at different positions ($y1$, $y2$) received different phase shifts.

For example, if the static field $\vec{B}_0$, the RF pulse $\vec{B}_1$ and the gradient g_z for slice selection is applied along the z-axis, a slice in the x-y plane will be selected. By applying the phase encoding gradient g_y for a duration of Δt and the readout gradient g_x, as shown in Figure (2.9), the acquired signal can be represented in the form shown in Equation (2.9).

$$s(t) = \int \rho(x,y) \cdot exp(-i \cdot \gamma \cdot B_0 \cdot t - i \cdot \gamma \cdot g_x \cdot x \cdot t - i \cdot \gamma \cdot g_y \cdot y \cdot \Delta t) \qquad (2.9)$$

In Equation (2.9) $\rho(x,y)$ represents the spin distribution in the selected slice. Since it is not difficult to filter the high frequency variation of the signal due to the strong

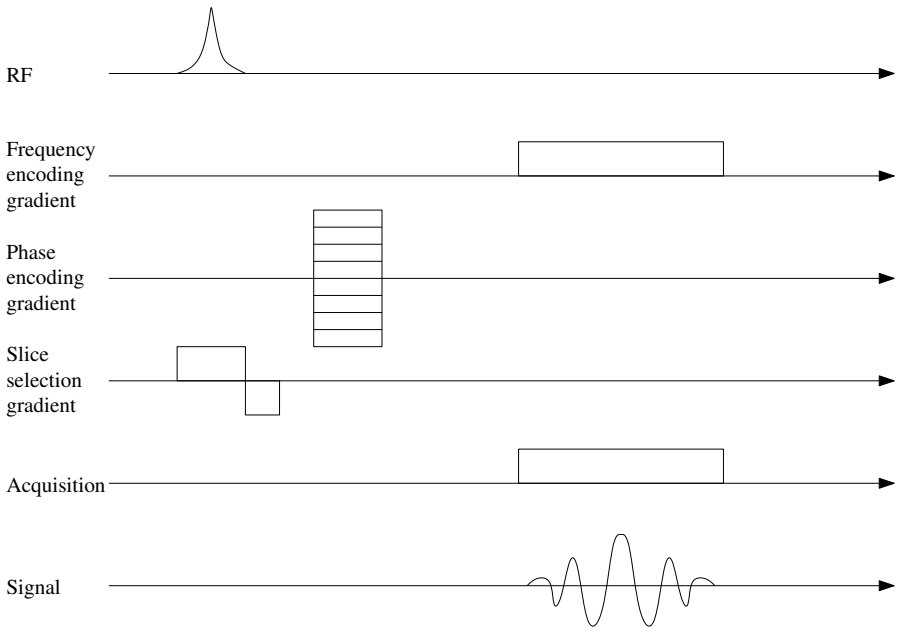

Figure 2.9: A schematic of a scan with slice selection, phase encoding and frequency encoding.

static field $\vec{B}_0$, the term with B_0 can be neglected, as shown in Equation (2.10).

$$s(t) = \int \rho(x,y) \cdot exp(-i \cdot \gamma \cdot g_x \cdot x \cdot t - i \cdot \gamma \cdot g_y \cdot y \cdot \Delta t) \tag{2.10}$$

Normally when the phase encoding step is repeated, the strength of the phase encoding gradient changes linearly, as shown in Equation (2.11).

$$g_y(k) = k \cdot g_{y0} \tag{2.11}$$

In Equation (2.11) k is the index of the phase encoding steps and g_{y0} is the base value of g_y. Equation (2.12) can be derived by combining Equation (2.10) and Equation (2.11).

$$s(t,k) = \int \rho(x,y) \cdot exp(-i \cdot \gamma \cdot g_x \cdot x \cdot t - i \cdot \gamma \cdot k \cdot g_{y0} \cdot y \cdot \Delta t) \tag{2.12}$$

Equation (2.12) can be written in a similar form to the Fourier transform, as shown

in Equation (2.13).

$$\begin{aligned} s(k_x,k_y) &= \int \rho(x,y)\cdot exp(-i\cdot k_x\cdot x - i\cdot k_y\cdot y) \\ k_x &= \gamma\cdot g_x\cdot t \\ k_y &= \gamma\cdot k\cdot g_{y0}\cdot \Delta t \end{aligned} \tag{2.13}$$

Equation (2.13) suggests the acquired signal will be the Fourier transform of the spin distribution $\rho(x,y)$ in the plane if appropriate settings of the gradients are applied.

Phase encoding can also be applied along both the y-axis and the z-axis. In this case slice encoding is replaced by phase encoding along the z-axis. In each repetition signals are excited at all the locations along the z-axis, as shown in Equation (2.14).

$$s(k_x,k_y,k_z) = \int \rho(x,y,z)\cdot exp(-i\cdot k_x\cdot x - i\cdot k_y\cdot y - i\cdot k_z\cdot z) \tag{2.14}$$

In Equation (2.14) $\rho(x,y,z)$ is the 3D spin distribution in the scanned object and k_y, k_z are the indices for the phase encoding steps. The signal is still the Fourier transform of the spin distribution. Conventionally the Fourier domain defined by Equation (2.14) is known as k-space. Images can be obtained by applying inverse Fourier transform to k-space data.

The concept of k-space is very useful because MRI signals are collected in k-space and the signal representation in k-space is equivalent to that in normal image-space. According to the properties of the Fourier transform, the sampling range in k-space determines the resolution in image-space, and the sampling resolution in k-space determines the image size or field of view (FOV). A complete coverage in k-space will be sufficient to produce a complete data set in image-space, and vice versa. The signals near the centre of k-space correspond to the spatially smooth contents in the images, and the signals near the edges of k-space represent the sharp features in the images. These properties work beyond the presented example and apply in general MRI experiments. As shown in Figure (2.10), in the presented example k-space is covered line by line. Each acquisition or phase encoding step covers a line in k-space. For each phase encoding step the data acquired in this fashion is often known as a k-space line. This method of sampling in k-space is not the only way. So long as k-space is reasonably covered, the order of the k-space positions or locations of the positions can be different depending on implementation requirements. The method of sampling in k-space or the route of travelling over k-space is often known as a k-space sampling pattern or

a k-space trajectory. The trajectory described in the example samples k-space at the positions on a Cartesian grid. Images can be obtained by directly applying discrete inverse Fourier transform to the collected signal. This is known as a Cartesian trajectory and it is the most widely used trajectory. Other types of trajectories have also been proposed [143], such as projection or spiral trajectory, as shown in Figure (2.10).

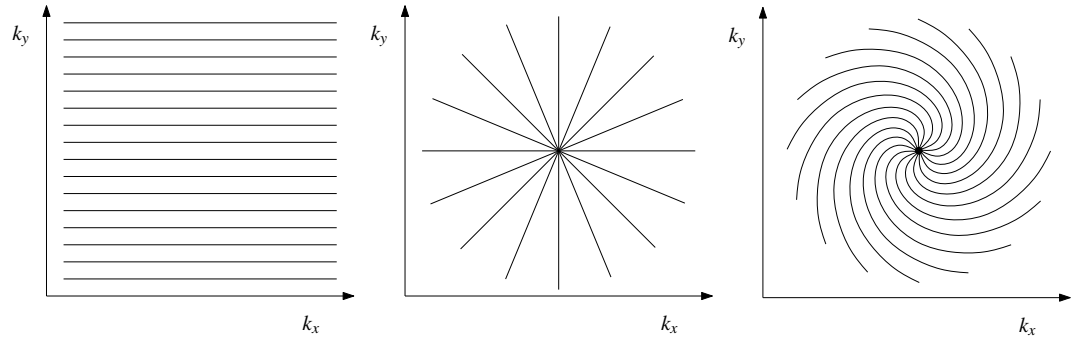

Figure 2.10: Three different k-space trajectories: Cartesian (left), projection (middle) and spiral (right).

2.2.4 Image contrast in MRI

The images obtained in the example presented in last section are maps of the spin distribution or proton density in the scanned object. Proton density depends on water content. Typical values of water content of human tissues are given in Table (2.1) [146]. Since the proton densities of soft tissues and blood are much higher than those of bones, MRI is more suitable for imaging of soft tissues and blood than for skeletal imaging.

	water content (%)
gray mater	70.6
white mater	84.3
heart	80.0
blood	93.0
bone	12.2

Table 2.1: Water content of human tissues

Most other contrasts result from other factors in addition to proton density contrast. The results are often in the form of proton density maps weighted by contributions from other factors.

Image contrast may also be made T_1 or T_2 dependent. T_2 contrast is straightforward. If some tissue has a shorter T_2 its signal will diminish faster. T_1 contrast is introduced through an RF pulse. If the flip angle is 180° no signal can be detected in the transverse plane. If an RF pulse is applied when little of the longitudinal component of the bulk magnetization is restored, the signal excited can be very weak. Since different tissues have different values of T_1 and T_2, these contrasts can be enhanced by changes in timing or strength of gradients and RF pulses.

The strength of MRI lies in the fact that many types of sample-related information can be encoded into MR signal via manipulation of gradients and RF pulses. Besides T_1 and T_2 contrasts, many other properties of the scanned object can be used as contrast, such as diffusion [147, 148] or blood oxygenation level [149]. Blood velocity can also be measured with MRI. This will be described in detail in the following sections.

2.2.5 Noise and artefacts

Many types of noise and artefacts can be observed in real MR images. As in any signal measurement, there is always background noise. In MRI, it might be electrical noise from the scanner or interference from other sources. This type of noise is usually characterized by the Signal-to-Noise Ratio (SNR). A common method to improve SNR is to repeat acquisition and average the images collected under same conditions.

Fat can be a source of artefacts [150]. It tends to have high signal at all contrasts, which can mask pathologies, and it can cause artefacts due to its structure, known as chemical shift artefacts. For example, the hydrogen atoms in fat have a lower Larmor frequency than those in water. In images the position of fat signals will be shifted if normal spatial encoding is applied. These chemical shift artefacts can be suppressed by selectively exciting only certain type of nucleus [151].

Imperfect spatial encoding may be one of the sources of artefacts. So far in the descriptions of spatial encoding the static field is assumed to be absolutely uniform across the sample. This is very rare in reality. The presence of a sample can also lead to inhomogeneities of the static field and the field generated by the RF pulse. Absolute linearity of the gradient fields cannot be guaranteed either. Then in the reconstructed

images some features of the sample may not appear at their true locations. Many methods have been proposed to correct this type of artefact [152, 153, 154, 155, 156].

Sampling limit can also be the reason of artefacts. The sampling resolution in k-space is always limited so sometimes the FOV in image-space is not large enough to cover the whole scanned object. In the images the signals from outside of the FOV will be wrapped around into the FOV, as shown in Figure (2.11). This can be corrected by increasing sampling resolution in k-space. The sampling range in k-space is also limited which determines the image resolution. If some image features are smaller than the image pixels, they cannot be correctly represented in images. This is known as partial volume effect, which can be avoided by increasing the sampling range in k-space.

Another source of artefact is unexpected sample displacement or motion during the scan, such as patient motions or blood flow in vessels. Improving scan speed helps to reduce this type of artefacts. Breath holding can be used to temporarily reduce respiratory motion. For repeating motions such as heart beating gating can be applied. This will be described in detail in the following sections.

Some noise and artefact are unavoidable. With the development of scanner hardware it is only possible to reduce them into an acceptable range. Some artefacts can be corrected with additional information such as a field map used for the corrections of field inhomogeneity artefacts. Some artefacts can be utilized to provide useful information such as blood flow velocities.

2.2.6 Pulse sequences

In scans a sequence of instructions is executed on the scanner to control the RF pulses, gradients and data acquisition. This is known as a pulse sequence. An example of a simple pulse sequence has been shown previously in Figure (2.9). A pulse sequence defines most settings of an MRI scan, such as the k-space trajectory, the contrast and the signal format. Two important control parameters, the repetition time T_R and the echo time T_E, are also defined with pulse sequences. The spin echo sequence [147] and the gradient echo sequence [157, 158, 159] are the two most basic imaging pulse sequences from which most other pulse sequences can be derived. The pulse sequence implemented in the following chapters for flow measurement is also based on the gradient echo sequence.

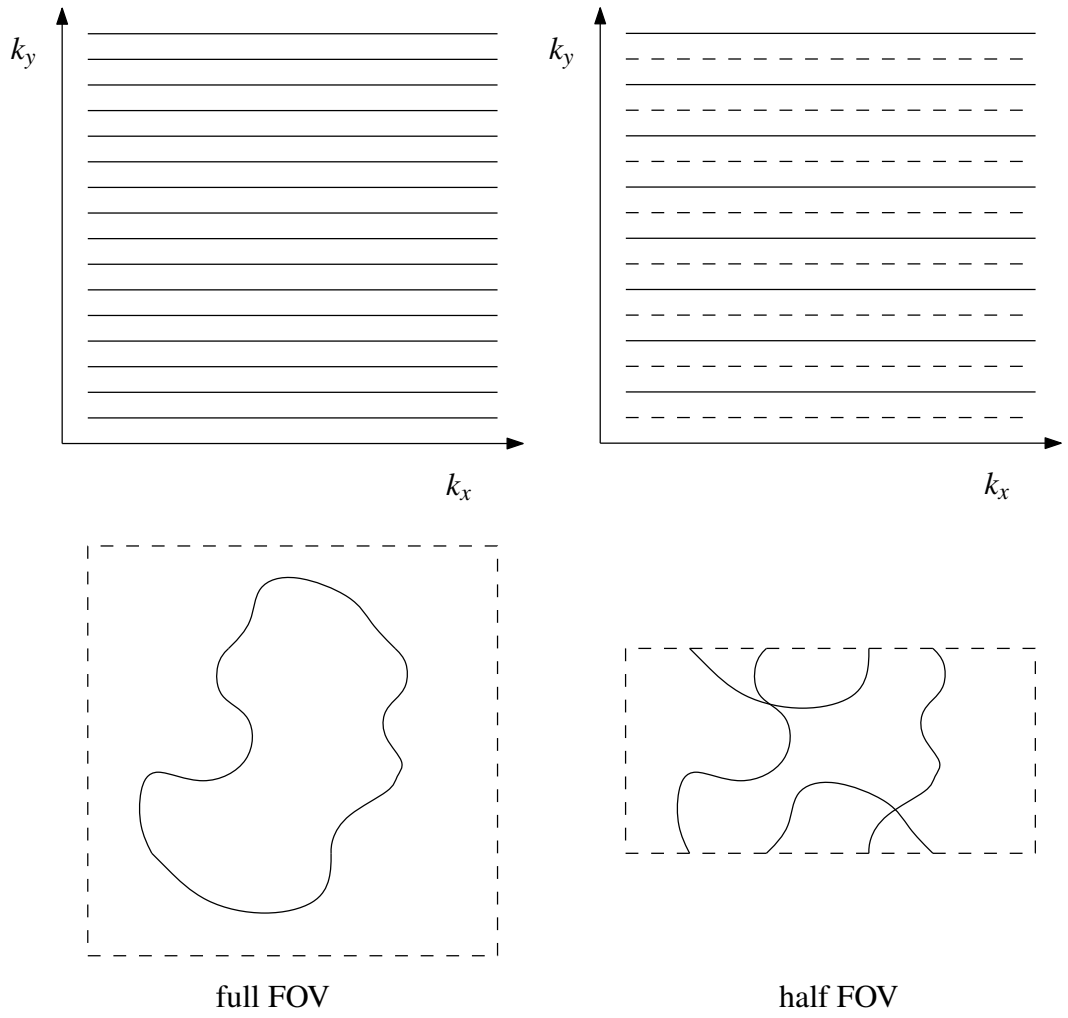

Figure 2.11: The signals from outside of the FOV are wrapped around into the FOV when k-space sampling resolution is not high enough. Dotted lines represent k-space lines omitted from acquisition. Doubling k-space line spacing gives halving of field of view.

The spin echo sequence is displayed in Figure (2.12). It is very similar to the pulse sequence shown in Figure (2.9). The slice selection, the phase encoding, and the frequency encoding gradient remain unchanged. The difference is an additional RF pulse applied between the phase encoding and the readout gradient. The first RF pulse is usually a 90° RF pulse. Due to field inhomogeneity after signal excitation the rotation speeds of the microscopic magnetic moments are slightly different. Up to the moment before the second RF pulse they have different phases and most components in the transverse plane cancel out as shown in Figure (2.13). This is known as dephasing and it is also the reason a much shorter T_2^* is often used instead of T_2, as mentioned previously. By applying the second RF pulse, which is normally a 180° and known as a refocusing pulse, the transverse components of the magnetic moments are flipped to the opposite side of the transverse plane, as shown in Figure (2.13). Phase gains are turned into phase losses. After the second RF pulse the magnetic moments keep rotating at different speeds. The phase differences will be reduced to zero at the echo time and a strong signal will appear, which is known as an echo. This reverse process of dephasing is known as rephasing. In Figure (2.12) the first frequency encoding gradient lobe and the slice encoding lobe in negative strength are also applied for rephasing. The time between the first RF pulse and the echo is known as the echo time T_E. After signal readout the sequence is repeated for other phase encoding steps. The time between subsequent 90° RF pulses is known as the repetition time T_R. T_R and the number of phase encoding steps determine the total scan time of the sequence. Appropriate settings of T_E and T_R help to control the amount of T_1 and T_2 contrast in MR images. The advantage of the spin echo sequence is it is robust against field inhomogeneity and chemical shift effects at the echo due to use of the refocusing RF pulse.

Figure (2.14) shows the timing diagram of the gradient echo pulse sequence. It uses a gradient pulse for dephasing and rephasing instead of the refocusing RF pulse used in the spin echo sequence. Since the dephasing due to field inhomogeneity is not avoided, the signal echo amplitude is determined by the shorter T_2^* rather than T_2. The gradient echo sequence is more sensitive to field inhomogeneities than the spin echo sequence. Without the refocusing RF pulse T_E and T_R can be shorter. If T_R is short and the flip angle of the first RF pulse is 90° the longitudinal component of the bulk magnetization may not be restored when the next signal excitation is applied. For this reason in scans with the gradient echo sequence the flip angles are normally small, between 10° and 60°, so after signal excitation the longitudinal component of the bulk

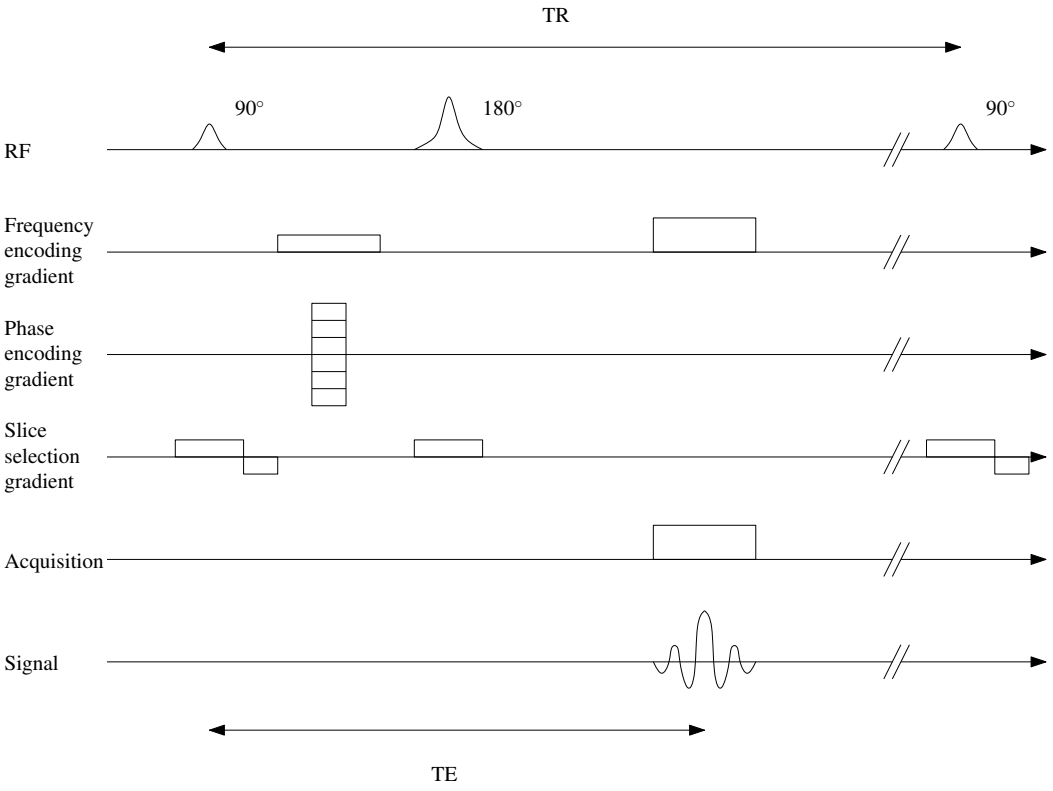

Figure 2.12: A schematic of a spin echo pulse sequence.

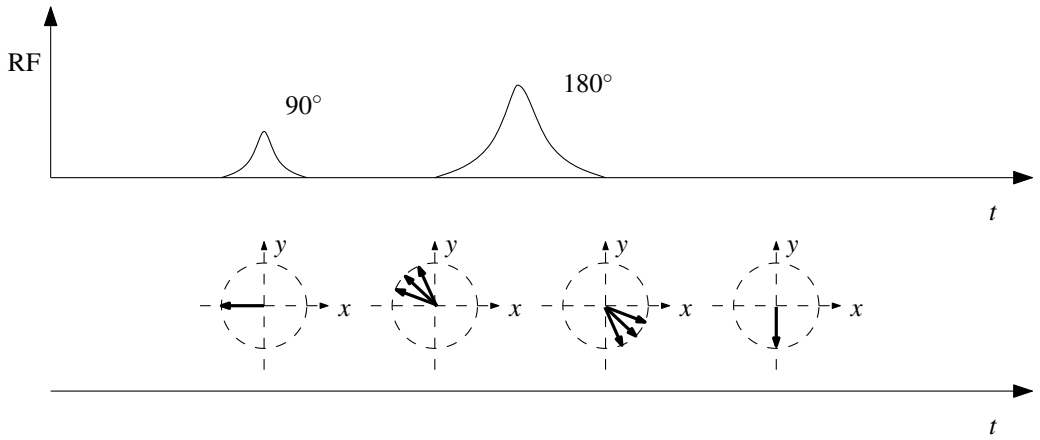

Figure 2.13: Dephasing and rephasing in a spin echo scan.

magnetization can be restored in a shorter duration. This also deposits less RF power in patient.

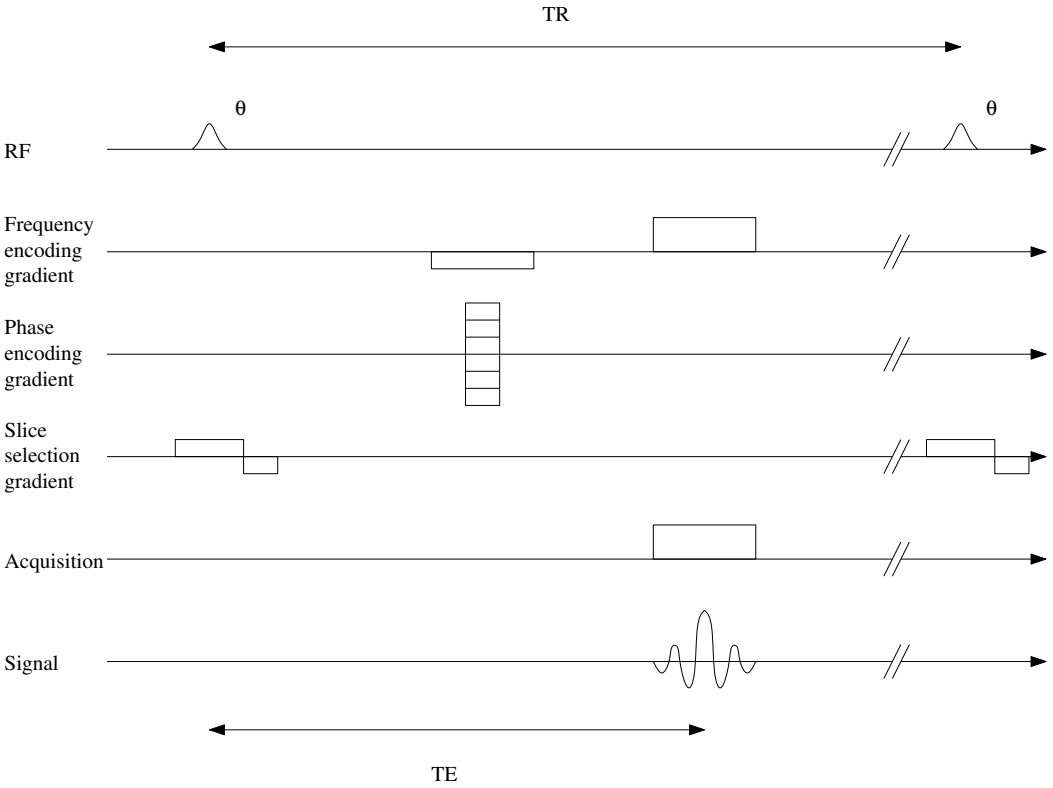

Figure 2.14: A schematic of a gradient echo pulse sequence.

2.2.7 Time-resolved MRI and Gating

In some cases MR signal changes over time, such as a heart beating or blood flowing. This adds an extra temporal dimension to the signal, and the signal acquisition is carried out in the so-called k-t space, an extension to the static k-space. The timing of the samples needs to be recorded, which is known as gating [160]. For carotid scans, most signal changes are caused by quasi-periodic heart beats. The cardiac cycle is divided into multiple phases and images need to be reconstructed for each cardiac phase. When a scan is not fast enough to collect a complete image in a single cardiac phase, k-space is divided into multiple parts and only one part is repeatedly sampled over the same cardiac cycle. For example, in each cardiac cycle all samples can be collected from the

same phase encoding position. When a scan covers multiple cardiac cycles, it is often assumed that there are no differences between the signal changes in different cycles.

There are generally two types of gating: prospective gating and retrospective gating, as shown in Figure (2.15). With prospective gating, the data acquisition starts upon a signal at the beginning of the cardiac cycle, typically a triggering signal from electrocardiogram (ECG). After a certain number of samples the acquisition stops to wait for the next triggering signal. With retrospective gating, the data acquisition and the recording of the triggering signals run simultaneously and continuously. The acquisition is asynchronous with respect to the cardiac cycle. The timing records of the acquisition and the triggering signals are used to retrospectively determine the positions of the samples in the cardiac cycle. The data acquisition is often divided into multiple cycles, known as sampling cycles. The sampling cycle should be longer than the cardiac cycle.

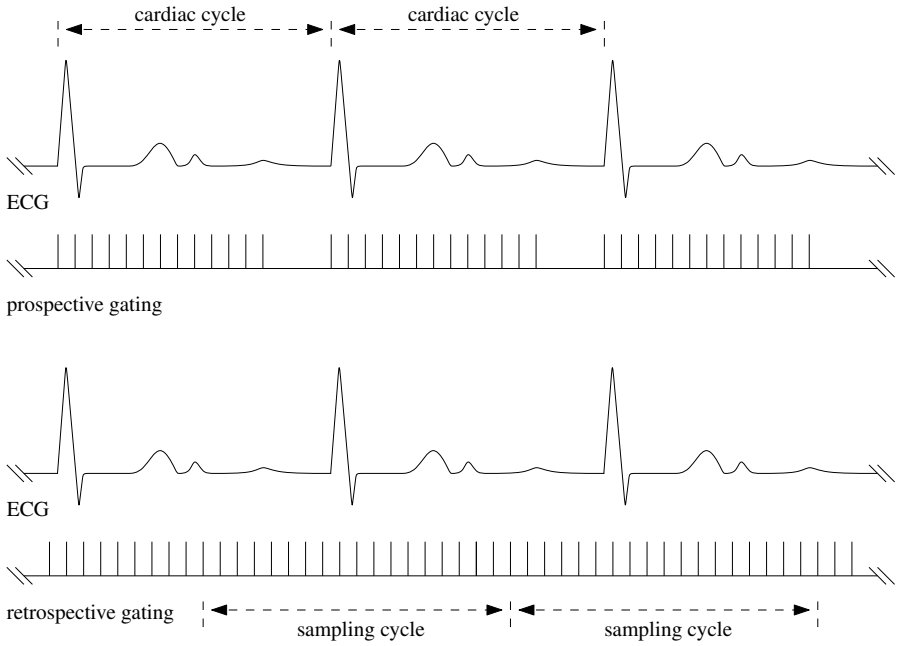

Figure 2.15: Prospective gating and retrospective gating with ECG.

Since with prospective gating the data acquisition has to stop to wait for the start of the next cardiac cycle, the signal near the end of each cardiac cycle is not measured. With retrospective gating, the cardiac cycle is fully covered, but this requires longer scan time. For example, if the cardiac cycle is one second, and it takes 30 ms to collect

a sample, the minimum number of samples required to completely cover the cardiac cycle will be 34 and the minimum time of the sampling cycle will be 1020 ms.

If the duration of the cardiac cycle remains constant throughout a scan, prospective gating will produce samples at fixed positions equally spaced in the cardiac cycle. The samples at the same position in the cardiac cycle can be directly used for the reconstruction of the corresponding time frame. With retrospective gating, the sampling cycle may start at any position in the cardiac cycle and the samples are not at fixed positions. Temporal gridding needs to be applied to interpolate the acquired signal to fixed positions of the cardiac cycles for reconstruction. An example of the source code for temporal gridding is presented in Appendix A.1. In real scans, the duration of the cardiac cycle is often variable. To combine the data collected in different cardiac cycles, it is assumed that the cycles of different lengths can be rescaled to a normalized cardiac cycle. After the stretching or shrinking of the cardiac cycles, the samples obtained with prospective gating are no longer at fixed positions in the normalized cardiac cycle, as shown in Figure (2.16), and gridding is necessary. For retrospectively gated data, gridding is always necessary.

The duration of the systole and the diastole changes non-linearly with that of the cardiac cycle [161, 162]. As the cardiac cycle becomes shorter, both the systole and the diastole are shorter, but the duration of the systole shortens much less than that of the diastole. This means that the systole and the diastole should not be rescaled in the same proportion to the cardiac cycle when the cycles of different lengths are normalized. Comparisons have been carried out for carotid scans between the linear and non-linear methods of the normalization of the cardiac cycles [163], and no significant differences have been observed between the results obtained with different methods.

With retrospective gating, the samples are equally spaced in each sampling cycle, whose duration does not change throughout the scan. Since the position of the start of the sampling cycle in the cardiac cycle is not in control, and the sampling cycle is longer than the cardiac cycle, each sampling cycle will have overlaps with at least two cardiac cycles. When the samples in the same sampling cycle are rearranged in the normalized cardiac cycle, the relative positions of the samples collected in different cardiac cycles are changed and they are no longer equally spaced in the normalized cardiac cycle, as shown in Figure (2.16). The variation of the duration of the cardiac cycles can have the same effect. This makes it almost impossible to sample the k-t space uniformly with retrospective gating, and the k-t positions of the samples do

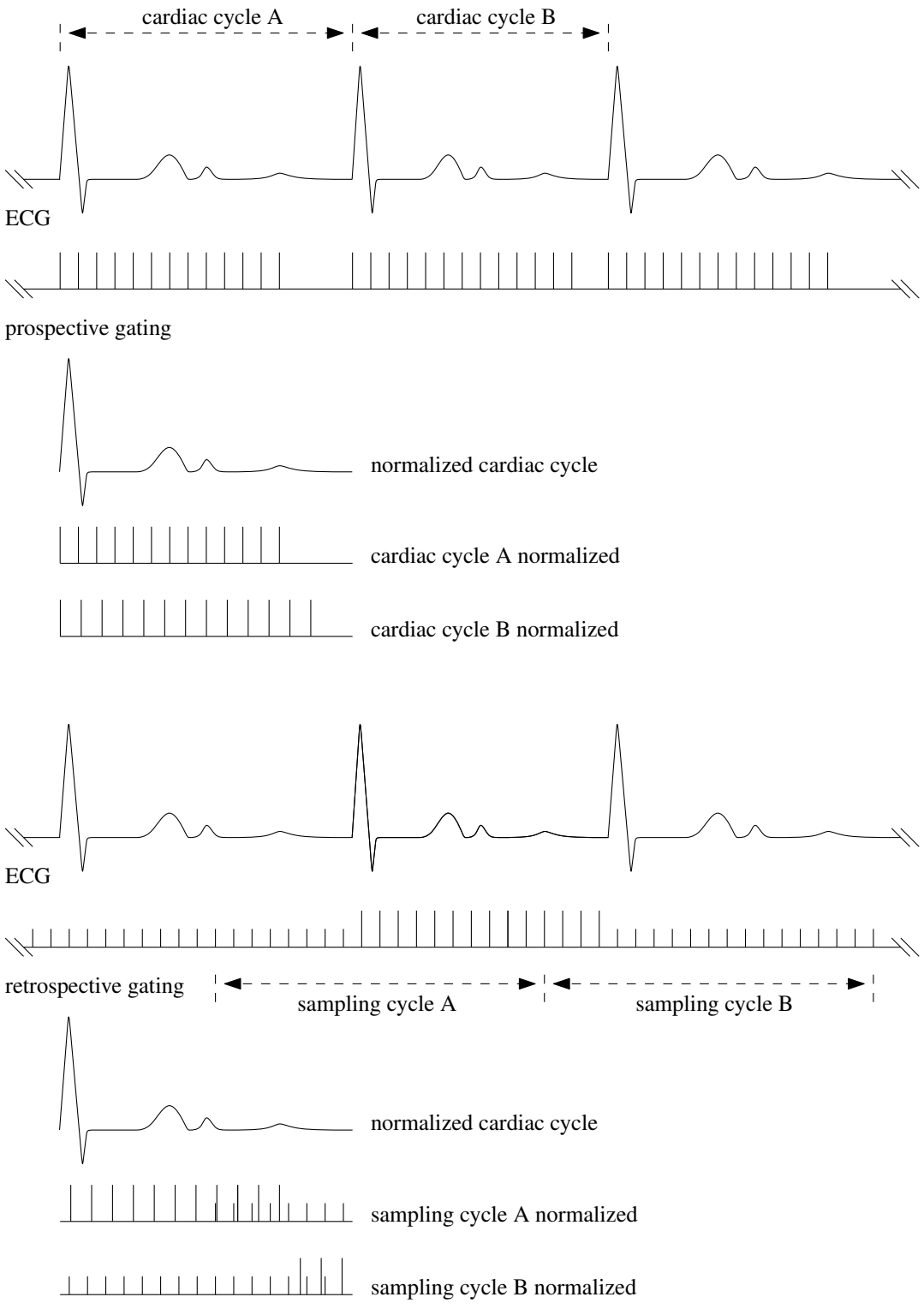

Figure 2.16: Linear normalization of the cardiac cycles of different lengths.

not conform to any regular pattern. When the variation of the duration of the cardiac cycles is not very fast or large, the duration of the sampling cycle is close to that of the cardiac cycle, and the number of samples in each sampling cycle is not too small, in the normalized cardiac cycle the distribution of the samples collected in the same sampling cycle is still nearly uniform.

Many methods can be applied for the gridding operation required for the reconstruction of retrospectively gated data [164, 165, 166, 167, 168, 169]. Simple methods such as linear interpolation from nearest neighbours can also be used for this purpose. When the signal is undersampled, the gridding problem is often ill conditioned, as shown in Figure (2.17). In this case simple methods like linear interpolation are often more effective because more sophisticated methods may need regularization [169] and they often require intensive computing. On the other hand, simple methods may produce less accurate results. For example, when linear interpolation is used, the results may be smoother than the true data.

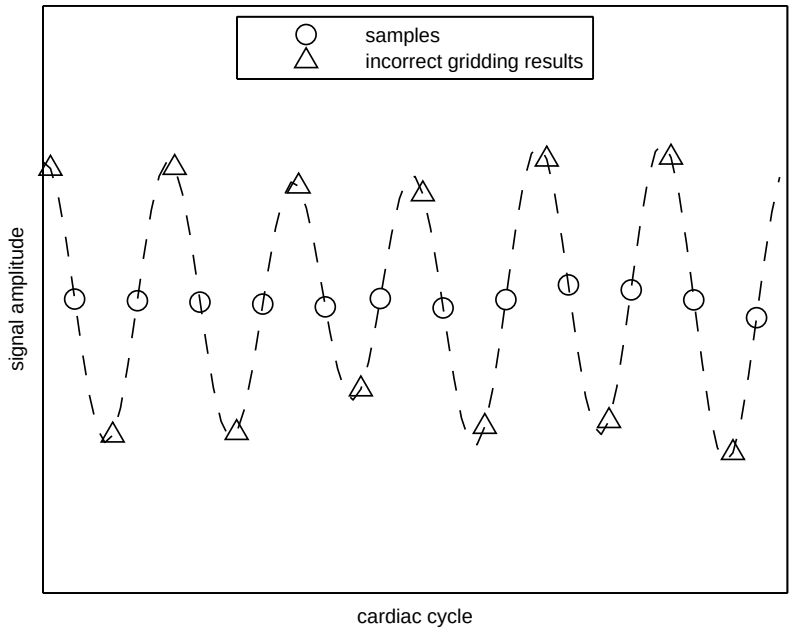

Figure 2.17: An example of incorrect results when the gridding problem is ill conditioned.

2.3 MR flow measurement

2.3.1 Overview

The effects of blood flow on MR signal had been treated as artefacts before they were used to provide velocity information [170, 171]. Flow measurement by introducing a phase shift was applied very early in NMR studies [148, 172, 173, 174, 175, 90]. Most of these methods focus on the effects of flow on signal intensity rather than phases. In 1982 bipolar phase encoding pulses were introduced to spin echo imaging sequence [176] and subsequently phase mapping techniques were proposed [89, 90]. There are two major types of flow imaging methods, the time-of-flight (TOF) and the phase-contrast techniques [150]. Both techniques rely on the endogenous contrast of moving spins to visualize blood vessel. Exogenous contrast agents, such as gadolinium chelates, can also be used to enhance vascular contrast.

2.3.2 Time-of-flight angiography

The TOF technique relies on flow dependent changes in longitudinal magnetization when some or all of the blood within an imaged slice is replaced during the repetition time, T_R, or the time between the 90° and 180° pulses ($T_E/2$), as shown in Figure (2.18). In a spin echo sequence, three types of signal behaviour can be identified depending on the blood velocity. In a very thick slice, slow flowing blood may appear to be almost stationary and the signal is hardly affected. When the blood flow is so fast that the blood within the slice completely leaves the slice between the 90° and 180° pulses, a spin echo is not generated and the vessel lumen has no signal, known as high-velocity signal loss or wash-out. The third type of signal behaviour occurs when the blood partially leaves the slice, partially reducing the signal. Gradient echo sequences only demonstrate flow-related enhancement and never show wash-out because there are no slice-selective 180° pulses. Depending on the velocity of the blood, differing degrees of flow-related enhancement may be observed. When the spins within the slice is completely replaced during T_R, there will be maximum signal enhancement since the spins will not have experienced any previous RF pulses.

TOF angiography uses gradient ehco sequences with short T_R and T_E to saturate the signal from stationary spins, whilst spins flowing into the imaging slice with full magnetization produce a high signal. Maximum intensity projection (MIP) algorithms

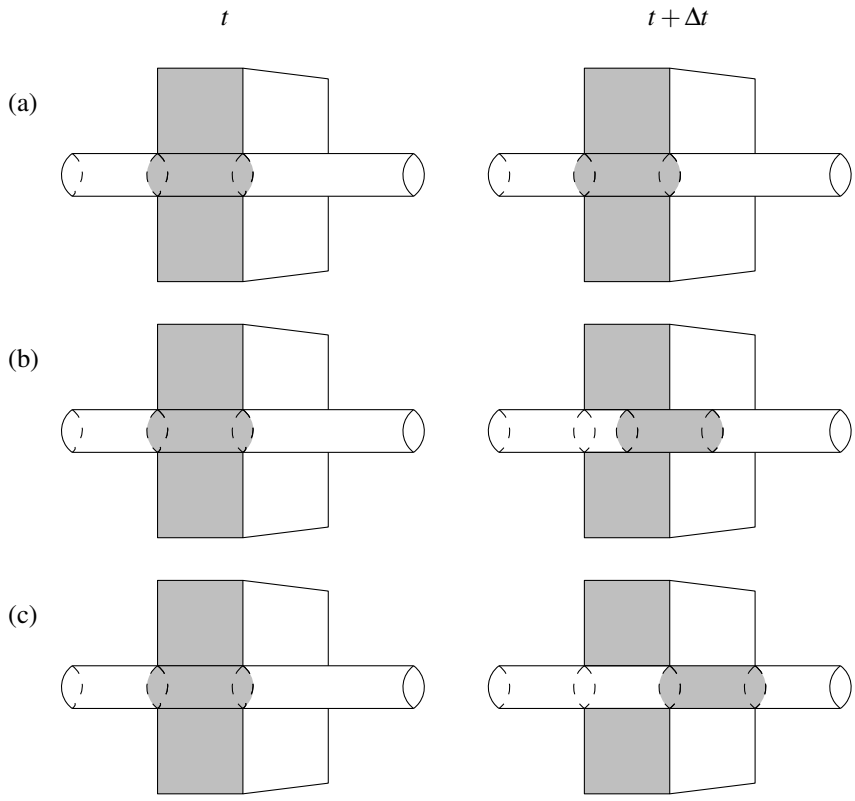

Figure 2.18: Time-of-flight effect: the blood within the slice may be almost stationary (a), partially replaced (b) or completely replaced (c).

are often applied to accentuate these differences and generate images resembling X-ray arteriograms. In order to maximize the TOF effect the slices are often acquired perpendicular to the major flow direction.

2.3.3 The phase contrast method

The phase contrast technique [89, 90] uses the gradient field in a fashion similar to phase encoding.

For example, as shown in Figure (2.19), a short pulse of field gradient g_{venc} is applied along the x axis for the duration of Δt and after that it is repeated in negative strength $-g_{venc}$ for the same period Δt. A static spin at the position x_0 will receive a phase change from the positive gradient pulse and lose the phase change after the negative gradient pulse so it will be unaffected, as shown in Equation (2.15).

$$\Delta\phi = \gamma \int_0^{\Delta t} g_{venc} x_0 dt + \gamma \int_{\Delta t}^{2\Delta t} -g_{venc} x_0 dt = 0 \tag{2.15}$$

In Equation (2.15), to simplify the description, it has been assumed that the field gradient does not change field strength at the position where x is zero. If this is not true the process will still lead to the same result.

For a spin moving along the x axis at a constant speed v, as shown in Equation (2.16), the phase changes caused by the two gradient pulses are different and can not cancel out. The net phase change $\Delta\phi$ is proportional to the velocity v, as shown in Equation (2.17).

$$x(t) = x_0 + vt \tag{2.16}$$

$$\Delta\phi = \gamma \int_0^{\Delta t} g_{venc} x(t) dt + \gamma \int_{\Delta t}^{2\Delta t} -g_{venc} x(t) dt = v\gamma \int_0^{\Delta t} -g_{venc} \Delta t dt \tag{2.17}$$

The pair of gradient pulses used for flow encoding is known as a bipolar pulse. The timing diagram of a gradient echo phase contrast sequence is shown in Figure (2.20). Since the phase of the spin is also affected by other factors, such as field inhomogeneities, at least two samples need to be collected to measure the net phase change. One of them is obtained with the bipolar pulse, and the other without. In order to measure velocities in three directions, the bipolar pulse gradient needs to be applied for three times in different directions, and four samples are required. This means that the scan time will be four times the time of a similar scan for only intensity images.

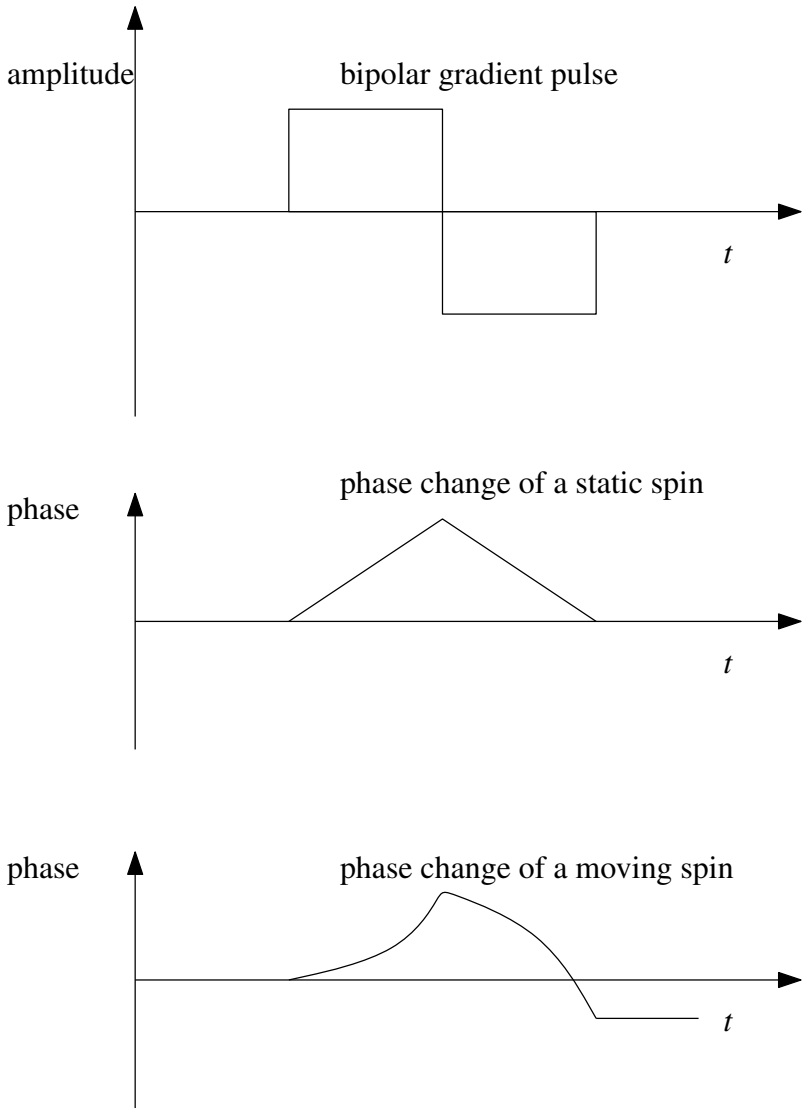

Figure 2.19: Flow encoding with a bipolar gradient.

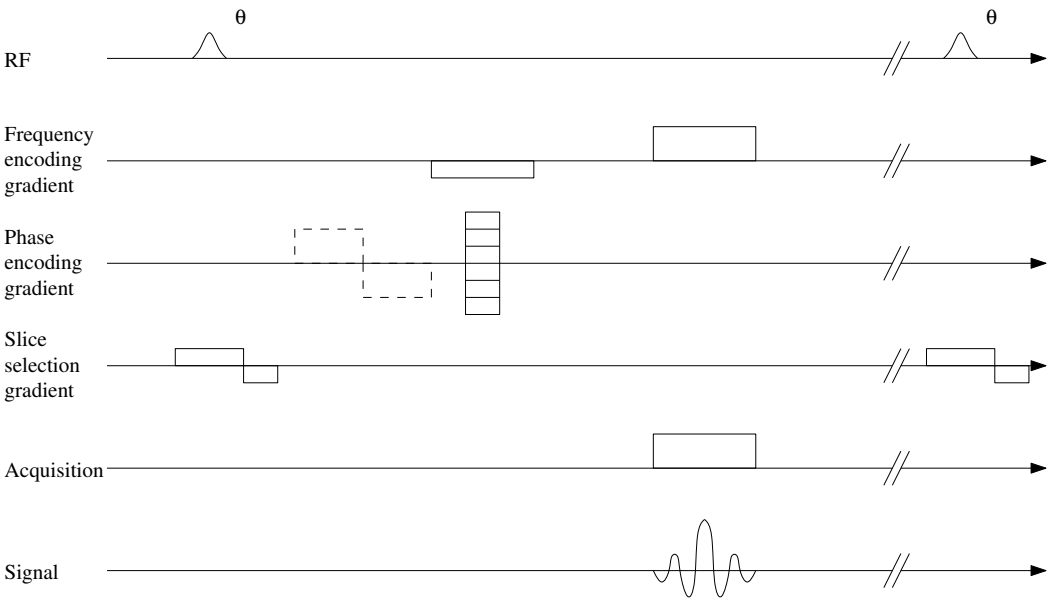

Figure 2.20: A schematic of a phase contrast sequence. Dashed lines represent the flow encoding gradient applied in the phase encoding direction.

To carry out a phase contrast scan, an encoding velocity (V_{ENC}) needs to be set before the scan, which in turn determines the strength and/or duration of the flow encoding gradient. The velocities can be calculated with the V_{ENC} and the complex phase differences of the images, as shown in Equation (2.18).

$$v(x,y) = \frac{V_{ENC}}{\pi} atan2(I_f(x,y) \cdot conj(I_{nf}(x,y))) \tag{2.18}$$

In Equation (2.18), $I_f(x,y)$ is the complex image value obtained with the flow encoding gradient, and $I_f(x,y)$ is the value obtained without. $conj(\,)$ calculates the conjugate of a complex number, $\cdot$ calculates the complex product, and $atan2(\,)$ calculates the angle of a complex number with the range in $(-\pi,\pi]$.

The value of the V_{ENC} should be set slightly larger than the expected maximum value of the velocities to be measured. If it is too large, the phase differences will have a small range in $(-\pi,\pi]$ and this will reduce the SNR of the velocity results. If the value is too small, velocity values larger than that of the V_{ENC} will not be correctly calculated. For example, if the net phase change of a spin is 1.25π, which means that the velocity is $1.25V_{ENC}$, the result obtained according to Equation (2.18) will be

$-0.75V_{ENC}$. This is known as phase wrap. Any net phase changes out of the range of $(-\pi, \pi]$ will be wrapped around into the range in Equation (2.18). Also because of this, the net phase changes are not calculated as direct differences between the phases of the image values. For example, if the phases of the image values are 0.75π and -0.75π, the direct phase difference will be 1.5π, but the correct phase difference should be 0.5π. The complex phase difference method used in Equation (2.18) will not lead to this error.

The variance in the complex phase difference as calculated in Equation (2.18) is inversely proportional to the square of the corresponding intensity value [177, 178]. This means that the measured velocities are less accurate in those regions of smaller intensity values. To increase signal intensity, the T_E should be kept as short as possible, and the settings of the T_R and the flip angle should also be adjusted accordingly.

Similar to the flow encoding process, when the gradient pulses for spatial encoding are applied, a moving spin may receive phase changes different from what are expected for spatial encoding. In normal reconstruction, these phase differences will be interpreted as wrong positions in the phase encoding direction. The techniques known as flow compensation or gradient moment nulling [88] are often applied to compensate this. Specially calculated forms of the spatial encoding gradient pulses are used in the pulse sequence. The phase changes produced with these gradient pulses are independent of the velocities of the spins. For example, the slice encoding gradient pulse can take the form of two bipolar pulses, using the second one in negative strength to cancel the velocity-dependent phase changes induced by the first one. Using these complex gradient pulses in the pulse sequence increases the T_E, which in turn leads to changes in image contrasts and reduces the temporal resolution.

So far the flow has been assumed to have a constant speed. Real flow often has acceleration or high order velocity components. This requires more complicated designs of the gradient pulses for flow encoding and flow compensation, at the cost of a longer T_E.

In the same voxel, the spins are assumed to have the same velocity. When the voxel size is large, there may be partial volume effect, and the measured velocity is the average of the velocities of the spins in each voxel. If the flow is complex and turbulent in some regions, the differences between the flow-induced phase changes of the spins in the same voxel may be large enough to cause dephasing or phase dispersion and reduce image intensities in these regions. Using smaller voxels can help to ease these

problems, but it can also lead to a lower SNR and longer scan time.

Chapter 3

Undersampling in k-t space

3.1 Introduction

Time-resolved MR flow measurement can be very time consuming because the signal has more than three dimensions and extra time has to be allowed for velocity encoding. This means the T_R would be longer than normal for proton density images and more repetitions have to be carried out to cover different phases of the time course and different directions of the flow. For example, if the T_R is 14 ms, the scan matrix is $192 \times 192 \times 32$, the period is divided into 24 phases, and four samples are collected to measure velocities in three directions, the scan will be longer than two hours, which is too long for human subjects.

Undersampling has been a popular approach to accelerate dynamic MR scans by acquiring only a subset of the signal normally collected to cover the selected range of k-t space. In reconstruction prior knowledge or assumptions are incorporated into the sampled signal to recover the skipped signal. This allows significant reduction of scan time, which is proportional to the number of repetitions. For example, if only half of the signal is collected, the scan time will be reduced by half. However, the challenge is how to recover the skipped signal. Ideally if enough prior knowledge or correct assumptions are available, the full set of the signal can be recovered losslessly. In practice this is very rare either because the prior information is inadequate or because the assumptions are not completely consistent with the signal under study. Another issue of undersampling is which part of the signal should be sampled or which part should be skipped. This depends on the prior knowledge or the assumptions made in

advance. For example, if a certain region of k-t space is known or assumed to provide little information, it can be covered with a relatively small number of samples to save scan time.

In this chapter several popular undersampling techniques are briefly reviewed. Then two methods that will be implemented in following chapters are described in detail. The method of the implementation of the undersampling methods on a clinical scanner is also introduced.

3.2 K-space undersampling methods

Early undersampling methods mainly deal with signal in k-space. For dynamic scans the temporal dimension of the signal is not undersampled. The fully sampled dimensions of the signal are omitted in the descriptions of these methods.

Since k-space signal is the Fourier transform of complex image values, the signal will be Hermitian symmetrical if all the complex values of an image are real. This means along the frequency encoding direction or the phase encoding direction, one half of k-space signal is the conjugate of the other half. Samples of one half of k-space signal will be enough to reconstruct the complete image and scan time can be reduced to half of that of a fully sampled scan. In reality due to effects such as field inhomogeneities and magnetic susceptibility k-space is not strictly Hermitian symmetrical and the real image assumption is often softened in implementation [179, 180, 181, 182, 183]. Slow phase changes across k-space are allowed and a small fraction of k-space near the centre is additionally sampled to resolve the phase variations in reconstruction. This family of undersampling methods are called partial-Fourier or half-Fourier techniques. An example half-Fourier sampling pattern is displayed in Figure (3.1). If undersampling is applied in the phase encoding dimension, the total scan time can be reduced by nearly half. If the frequency encoding dimension is undersampled, it will allow a shorter TE. In phase contrast velocity measurement, the phase changes caused by flow are not spatially smooth over the whole image domain in most cases and half-Fourier methods should not be used.

Another approach is to sample k-space signal with variable sampling density [184, 185, 186], which is named the variable-density technique. The central region of k-space is densely sampled and the regions near the edges of k-space are sparsely sam-

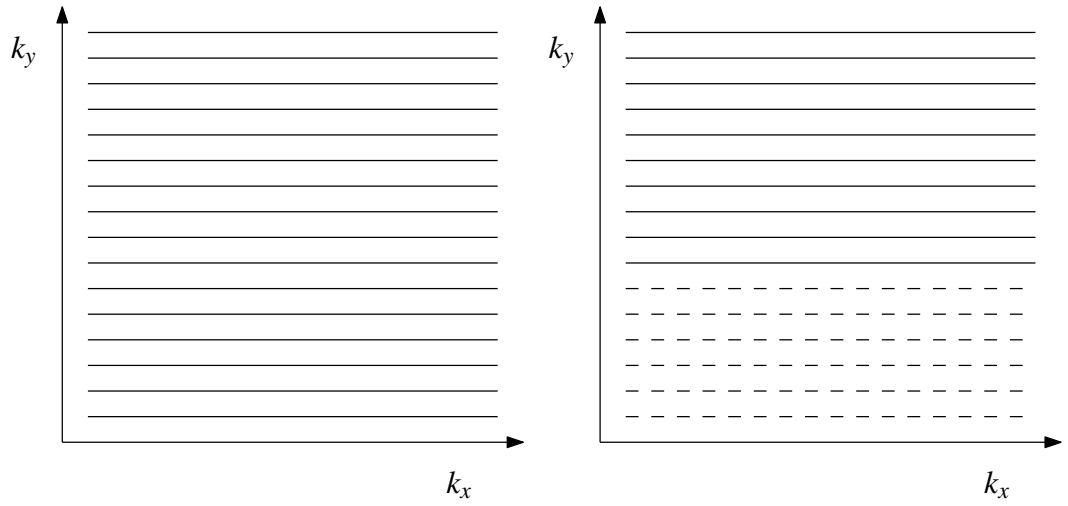

Figure 3.1: An example of the sampling patterns used by the half-Fourier technique (right). The k-space sampling pattern of a fully sampled scan is also displayed (left). Dashed lines represent skipped k-space lines.

pled. It is assumed the central region of k-space provides most signal power of the images and the outer regions are less important. In reconstruction, interpolation is applied to calculate the signal values at the positions uniformly spaced in k-space according to the non-uniformly sampled data. Sparse sampling in the outer regions causes artefacts. Since the outer regions correspond to high spatial frequencies, the artefacts are usually spread over the images and appear to be noise-like. Variable-density undersampling can be implemented for either Cartesian trajectories or non-Cartesian trajectories, as shown in Figure (3.2). For Cartesian trajectories the sampling density is changed by skipping more k-space lines in outer regions of k-space. It is more convenient to apply variable-density sampling with non-Cartesian trajectories such as projection-reconstruction or spiral imaging because these trajectories are naturally non-uniform in k-space with a higher sampling density in the central area. The performance of variable-density sampling depends on the signal content in study. If the images are rich in sharp spatial details, which means the outer regions of k-space also provide important information, the reconstruction results will usually show blurring. The performance also depends on scan resolution. For example, if the image resolution becomes unnecessarily higher, the signal will become relatively more redundant.

K-space can also be undersampled uniformly, as shown in Figure (3.3). Uniform

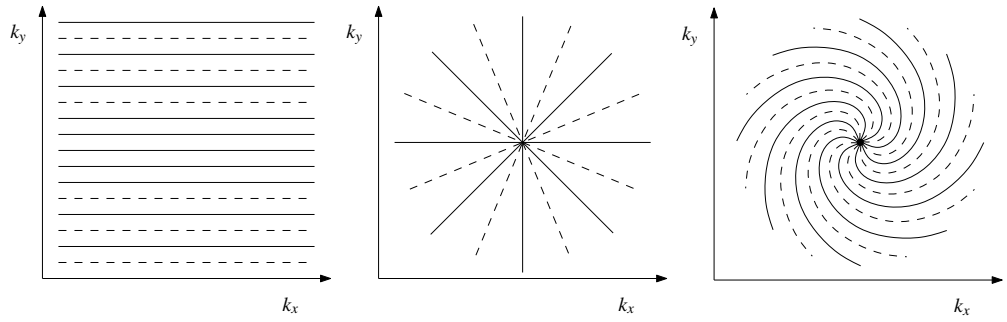

Figure 3.2: Examples of the sampling patterns used by the variable-density technique for different trajectories: Cartesian (left), projection (middle) and spiral (right). Dashed lines represent skipped k-space positions.

undersampling results in reduced FOV and this gives the name reduced-FOV technique [187, 188, 189, 190, 191]. The technique is based on the assumption that in dynamic studies the changing part of the timeframes are sometimes localized, and a smaller FOV can be used to reduce imaging time. If the size of the dynamic region represents a fraction 1/K of the total FOV, reduced-FOV techniques offer scan-time reduction by a factor exactly or approximately equal to K. In reconstruction, the image data of the static regions will be wrapped to the dynamic region if the undersampled k-space data is directly inverse Fourier transformed. The foldover artefacts can be removed with prior knowledge of the image data of the static regions such as a preacquired reference image. It is also possible to reconstruct the dynamic images without the conventional inverse Fourier transform [191]. The reconstruction of the full-FOV images over the time course is treated as an inverse problem in which the number of unknown image values can be greatly reduced when the values in the static regions are assumed to be unchanged over time. This reconstruction method still requires the knowledge of the range of the dynamic region, but the reference image is no longer necessary. In general reduced-FOV techniques allow scan-time reduction at the cost of a reduced SNR. If there are dynamic changes in the assumed static regions, artefacts can also be introduced to the assumed dynamic region.

Spatial information inherent in the geometry of a coil array can also be used to reconstruct k-space signal undersampled uniformly [192, 193]. For example, if every other k-space line is skipped, as shown in Figure (3.3), the FOV will be reduced to a half. At each position in the reduced FOV the image value is the sum of those at

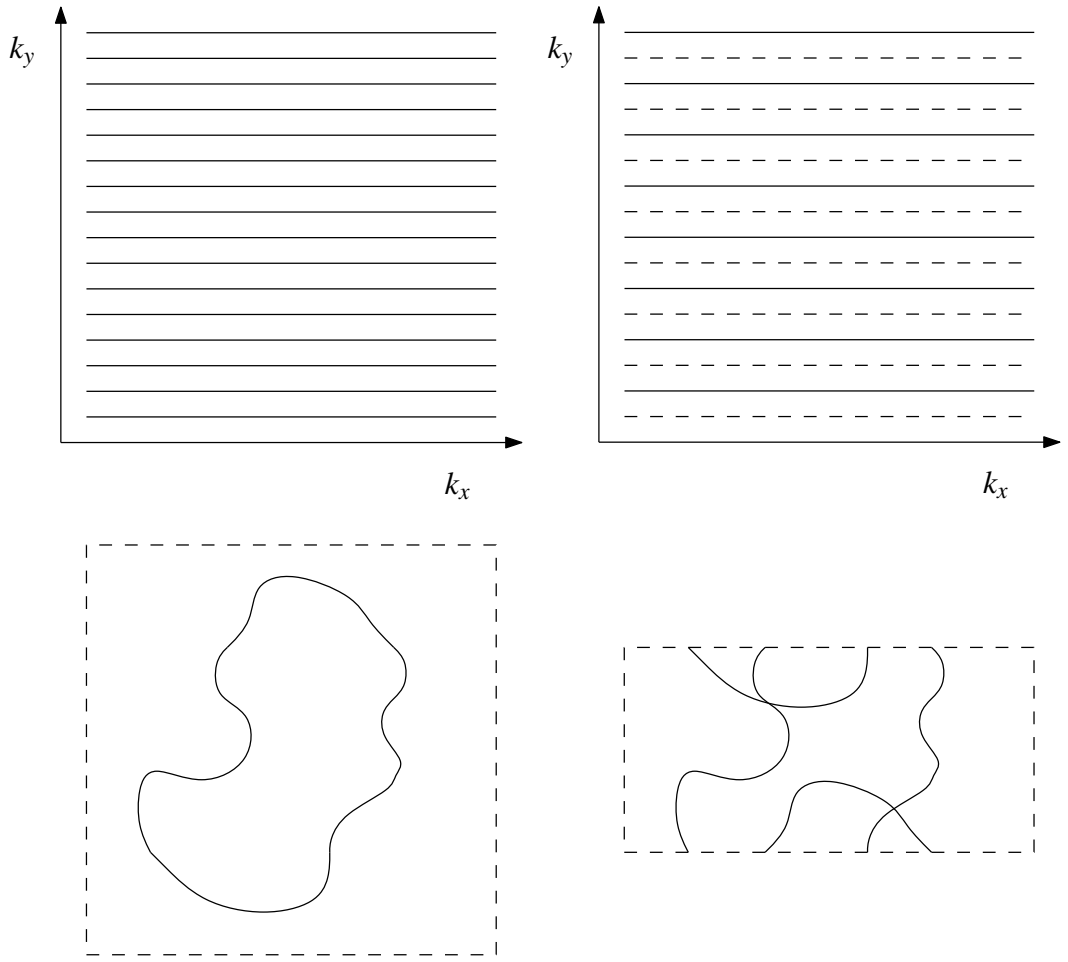

Figure 3.3: An example of the sampling patterns used by the reduced-FOV technique. Dashed lines represent skipped k-space positions. The k-space sampling pattern of a fully sampled scan is also displayed (top left). Uniform undersampling results in reduced FOV (bottom).

two positions in the full FOV. If a two-coil array is used for the acquisition, each coil will provide different measurements weighted by its sensitivity at those two positions in the full FOV. The image values can be calculated with the knowledge of the spatial sensitivity of the coils. Theoretically, if K coils are used simultaneously, the scan time can be reduced to 1/K. In practice scan time reduction is less than that due to limited coil sensitivity and the loss in SNR.

The keyhole technique [194, 195] assumes dynamic regions of the timeframes are spatially smooth and the edge information is not very dynamic. In k-space this means the outer regions of k-space are almost static and only the central region needs to be sampled at full temporal resolution. As shown in Figure (3.4), it is often implemented by measuring only the central k-space over the time course in addition to one or two reference images before or/and after the dynamic acquisition. In reconstruction, the outer k-space data of each timeframe is copied or temporally interpolated from the reference images. A generalized series based algorithm was also proposed for reconstruction [196, 197, 198]. Scan-time reduction with the keyhole technique depends on how spatially smooth the dynamic k-space region is. In applications such as contrast uptake monitoring the dynamic region is bandwidth limited in k-space and the technique gives good performance [194, 199]. In some cases, such as cardiac applications or interventional MRI [200] where sharp edges may move rapidly, errors may be introduced into the images. It has also been shown that the keyhole technique compromises spatial resolution for an improvement in the temporal resolution [201] and a hybrid method of the keyhole and reduced-FOV techniques has been proposed [202].

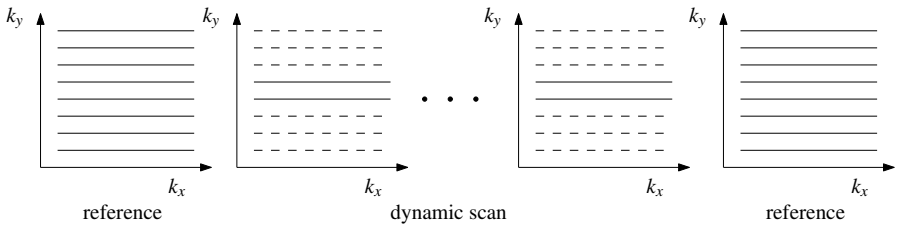

Figure 3.4: An example of the sampling patterns used by the keyhole technique. Dashed lines represent skipped k-space lines.

The undersampling techniques described so far exploit signal redundancy either in the image domain or in k-space. Signal representations in other domains can also be sparse, or even sparser than those in the image domain or k-space. When adequate prior

information is available, it is possible to break down an image into a limited number of known image features or image components. For example, the images at the same position of different patients show similar anatomy. By measuring only several or a small number of image features the scan can be extremely fast. This undersampling method is named the singular value decomposition (SVD) [203, 204] or feature-recognition technique [205, 206]. The image features or components are chosen by analysing with SVD or principal component analysis a previously obtained image or a set of training images thought to be similar to the target image. Alternatively, wavelet transform can be used to obtain a sparse representation of images [207]. In the acquisition, the features or components are measured by using spatially selective RF pulses or a subset of k-space signal. When the latter is used, k-space is often sampled non-uniformly, depending on the prior information. The fewer features or components are selected to represent the target image, the faster the scan can be. Obviously errors will be introduced if the target image contains information not present in the selected features or components.

3.3 K-t space undersampling methods

Undersampling only in the spatial dimensions of k-space generally offers limited scan-time reduction, and often at the cost of spatial resolution. The temporal dimension of dynamic MR signal may allow further undersampling. It is very common that different timeframes acquired in a dynamic scan have large regions which remain nearly unchanged throughout the time course or the timeframes are very similar to each other. Temporal signal redundancy has already been used in k-space methods such as the keyhole technique and the reduced-FOV technique described previously. However, it is only used in reconstruction and the same k-space sampling pattern is used for all the timeframes in dynamic acquisition excluding the collection of the baseline images (some later variants such as in [191] can also use changing patterns). Recent undersampling methods often use different sampling patterns for different timeframes and the signal is undersampled in both the temporal and the spatial dimensions.

A straightforward approach is to undersample k-t space uniformly. The samples are equally spaced in both the temporal and the spatial dimensions. This often results in a k-t sampling pattern like a sheared grid for Cartesian trajectories, as shown in

Figure (3.5). An early method of this type is the sliding-window technique [208]. Complete k-space signal of each timeframe is obtained by assembling undersampled data sets collected for nearby timeframes in a temporal window. For example, if one fourth of k-space data is acquired for each timeframe, the signal of each reconstructed timeframe consists of data copied from four neighbouring timeframes. Basically the reconstruction is temporal interpolation. Temporal resolution remains unchanged. The advantage of the sliding-window technique is its simplicity. Images can be updated continuously after several initial frames.

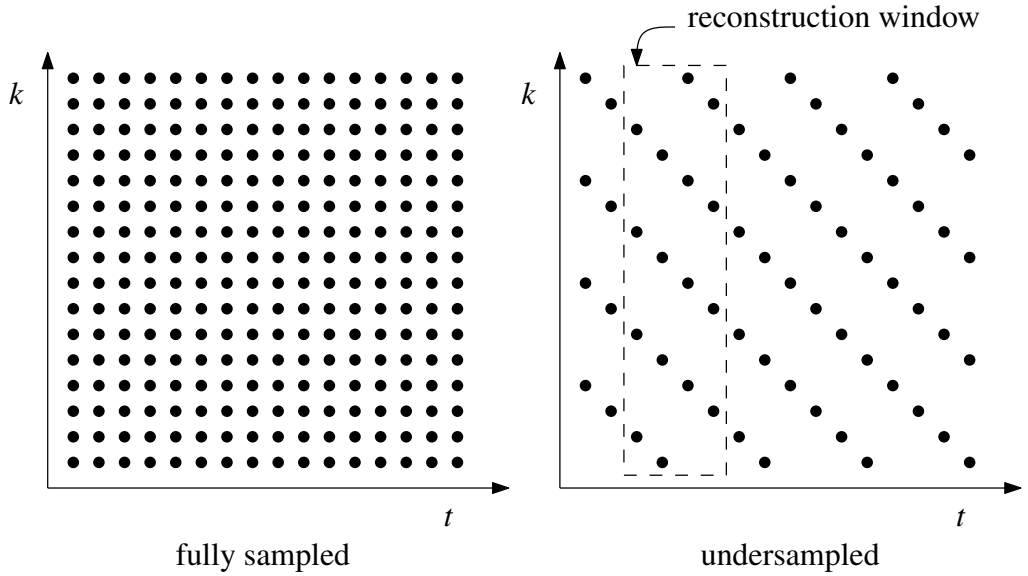

Figure 3.5: An example (right) of the sampling patterns used by the sliding-window technique. Each dot represents a k-space line collected in acquisition. Skipped k-space lines are not displayed. The k-t sampling pattern of a fully sampled scan is also displayed (left). In reconstruction signals from four undersampled timeframes in the temporal window are assembled into one timeframe.

Uniform undersampling and zero-filling at skipped positions will cause aliasing in a corresponding Fourier domain, as shown in Figure (3.6). If k-space signal is undersampled aliasing will appear in the images. In a similar fashion, temporal undersampling will also lead to aliasing in a temporal-frequency domain. The signal representation in the temporal-frequency domain is the inverse Fourier transform of the signal in the temporal dimension. The corresponding Fourier domain of k-t space is named x-f space, where x represents spatial positions and f represents temporal frequencies.

It has been observed [209, 210] when a uniform undersampling pattern like a sheared grid is applied, the aliasing in x-f space appears to be several equidistant replicas of the true signal, as shown in Figure (3.7). If the true signal covers a limited area in x-f space and the area of the overlaps between the true signal and the replicas are also small, the aliasing can be easily removed with a low pass filter in x-f space. Two widely applied methods using this type of k-t undersampling patterns are the UNFOLD technique [209] (UNaliasing by Fourier-encoding the Overlaps using the temporaL Dimension) and the k-t BLAST technique [211] (k-t Broad-use Linear Acquisition Speed-up Technique). Both techniques use prior information to separate the aliasing from the true signal. The UNFOLD technique applies filters according to known or estimated signal temporal bandwidth as described previously. The k-t BLAST technique uses low resolution images acquired in a separate training scan as prior knowledge about signal distribution in x-f space and the unaliasing process is formulated as an optimization problem so the training images can be used adaptively instead of the filters in the UNFOLD technique. Since the k-t BLAST technique will be implemented later, it will be described in detail in the next section. Ghosting artefacts may be generated with these two techniques when too many samples in k-t space are skipped in the acquisition, which results in large area of overlaps between the replicas and the true signal in x-f space.

Non-uniform undersampling patterns in k-t space have also been used to accelerate dynamic scans. As illustrated in Figure (3.8), the TRICKS technique [212, 213] (Time-Resolved Imaging of Contrast Kinetics) divides k-space into several regions and those at high spatial frequencies are updated less frequently in a dynamic acquisition. Linear temporal interpolation is applied in reconstruction to recover the full signal. The outer regions of k-space are sampled more regularly by the TRICKS technique than by the keyhole technique, which only samples these regions once or twice for the reference images. The BRISK technique [214, 215] (Block Regional Interpolation Scheme for K-space) is similar to the TRICKS technique but k-space is divided into more parts and acquisition of multiple parts is scheduled for each time frame, as shown in Figure (3.8). Missing data is also recovered by temporal interpolation. The STBB scheme [216] (Spatio-Temporal Bandwidth-Based acquisition) explicitly analyses signal energy distribution in x-f space and a sampling pattern similar to those proposed in the BRISK technique is designed accordingly. A random phase-encoding strategy is proposed in the CURE technique [217] (Continuous Update with Random Encod-

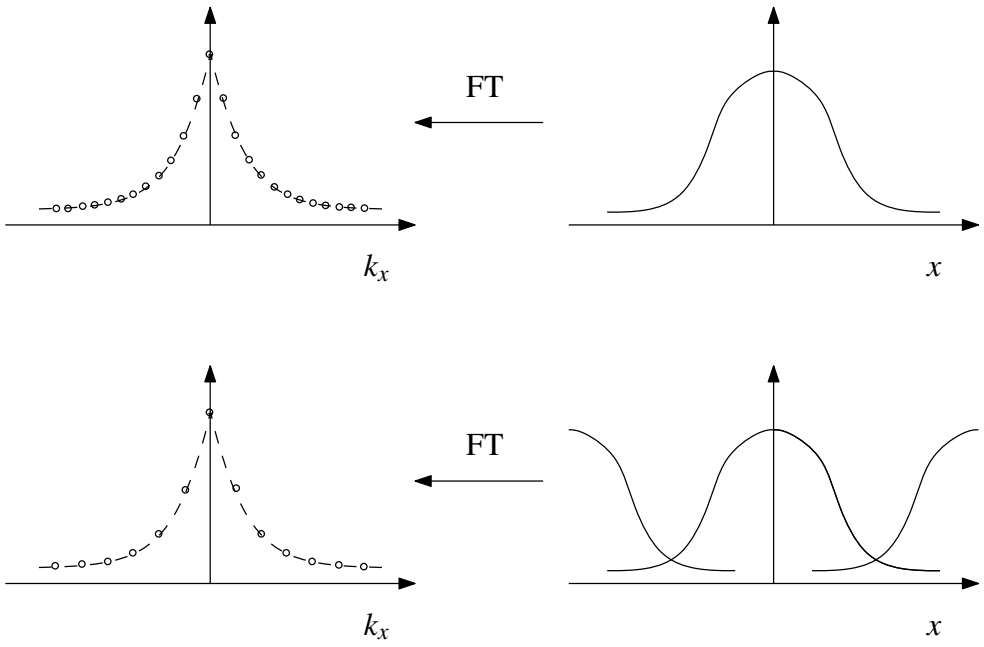

Figure 3.6: Uniform undersampling (bottom left) and zero-filling at skipped positions will cause aliasing (bottom right) in a corresponding Fourier domain. There is no aliasing if the signal is fully sampled (top).

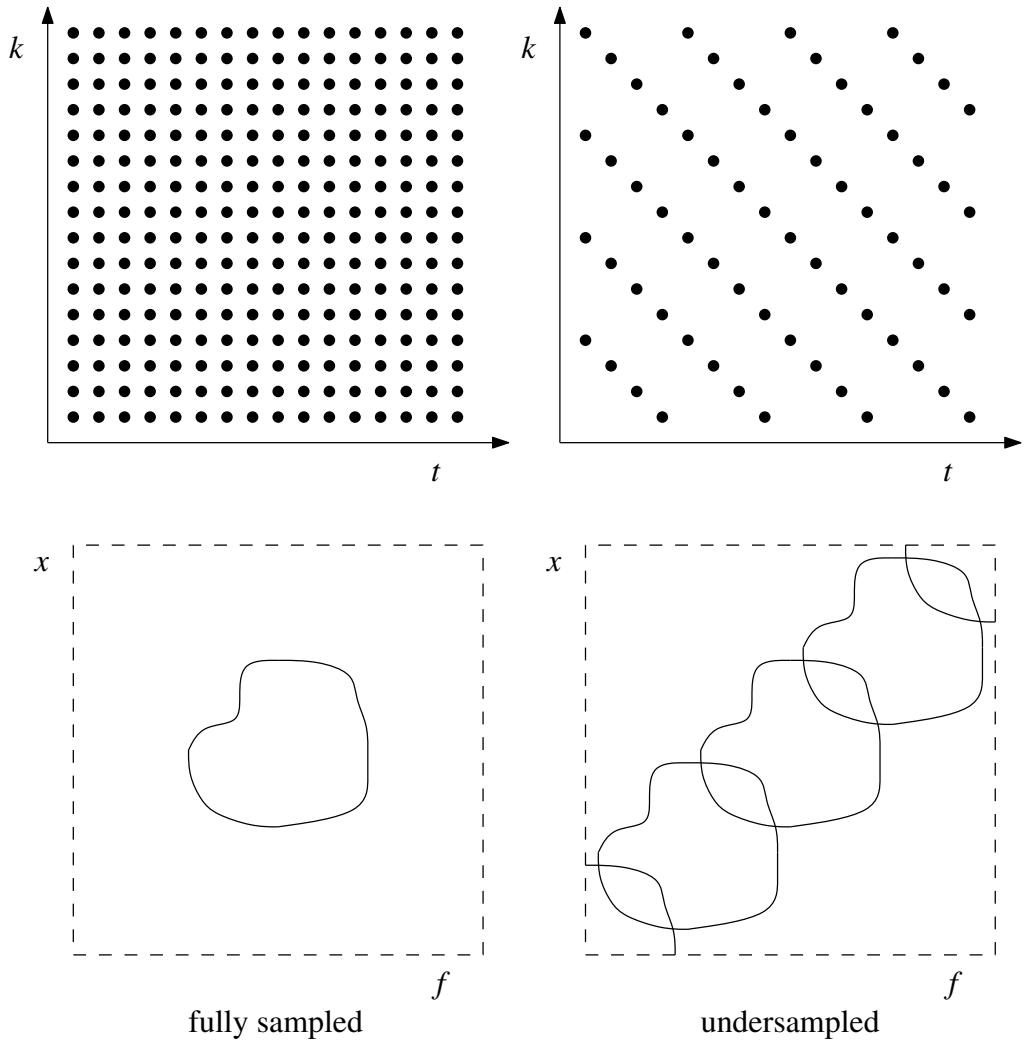

Figure 3.7: The aliasing in x-f space (bottom right) appears to be several equidistant replicas of the true signal in x-f space (bottom left) when a uniform undersampling pattern (top right) is applied in k-t space. Each dot represents a k-space line collected in acquisition. Skipped k-space lines are not displayed. The k-t sampling pattern of a fully sampled scan is also displayed (top left).

ing), which aims to produce a random and nearly uniform coverage of each region of k-t space. Central k-space is still sampled more frequently than outer regions. The non-uniform k-t undersampling methods described above share a common assumption that central k-space is more dynamic than the outer regions. If this assumption is not valid aliasing will appear in images. The allocation of samples into k-t space is often based on prior information or empirical estimation, which may be inaccurate and leads to aliasing as well.

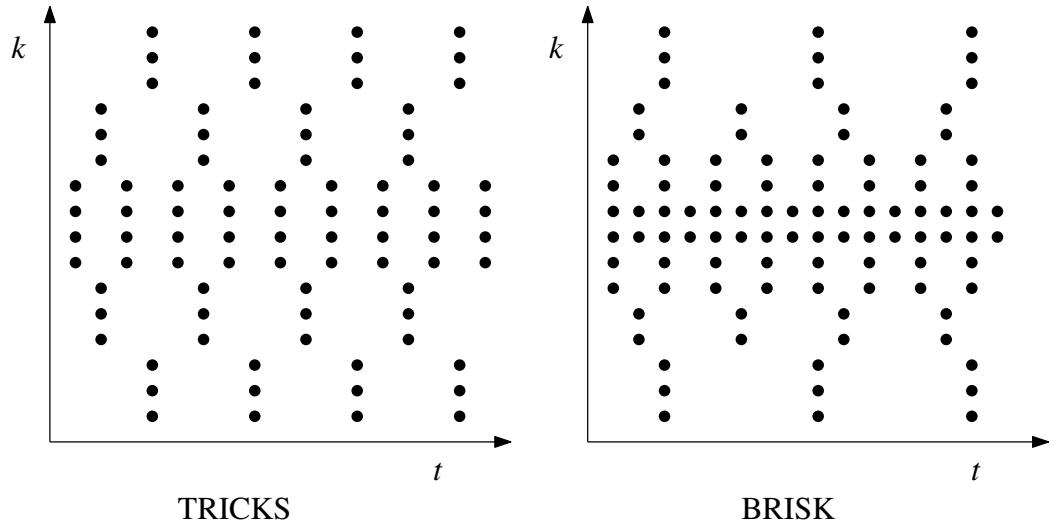

Figure 3.8: Examples of the sampling patterns used by the TRICKS technique (left) and the BRISK technique (right). Each dot represents a k-space line collected in acquisition. Skipped k-space lines are not displayed.

It has been proposed that an appropriate temporal model can be used as a constraint on the reconstruction in order to remove artefacts caused by undersampling and to preserve or increase SNR [218]. The reconstruction in x-f space is treated as an inverse problem and mild temporal constraints are applied according to prior knowledge. This reconstruction method can be applied with either a uniform or a non-uniform sampling pattern. It was reported that the non-uniform sampling pattern produced better results than those from the uniform sampling pattern for dynamic myocardial perfusion data.

Recently, compressed sensing theory [219, 220] has been applied to dynamic MRI [221, 222]. Data sparsity can be introduced by applying Fourier transformation along the temporal dimension assuming that only some parts of the FOV change at a high temporal rate while other parts remain stationary or change slowly. Incoherent under-

sampling can be realized by randomly skipping phase-encoding lines in each dynamic frame. It has been demonstrated that given sufficient data sparsity and base SNR the compressed sensing framework can produce results with improved temporal fidelity compared to k-t BLAST reconstructions [222].

There has not been a general consensus on which type of sampling pattern is the best. Scan-time reduction and reconstruction accuracy often depend on signal content in specific applications. It is one of the aims of this study to evaluate the performance of different sampling patterns in scans measuring velocities of carotid blood flow. Among the k-t undersampling techniques using a uniform sampling pattern, the k-t BLAST method is the most widely applied and in most cases scan-time reduction by a factor of four was achieved [223, 224, 225, 226, 227, 228]. Its adaptive use of training data in reconstruction makes the incorporation of prior knowledge easier than in other similar techniques, and its reconstruction algorithm can be generalized to handle signals from retrospectively gated scans. Due to these advantages the k-t BLAST method was selected to be implemented in the following chapters as a representative method using uniform undersampling patterns in k-t space. A generalized version of the non-uniform k-t undersampling techniques, named k-t variable-density undersampling technique (ktVD) [229], is proposed in the following sections to evaluate the performance of non-uniform undersampling patterns. In the following chapters the k-t BLAST method and the ktVD method will be implemented and compared against each other in similar settings for retrospectively gated carotid velocity measurement.

3.4 The k-t BLAST method

The k-t BLAST method can be applied for uniform as well as non-uniform sampling patterns in k-t space. It is much easier to explain how the method works with a uniform Cartesian sampling pattern. This will be introduced first before the general form of the method is described. Without loss of generality, the signal is assumed to have only two dimensions in k-t space.

As shown in Figure (3.9), when the uniform undersampling pattern in k-t space is applied, which collects one fourth of the fully sampled signal, the result obtained after zero-filling and inverse Fourier transform shows aliasing in x-f space. The fully sampled signal (the true data) in x-f space is also displayed in Figure (3.9) as a reference.

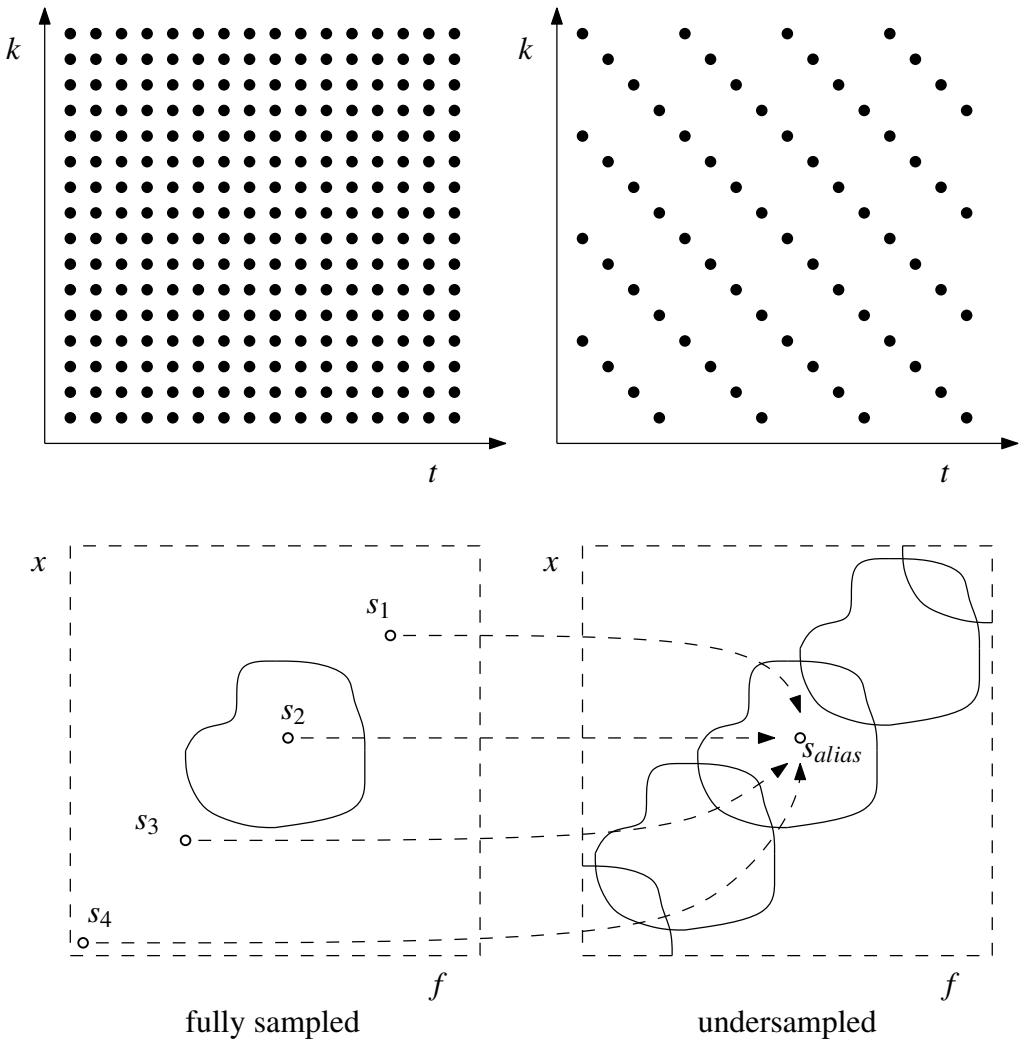

Figure 3.9: Signals at four equally spaced positions in x-f space from the true data (bottom left) accumulate at the same position in the undersampled result (bottom right) when a uniform undersampling pattern (top right) is applied in k-t space. Each dot represents a k-space line collected in acquisition. Skipped k-space lines are not displayed. The k-t sampling pattern of a fully sampled scan is also displayed (top left). Only one of the four positions is not in empty background.

Due to aliasing, signals at four equally spaced positions (the source positions) in x-f space from the true data accumulate at the same position in the undersampled result. In fact this happens at every position in the undersampled result, as described in Equation (3.1).

$$\begin{bmatrix} 1 & 1 & 1 & 1 \end{bmatrix} \cdot \begin{bmatrix} s_1 \\ s_2 \\ s_3 \\ s_4 \end{bmatrix} = s_{alias} \tag{3.1}$$

In Equation (3.1) s_1, s_2, s_3 and s_4 refer to the true signals at the four positions contributing to a measurement s_{alias} at a single position in the undersampled result. They need to be estimated from s_{alias}. $A \cdot B$ calculates matrix product of a matrix A and a marix B.

Equation (3.1) is underdetermined and has an infinite number of solutions. It is necessary to introduce additional constraints to obtain a unique solution. This is where assumptions or prior knowledge are incorporated into the reconstruction. For example, if it is known that the positions except the one corresponding to s_2 are in empty background, as shown in Figure (3.9), s_1, s_3 and s_4 can be simply set to zero and the value of s_{alias} can be copied to s_2. This is the simplest situation, which was also used in the UNFOLD method for reconstruction. In more complicated circumstances, when more than one position are not in empty background, such as s_2 and s_3 in Figure (3.10), the unique solution is calculated by distributing the value of s_{alias} to the four positions according to their expected signal power, as shown in Equation (3.2).

$$\begin{gathered} s_i = \frac{m_i^2}{m_1^2+m_2^2+m_3^2+m_4^2} s_{alias} \\ i = 1,2,3,4 \end{gathered} \tag{3.2}$$

In Equation (3.2) m_1, m_2, m_3 and m_4 refer to the signal magnitudes obtained from the training data in x-f space at the positions corresponding to s_1, s_2, s_3 and s_4. An example sampling pattern of the training scan is displayed in Figure (3.11). Filtering has been applied to the training data to reduce ringing artefacts from truncation and after zero-filing and filtering the training data has the same matrix size as that of the true data in k-t space or x-f space. In case only s_2 is not in empty background, m_1, m_3 and m_4 are all zeros so s_2 equals s_{alias}, as described previously.

It should be noted that in Equation (3.2) s_1, s_2, s_3, s_4 and s_{alias} are all complex

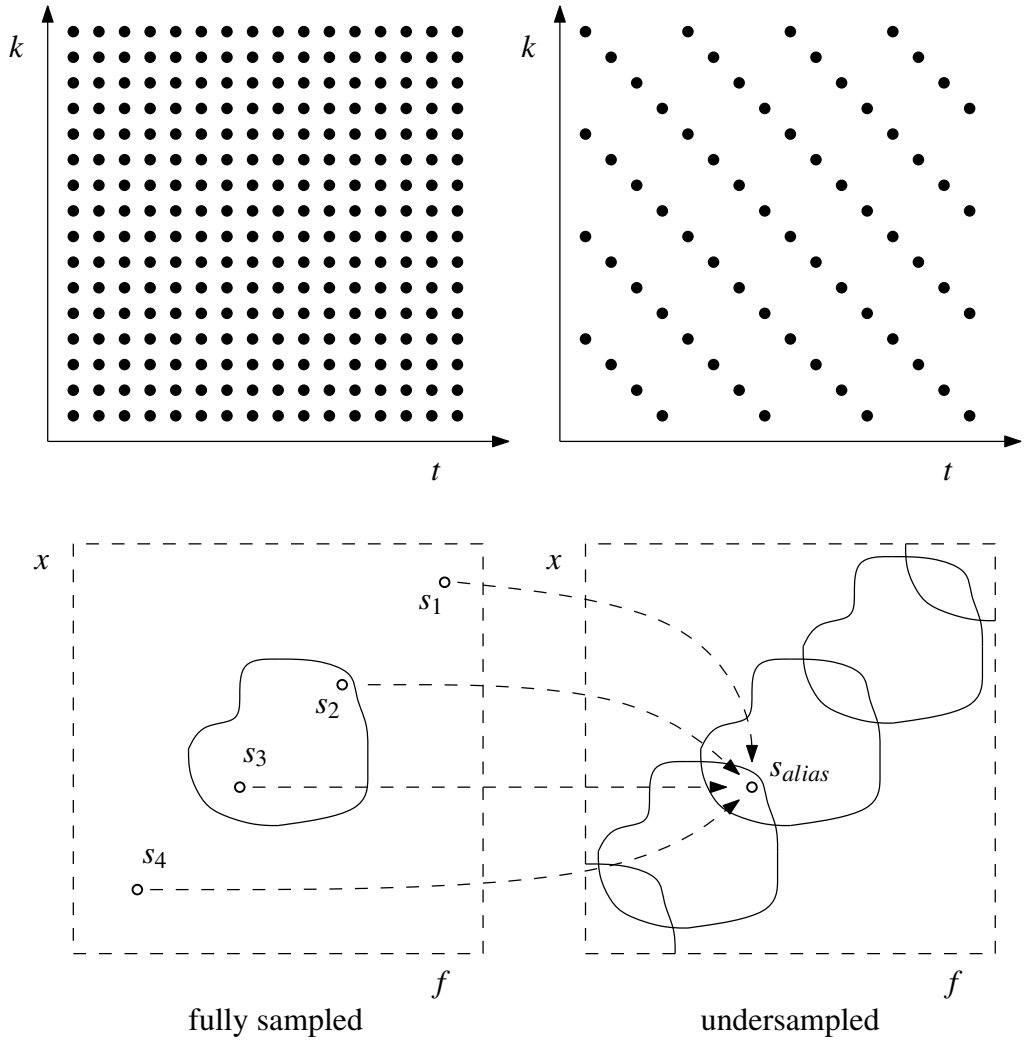

Figure 3.10: Signals at four equally spaced positions in x-f space from the true data (bottom left) accumulate at the same position in the undersampled result (bottom right) when a uniform undersampling pattern (top right) is applied in k-t space. Each dot represents a k-space line collected in acquisition. Skipped k-space lines are not displayed. The k-t sampling pattern of a fully sampled scan is also displayed (top left). Two of the four positions are not in empty background.

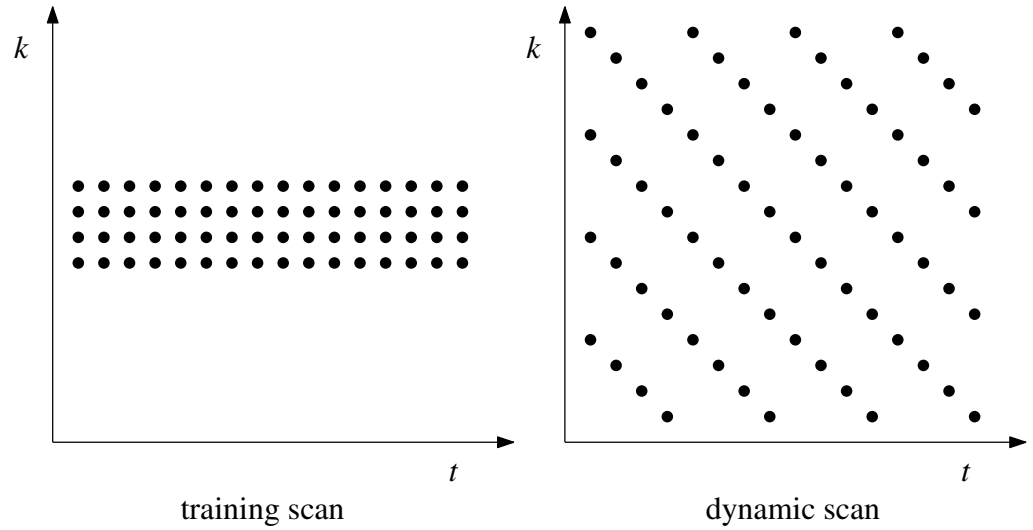

Figure 3.11: An example of the sampling patterns for the training scan (left) and the dynamic scan (right) used by the k-t BLAST technique. Each dot represents a k-space line collected in acquisition. Skipped k-space lines are not displayed.

numbers. As a result s_1, s_2, s_3, and s_4 will have the same phase as that of s_{alias}. This is generally not consistent with realistic signal.

Equation (3.2) is the solution of an optimization problem described in Equation (3.3) subject to conditions in Equation (3.1).

$$\min_{s_1,s_2,s_3,s_4} \quad \sqrt{\sum_i^4 \left\| \frac{s_i}{m_i} \right\|^2} \tag{3.3}$$

In Equation (3.3) $||\ ||$ calculates the magnitude of a complex number. By minimizing the total of the weighted signal power at all the source positions, more signal power of s_{alias} is distributed to the source positions with higher expected signal power, and the aliasing is resolved.

The process described above is the most widely applied and the simplest form of the k-t BLAST method. Reconstruction requires knowledge of the locations of the source positions of the true signals contributing to the measurement at each position in the undersampled result. The locations of the source positions are solely determined by the applied undersampling pattern. When a sampling pattern like a sheared grid is applied, such as the example shown in Figure (3.11), the locations of the source positions

are easy to calculate and the number of the source positions for each measurement in the undersampled result is small. This is also the most significant benefit of the use of this type of sampling pattern. The number of source positions is determined by the sampling ratio of the undersampling pattern applied. In Figure (3.9) only four source positions are involved since one fourth of k-t space is sampled. The four source positions are equally spaced and one of them is at the same location of the corresponding position in the undersampled result. If one third of k-t space is sampled, three source positions will be involved and they are still equally spaced. If the size of the sampled fraction of k-t space decreases, the number of the source positions for each measurement in the undersampled result will increase and it will be likely more positions are not in empty background.

Equation (3.1) only describes the aliasing process in the special case shown in Figure (3.9), in which every four source positions are grouped together and each group is processed separately. In the general form of the k-t BLAST method, all the true signal values in k-t space are processed together. Since discrete Fourier transform from x-f space to k-t space is a linear operation, it can be represented as a matrix product of a Fourier transform operator F and the signal in x-f space s_{xf} as a vector, as shown in Equation (3.4).

$$s_{kt} = F \cdot s_{xf} \tag{3.4}$$

In Equation (3.4) s_{kt} represents the signal in k-t space after the transform. Both s_{kt} and s_{xf} have $N_k \times N_t$ elements, where N_k and N_t are the spatial and temporal resolution respectively. F has $N_k \times N_t \times N_k \times N_t$ elements. It should be noted this can be a very large number. If N_k is 256 and N_t is 24, F will have 6144×6144 elements. Normally it is necessary to use fast Fourier transform to reduce computing time. The inverse of F is the inverse Fourier transform operator F^{-1}, as shown in Equation (3.5).

$$s_{xf} = F^{-1} \cdot s_{kt} \tag{3.5}$$

The sampling process can also be represented as the matrix product of sampling operator E and the signal in k-t space s_{kt}, as shown in Equation (3.6).

$$E \cdot s_{kt} = d_{kt} \tag{3.6}$$

E and F have the same size, while d_{kt} represents the undersampling result in k-t

space. The applied sampling pattern is solely described by E. E is a diagonal matrix when all the samples are collected at the positions on a Cartesian grid in k-t space, as shown in Equation (3.7).

$$\begin{aligned} &E(i,i) = 1 \quad if \;\; s_{kt}(i) \;\; is \;\; sampled \\ &E(i,i) = 0 \quad if \;\; s_{kt}(i) \;\; is \;\; not \;\; sampled \\ &E(i,j) = 0 \quad if \;\; i \neq j \\ &\qquad i = 1,2,...,N_k \times N_t \\ &\qquad j = 1,2,...,N_k \times N_t \end{aligned} \tag{3.7}$$

If some samples are not collected at the positions on a Cartesian grid, they can be regarded as interpolation results from those samples on the grid. In this case E is no longer a diagonal matrix, whose form depends on the selected interpolation method. It can also be regarded as a combination of a non-diagonal interpolation operator and a diagonal sampling operator. If the scan is undersampled, some entries of d_{kt} will be zero, and the entries in the corresponding rows in E are all zeros.

The relationship between the true signal s_{xf} and the undersampling result with aliasing d_{xf} in x-f space can be obtained by combining Equation (3.6), Equation (3.4) and Equation (3.5), as shown in Equation (3.8).

$$F^{-1} \cdot E \cdot F \cdot s_{xf} = F^{-1} \cdot d_{kt} = d_{xf} \tag{3.8}$$

If the scan is fully sampled, E will be a unit matrix and d_{xf} will equal s_{xf}. If the scan is undersampled, the combined operator $F^{-1} \cdot E \cdot F$ is neither a unit matrix nor a diagonal matrix. It has $N_k \times N_t \times N_k \times N_t$ elements or the linear equation system in Equation (3.8) has $N_k \times N_t$ variables and $N_k \times N_t$ equations. In the special case of a sampling pattern like a sheared grid, as shown in Figure (3.11), the combined operator has many zero entries. Only $N_k \times N_t/4$ rows have non-zero entries. In each of these rows only four entries have non-zero values. Each equation in the equation system has the same form as described in Equation (3.1). This explains how Equation (3.1) is derived. If a less regular sampling pattern is applied, such as a non-uniform one, most of the entries of the combined operator $F^{-1} \cdot E \cdot F$ will not be zero. This means that true signal at almost all the positions in x-f space contributes to the undersampled result at each position in x-f space.

Since operator E has many rows of all zero values and d_{kt} also have many zero

entries, an equivalent and simpler form of Equation (3.8) can be obtained by applying the Fourier transform operator F on both sides of Equation (3.8).

$$E \cdot F \cdot s_{xf} = d_{kt} \tag{3.9}$$

The linear equation system described in Equation (3.9) has only N_s equations, where N_s is the number of samples collected in k-t space. In the example shown in Figure (3.9), N_s equals $N_k \times N_t/4$. The matrix size of $E \cdot F$ is only one fourth of that of $F^{-1} \cdot E \cdot F$. Another benefit of using Equation (3.9) for reconstruction is that the undersampled raw data d_{kt} no longer needs to be inverse Fourier transformed into x-f space, which is difficult for non-uniformly sampled data.

By removing the rows of all zeros in $E \cdot F$ and the corresponding zero entries in d_{kt}, Equation (3.9) can be simplified to Equation (3.10).

$$C \cdot s_{xf} = d_{kt} \tag{3.10}$$

In Equation (3.10) C consists of all the rows from $E \cdot F$ with at least one non-zero entry. C has N_s rows and $N_k \times N_t$ columns. d_{kt} in Equation (3.10) has N_s entries, which is a compact version of d_{kt} in Equation (3.9) with all the zero entries removed. Obviously Equation (3.10) is underdetermined since the number of rows of C is smaller than the number of columns when the scan is undersampled. Equation (3.10) solely defines the sampling process.

In order to find the desired solution of Equation (3.10), a reconstruction operator R is defined in Equation (3.11).

$$s_{xf} = R \cdot d_{kt} \tag{3.11}$$

R has $N_k \times N_t$ rows and N_s columns. The relationship between R and C can be obtained according to Equation (3.10) and Equation (3.11), as shown in Equation (3.13).

$$R \cdot C \cdot s_{xf} = R \cdot d_{kt} = s_{xf} \tag{3.12}$$

$$(R \cdot C - I) \cdot s_{xf} = 0 \tag{3.13}$$

In Equation (3.13) I is a unit matrix of $N_k \times N_t$ rows and $N_k \times N_t$ columns.

The reconstruction operator R is calculated by solving an optimization problem

shown in Equation (3.14) [211, 230].

$$\min_{R} \quad w_{regu} \cdot ||R \cdot l_{kt}||^2 + ||(R \cdot C - I) \cdot m_{xf}||^2 \tag{3.14}$$

In Equation (3.14), $||\ \ ||$ calculates Frobenius norm (the square root of the sum of the absolute squares the elements of a matrix), l_{kt} is an estimate of background noises in k-t space as a vector of N_s entries, m_{xf} is the processed training data magnitudes in x-f space with $N_k \times N_t$ entries, and w_{regu} is a scalar used as a weight. The first part of Equation (3.14) (with l_{kt}) regularizes noise propagation in reconstruction. $R \cdot l_{kt}$ describes noise in x-f space after reconstruction. The other part of Equation (3.14) makes the result consistent with the sampling process and redistributes signal power according to the training data. w_{regu} is set according to the relative importance of the control of noise propagation in reconstruction compared with that of consistency with the samping process. Normally w_{regu} is empirically set to a small number. If w_{regu} is set to zero, which means that no noise regularization is applied, and C is ill conditioned, R will probably lead to irregular results in s_{xf}. The solution R from Equation (3.14) is shown in Equation (3.15).

$$\begin{aligned} R &= M \cdot C^H \cdot (C \cdot M \cdot C^H + w_{regu} \cdot \Psi)^{-1} \\ M &= m_{xf} \cdot m_{xf}^H \\ \Psi &= l_{kt} \cdot l_{kt}^H \end{aligned} \tag{3.15}$$

In Equation (3.15) X^H calculates the conjugate transpose of a matrix X, X^{-1} calculates the inverse of a matrix X, M is the covariance matrix of the training data, and Ψ is the covariance matrix of background noise. In practice the two covariance matrixes are simplified to diagonal matrices, as shown in Equation (3.16) and Equation (3.17).

$$\begin{aligned} &M(i,i) = m_{xf}^2(i) \\ &M(i,j) = 0 \quad if \ \ i \neq j \\ &\qquad i = 1,2,...,N_k \times N_t \\ &\qquad j = 1,2,...,N_k \times N_t \end{aligned} \tag{3.16}$$

$$\begin{aligned} \Psi(i,i) &= \sigma^2 \\ \Psi(i,j) &= 0 \quad if \;\; i \neq j \\ i &= 1,2,...,N_s \\ j &= 1,2,...,N_s \end{aligned} \tag{3.17}$$

In Equation (3.17) σ is the noise covariance, which can be measured in empty background of undersampled k-t data.

It has been suggested [211] that the baseline (static) part of the signal should be processed separately. If the temporal average of d_{kt} is defined as d_{kt0} and its representation in x-f space is named as d_{xf0}, the general form of the solution from the k-t BLAST method is given in Equation (3.18).

$$s_{xf} = d_{xf0} + R \cdot (d_{kt} - d_{kt0}) \tag{3.18}$$

In Equation (3.18) it is also necessary to remove the baseline part of the training data to obtain the correct M and R.

The separate treatment of the baseline part of the undersampled signal may introduce errors when the temporal dimension is not uniformly sampled. In this case the temporal average of d_{kt} may have significant differences from the true baseline signal.

This general form of the reconstruction method is computing intensive as the inverse of a large matrix is required to calculate the reconstruction operator R in Equation (3.15). The matrix has N_s rows and N_s columns. When a non-uniform sampling pattern in k-t space is applied the matrix is generally not sparse. It has been proposed that the conjugate gradient method can be used to reduce reconstruction time in this case [231].

Figure (3.12) summarizes the k-t BLAST reconstruction method. An example of the source code for k-t BLAST reconstruction is presented in Appendix A.2. The acquisition includes a training scan and a dynamic scan. In the training scan only central k-space is sampled at good temporal resolution. This produces the low spatial resolution raw training data. The raw training data is optionally filtered to reduce ringing artefacts when it is zero-filled to the same spatial resolution as in the dynamic scan. Then the training data is transformed into x-f space and optional filtering is applied in the temporal dimension to reduce noise in high temporal frequencies. In [211] the k-space filter was a Hamming filter and the temporal frequency filter was a low-pass filter, with a central pass band of 50% bandwidth and half-Hanning-shaped transition bands of 20% bandwidth on either side. The same filters will be used in

the implementations in following chapters, if not otherwise specified. In the dynamic scan k-t space is sampled sparsely according to a selected sampling pattern. In the fully sampled dimensions such as the frequency encoding dimension inverse Fourier transform is applied and after this the reconstruction for the data at each position in these dimensions is carried out separately. If the sampling pattern is like a sheared grid, for example in a scan prospectively gated, the simple form of the reconstruction method described in Equation (3.3) and Equation (3.2) can be used. The undersampled data is filled with zeros at the positions skipped during acquisition and inverse Fourier transformed into x-f space. Aliasing is resolved according to the magnitude of the proccessed training data in x-f space. If the sampling pattern does not have the form of a sheared grid, for example in a scan retrospectively gated, the general form of the reconstruction method described in Equation (3.14) and Equation (3.15) will be used.

In order to carry out a scan with the k-t BLAST method, several parameters have to be determined in advance. First the sampling patterns of the dynamic scan and the training scan have to be built. If a sampling pattern like a sheared grid is to be used for the dynamic scan, the total number of samples needs to be known. In [232] it has been suggested the sheared grid sampling pattern is the near-optimal sampling pattern for the k-t BLAST method since it minimizes the amount of signal overlap in x-f space. The parameter controlling the training scan sampling pattern is the number of k-space positions sampled at full temporal resolution, also known as the number of training k-space lines since the frequency encoding dimension is usually fully sampled. In [233] it has been reported reconstruction error continues to decrease, albeit by a diminishing amount, as the amount of training data increases, but an increased amount of training data also increases susceptibility to misregistration of the training data. The total scan time includes the time spent on both the dynamic and the training scans. For reconstruction, the noise regularization weight w_{regu} also needs to be set empirically. Different settings of these parameters will be tested in following chapters.

Applications of the k-t BLAST method so far are mostly for cardiac imaging [223, 224, 226, 227, 228]. In most cases good results can be reconstructed from about one fourth of full signal. The feasibility of using the method for measuring carotid flow has also been investigated in [225]. It has been shown the flow velocity waveforms from k-t BLAST reconstruction were in good agreement with fully sampled results, but as the amount of collected samples decreased, the waveforms from the undersampled data became smoother suggesting losses in temporal resolution. It has also been

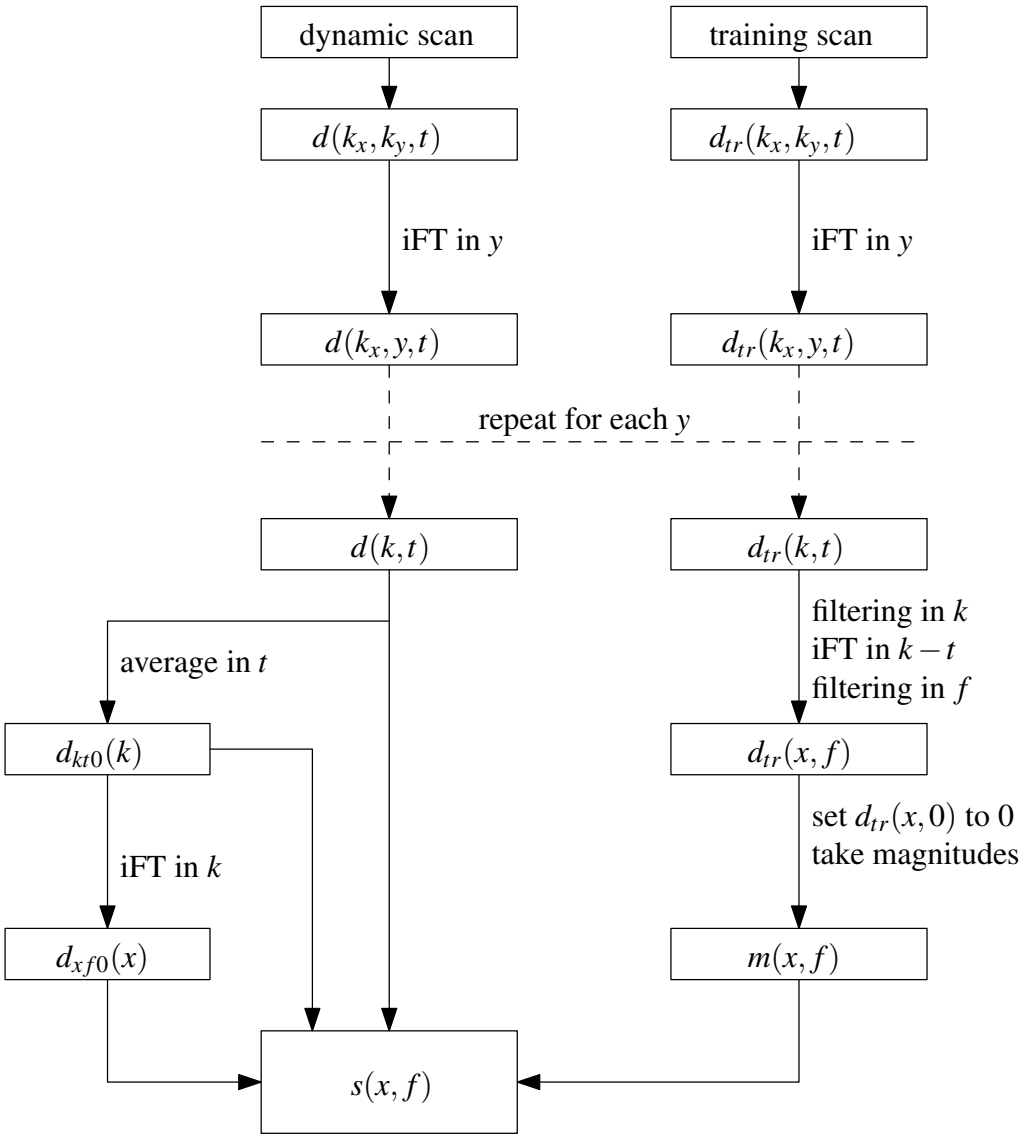

Figure 3.12: Processing of the data from the training scan and the dynamic scan in the k-t BLAST technique. Frequency encoding is applied along the y axis, and phase encoding along the x axis.

reported [234] that the results from k-t BLAST reconstruction are visually appealing, even with high undersampling, in single timeframes, but when temporal variations are considered it becomes apparent that temporal fidelity is suffering from the regularization. Both spatial and temporal fidelity of k-t BLAST reconstruction will be examined in following chapters.

3.5 The k-t variable-density method

When a scan is retrospectively gated, the resulting sampling pattern does not conform to a Cartesian grid. For the k-t BLAST method, the general form of the method has to be used. The general form of the reconstruction method is complicated and computing intensive, which makes it difficult to acquire. In addition to that, a separate training scan may also be inconvenient to implement. To overcome these problems and to evaluate the performance of non-uniform k-t undersdampling patterns, a k-t variable-density undersampling method is proposed.

In acquisition, the ktVD method samples k-t space non-uniformly according to a pre-scheduled sampling pattern. An example of the source code for building ktVD sampling patterns is presented in Appendix A.3. Every k-space position is sampled at least once. The number of samples over the time course at each position decreases gradually from the centre to the edges of k-space. A small central region of k-space is sampled at full temporal resolution. The samples of the same k-space position are equally spaced in the temporal dimension. Several examples of such sampling patterns in 2D k-t space are shown in Figure (3.13). The sampling patterns used for the ktVD method are empirically designed according to the total number of samples to be collected. In reconstruction, data at each k-space position is processed separately. Temporal interpolation is applied at each k-space position to recover the full data set in k-t space.

The ktVD method can be regarded as a generalized version of the aforementioned non-uniform k-t undersampling techniques, such as the TRICKS technique and the BRISK technique. The sampling patterns are designed in k-t space, not on a frame-to-frame basis. It is not necessary to divide k-space into blocks, although this may be convenient in implementation. The numbers of samples at neighbouring k-space positions can be different. No training scan or reference images are required.

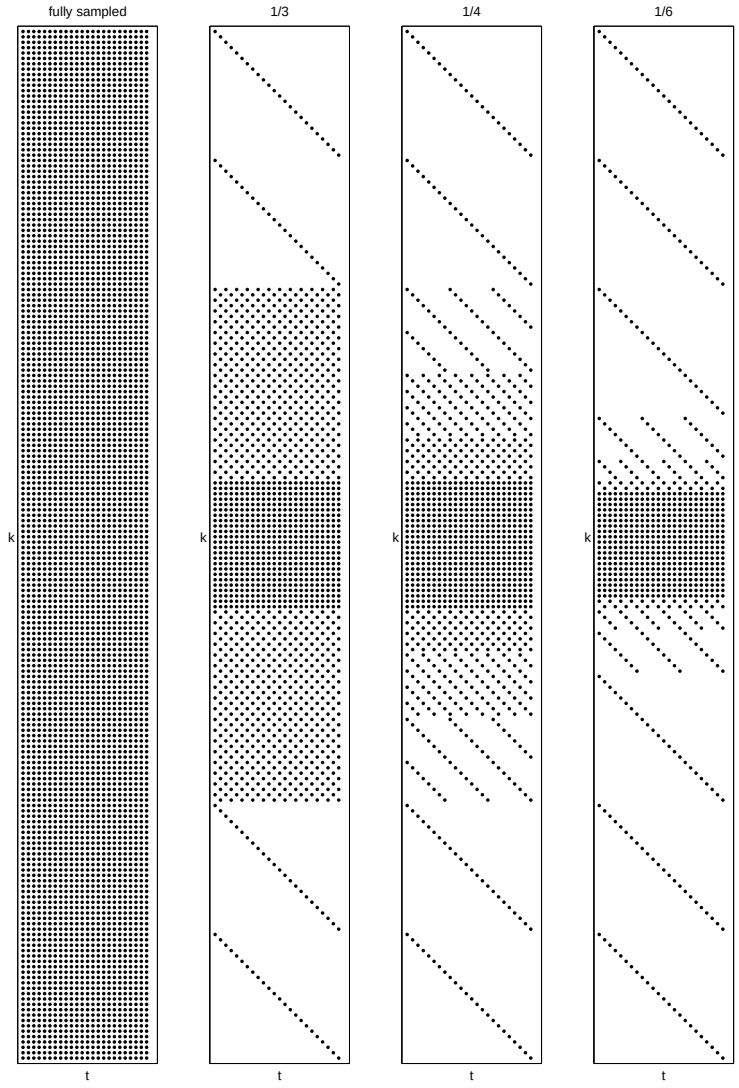

Figure 3.13: Examples of the sampling patterns used by the ktVD technique. Each dot represents a k-space line collected in acquisition. Skipped k-space lines are not displayed. The k-t sampling pattern of a fully sampled scan is also displayed (left).

The underlying assumption of the ktVD method is also slightly different from those of the early techniques. The ktVD method does not assume sharp image features change more slowly than spatially smooth image contents. If background noise is not taken into consideration, signal temporal bandwidth in high spatial frequencies may be similar to that in low spatial frequencies. This means outer regions of k-space should also be sampled at a good temporal resolution. However, SNR of realistic MR data is often low in outer regions of k-space. Since background noise may produce random temporal changes, the total of background noise and the desired signals from the scanned dynamic subject may also appear random over time. It will not help to reduce contributions from noise by collecting more samples at those k-space positions. The ktVD method assumes it is not necessary to sample at high temporal resolution in those regions of k-space where SNR is low. Generally realistic MR signal power decreases gradually from the centre to the edges of k-space and background noise is at the same level, so SNR also decreases gradually across k-space in most cases. Ideally the sampling density in k-t space changes according to the variation of SNR in k-space, but this is difficult in practice because signal power distribution over k-space is not known in advance. Sampling at a temporal resolution higher than necessary may help to improve coverage of high SNR areas in k-space.

The reconstruction of the ktVD method recovers full signal for each k-space position separately. An example of the source code for ktVD reconstruction is presented in Appendix A.4. This reduces computation burden. For example, if the cardiac cycle is divided into 24 phases, only 24 unknown variables are involved in the reconstruction of each k-space position. Since it is assumed that the applied sampling pattern has covered k-t space at the necessary temporal resolution, no additional prior knowledge is required in reconstruction. For example, if only one sample is collected in the cardiac cycle at a k-space position, the value of the sample is simply copied to all the cardiac phases in reconstruction. If a k-space position is sampled at half of the full temporal resolution, the signal values at this position for the 24 cardiac phases are interpolated from the twelve samples. Simple linear interpolation can be used and reconstruction can be very fast. If complicated interpolation algorithm is adopted, reconstruction time will be longer. Since for each interpolation the number of unknown values is at most 24, the increase in reconstruction time is not very significant.

When a sampling pattern does not cover k-t space at the necessary temporal resolution, it can be expected at some k-space positions, especially those in outer k-space,

dynamic information may be lost. This suggests temporal smoothing is more likely to happen in high spatial frequencies. It also suggests the performance of the ktVD method will be affected by signal content and the applied sampling pattern. A sampling pattern is determined by the number of samples to be collected and the sampling density distribution in k-t space. The effects of these two factors will be investigated in the following chapters.

3.6 Implementation of the undersampling patterns on the scanner

All scans in this work were carried out on a 1.5 T GE Signa scanner (GE Medical, Slough, UK), whose gradients had a maximum amplitude of 23 $mT\ m^{-1}$ and a slew rate of 120 $mT\ m^{-1}\ ms^{-1}$. The scanner was controlled by two computer systems, known as the host system and the scanner system. The software on the host system was a LINUX operating system, providing user interface for the scan operator. The software on the scanner system was a real-time operating system (VxWorks), providing controls of the devices such as the gradients and the RF transmitter. Each pulse sequence program consisted of two executables, one for each system. An Environment for Pulse programming In C (EPIC) and the source codes of installed pulse sequence programs were provided with the scanner. The EPIC version used in this work was 14M4. The provided source codes were written in an EPIC programming language similar to ANSI C, with predefined libraries and macros. They could be modified and recompiled to introduce new pulse sequence programs to the scanner. Image reconstruction could be completed automatically on the scanner after the scan, or switched off to allow offline processing of the raw signal files. In the raw signal files the data was saved in exactly the same order as in acquisition.

In the original 2D phase contrast pulse sequence program installed on the scanner, the repetitions were organized as nested loops, as shown in Figure (3.14). In each T_R, only one k-space line was acquired. This was repeated for different settings of flow encoding, phase encoding, and different cardiac phases. The flow encoding loop was in the excitation loop, which was an inner loop of the phase encoding loop. The original 3D phase contrast pulse sequence program, for 3D scans, had a similar structure with an extra slice encoding loop. In each pass of the excitation loop, the excitation steps

were repeated without any changes of the scan setting. If the signal of interest does not change over time, the differences between the samples from different excitation steps will be noise. These samples can be averaged to improve SNR. For this reason, the number of excitations (NEX) in each pass of the excitation loop is often used to specify the number of copies of the data averaged to improve SNR. In this work the excitation loop was used to cover one or more cardiac cycles for retrospective gating. For example, if each pass of the excitation loop was to cover one cardiac cycle, the NEX would need to be large enough so the duration of each pass of the excitation loop could be longer than the cardiac cycle.

In the original 2D phase contrast pulse sequence program, the excitation loop and the phase encoding loop determined the sampling pattern in k-t space. All the samples at the same phase encoding position were collected before the next phase encoding position was sampled. In the modified pulse sequence program, as shown in Figure (3.15), the excitation loop and the phase encoding loop were replaced with a new loop specified by a predetermined undersampling pattern, which was a list of phase encoding positions. Each step of the new loop was similar to the steps of the excitation loop in the original pulse sequence program, but the phase encoding position was set according to the list. For example, if 24 steps were used to cover a cardiac cycle, and two neighbouring phase encoding positions were sampled at half temporal resolution, the two positions could be listed in the undersampling pattern interleaved for twelve times. In this way for each phase encoding position the samples were still equally spaced in the cardiac cycle, and in the 24 steps two phase encoding positions were covered. Similar modifications were made to the 3D phase contrast pulse sequence program, as shown in Figure (3.16). For different slice encoding steps, the lists of the phase encoding positions could be different.

It should be noted that with retrospective gating the position of each repetition in the cardiac cycle is unknown before the scan, and for different steps of the flow encoding loop or the slice encoding loop the actual sampling patterns are different. All sampling patterns presented previously were displayed in the form as in a prospectively gated scan of constant heart beats to illustrate the design of the patterns. With retrospective gating the sampling patterns were less regular, as shown in Figure (3.17). For the k-t BLAST method this was a problem because the sampling patterns did not conform to the sheared grid pattern and the general reconstruction method had to be used, which was computing intensive. For the ktVD method, there was no significant

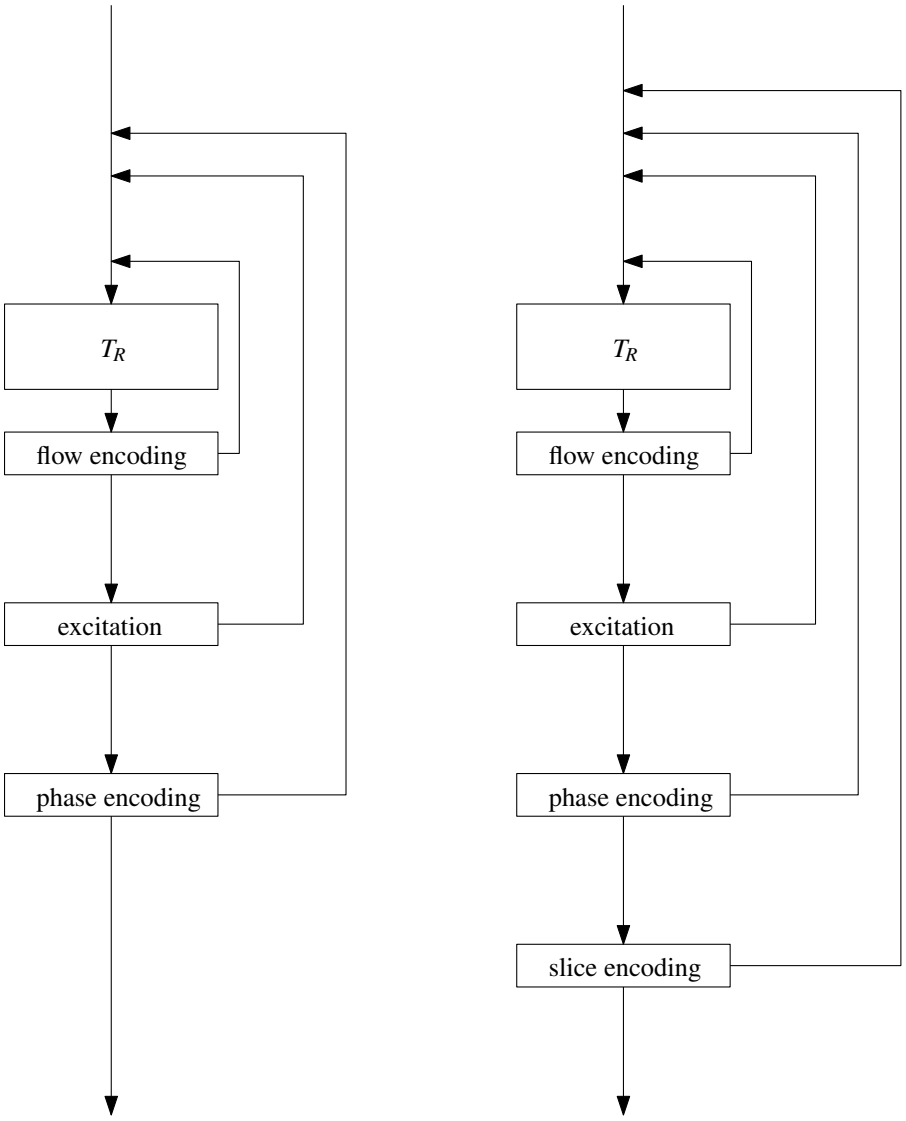

Figure 3.14: The structures of the original 2D (left) and 3D (right) phase contrast pulse sequence programs installed on the scanner.

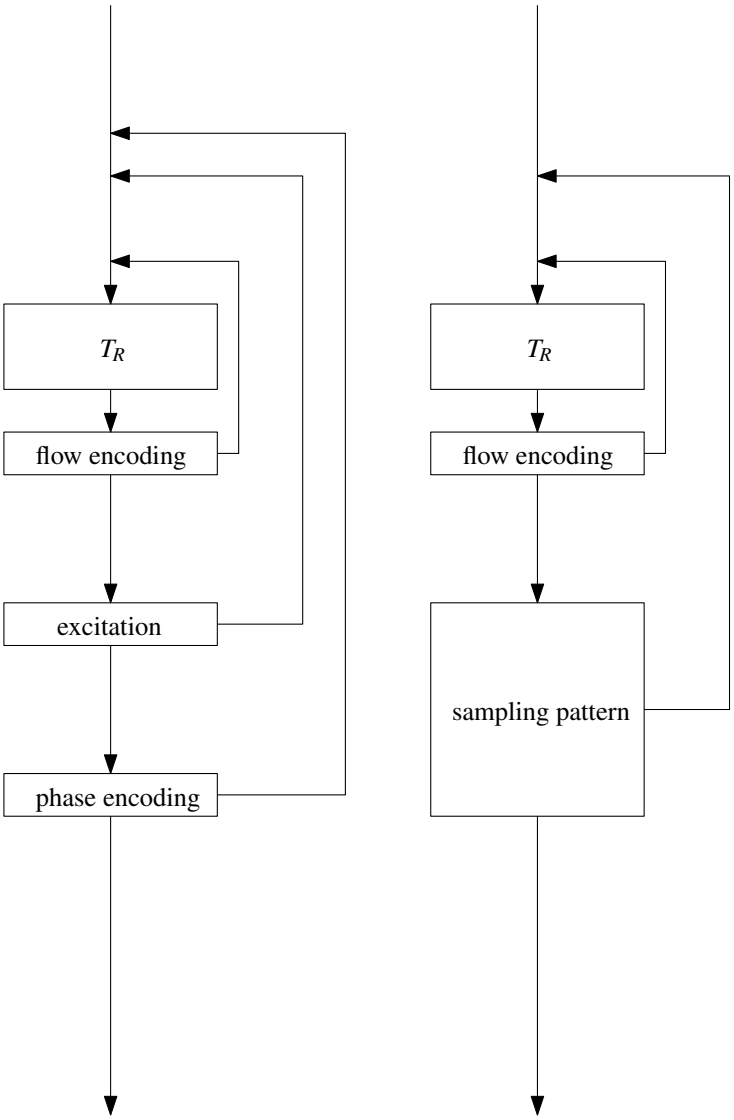

Figure 3.15: The modifications (right) to the original 2D phase contrast pulse sequence program (left).

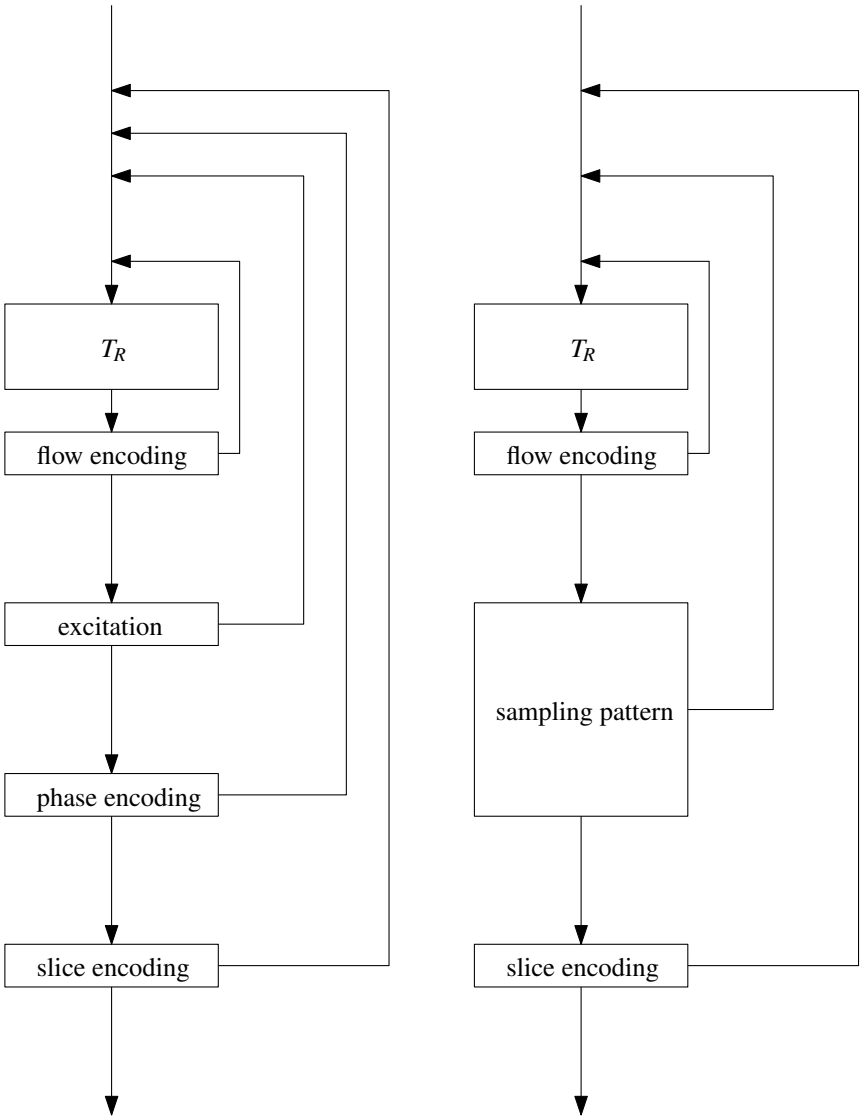

Figure 3.16: The modifications (right) to the original 3D phase contrast pulse sequence program (left).

difference, since at each phase encoding position the distribution of the samples in the normalized cardiac cycle was still nearly uniform. All sampling patterns presented in the following chapters are displayed in their design form without retrospective gating, unless otherwise specified.

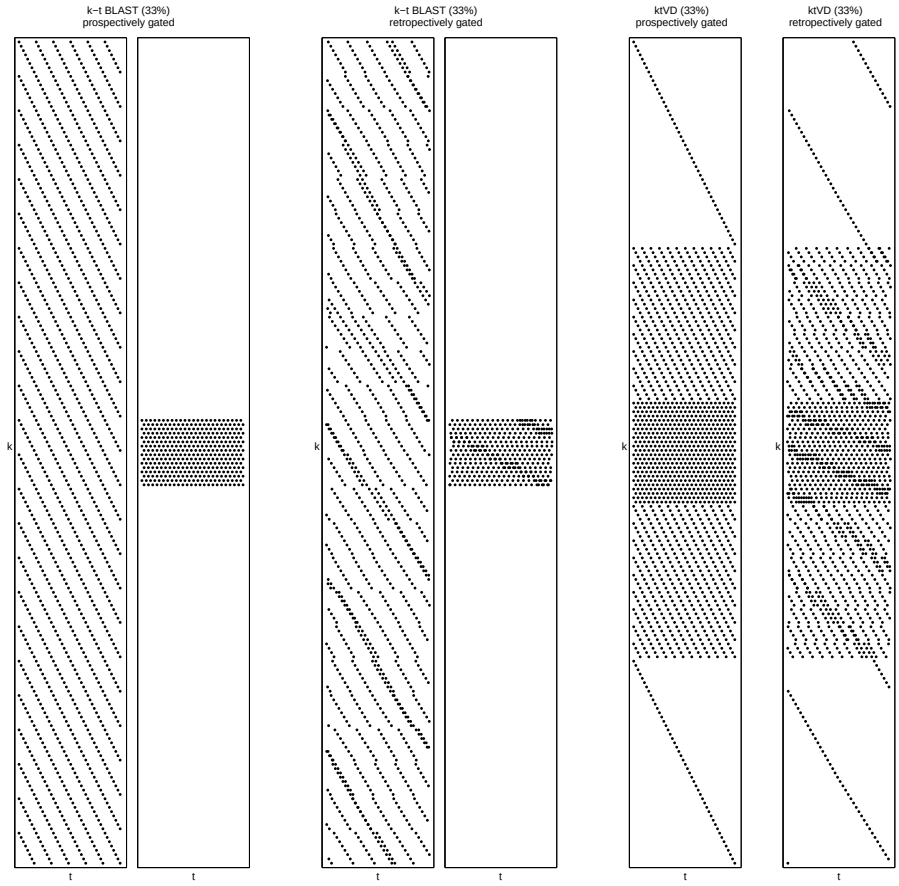

Figure 3.17: Sampling patterns with and without retrospective gating.

Chapter 4

Simulations of undersampling in two dimensions of k-t space

4.1 Introduction

The quality of the results obtained from an undersampled scan is affected by many factors, such as the scan setting or the undersampling method. First of all, several control parameters of the undersampling methods need to be empirically determined. The setting of these parameters will have an influence on the reconstruction results. In order to find an optimal setting, a large number of tests need to be carried out to try different settings. Simulations are good for this purpose because hundreds of scans can be simulated without involving any human subjects.

In the simulations it is better to apply undersampling in only two dimensions of k-t space. This is simpler than undersampling in three dimensions and easier to implement. Since signal acquisition in the frequency encoding dimension is fast, undersampling is only applied in the temporal and the phase encoding dimensions. Undersampling in two dimensions can be tested in 2D time-resolved scans of single slices. In 3D time-resolved scans of multiple slices, k-t space can be undersampled in three dimensions, but the minimum scan time of 3D scans were much longer than that of 2D scans of single slices at the same spatiotemporal resolution. In 3D scans 3D Fourier transform needs to be used in image reconstruction and this will complicate error propagation. Another benefit of using 2D scans is that the optimal setting of the control parameters obtained in 2D scans can also be useful in 3D scans.

In this chapter the k-t BLAST and the ktVD method are tested in simulations. Realistic data sets collected in a fully sampled 2D time-resolved scan are used as source data sets for simulated undersampling. Different settings of the control parameters of each undersampling method are tested. The differences between the reconstruction results obtained from the undersampled data and those from the source data sets are used to evaluate undersampling errors. Optimal settings of the control parameters are selected accordingly. The performances of the two undersampling methods are also compared.

4.2 Method

4.2.1 Simulation overview

In general, the simulations use interpolation to simulate real signal acquisition. Real dynamic data sets are collected in a fully sampled scan with retrospective gating. With temporal gridding these data sets are converted into source data sets providing signal values at equally spaced positions in the cardiac cycle. The signals of the simulated scans are interpolated from the source data sets. The corresponding phase encoding positions of the samples are specified in the undersampling pattern. A real gating record is used to provide the timing of the cardiac cycles and determine each sample's corresponding position in the cardiac cycle. Since the source data sets are collected at a high temporal resolution, linear temporal interpolations are used to generate the signal values of the samples.

4.2.2 Control parameters of the simulations

The sampling ratio R_s is the most important control parameter in an undersampled scan. It determines how much scan time can be saved and it also affects the quality of the undersampling results. Three different R_s (50%, 33%, 25%) were tested in the simulations. If each phase encoding position is sampled 24 times over the cardiac cycle in a fully sampled scan, in average six samples will be collected at each position in an undersampled scan at the R_s of 25%. A lower R_s is desirable, which means further scan time reduction, but results from preliminary tests suggested there would be significant loss in signal quality. An R_s higher than 50% is not very useful because of limited scan

acceleration. The three values of the R_s are also selected to make it easy for the design and implementation of the undersampling patterns.

Another important control parameter is the noise level of the signal. There is always noise in real MRI signal. In an undersampled acquisition, both useful signal and noise are undersampled. When the skipped part of the signal is recovered according to prior knowledge or assumptions, noise in the signal may be changed or even amplified, depending on the reconstruction method. In k-t BLAST reconstruction, the noise regularization aims to minimize noise amplification. For the ktVD method, a higher noise level means that a larger part of the signal can not be accurately measured and more samples can be skipped in acquisition. In real scans the noise level of the signal is difficult to control. In the simulations the source data sets can be the averages of different sets of signal collected with the same scan setting. For example, the background noise standard deviation was reduced to 0.74/0.59/0.51 of that of a single signal set when two/three/four signal sets were averaged to generate the source data sets. Four sets of signal provide source data sets of four different noise levels (NEX 1/2/3/4).

For the k-t BLAST method, two control parameters were tested. The first is the number (N_{tr}) of central k-space lines sampled at full temporal resolution in the training scan and used as training data in reconstruction. The scan time of the training scan was also included in the calculation of total scan time and the sampling ratio. More dynamic information in central k-t space was collected when the N_{tr} was larger, at the cost of more scan time spent in the training scan. For a fixed R_s, larger N_{tr} also meant fewer samples in the dynamic scan. It is necessary to investigate how the N_{tr} affects the results from k-t BLAST reconstruction. If the results do not change much at different N_{tr}, a small N_{tr} can be used to reduce san time or improve signal quality. In the simulations, six values of the N_{tr} (12, 16, 20, 24, 28 and 32) were tested. These values were selected according to the total number of k-space lines, which was set to 192. 12 k-space lines covered 1/16 of k-space FOV, and 32 lines covered 1/6. It should be noted that the same sampling pattern for the dynamic scan was used in the tests of different values of the N_{tr}, so the sampling ratio changed slightly.

The other control parameter for the k-t BLAST method is the weight (W_{regu}) of noise regularization in k-t BLAST reconstruction. A larger W_{regu} will reduce noise amplification more effectively, while the reconstruction results will be less consistent with the sampling process. No regularization is applied when the W_{regu} is set to zero. In the simulations four values (0, 0.2, 1 and 2) of the W_{regu} were tested.

For the ktVD method, the sampling density variation over k-t space can be different for the same sampling ratio. The sampling ratio only determines the total number of samples to be collected. It does not specify the positions of these samples in k-t space. Given a fixed sampling ratio, more samples in central k-t space leave fewer samples in the outer regions. Ideally the sampling density variation should match the signal content, but this is unknown in advance for real scans. The tests of different sampling density variations can show how this will affect undersampling results and help design sampling patterns for similar applications. In the simulations, for each sampling ratio two variable-density sampling patterns were tested. Central k-t space was more densely sampled and fewer samples were allocated to the outer regions in one of sampling patterns than in the other one. Overall six sampling patterns were tested for the ktVD method.

In summary, for the k-t BLAST method, all combinations of three sampling ratios, four noise levels, four values of the noise regularization weight and six numbers of training k-space lines were tested. In total 288 sets of simulation results were obtained. For the ktVD method, 24 sets of results were obtained, corresponding to six sampling patterns and four noise levels.

4.2.3 Source data sets

The signals from a fully sampled scan were divided into four parts to generate four source data sets at different noise levels. The fully sampled scan was retrospectively gated. The T_R was set to the minimum value, 20 ms. Flow encoding was only applied in the superior/inferior direction so for each phase encoding step and each cardiac phase two k-space lines (referred to as a sample in the following descriptions) needed to be collected, which required twice the T_R. The average length of the cardiac cycle was about 1.1 second. For each phase encoding step 96 samples were collected, covering two cardiac cycles. Each cardiac cycle was covered by 48 samples. These 48 samples were divided into two groups, as shown in Figure (4.1). Each group consisted of 24 samples. The interval between two neighbouring samples in the same group was four times the T_R. In this way the data from the fully sampled scan was divided into four signal sets of the same temporal resolution. After gridding, each signal set had the same timing and they were averaged to generate four source data sets at different noise levels. 24 timeframes can be reconstructed from each source data set.

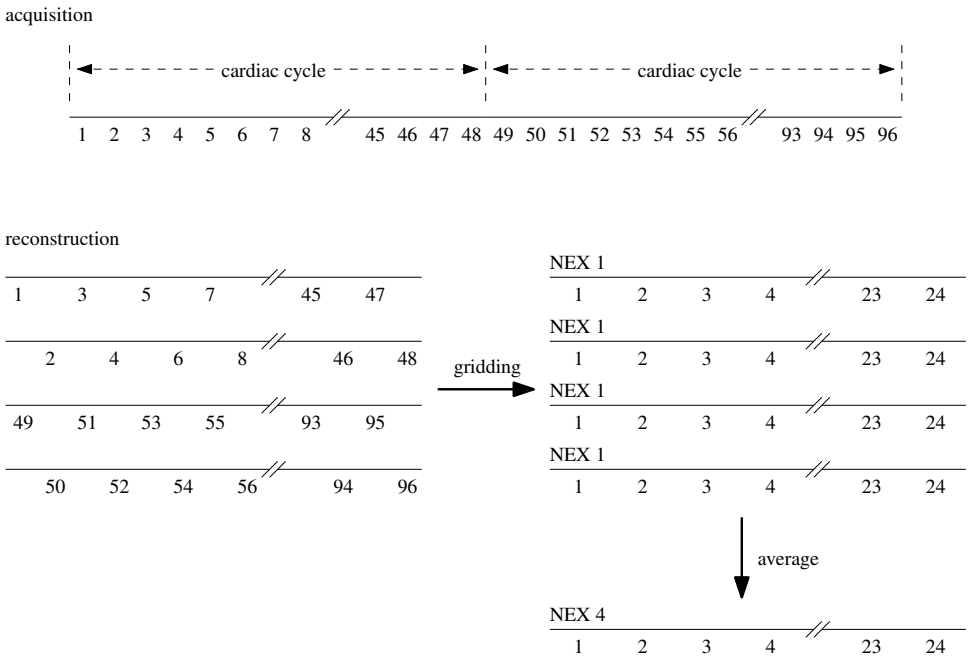

Figure 4.1: In the fully sampled scan 96 samples (k-space lines) were collected for each phase-encoding position to cover two cardiac cycles. In reconstruction they were divided into four data sets of the same temporal resolution, and averaged to generate a high-SNR data set (NEX 4).

In the fully sampled scan, an axial slice 1 cm below the carotid bifurcation of a healthy male volunteer was scanned with the 2D phase-contrast sequence installed on the scanner. The study was approved by a local ethics committee, and informed consent was obtained from the volunteer. The subject lay supine. Frequency encoding was in the anterior/posterior direction and phase encoding was in the left/right direction. A 4-element phased-array carotid surface coil was used for signal reception. All the channels of the coil were used in the scan. The signal from only one channel was selected for generating the source data sets. The signal set of the highest SNR was selected.

Timing signals coincident with the RF pulses from the scanner and the triggering pulses from a pulse oximeter were recorded simultaneously during the scan as a retrospective gating record for the reconstruction of the actual sampling patterns in k-t space. The average heart rate of the volunteer was around 55 beat/min.

The FOV was 12 cm, the scan matrix was 192×192, the slice thickness was 2.0 mm, and the voxel size was $0.625 \times 0.625 \times 2\ mm^3$. The V_{ENC} was 100 cm/s, the acquisition bandwidth was 15.63 kHz, the T_E was 8 ms, and the Flip Angle was 30°. The total scan time was about 737 seconds. Raw signals were saved without post-processing on the scanner for offline reconstruction.

4.2.4 Sampling patterns

For the k-t BLAST method three sampling patterns (#1, #2 and #3) were tested, as shown in Figure (4.2). For sampling pattern #1 the dynamic scan covered 1/3 of k-t space FOV and the training scan covered 1/6. The R_s was 50% and the N_{tr} was 32. For sampling pattern #2 the R_s was 33% and the N_{tr} was 16. For sampling pattern #3 the R_s was 25% and the N_{tr} was 16. The design of the sampling pattern was limited by the scan matrix and gating requirements. The samples at the same phase encoding position should be equally spaced over the cardiac cycle. For a scan of 24 time frames, it means that the possible number of samples over the cardiac cycle for each phase encoding position can only be 24, 12, 8, 6, 4, 3, 2 or 1. The number of samples for the dynamic scan was selected first, and then the N_{tr} was determined according to the R_s. As described previously, when different values of the N_{tr} were tested, the sampling patterns for the dynamic scans were not changed.

For the ktVD method six variable-density sampling patterns (#4 to #9) were tested,

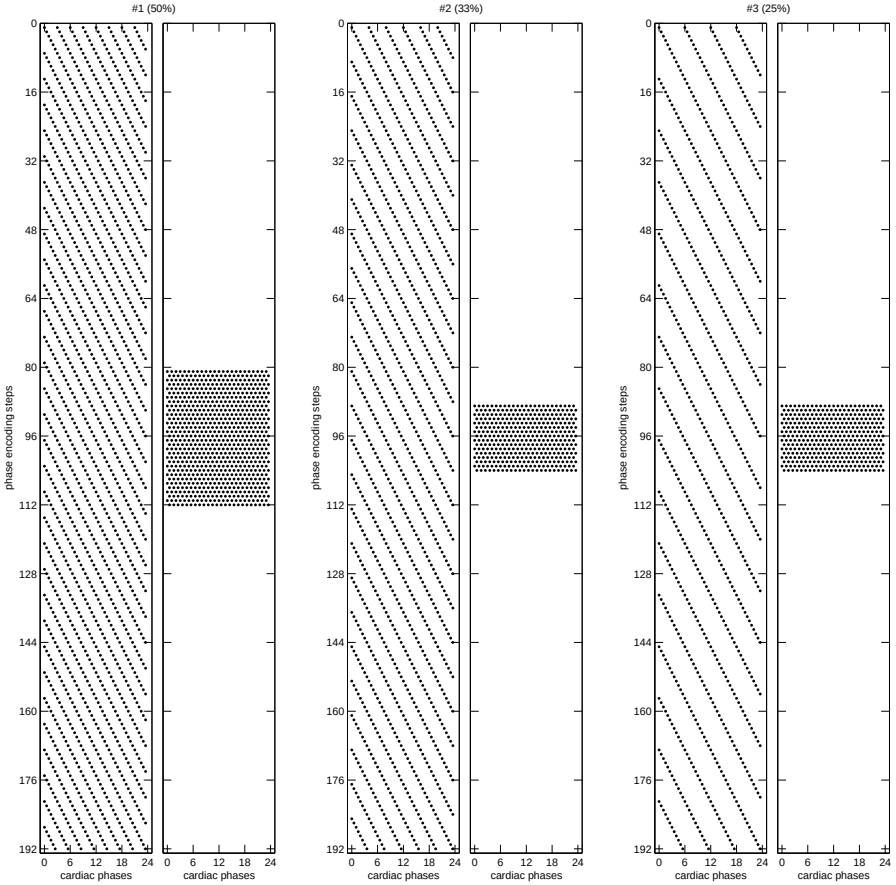

Figure 4.2: The sampling patterns for the k-t BLAST simulations. The left half of each sampling pattern is for the dynamic scan, and the right half is for the training scan. Each black dot in the sampling patterns represents a k-space line.

as shown in Figure (4.3). Ideally the number of samples at the same phase encoding position should decrease gradually from the centre to the edges of k-space. Due to limited choices for the number, k-t space was divided into bands and each band is uniformly undersampled. For a given sampling ratio and a scan matrix, there were only limited combinations of the sizes of the bands of different sampling densities. Two of the combinations at each sampling ratio were selected for the tests of different sampling density variations over k-t space. The R_s was 50% for sampling patterns #4 and #5. More samples were collected in central k-t space in sampling pattern #5 than in sampling pattern #4. Similarly the R_s of sampling patterns #6 and #7 was 33%, and for sampling patterns #8 and #9 it was 25%.

4.2.5 Methods of comparisons between simulations

First the simulation results obtained with the same undersampling method were compared to investigate the effects of the control parameters on the results. A set of optimal control parameters were selected accordingly, and the results obtained with the nine sampling patterns were compared.

For the comparisons between the results obtained with different settings of the control parameters, intensity differences D_i and phase differences D_p were calculated to evaluate undersampling errors. They are averaged voxel-wise differences between the image values recovered from the undersampled data and those reconstructed from the corresponding source data set. Only the images with flow encoding were used in these comparisons. The absolute values of the differences were averaged in selected regions and over the cardiac cycle, as shown in Equation (4.1) and Equation (4.2). The absolute values of the differences between the intensity values in the images from the simulation results and those in the images from the source data sets were normalized to the mean intensity value I_{MA} in the RCCA lumen. Complex phase differences were calculated for the phase differences to avoid phase wrap and the phase differences were presented in form of velocities. The value of V_{ENC} was used to convert the phase differences into velocities. Two regions of interest (ROI) were selected, as shown in Figure (4.4). The intensity ROI included the RCCA and a small area surrounding it. The phase ROI was placed inside the lumen of the common carotid artery because only

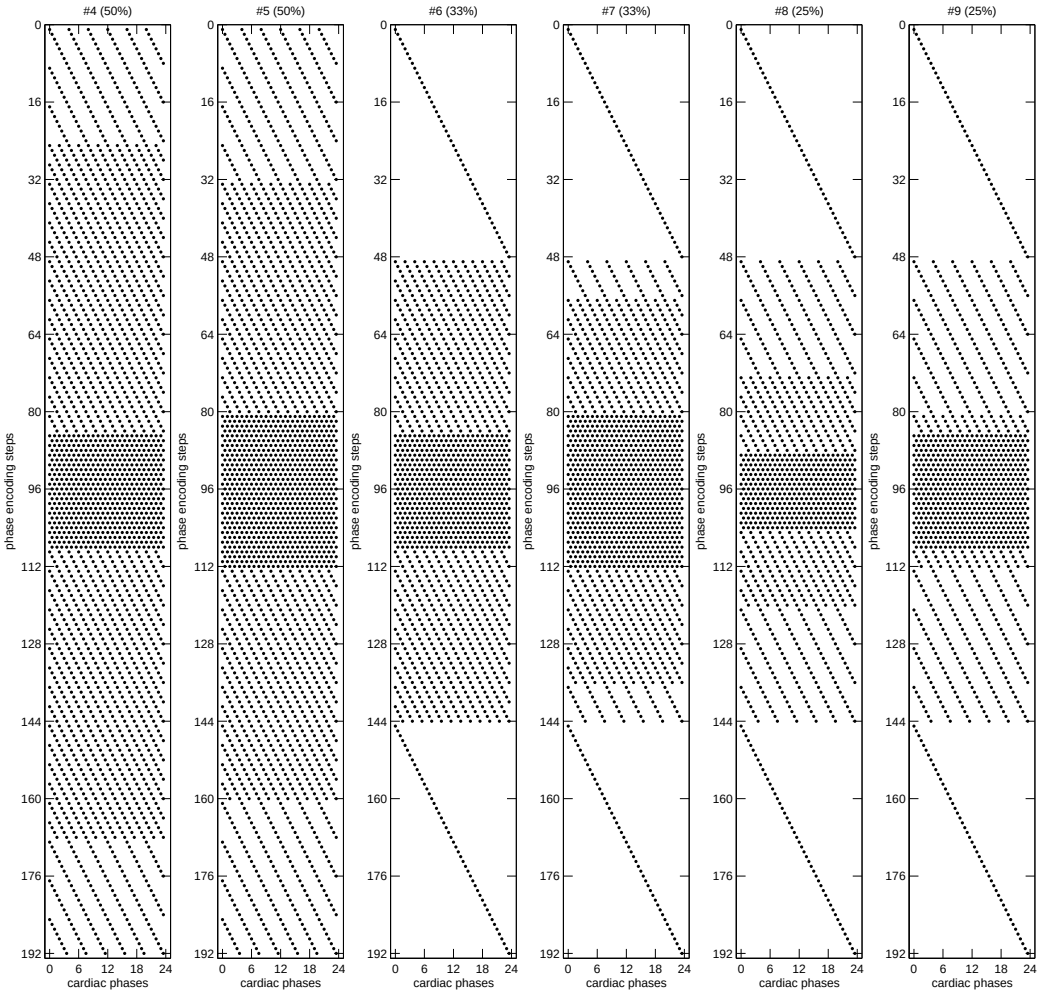

Figure 4.3: The sampling patterns for the ktVD simulations. Each black dot in the sampling patterns represents a k-space line.

the phase values in the lumen were useful for velocity calculation.

$$D_i = \frac{1}{I_{MA} \cdot N_{vox} \cdot N_t} \sum_{x,y,t} |I_S(x,y,t) - I_F(x,y,t)| \tag{4.1}$$

$$D_p = \frac{V_{ENC}}{\pi \cdot N_{vox} \cdot N_t} \sum_{x,y,t} \left| atan2(S_f(x,y,t) \cdot conj(F_f(x,y,t))) \right| \tag{4.2}$$

In Equation (4.1) I_S is the intensity value from the undersampled scan with flow encoding, and I_F is the intensity value from the fully sampled scan with flow encoding. $|\quad|$ calculates the modulus of a real number, x and y refer to the positions of the voxels, t refers to the cardiac phases in the selected period, N_{vox} is the number of voxels in the selected region, and N_t is the number of cardiac phases in the selected period. In Equation (4.2) S_f is the complex image value from the undersampled scan with flow encoding, and F_f is the complex image value from the fully sampled scan with flow encoding. $conj()$ calculates the conjugate of a complex number, $\cdot$ calculates the complex product, and $atan2()$ calculates the angle of a complex number with the range in $(-\pi, \pi]$.

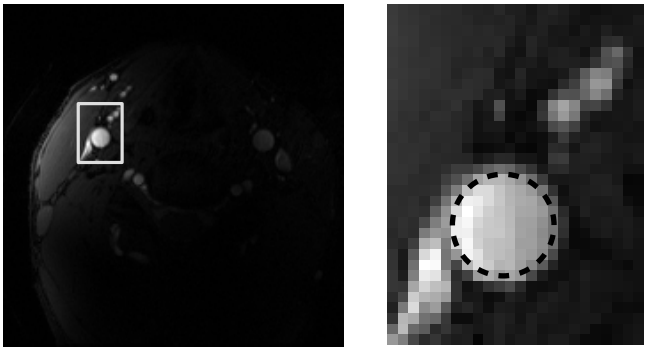

intensity ROI phase ROI

Figure 4.4: The position of the intensity ROI (left) in the image and the position of the phase ROI (right) in the intensity ROI.

For each one of nine sampling patterns, one set of simulation results corresponding to the highest noise level (NEX 1) was selected for comparisons with the results reconstructed from the source data set of the lowest noise level (NEX 4). Since the R_s, the N_{tr} and the sampling density variation were specified in the sampling patterns, only the value of the W_{regu} was set according to the simulation results. In total, ten

sets of results were compared, as summarized in Table (4.1). For convenience, the nine simulated scans were named after the sampling patterns, such as scan #1 using sampling pattern #1. The fully sampled scan were named as scan #0, corresponding to the results reconstructed from the selected source data set.

scan	method	sampling pattern	sampling ratio
#0			400%
#1	k-t BLAST	#1	50%
#2	k-t BLAST	#2	33%
#3	k-t BLAST	#3	25%
#4	ktVD	#4	50%
#5	ktVD	#5	50%
#6	ktVD	#6	33%
#7	ktVD	#7	33%
#8	ktVD	#8	25%
#9	ktVD	#9	25%

Table 4.1: The sampling ratios and sampling patterns of the simulated scans.

The difference images between the intensity images from scan #0 and those from the nine undersampled scans were compared in selected regions. The difference images were obtained by calculating the absolute values of the voxel-wise intensity differences between two sets of images. In the region without blood vessels, the difference images can be used to examine undersampling errors in static signals. In the region including the RCCA, they can show the effects of undersampling on dynamic signals.

Intensity difference (D_i) and velocity difference (D_v) between scan #0 and the undersampled scans were then evaluated. Equation (4.3) shows the calculation of the velocity differences. D_v is proportional to the differences between the phase differences from scan #0 and the phase differences from an undersampled scan. The calculation of the phase differences from the same scan and the phase differences between different scans were combined to avoid phase wrap. The absolute values of the voxel-wise phase differences were averaged in selected regions and periods and converted into velocities differences.

$$D_v = \frac{V_{ENC}}{\pi \cdot N_{vox} \cdot N_t} \sum_{x,y,t} \left| atan2(S_f(x,y,t) \cdot conj(S_{nf}(x,y,t)) \cdot conj(F_f(x,y,t)) \cdot F_{nf}(x,y,t)) \right| \tag{4.3}$$

In Equation (4.3) S_{nf} is the complex image value from the undersampled scan without flow encoding, and F_{nf} is the complex image value from the fully sampled scan without flow encoding.

To compare the differences along the spatial dimensions, four regions of interest were selected. An illustration of the positions of the ROIs is shown in Figure (4.5). The first ROI (the static ROI) contained only static tissues without any blood vessels. Another ROI (the large ROI) included the RCCA, the arterial wall and a small surrounding area. This ROI contained all the spatial features of the artery in the image. Both static tissue and dynamic flow were included. A third ROI (the flow ROI) contained all the voxels in the lumen of the RCCA. Arterial wall was not included in the flow ROI, but some voxels near the edge of the ROI were close to the wall. The last ROI (the core ROI) included only the core area in the lumen. The statistics from this ROI provided information about the flow near the central line of the RCCA. The flow ROI was first placed after the segmentation of the RCCA. Then the large and the core ROIs were placed according to the positions of the flow ROI. Generally the boundaries of the large and the core ROIs were two or three voxels away from the boundary of the flow ROI. For the segmentation, the intensity images without flow encoding from scan #0 (NEX 4) were averaged over the cardiac cycle to produce a high SNR intensity image. The voxels in the lumen of the RCCA were manually labelled according to the intensity values in the temporal averaged image. Those voxels very close to the wall and difficult to classify were not included in the flow ROI.

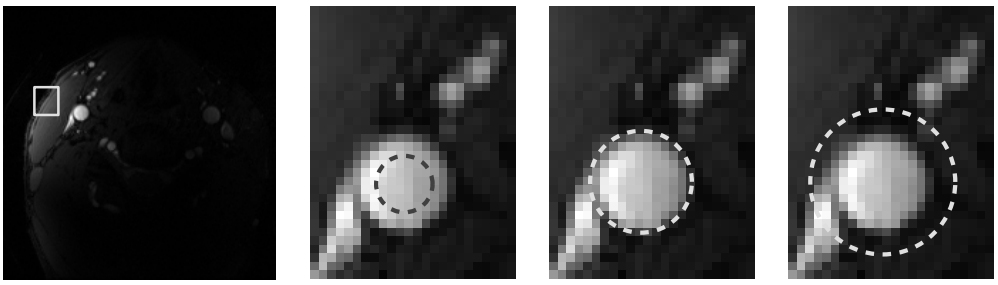

Figure 4.5: The positions of the static , core, flow and large ROIs (from left to right).

To compare the differences in the temporal dimension, the cardiac cycle was divided into two parts, the systolic period and the diastolic period. Figure (4.6) shows the positions of the two periods in the cardiac cycle.

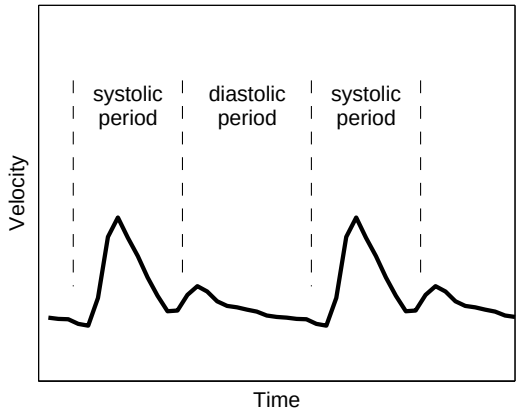

Figure 4.6: The positions of the systolic period and the diastolic period in the cardiac cycle. Typical carotid velocity waveforms over two cardiac cycles are also displayed.

When D_i or D_v was compared in different ROIs, results were averaged over the cardiac cycle. For D_i all four ROIs were used. Only the flow and the core ROIs were used for the comparisons of D_v. When D_i or D_v was compared in the two periods, only the core ROI was used.

In addition to the averaged velocity differences, velocity waveforms measured from four selected voxels in the RCCA were compared between different scans. Although it is impossible to present the velocity waveforms from all the voxels in the RCCA, the direct comparisons of single-voxel velocity measurements are important because this study aims to measure high-resolution velocity field in carotid arteries.

The measurements of the volume flow rates of the RCCA were also compared between scans. The flow rates were obtained from the spatial averages of the velocities in the lumen and the cross-sectional area of the RCCA, as shown in Equation (4.4). The flow ROI was used for the calculation of the flow rates.

$$R_f(t) = \frac{S_{ROI}}{N_{ROI}} \sum_{x,y} V_{SI}(x,y,t) \tag{4.4}$$

In Equation (4.4) R_f is the time-resolved flow rate, V_{SI} is the velocity in the superior/inferior direction of a voxel in the selected ROI, S_{ROI} is the area of the selected ROI, and N_{ROI} is the number of voxels in the selected ROI.

4.2.6 Reconstruction

In the image reconstructions for the fully sampled scan and the simulations using the ktVD method, gridding (linear interpolation from nearest neighbours) was applied to each phase encoding position separately according to the sampling patterns and the gating records. Then the signals were inverse Fourier transformed into images. Matlab (MathWorks, Cambridge, UK) was used for the calculations. For the fully sampled scan or each simulation the reconstruction time was less than one second.

The image reconstructions for the simulations using the k-t BLAST method required solving large linear equation systems because the sampling patterns did not conform to a regular sheared grid in k-t space due to retrospective gating, as described in Chapter 3. The size of the equation system was determined by the scan matrix and the number of samples collected in the dynamic scan. The equation system was larger when more samples were acquired in the dynamic scan. ANSI C was used for these reconstructions. The solutions of the equation systems were computed using singular value decomposition and a divide and conquer method (ZGELSD, CLAPACK [235]). With a 3.0 GHz Intel Xeon processor, the reconstruction time for each simulation using sampling pattern #1 was about 294 minutes. For those using sampling patterns #2 and #3, it was 116 and 30 minutes, respectively.

Similar methods and software were used for the image reconstructions in other chapters, unless otherwise specified.

4.3 Results

4.3.1 Coil selection

Figure (4.7) shows the images of the slice from all the coils. The images are the temporal averages over the cardiac cycle of the images without flow encoding from scan #0. The orientation of the images follows the radiological convention. Left/right in the images corresponds to right/left of the subject. Top/bottom in the image corresponds to anterior/posterior of the subject. The colour scales of the images are set by using the maximum intensity value in the lumen of the RCCA as the intensity range. Unless otherwise specified, these conventions of colour scale setting and image orientation are used for all intensity images presented in this and other chapters. The data from coil

#2 was used for generating the source data sets. The position of the RCCA is shown in the selected temporal averaged image in Figure (4.8).

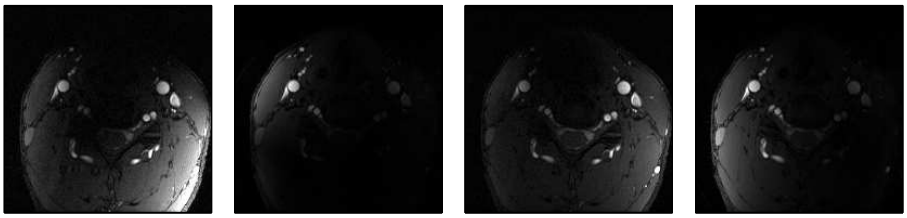

Figure 4.7: The images of the slice from all coils. The images are the temporal averages of the images without flow encoding from the fully sampled scan.

Figure 4.8: The position of the RCCA in the image from the selected coil.

4.3.2 Comparisons of the results from the simulations using the k-t BLAST method

Figure (4.9) shows the intensity differences obtained with different settings of the control parameters of the k-t BLAST method from the simulations using sampling pattern #1. Figure (4.10) and (4.11) show the same type of results from those using sampling patterns #2 and #3. Figure (4.12) shows the phase differences obtained with different

settings of the control parameters of the k-t BLAST method from the simulations using sampling pattern #1. Figure (4.13) and (4.14) show the same type of results from those using sampling patterns #2 and #3.

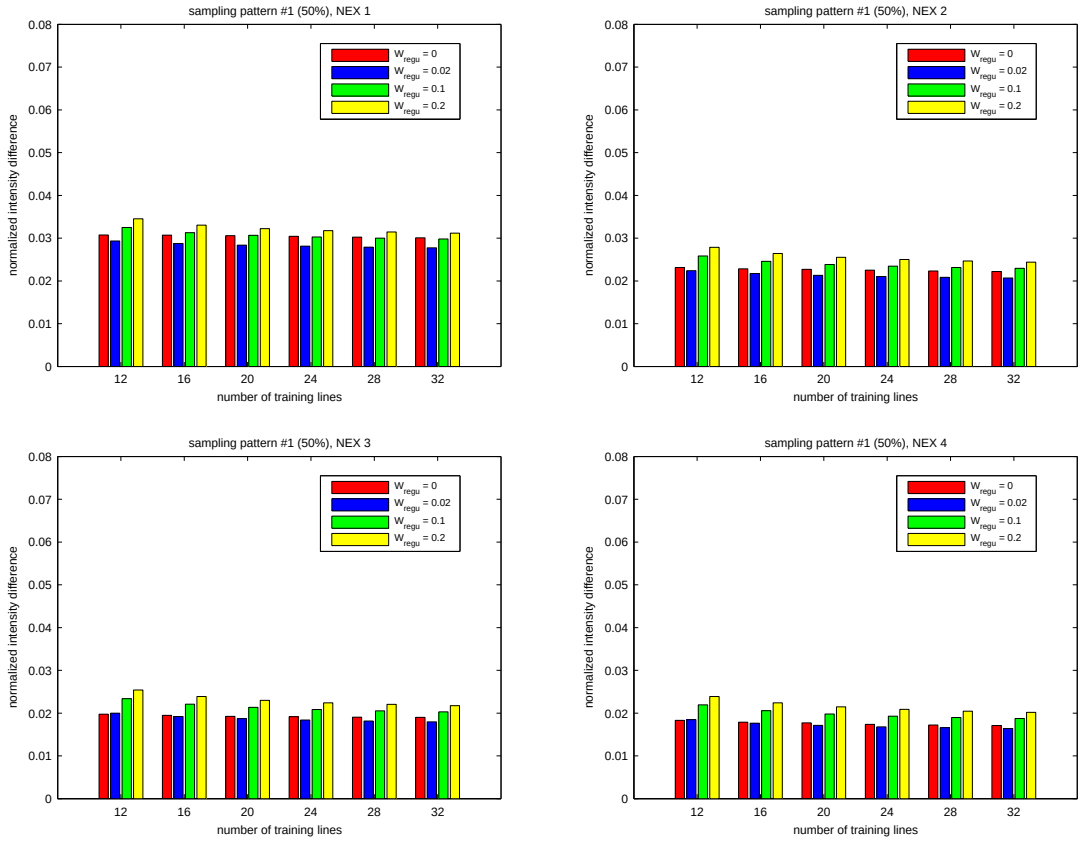

Figure 4.9: The normalized intensity differences obtained with different settings of the control parameters of the k-t BLAST method from the simulations using sampling pattern #1.

As shown in Figure (4.9), (4.10) and (4.11), for each of almost all different settings of the N_{tr} and the NEX, the simulations where W_{regu} was set to 0.02 produced the smallest values of D_i. In most cases the values of D_i increased with the W_{regu} when it was not set to zero, but the changes were not large, especially in those results obtained with sampling pattern #3. This suggests noise regularization will improve intensity results, and a smaller weight of noise regularization will be better. The phase difference results, as shown in Figure (4.12), (4.13) and (4.14), follow the same pattern.

Since 0.02 appears to be the best setting for the W_{regu} in the simulation results, only

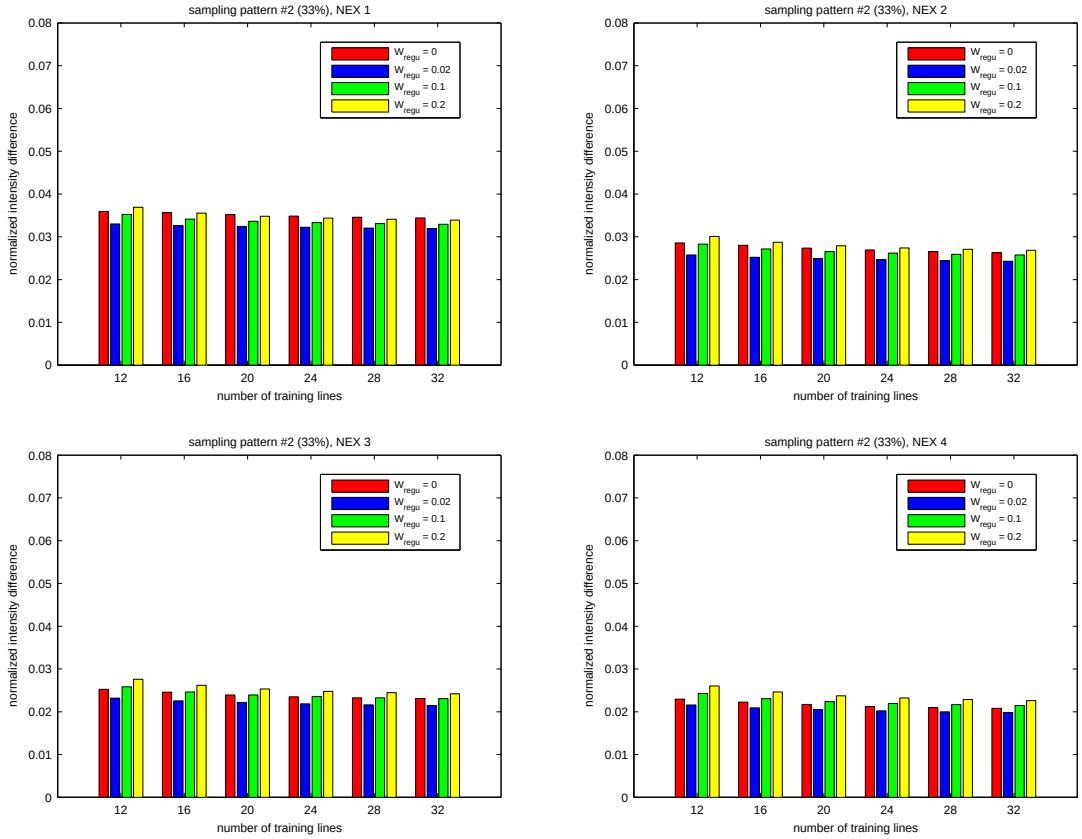

Figure 4.10: The normalized intensity differences obtained with different settings of the control parameters of the k-t BLAST method from the simulations using sampling pattern #2.

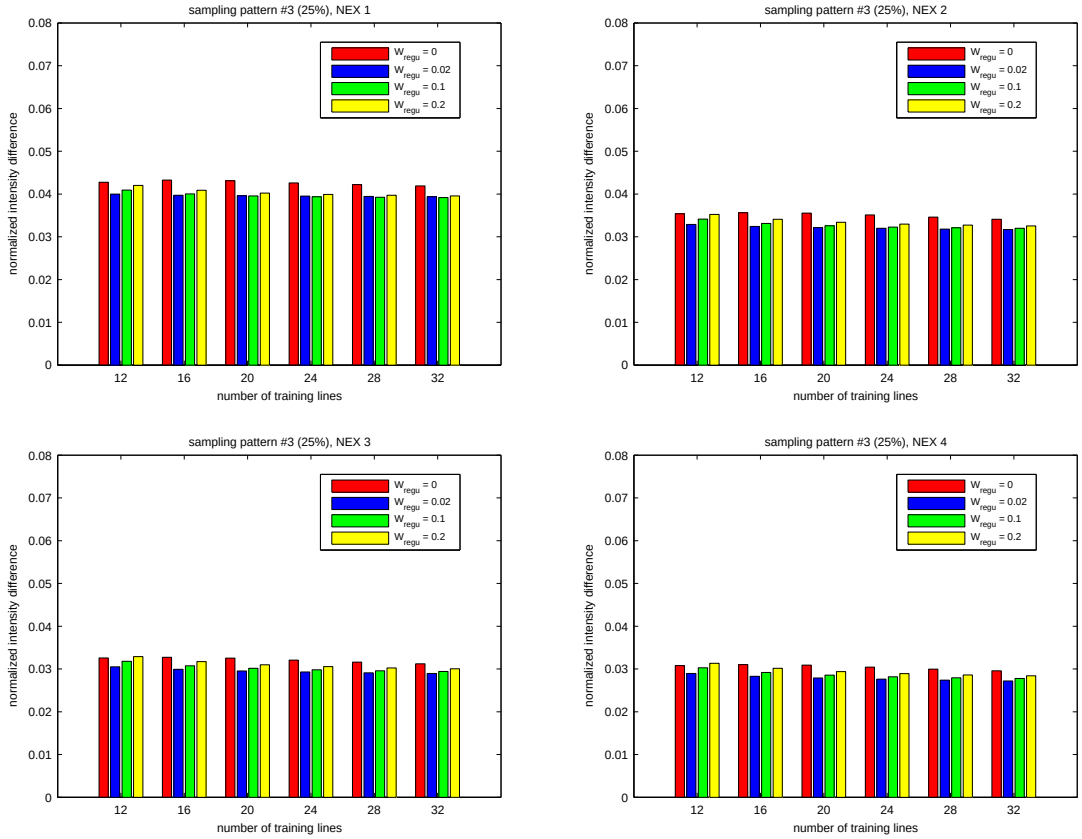

Figure 4.11: The normalized intensity differences obtained with different settings of the control parameters of the k-t BLAST method from the simulations using sampling pattern #3.

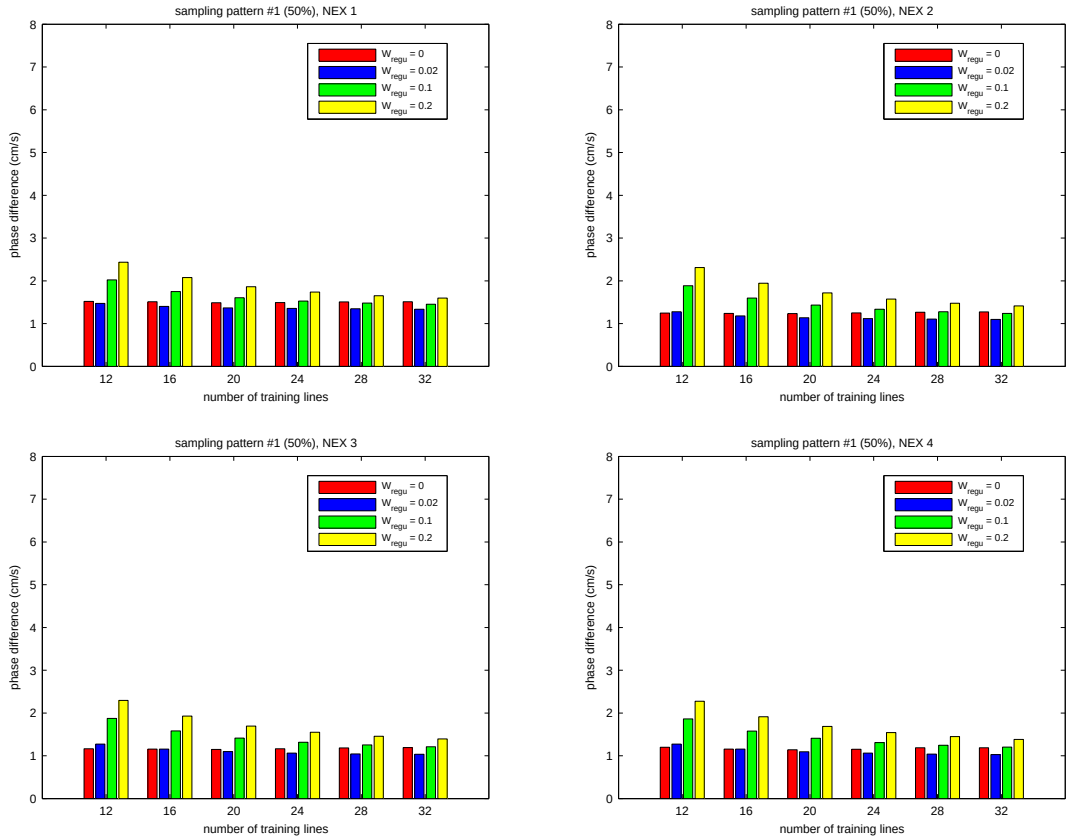

Figure 4.12: The phase differences obtained with different settings of the control parameters of the k-t BLAST method from the simulations using sampling pattern #1.

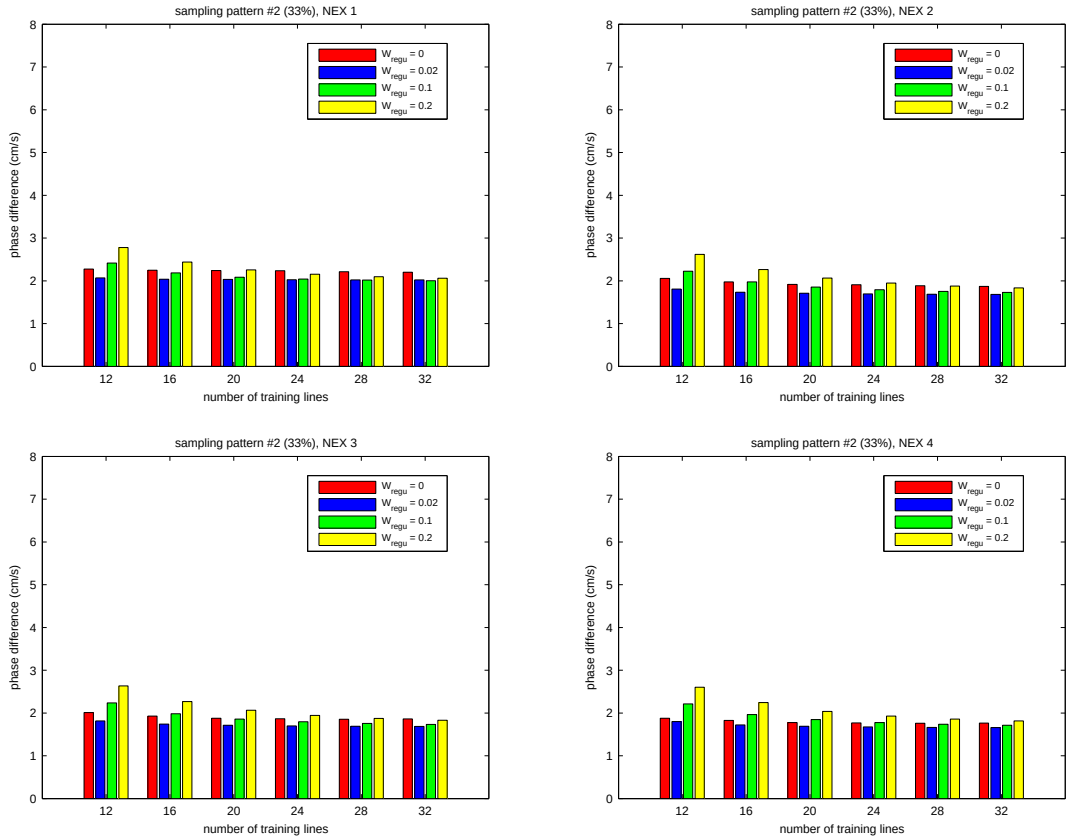

Figure 4.13: The phase differences obtained with different settings of the control parameters of the k-t BLAST method from the simulations using sampling pattern #2.

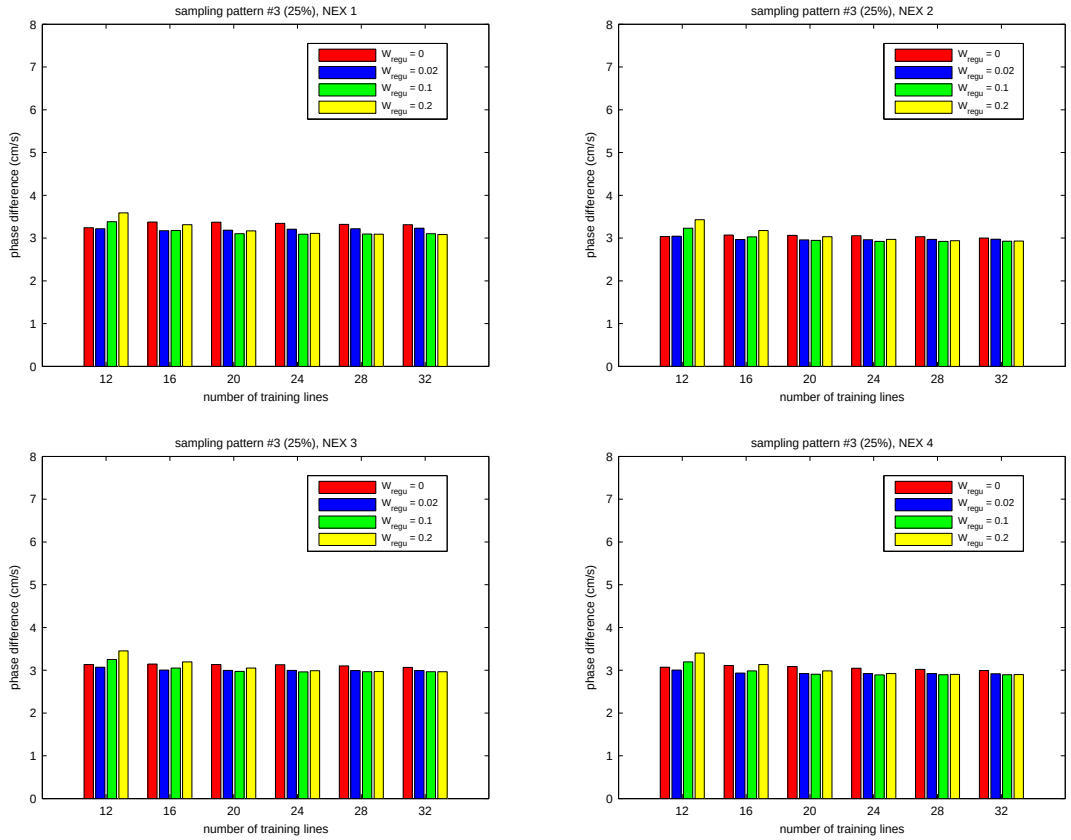

Figure 4.14: The phase differences obtained with different settings of the control parameters of the k-t BLAST method from the simulations using sampling pattern #3.

those results using this setting will be included in the following comparisons. The W_{regu} will also be set to 0.02 for the k-t BLAST reconstructions in other chapters.

Figure (4.15) shows the intensity differences obtained with different settings of the N_{tr}, different noise levels, and different sampling patterns. The results obtained with the same sampling pattern were grouped together. Figure (4.16) shows the same type of comparisons of the phase difference results.

As shown in Figure (4.15), for each sampling pattern and each N_{tr}, the values of D_i were always smaller at lower noise levels. The differences between the results at different noise levels did not change much with the sampling pattern or the N_{tr}. This suggests at lower noise levels the intensity results from the k-t BLAST simulations were more accurate, and the improvements did not change much with the sampling pattern or the N_{tr}. In Figure (4.16), the simulations at the highest noise level always produced slightly larger phase differences for each sampling pattern and each N_{tr}. The differences between the values of D_p corresponding to NEX 2/3/4 were smaller than 0.2 cm/s, much smaller compared with those values of D_p. This suggests at high noise levels the phase results might be less accurate and at low noise levels they did not change much with the noise level.

In Figure (4.15) and (4.16), for each sampling pattern and each noise level, the results obtained with different numbers of training lines were very close to each other. This suggests in the k-t BLAST simulations longer training scans led to almost no benefit.

4.3.3 Comparisons of the results from the simulations using the ktVD method

Figure (4.17) shows the intensity differences obtained with different sampling patterns at different noise levels from the simulations using the ktVD method. Figure (4.18) shows the same type of comparisons of the phase difference results.

At the same noise level, the values of D_i corresponding to the R_s of 50% were about half of those obtained with other sampling patterns. In the simulations where the R_s was less than 50%, the differences between the values of D_i obtained with different sampling patterns at the same noise level were smaller than 0.5%, much smaller compared with those values of D_i around 3%. For each pair of sampling patterns at the same R_s, the results were almost the same. This suggests at high sampling ratios the

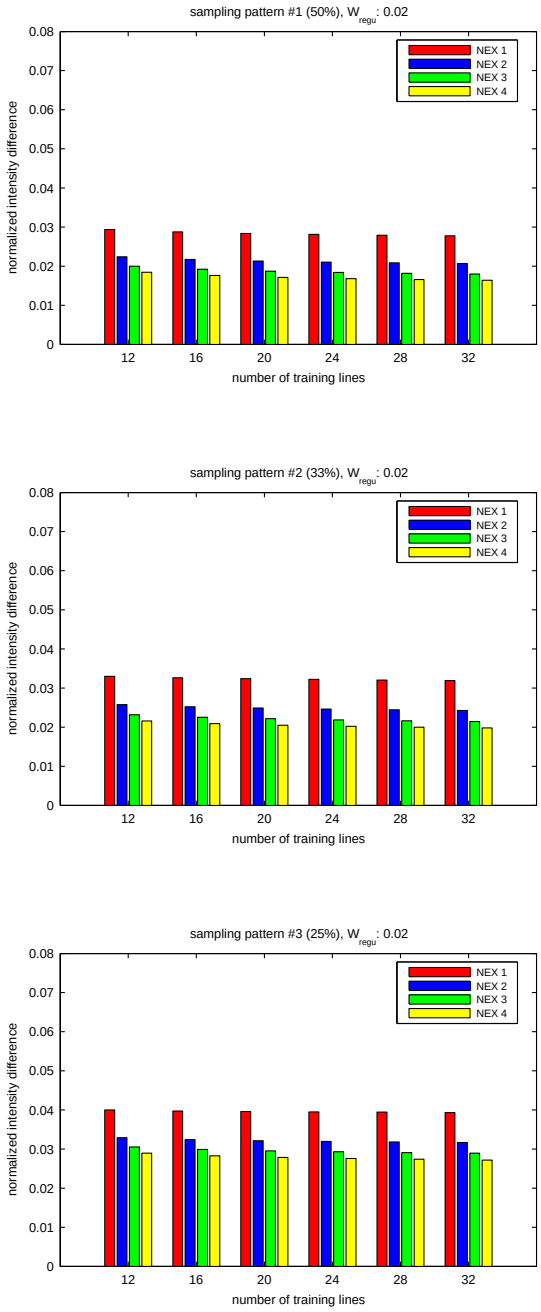

Figure 4.15: The normalized intensity differences obtained with different settings of the N_{tr}, different noise levels, and different sampling patterns. The W_{regu} was set to 0.02.

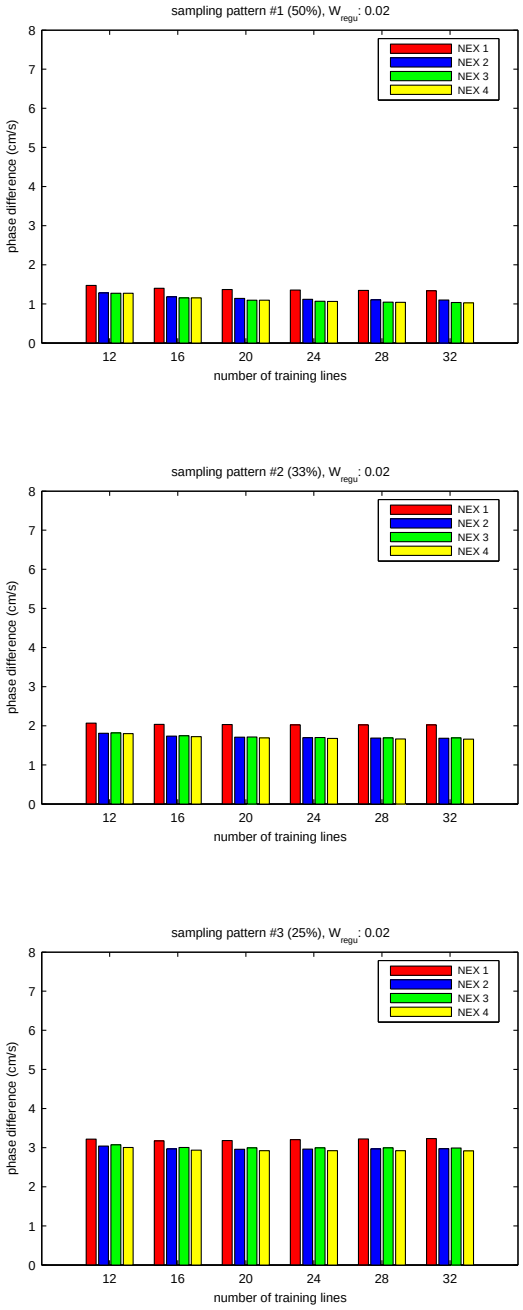

Figure 4.16: The phase differences obtained with different settings of the N_{tr}, different noise levels, and different sampling patterns. The W_{regu} was set to 0.02.

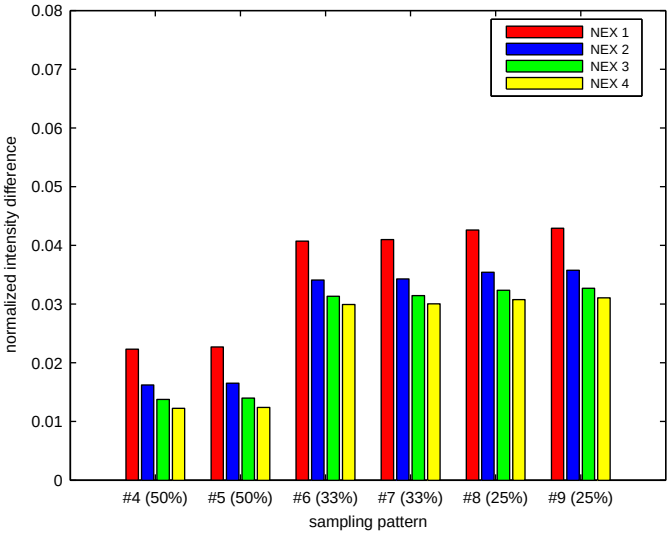

Figure 4.17: The normalized intensity differences obtained with different sampling patterns at different noise levels from the simulations using the ktVD method.

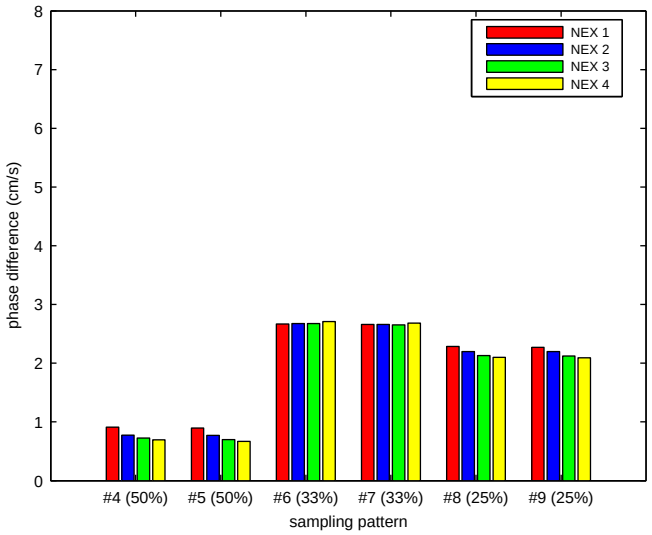

Figure 4.18: The phase differences obtained with different sampling patterns at different noise levels from the simulations using the ktVD method.

intensity results were more accurate, and at low sampling ratio they were not sensitive to the changes of the sampling pattern. For each sampling pattern the values of D_i became smaller at lower noise levels. The reductions in D_i with the noise level were similar for different sampling patterns. At the R_s of 50%, the reductions in D_i were between 0.2-0.5%, around 10-20% of those values of D_i. For other sampling patterns, similar changes of D_i with the noise level were observed, but they are small compared to those values of D_i around 3-4%. This suggests intensity results obtained with the ktVD results were more accurate at lower noise levels, and the changes with the noise level were not sensitive to the changes of the sampling pattern.

As shown in Figure (4.18), the values of D_p corresponding to the R_s of 50% were around 0.6- cm/s, much smaller compared with other results around 2-2.5 cm/s. The phase differences at the R_s of 33% were slightly larger than those at the R_s of 25%. For each pair of sampling patterns of the same R_s, the results were almost the same. This suggests phase results were more accurate at high sampling ratios, and for low sampling ratios, longer scan time did not improve phase results. It is also suggested that the phase differences did not change much with the changes in the sampling density variation of the sampling pattern. At the R_s of 50% and 25%, the values of D_p decreased slightly at lower noise levels for each sampling pattern. For the sampling patterns of the R_s of 33%, the values of D_p were slightly larger at lower noise levels. For all the sampling patterns the changes of D_p with the noise level were not large compared with the values of D_p. This suggests phase results were not sensitive to the changes in noise level.

4.3.4 Intensity difference images

Figure (4.19) shows the intensity difference images between the intensity image from scan #0 and those from the undersampled scans in a selected region without blood vessels and another region including the RCCA. All the intensity images correspond to the peak flow moment in the cardiac cycle (eighth timeframe). The intensity images from scan #0 are also shown. The colour scale of the difference images are set to the same as that of the image from scan #0. Brighter colour indicates larger value of intensity or intensity difference.

For the region without blood vessels, it was difficult to observe the intensity differences in the images from all undersampled scans. For the region including the RCCA

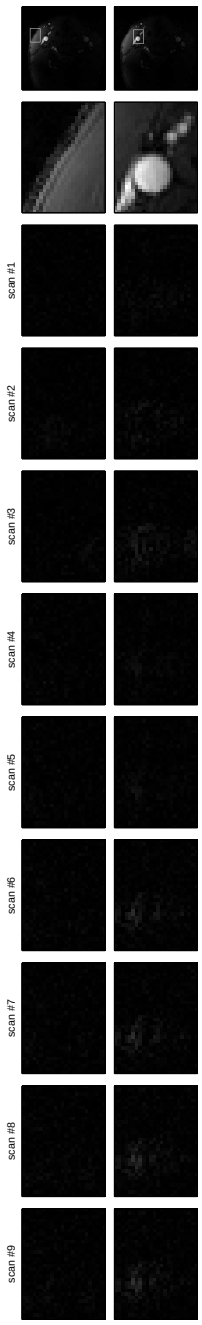

Figure 4.19: The intensity difference images between the intensity image from scan #0 and those from the undersampled scans in selected regions. The positions of the regions are shown in the top row. The images from scan #0 are shown in the second row. The colour scale of the difference images are set to the same as that of the image from scan #0. Brighter colour indicates larger value of intensity or intensity difference.

the difference images from scans #3, #6, #7, #8 and #9 showed small intensity differences at the position of the RCCA. In the images from other scans the intensity differences were much smaller. This suggests undersampling would mostly produce intensity changes in the regions with dynamic changes and at high sampling ratios the intensity changes were small.

4.3.5 Intensity differences in different regions

Figure (4.20) shows the intensity differences in different regions averaged over the cardiac cycle.

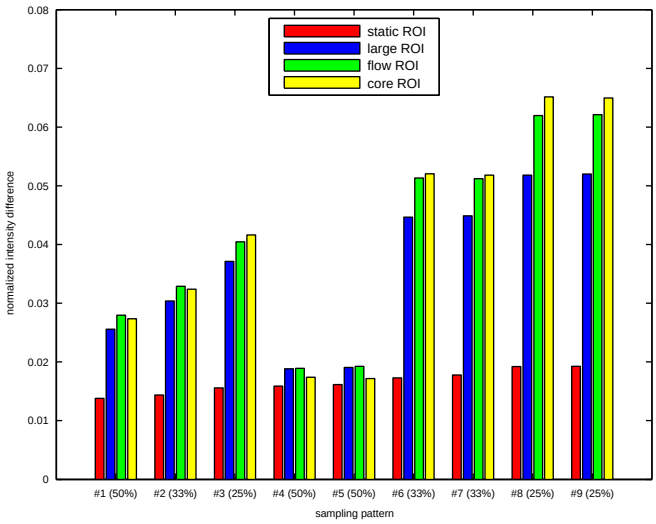

Figure 4.20: The normalized intensity differences in different regions averaged over the cardiac cycle.

Most values of D_i were smaller than or close to 0.05. This suggests for all nine scans the intensity differences were small compared with the intensity values in the lumen of the RCCA. For most scans the values of D_i in the large ROI were smaller than those in the flow or core ROI. This suggests undersampling caused more intensity errors in the lumen. In most cases the values of D_i in the flow ROI were close to those in the core ROI. This suggests inside the lumen the intensity differences were not all close to the centre or the wall. At the R_s of 33% or 25%, the values of D_i from the ktVD simulations were larger than those from the k-t BLAST simulations. The differences between the values of D_i in the large ROI and those in the flow ROI obtained with the

ktVD method were larger than the differences obtained with the k-t BLAST method. This suggests at low sampling ratios, intensity results from the ktVD simulations were less accurate than the k-t BLAST results, and the intensity errors were less uniform than those in the k-t BLAST results.

4.3.6 Intensity differences in different periods

Figure (4.21) shows the intensity differences in different periods of the cardiac cycle in the core ROI.

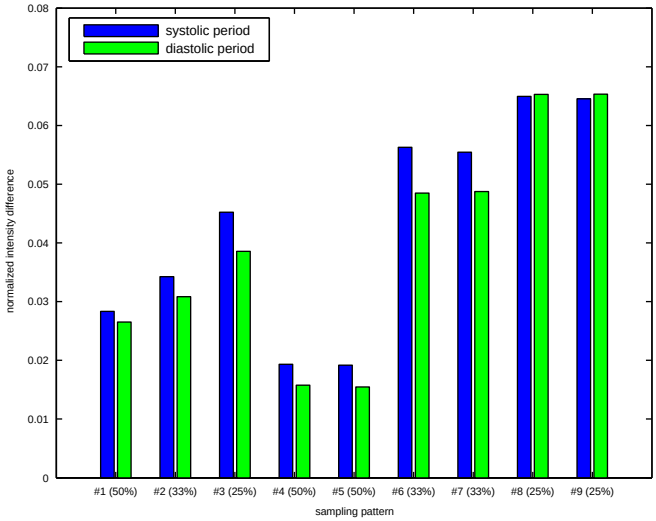

Figure 4.21: The normalized intensity differences in different periods of the cardiac cycle in the core ROI.

In most scans the values of D_i in the systolic period were larger than those in the diastolic period. The differences between the values of D_i in the two periods were not large. This suggests intensity measurements from the undersampled scans were slightly less accurate when the blood flow was faster. For scans #6 and #7, the values of D_i in the systolic period were larger than those in the diastolic period, and for scans #8 and #9, the values of D_i in the two period were close to each other, both larger than those obtained from scans #6 and #7. This suggests for the ktVD method as the sampling ratio decreased, more intensity errors occurred in those timeframes corresponding to faster blood flow than in other timeframes.

4.3.7 Velocity differences in different regions

Figure (4.22) shows the velocity differences in the flow ROI and the core ROI averaged over the cardiac cycle.

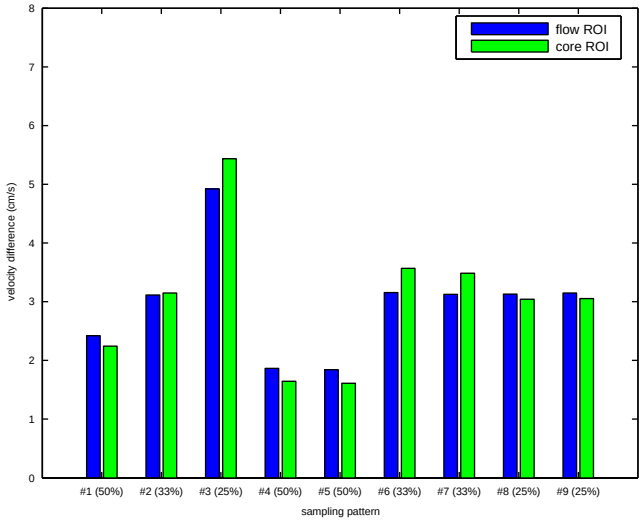

Figure 4.22: The velocity differences in the flow ROI and the core ROI averaged over the cardiac cycle.

For most scans except scan #3, the values of D_v were smaller than or close to 3 cm/s. The results from scan #3 were about 5 cm/s. This suggests in average the velocity errors were small compared with the peak velocity in the RCCA. The differences between the values of D_v in the two ROIs were also small. This suggests the velocity errors near the RCCA wall were close to those in the central area. At the same R_s, the values of D_v from the k-t BLAST scans were larger than or very close to those from the ktVD scans. This suggests on average the velocity measurements from the ktVD scans were more accurate. At the R_s of 25%, the values of D_v from scan #3 were around 5%, about 50% larger than those from scan #8 and #9. This suggests at low sampling ratios the velocity errors in the k-t BLAST results were larger than those in the ktVD results.

4.3.8 Velocity differences in different periods

Figure (4.23) shows the velocity differences in different periods of the cardiac cycle in the core ROI.

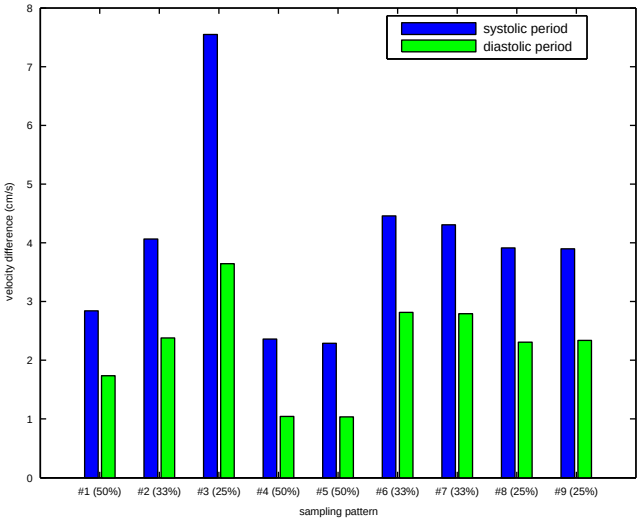

Figure 4.23: The velocity differences in different periods of the cardiac cycle in the core ROI.

For all scans the values of D_v in the systolic period were at least 1 cm/s larger than those in the diastolic period. This suggests velocity measurements in the systolic period were less accurate than those in the diastolic period. For the k-t BLAST scans, the differences between the values of D_v in the two periods increased as the sampling ratio decreased. For the ktVD scans, the differences between the values of D_v in the two periods were at the same level for different sampling ratios and sampling patterns. This suggests at lower sampling ratios the temporal resolution loss in the k-t BLAST results were more serious than in the ktVD results.

4.3.9 Velocity waveforms of single voxels

Figure (4.24) and (4.25) show the velocity waveforms of a selected voxel in the RCCA from all scans. In Figure (4.24) the results from the k-t BLAST and the ktVD scans were displayed separately. In Figure (4.25) the results obtained at the same sampling ratio were grouped and displayed together. The waveform from scan #0 was also displayed. Figure (4.26), (4.27), (4.28), (4.29), (4.30) and (4.31) show the same type of results of other three selected voxels. As displayed, voxel #1 was close to the centre of the lumen, voxel #4 was close to the RCCA wall, and the other two voxels were between them.

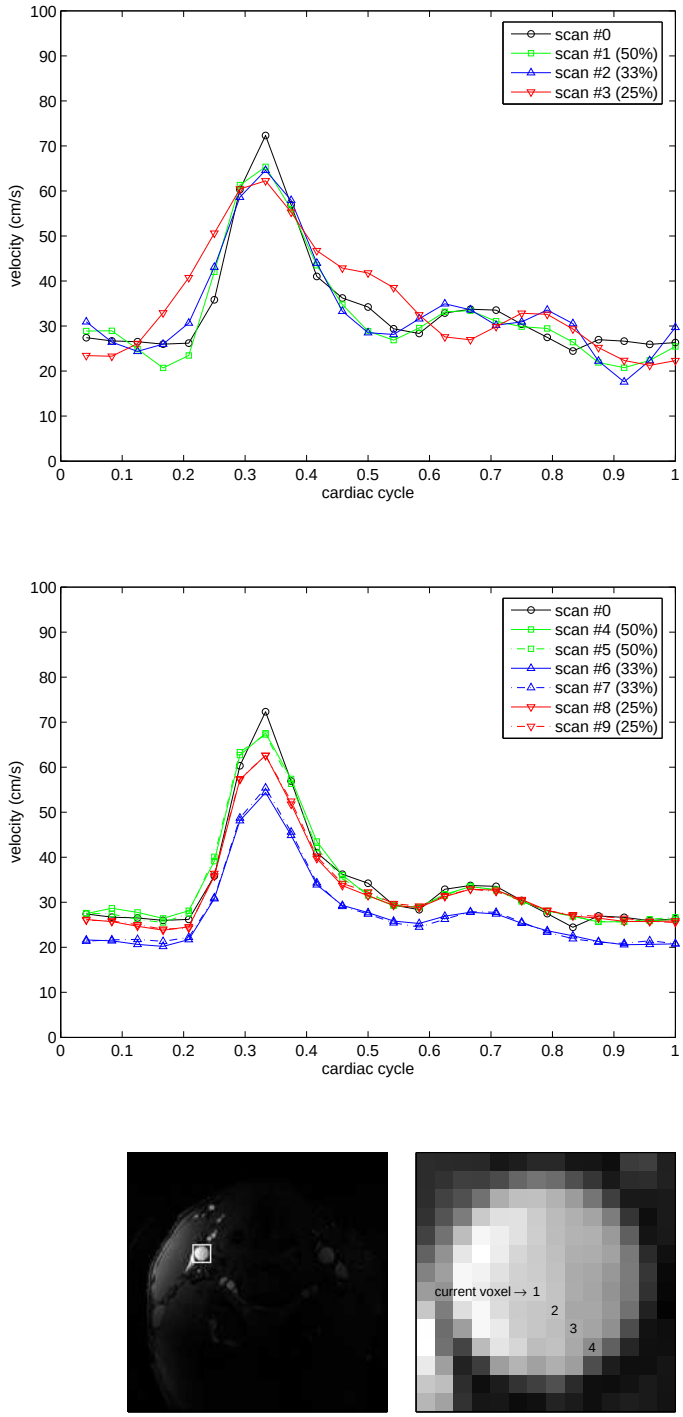

Figure 4.24: The velocity waveforms of voxel #1 in the RCCA from all scans. The results from the k-t BLAST scans and the ktVD scans were displayed separately. The position of the voxel is also displayed.

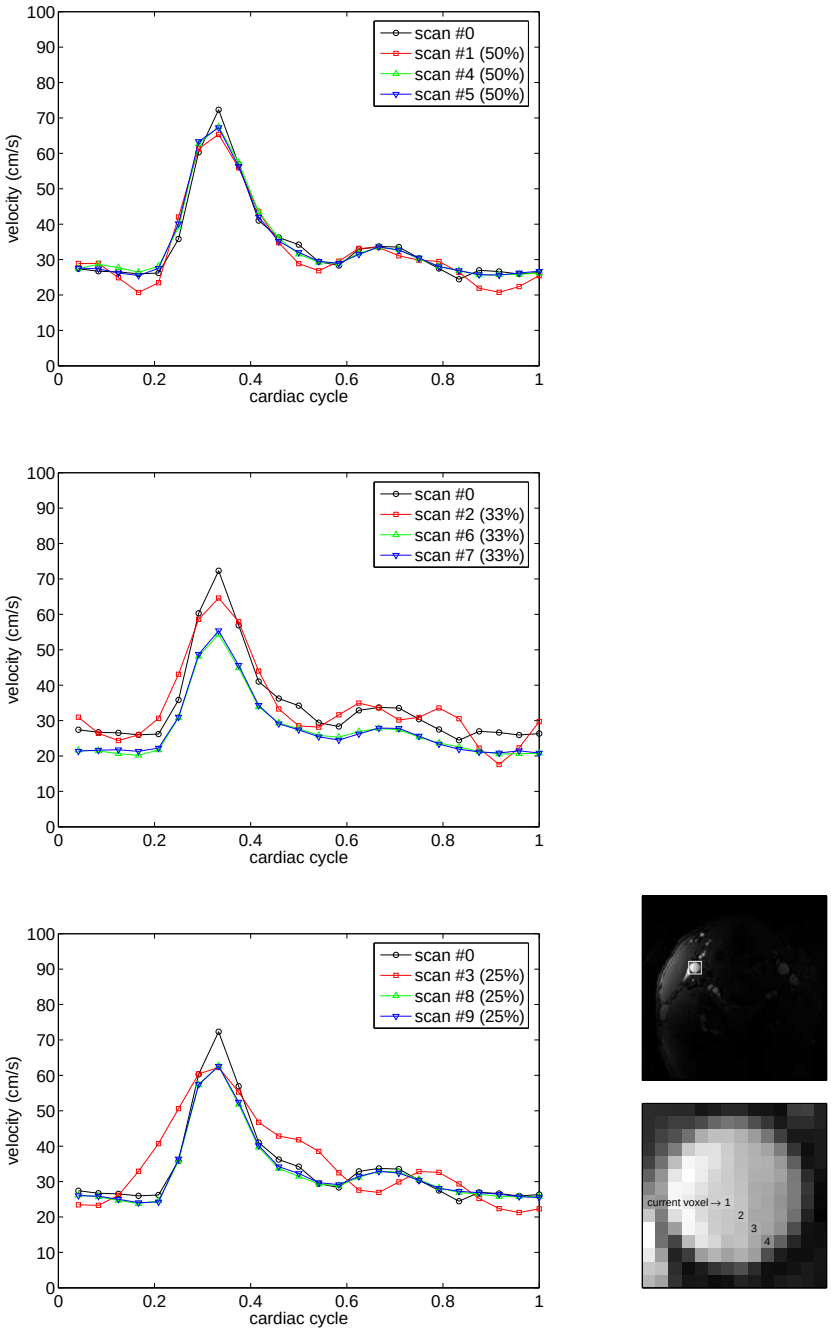

Figure 4.25: The velocity waveforms of voxel #1 in the RCCA from all scans. The results obtained at the same sampling ratio were grouped and displayed together. The position of the voxel is also displayed.

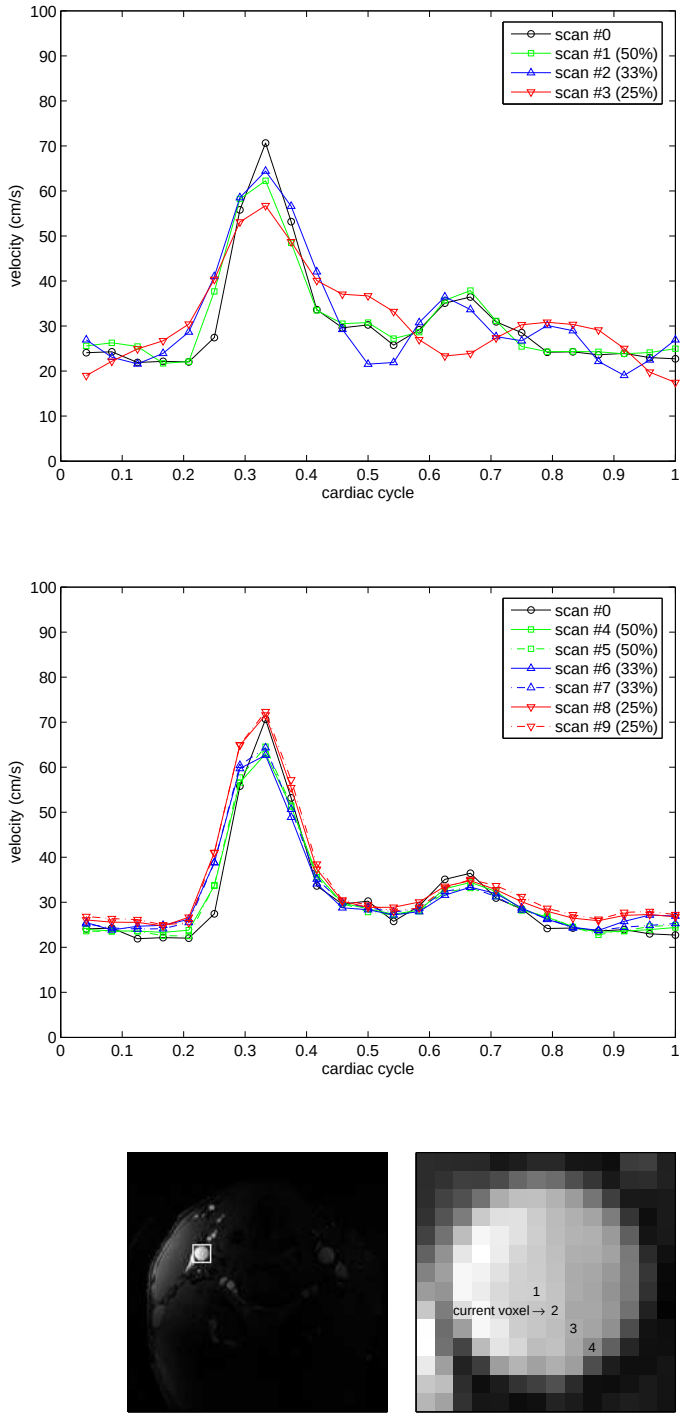

Figure 4.26: The velocity waveforms of voxel #2 in the RCCA from all scans. The results from the k-t BLAST scans and the ktVD scans were displayed separately. The position of the voxel is also displayed.

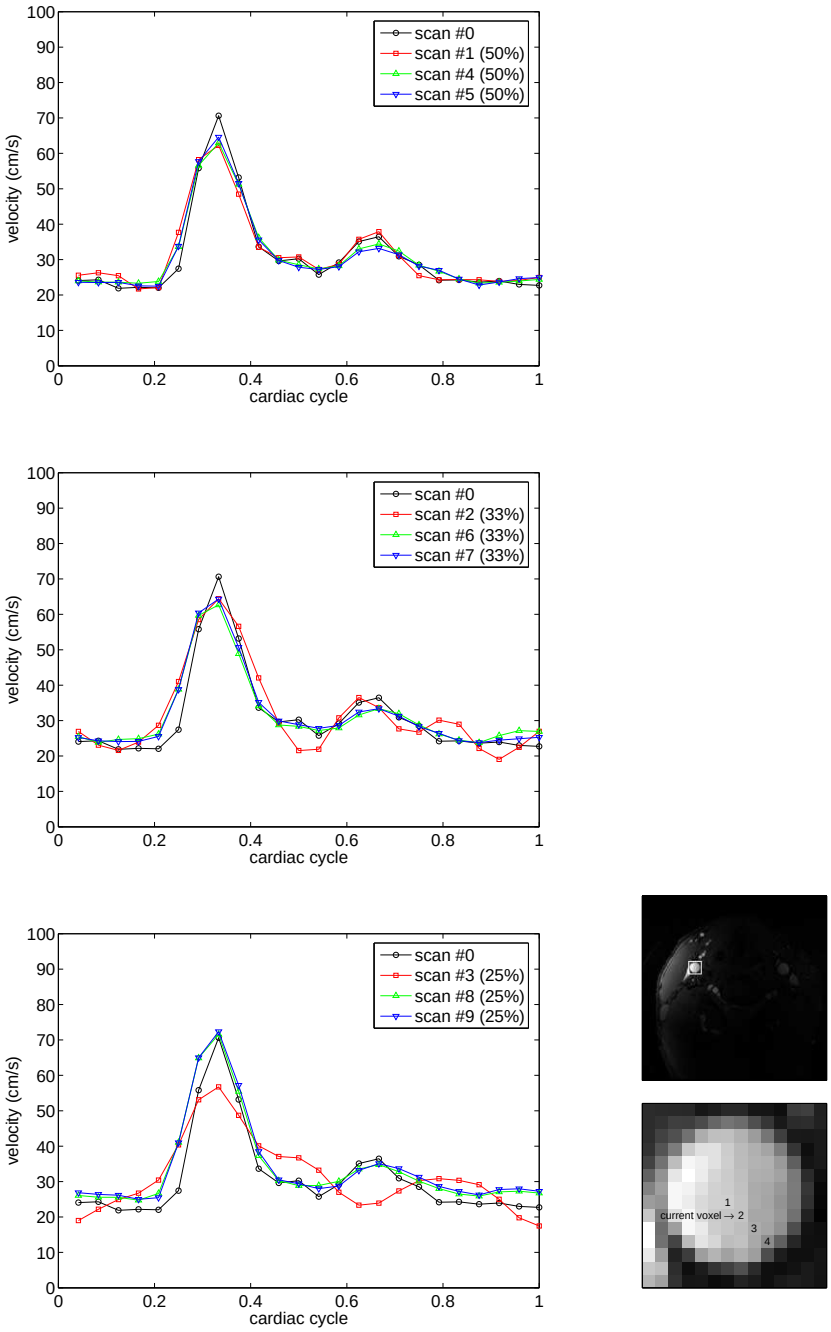

Figure 4.27: The velocity waveforms of voxel #2 in the RCCA from all scans. The results obtained at the same sampling ratio were grouped and displayed together. The position of the voxel is also displayed.

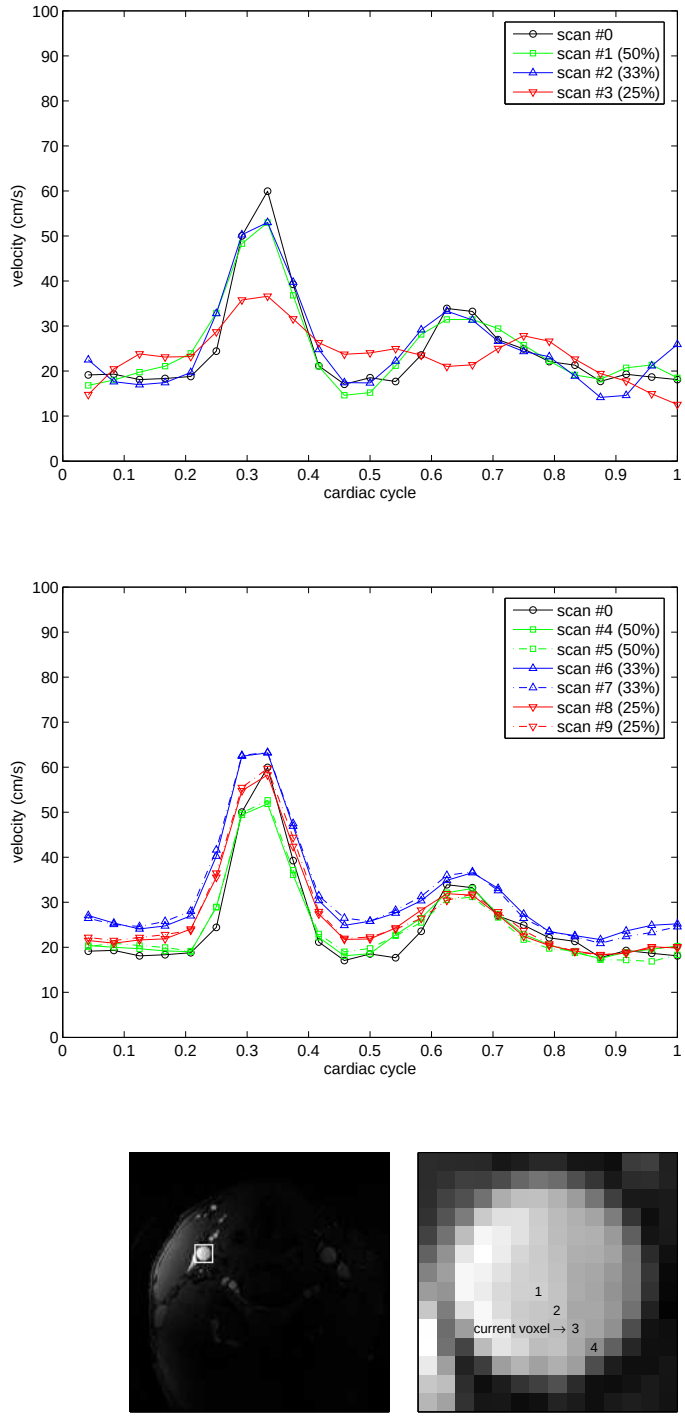

Figure 4.28: The velocity waveforms of voxel #3 in the RCCA from all scans. The results from the k-t BLAST scans and the ktVD scans were displayed separately. The position of the voxel is also displayed.

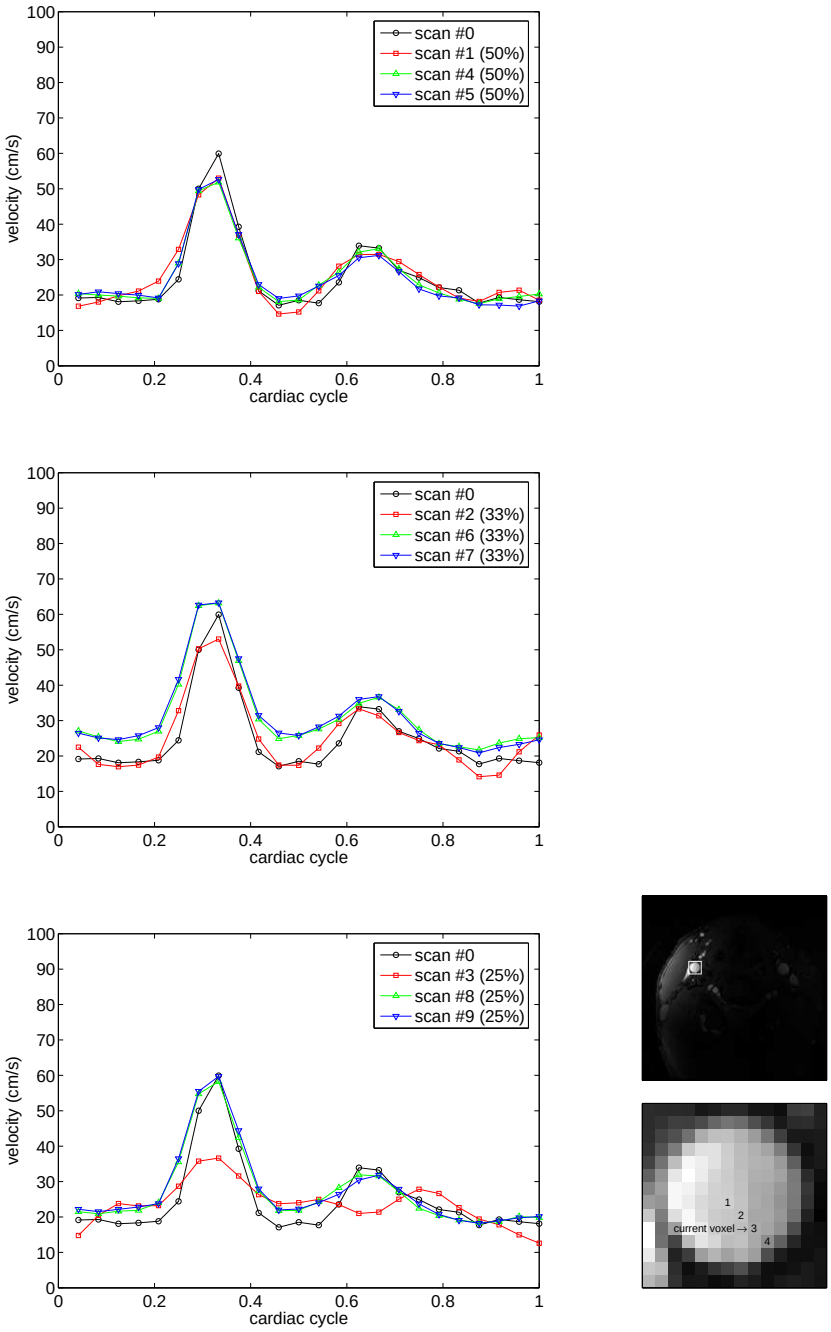

Figure 4.29: The velocity waveforms of voxel #3 in the RCCA from all scans. The results obtained at the same sampling ratio were grouped and displayed together. The position of the voxel is also displayed.

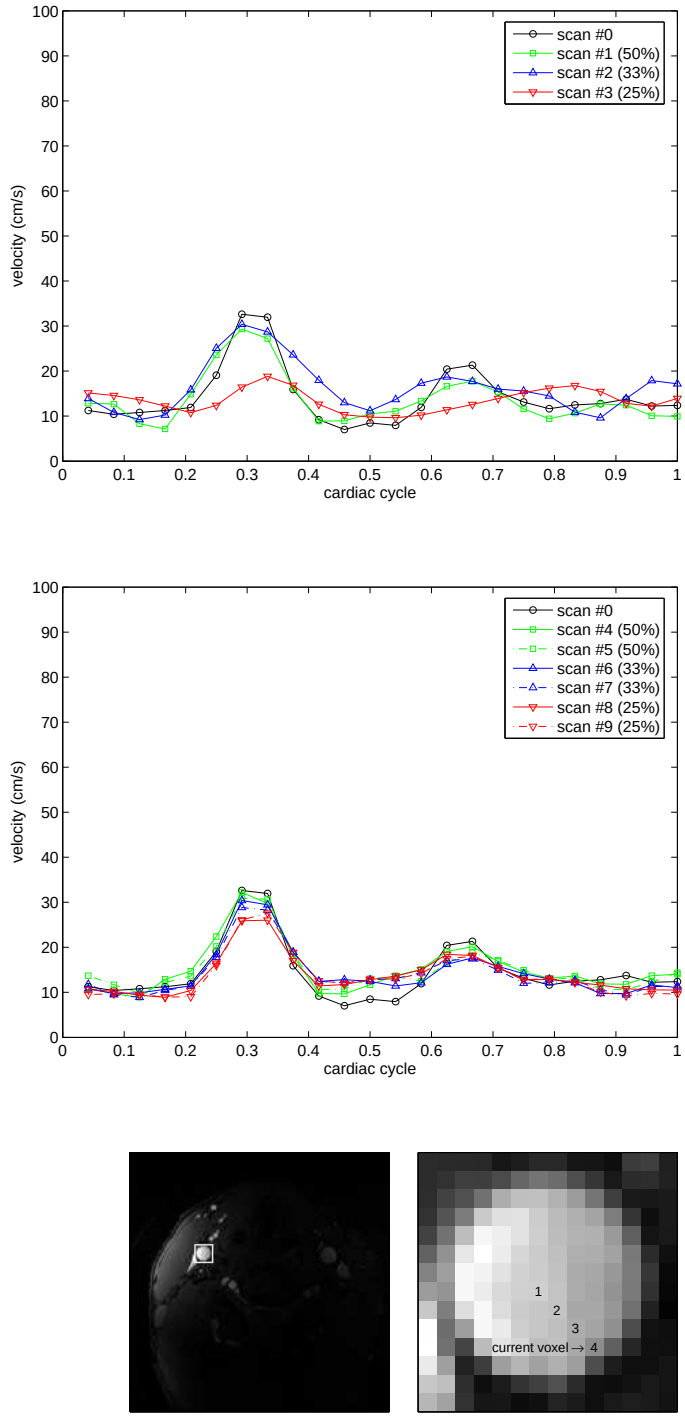

Figure 4.30: The velocity waveforms of voxel #4 in the RCCA from all scans. The results from the k-t BLAST scans and the ktVD scans were displayed separately. The position of the voxel is also displayed.

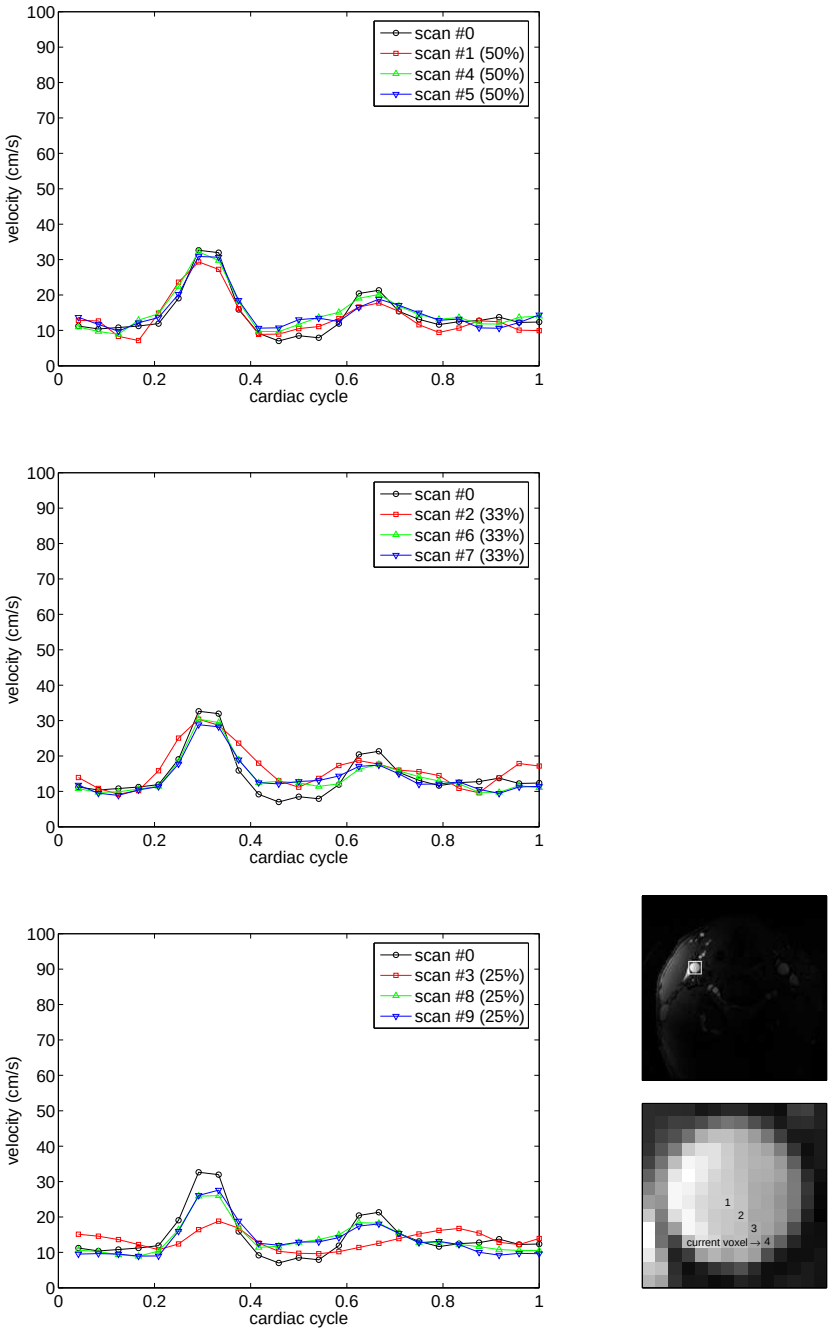

Figure 4.31: The velocity waveforms of voxel #4 in the RCCA from all scans. The results obtained at the same sampling ratio were grouped and displayed together. The position of the voxel is also displayed.

For voxel #1, the differences between the shapes of the velocity waveforms from the k-t BLAST scans and those from scan #0 were larger at lower sampling ratios. The waveforms became smoother as the R_s decreased, and the peak velocities were underestimated. This suggests the temporal resolution loss in the k-t BLAST results were more serious at lower sampling ratios. The shapes of the velocity waveforms from the ktVD scans were all close to the shape of the waveform from scan #0. The peak velocities were also underestimated. At the R_s of 33%, the velocity errors were larger than those obtained at the R_s of 25%, and they were at the same level for almost all the cardiac phases. The waveforms from two ktVD scans at the same R_s were very close to each other. This suggests the temporal resolution of the ktVD measurements was good and it was not sensitive to the changes of the sampling ratio or the sampling pattern. At the R_s of 50% or 25%, the waveforms from the ktVD scans were more accurate than those from the k-t BLAST results. At the R_s of 33%, the velocity underestimation in the ktVD results was more serious than that in the k-t BLAST results, but the shapes of the waveforms from the ktVD scans were closer to that from scan #0 than the k-t BLAST results. This suggests in most cases the velocity results from the ktVD scans were more accurate than the k-t BLAST results, and the temporal resolution of the ktVD results were better than that of the k-t BLAST results.

For voxels #2, #3 and #4, the changes of the velocity waveforms from the k-t BLAST scans with the sampling ratio followed the same pattern as for voxel #1. For voxel #2 the waveforms from the ktVD scans were all close to the waveform from scan #0. For voxel #3 at the R_s of 33% the velocities from the ktVD scans were overestimated for most cardiac phases. Velocity errors were larger at this sampling ratio than those obtained at other sampling ratios, and at the R_s of 50% the velocity errors were smaller than others. For voxel #4, the waveforms from the ktVD scans were all close to each other and to that from scan #0. For voxels #3 and #4 the ktVD waveforms were slightly smoother than those from scan #0, especially near the velocity peak. For all four voxels, the waveforms from two ktVD scans at the same sampling ratio were very close to each other. This suggests velocity results from the ktVD scans were not sensitive to the changes of sampling density variation in k-t space, and close to the arterial wall there might be small loss in temporal resolution. For voxels #2, #3 and #4, in most cases the velocity errors from the k-t BLAST scans were larger than those from the ktVD scans. At the R_s of 25%, the k-t BLAST waveforms were smoother than those from the ktVD scans and scan #0, with velocity errors about 15

cm/s at the peak velocity moment and errors as large as 10 cm/s in the diastolic period. Only for voxel #3 at the R_s of 33% the k-t BLAST results were more accurate while the velocities were overestimated over the cardiac cycle in the ktVD scans. This suggests overall the velocity results from the ktVD scans were more accurate and had better temporal resolution than the k-t BLAST results, especially at low sampling ratios.

4.3.10 Flow rates of the RCCA

Figure (4.32) and (4.33) show the flow rates of the RCCA from all scans. In Figure (4.32) the results from the k-t BLAST scans and the ktVD scans were displayed separately. In Figure (4.33) the results obtained at the same sampling ratio were grouped and displayed together. The results from scan #0 were also displayed.

The flow rate waveforms from the k-t BLAST scans became smoother as the sampling ratio decreased. The waveforms obtained at the R_s of 50% and 33% were close to each other, showing large errors around 1-2 ml/s only for those cardiac phases at or close to the peak flow moment. At the R_s of 25%, errors in flow rate were much larger, around 3-6 ml/s close to the peak, and for most part of the cardiac cycle the errors were 1-2 ml/s larger than those obtained at the R_s of 50% and 33%. This suggests flow rate results from the k-t BLAST scans became less accurate as the sampling ratio decreased, and temporal resolution loss was more serious at low sampling ratios. The flow rate waveforms from the ktVD scans were all very close to each other and the waveform from scan #0. Close to the peak flow moment the ktVD waveforms were slightly smoother than that from scan #0. This suggests the ktVD measurements of flow rates were not sensitive to the changes of the sampling pattern or the sampling ratio, and they had good temporal resolution. At the R_s of 50% or 33%, the waveforms from the k-t BLAST and the ktVD scans were close to each other. The errors from the k-t BLAST scans at the R_s of 33% were slightly larger than those from the ktVD scans at the same sampling ratio for most cardiac phases. At the R_s of 25%, the errors from the k-t BLAST scan were about 2-4 ml/s larger than those from the ktVD scans, which were less than 1 ml/s for most cardiac phases. This suggests at high sampling ratios the ktVD results were as accurate as the k-t BLAST flow rate results, and at low sampling ratios the ktVD results were more accurate.

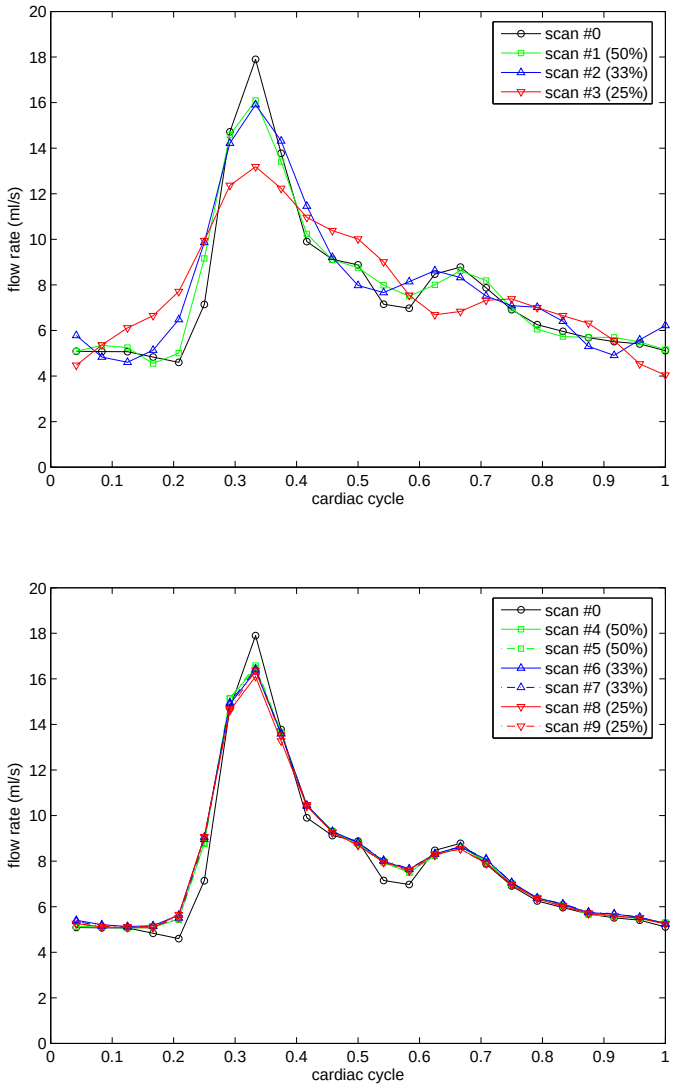

Figure 4.32: The flow rates of the RCCA from all scans. The results from the k-t BLAST scans and the ktVD scans were displayed separately.

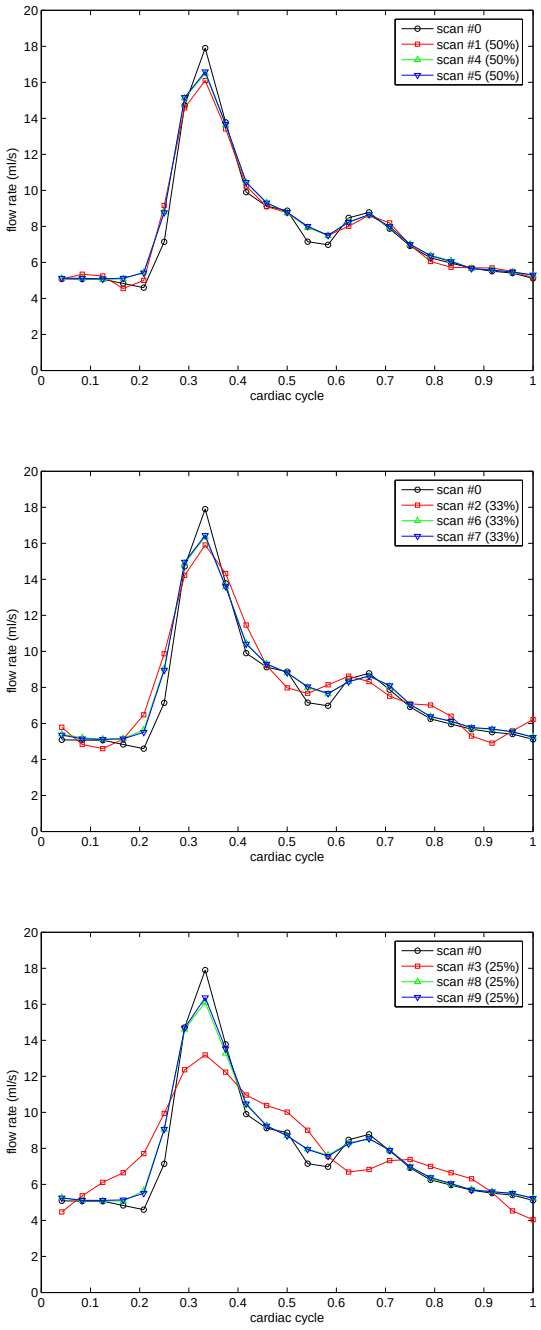

Figure 4.33: The flow rates of the RCCA from all scans. The results obtained at the same sampling ratio were grouped and displayed together

4.4 Discussion

Due to long scan time, swallowing suppression requirement, and limited access to scanning sessions, only one slice below the carotid bifurcation from one volunteer was scanned for all source data sets used in the simulations. As described previously, undersampling performance may depend on the degree of redundancy of the signal, which may change with the morphology within the slice. With only one subject and one slice, inter-subject reproducibility could not be tested, and statistical comparisons could not be made between different undersampling methods. In future work, it is necessary to carry out similar studies with data from more volunteers.

Within each data set, the signal structure was complicated due to the inter-relationships between the voxels. A full-blown statistical analysis would require the development of statistical nonlinear models, which is beyond the scope of the current study and can be included in future work.

In the k-t BLAST simulations, a large number of combinations of different values of the control parameters needed to be tested, and the k-t BLAST reconstructions were computing intensive. The simulations took several days in total. In future work, faster algorithms, such as the conjugate gradient method [231], can be used to accelerate the k-t BLAST reconstructions.

The scan location of the slice was placed below the bifurcation because the RCCA was wider than the RICA or the RECA and the flow in the RCCA was less turbulent. The velocity measurements in the RICA or RECA would be less reliable than those acquired in the fully sampled scan. Large errors in the source data sets would make it difficult to assess the undersampling results from the simulations.

The scan matrix was set to 192×192. The resolution was not very high because the SNR would be lower if the voxel size had been smaller. The width of the RCCA in the scanned slice was about 7.5 mm. If the resolution had been lower, for example 128×128, there would be only seven or eight voxels across the lumen and the velocity results would suffer from partial volume effects. The cardiac cycle was divided into 24 phases. It has been reported in an ultrasound study of common carotid artery blood flow waveforms [236] that frequency components below 12 Hz constituted 95% of the amplitude spectrum. Since the heart rate of the subject is close to 60 beat/min, the selected temporal resolution is adequate to cover the dynamic changes of the flow. In clinics a frame rate of 16 or 20 is often selected. In this study the temporal resolution

is set to be slightly higher so that the degree of signal redundancy of the source data sets was not too low, and the gridding of the retrospectively gated results from the fully sampled scan would also be more accurate.

In the comparisons of different settings of the control parameters, phase differences were used to measure undersampling errors instead of velocity differences. The phase differences are more direct measures of the undersampling errors because the velocity differences are proportional to the differences between the phase differences. Only the results with flow encoding were used in the comparisons so the undersampling errors would not be cancelled out or amplified by the undersampling errors in the data without flow encoding. After these direct comparisons, velocity differences were used as measures in the comparisons of different sampling patterns because the goal of the scans was velocity measurements. In future work the phase errors caused by undersampling can also be compared for different sampling patterns.

In order to place the flow ROI only simple segmentation was applied manually according to the intensity values. The contrast of the temporal averaged intensity images used for the segmentation was high so it was not difficult. Those voxels at the edge might be partially in the lumen and partially in the wall. They are simply labelled out of the lumen in the segmentation, so all the voxels in the flow ROI were surely inside the RCCA. This allows the comparisons of velocity and flow rate results in the flow ROI. Since at the edge of the lumen the blood flow was slow, the flow rate results would not be changed substantially if several voxels in the lumen were incorrectly left out.

Both the intensity and phase results of the two methods suggest undersampling errors were smaller at lower noise levels, and the improvement did not change much with the sampling ratio or the sampling pattern. This may suggest noise was not amplified in the reconstructions using either one of the methods. It is also possible that the tested noise levels were not high or low enough to show the correlations with the sampling pattern. For the tests of different noise levels, the fully sampled data were averaged to generate the source data sets. The background noise standard deviation was roughly inversely proportional to the square root of the number of data sets averaged. This means that the noise level did not decrease linearly with the NEX. The relationship between the undersampling errors and the noise level was not quantified. More quantitative analysis can be included in future work. In the comparisons of different sampling patterns, all nine sets of results were obtained from the source data set of the

highest noise level (NEX 1). This noise level was selected for comparison because in real undersampled scans the signal noise level should be similar.

The comparisons of different values of the weight of noise regularization for the k-t BLAST method suggest 0.02 was the best setting for the W_{regu} and smaller values of the W_{regu} produced better results. It is possible some values of the W_{regu} smaller than 0.02 and larger than zero could produce even better results. They can be tested in future work. According to the comparisons, the differences between the results obtained with different settings of the W_{regu} were not large. This may also be true for the values of the W_{regu} smaller than 0.02.

The comparisons of the k-t BLAST results suggest undersampling errors were not sensitive to the changes in the number of training k-space lines. This agrees with the results reported in other studies [233]. The reason could be in the reconstruction the training data was not directly passed to the final results. If the training data had been directly copied to the final results after gridding [224], undersampling errors might decrease as the N_{tr} increased. This can also be tested in future work.

The comparisons of the ktVD results suggest neither intensity nor phase errors changed much with the sampling density variation of the sampling pattern. The comparisons of velocity and flow rate results also show the same pattern. This may suggest for the ktVD method the undersampling errors were not sensitive to the changes of the sampling pattern at the same sampling ratio. It is also possible that the differences in sampling density variation between the two sampling patterns might not be large enough to cause observable differences in undersampling results. At each sampling ratio, only two sampling patterns were used to test different sampling density variations in k-t space for the ktVD method. Since the sampling patterns needed to fit the sampling ratio and keep the samples at each phase encoding position equally spaced, limited options were available for the design of the sampling patterns. In future work scans of larger scan matrix can be used for this type of comparisons because at higher resolutions more sampling patterns are available for comparison at the same sampling ratio.

The comparisons of undersampling errors and velocity measurements from the ktVD simulations suggest the results obtained at the sampling ratio of 33% was not better than those at the R_s of 25%. For example, the phase errors at the R_s of 33% were larger than those at the R_s of 25%, and errors in the velocity waveforms of single voxels from scan #6 or #7 were also larger than those from scans #8 or #9. This is opposite

to the trend observed in other comparisons that results became more accurate at higher sampling ratios. It might be caused by the correlations between the noise level and the sampling ratio. At the R_s of 25% less samples were collected over k-t space. At each phase encoding position the temporal resolution is lower than that in the scans at the R_s of 33%. Noise in the signal at each phase encoding position might be reduced by temporal smoothing due to undersampling. As the R_s decreased from 33% to 25%, the benefit from noise reduction might be larger than the loss in temporal resolution, so overall errors became smaller. As shown in the comparisons of the ktVD phase errors at different noise levels, the phase differences decreased with the noise level at the R_s of 25% and 50%, but increased slightly at the R_s of 33% as the noise level decreased. These results may suggest at low sampling ratios noise reduction due to undersampling had a larger influence as the sampling ratio decreased. This may be useful for clinical applications because results were improved by reducing scan time. In future work the correlations between the noise level and the sampling ratio can be studied in detail.

In summary, according to the simulation results, at high sampling ratios the intensity and velocity errors from both methods were small. The averaged intensity errors were less than or close to 5% of the mean intensity value in the RCCA lumen. The averaged velocity errors were less than or close to 3 cm/s. At low sampling ratios the intensity errors obtained with the ktVD method became larger, around 5-6%, and at the sampling ratio of 25% the velocity errors obtained with the k-t BLAST method were close to 5 cm/s, about 2-3 cm/s larger than those obtained at other sampling ratios or with the ktVD method. The intensity results were slightly less accurate in the lumen than outside, and the velocity errors were 1-4 cm/s larger in the systolic period than in the diastolic period. In general, results were more accurate at higher sampling ratios. At the R_s of 25% the velocity results obtained with the ktVD method were slightly better than those at the R_s of 33%. For the k-t BLAST method, a smaller value of the noise regularization weight or a lower noise level led to better results, and the undersampling errors were not sensitive to the changes of the number of training k-space lines. For the ktVD method, the results did not change much with the changes of the noise level or the sampling density variation of the sampling pattern at the same sampling ratio. The intensity results from the k-t BLAST simulations were close to or slightly better than those from the ktVD simulations. At high sampling ratios the velocity and flow rate results from the k-t BLAST simulations were similar to those from the ktVD simulations. At the sampling ratio of 25% the errors in velocity or flow rate from the k-t

BLAST method were often about 2-3 times of those from the ktVD method.

Chapter 5

In vivo test of undersampling in two dimensions of k-t space

5.1 Introduction

In the previous chapter all the undersampling methods were tested in simulations. The numerical undersampling used in the simulations is different from real undersampling. With numerical undersampling all the samples were copied or interpolated from the fully sampled data set. The signal content did not change with the degree of undersampling. In real undersampled scans the signal content changes with scan time. For example, if a scan is shorter there may be less motion artefacts. So it is necessary to apply the undersampling methods in real undersampled scans and compare the results from different undersampling schemes.

In this chapter the two undersampling methods are implemented on a clinical scanner and tested in 2D *in vivo* scans. Each undersampling pattern previously tested in the simulations is implemented. A fully sampled scan is also carried out to produce reference data sets. The results obtained with different undersampling methods and different sampling patterns were compared with those from the fully sampled scan in both spatial and temporal dimensions.

5.2 Method

5.2.1 The scanning protocol

The design of the scanning protocol is limited by the total scan time. A volunteer was scanned with the same scan settings except the undersampling patterns. In each scan only one undersampling pattern was tested. For the nine sampling patterns tested previously in simulation at least nine scans need to be conducted. In order to reduce scan-to-scan differences, all the scans were carried out one immediately after another. The total scan time is the sum of those of all the scans. During this period the scanned subject is not supposed to have any motions, such as involuntary swallowing. In practice this is very difficult to achieve, especially when the total scan time is longer than ten minutes. So the total scan time should be kept as short as possible to make the comparisons of the measurements from different scans valid. Additionally, since a volunteer was scanned the total scan time should not be too long, preferably less than one hour.

The total scan time is determined by T_R, the number of flow encoding directions, the temporal resolution, the phase encoding resolution, the number of slices, the sampling ratio of the applied sampling pattern, and the number of scans in the protocol. T_R changes with FOV and slice thickness. The minimum T_R, 20 ms, was used for the selected FOV and slice thickness. Flow encoding was applied in only one direction to save time. This means every sample in the k-t sampling patterns was sampled twice, with and without flow encoding. The temporal resolution and phase encoding resolution were not sacrificed to reduce scan time. At the full temporal resolution 24 samples equally spaced along the temporal dimension were collected at each k-space position. The scan matrix was 192×192 in frequency and phase encoding. Under these conditions it took about 184 seconds to fully sample the signal of a single slice. In each scan only one slice was covered to reduce total scan time of each run of the scan protocol. For multiple slices, the protocol can be repeated many times. In this way if the subject had moved during the scans of one slice, the results of other slices would not be affected.

The scanning protocol consisted of one fully sampled scan and nine undersampled scans. The parameters of the fully sampled scan (scan #0) was exactly the same as that of the fully sampled scan in Chapter 4. The nine undersampled scans following the

fully sampled scan correspond to the nine undersampling patterns tested in Chapter 4 (#1 to #9).

Table 5.1 shows the sampling patterns, the sampling ratios and the scan time of all the scans in the protocol.

scan	method	sampling pattern	sampling ratio	scan time (s)
#0		full	400%	737
#1	k-t BLAST	#1	50%	92
#2	k-t BLAST	#2	33%	62
#3	k-t BLAST	#3	25%	46
#4	ktVD	#4	50%	92
#5	ktVD	#5	50%	92
#6	ktVD	#6	33%	62
#7	ktVD	#7	33%	62
#8	ktVD	#8	25%	46
#9	ktVD	#9	25%	46

Table 5.1: The scanning protocol (For reference, the scan time at the sampling ratio of 100% was 184 seconds.)

The scanning protocol of ten scans described above took about 22 minutes for a single slice. Two slices were scanned, one above the carotid bifurcation (slice AB) and the other below the bifurcation (slice BB). Before the fully sampled and undersampled scans a 2D TOF scan was conducted in order to set the position of the two slices.

5.2.2 Other scan settings

The scanned subject was a male healthy volunteer. The study was approved by a local ethics committee, and informed consent was obtained from the volunteer. The subject lay supine throughout the scans. Frequency encoding was in the anterior/posterior direction and phase encoding was in the left/right direction. A 4-element phased-array carotid surface coil was used for signal reception. All the channels of the coil were used in the scan.

For the 2D TOF scan, the FOV was 12 cm and the in-plane resolution was 192×192. Although the FOV size and the in-plane resolution of this scan were the same as those of other scans, the spatial positions were different. 28 slices were scanned and the slice thickness was 2 mm. Spacing between slices was also set to 2 mm so the 28

slices covered 56 mm along the superior/inferior direction. The T_E was 4.2 ms, the T_R was 21 ms, and the Flip Angle was 50°.

All the following scans were retrospectively gated in the same way as in Chapter 4. The average heart rate of the volunteer was around 59 beat/min.

The FOV was 12 cm, the slice thickness was 2.0 mm, and the voxel size was $0.625 \times 0.625 \times 2\ mm^3$. Flow encoding was in the superior/inferior direction (or in/out the slice). The VENC was 100 cm/s, the acquisition bandwidth was 15.63 kHz, the T_R was 20 ms, the T_E was 8 ms, and the Flip Angle was 30°. Raw signals were saved without post-processing on the scanner for offline reconstruction.

5.2.3 Reconstruction

For the 2D TOF scan the image reconstruction was completed immediately after the scan with the standard software installed on the scanner. The images were used to set the positions of the slices and the FOV of the following scans. These images were also saved to files in DICOM format.

The reconstruction for the fully sampled scan was the same as that in Chapter 4. The differences between the results from the signal set of the lowest noise level (NEX 4) and those of the set of the highest noise level (NEX 1) were used as a reference of noise in the comparisons.

The reconstructions for the nine undersampled scans were carried out in the same way as in Chapter 4. W_{regu} was set to 0.02.

5.2.4 Methods of comparisons between scans

The results from different scans were compared in the same way as in Chapter 4. The comparisons were carried out for each slice separately.

5.2.5 Segmentation

When the ROIs were placed in the images it was necessary to determine the ranges of the arteries. This was especially important for the flow ROI since all the voxels in this ROI should be inside the arteries and to include more voxels the flow ROI should fully cover the inner area of the arteries. Segmentation was also needed in the calculation of the cross-sectional area of the arteries.

Three sets of images were used for identification of the ranges of the arteries. The images from the 2D TOF scan were used as references of the shapes and sizes of the arteries. Although the TOF images had high contrast for the arteries, the anterior/posterior and left/right positions of the FOVs were different from those of the images from the gated scans. The reconstruction with the standard software on the scanner also included post-processing operations such as interpolation into a 256×256 image matrix. The 2D TOF scan was not gated so there were flow artefacts in the images. For above reasons the TOF images were not used as the absolute standard in segmentation. For each slice the intensity images without flow encoding from the fully sampled scan were averaged over the cardiac cycle to produce a high SNR intensity image. This set of temporal averaged images provided good details of the artery walls in most slices. Another set of images was generated from the complex difference images between the images with and without flow encoding. The phase differences caused by flow resulted in high intensities in the complex difference images. The intensity images of the complex difference images were averaged over the cardiac cycle to increase contrast. This set of images had good contrast for the voxels with flow and good suppression of static tissues close to the arteries. Figure (5.1) shows examples of the three sets of images.

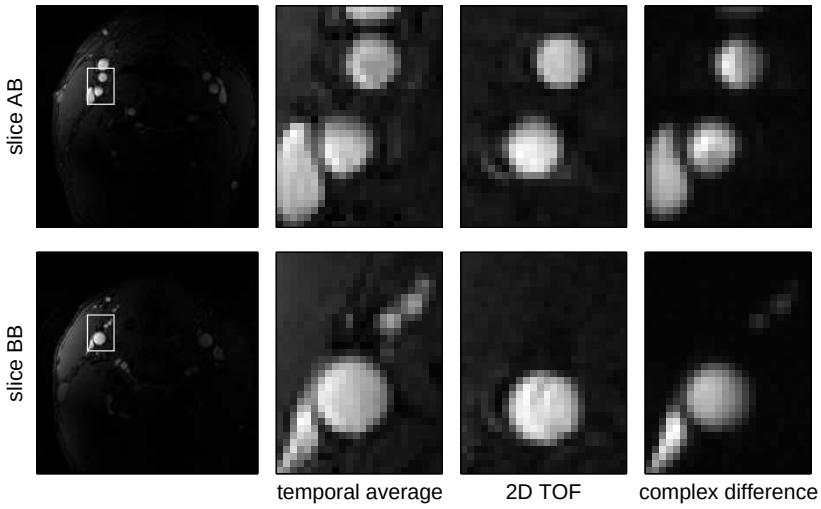

Figure 5.1: An example of the three types of images used in segmentation.

In each slice every voxel was manually labelled as inside or outside of the arteries. The segmentation started with the temporal averaged images. Normally the boundaries

of the arteries were clear because the arteries showed higher intensities than most of the surrounding tissues. The shapes of the artery walls were also shown in the TOF images. When a voxel with high intensity was out of and close to the artery walls suggested in the TOF images, the complex difference images were used to classify the voxel. Those voxels very close to the artery walls and not able to be classified according to the three sets of images were labelled as outside of the arteries.

5.3 Results

5.3.1 Slice positions

Figure (5.2) shows the positions of the slice AB and BB scanned with different sampling patterns. The 3D structure of the arteries was obtained from the 28 images collected in the 2D TOF scan.

5.3.2 Coil selection

Figure (5.3) shows images of the slice AB and the slice BB from all coils. The images were the temporal averages of the images without flow encoding from the fully sampled scan. The images from coil #2 were selected for the comparisons between scans. It had high sensitivity coverage of the RCCA, RICA and RECA, as shown in Figure (5.4). The SNR of the images from coil #2 was higher than those of the images from other coils.

5.3.3 Intensity difference images

Figure (5.5) shows the intensity difference images between the intensity images from the fully sampled scan and those from the undersampled scans in the regions without arteries. Figure (5.6) shows similar difference images in the regions with arteries. All the intensity images correspond to the peak flow moment in the cardiac cycle (eighth timeframe). The intensity images from the fully sampled scan were also shown. The colourscales of the difference images were set to the same of those of the fully sampled images. Brighter colour indicates larger value of intensity or intensity difference.

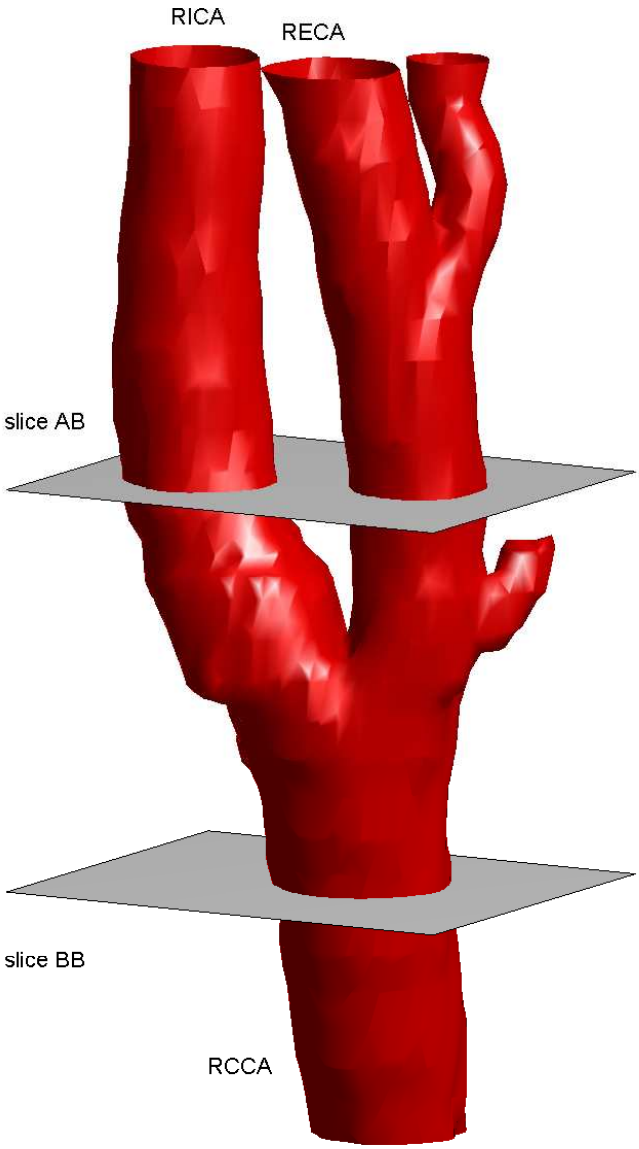

Figure 5.2: The positions of the slice AB and BB examined in the comparisons.

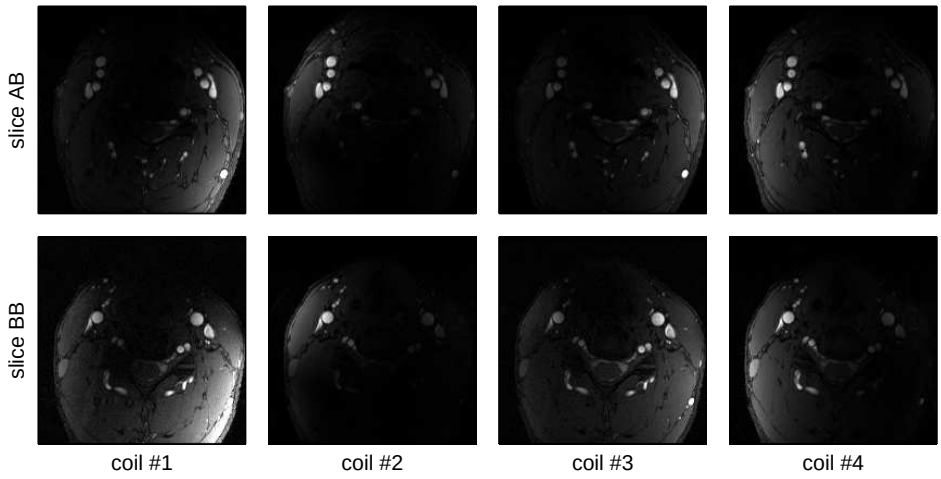

Figure 5.3: The images of the two slices from all coils. The images were the temporal averages of the images without flow encoding from the fully sampled scan.

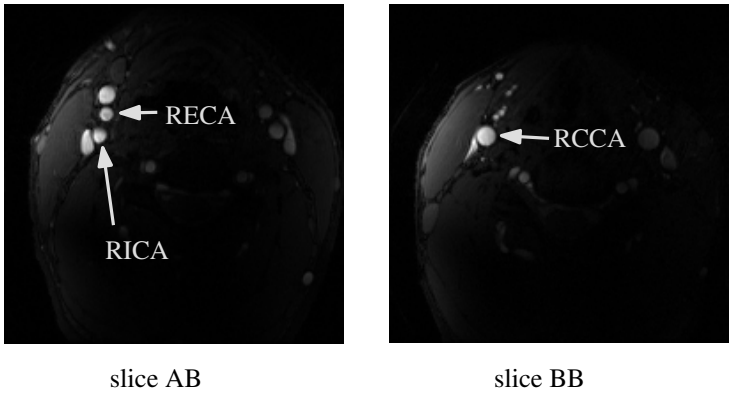

Figure 5.4: The positions of the carotid arteries in the images of the two slices from the selected coil.

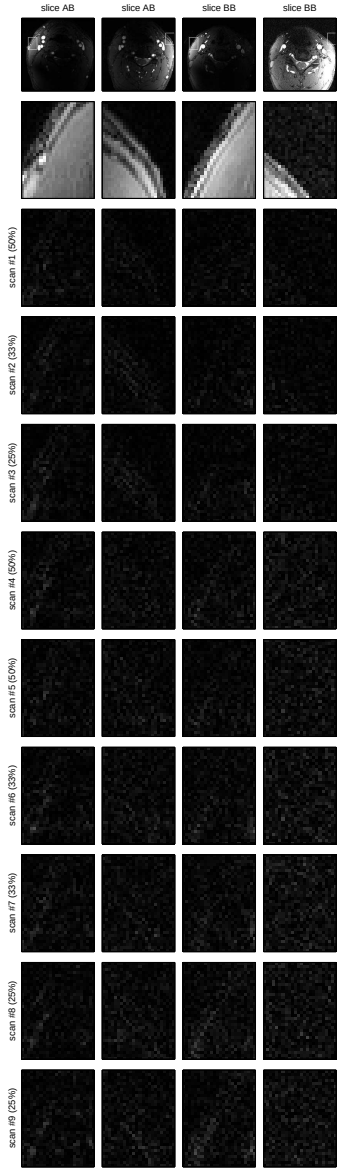

Figure 5.5: The intensity difference images between the intensity images from the fully sampled scan and those from the undersampled scans in the regions without arteries at the peak flow moment. The intensity images from the fully sampled scan are shown in the second row. The colourscales of the difference images are set to the same of those from the fully sampled scan. Bright colour indicates large value of intensity or intensity difference.

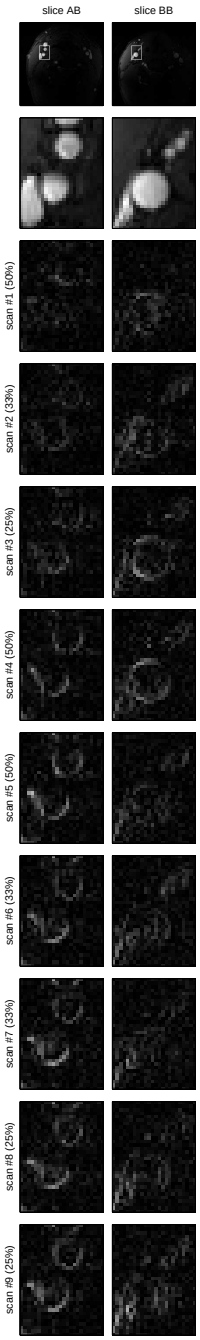

Figure 5.6: The intensity difference images between the intensity images from the fully sampled scan and those from the undersampled scans in the regions with arteries at the peak flow moment. The intensity images from the fully sampled scan are shown in the second row.

In the static regions without arteries, the intensity differences were small compared with the fully sampled images. This suggests in these regions the changes of sampling patterns did not lead to large changes in the intensity values. It also suggests no apparent subject movement happened during the scans of each slice. The static regions included both left and right edges of the neck in the images. If there were large subject displacements between the fully sampled scan and the undersampled scans there would be bright stripes near the edges of the high intensity areas in the difference images. The intensity differences were slightly larger at the positions near the edges of the neck in the images from scan #8 and #9. This may be caused by the low sampling ratio of these two scans. It is also possible the scan-to-scan differences were larger due to the long duration between the fully sampled scan and these two scans.

In the regions including arteries, the intensity differences were larger near the artery walls. This suggests undersampling might cause loss in spatial resolution. The SNR near the artery walls was also low and this might also make the intensity differences larger. The intensity differences in the images from scan #1 and #2 were slightly smaller than those from other scans. This may suggest at high sampling ratios k-t BLAST produced better intensity measurements than ktVD. Another possible reason is these two scans were conducted immediately after the fully sampled scan so the scan-to-scan differences were less serious than in other scans.

5.3.4 Intensity differences in different regions

Figure (5.7) shows the intensity differences in different ROIs in the slice AB. Figure (5.8) shows the same type of results from the slice BB.

For both slices, the values of D_i in the static ROI from the undersampled scans were at the same level, about 2% of the average intensity in the arteries. The values of D_i from the fully sampled scan in all ROIs were all close to or less than 2%. The small differences between the results in the static ROI from the undersampled scans and those from the fully sampled scan suggest the intensity differences measured in the static ROI were mainly caused by noise. The results from the static ROI were consistent with those shown in the intensity difference images in the previous section.

For the ROIs with arteries in the slice AB, the values of D_i from the three k-t BLAST scans were close to each other, between 5% and 7%. This suggests the intensity results from the k-t BLAST scans did not change much with the changes of the

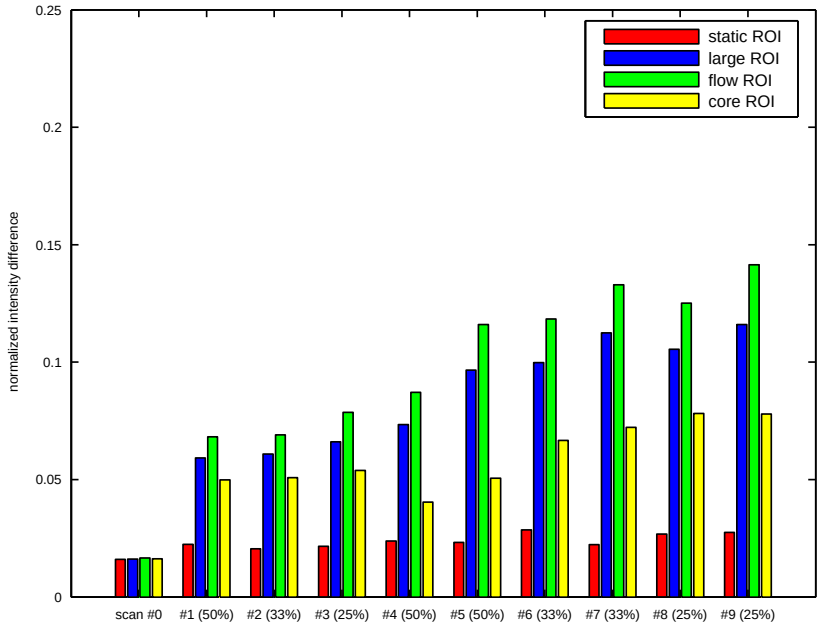

Figure 5.7: The normalized intensity differences in different ROIs in the slice AB.

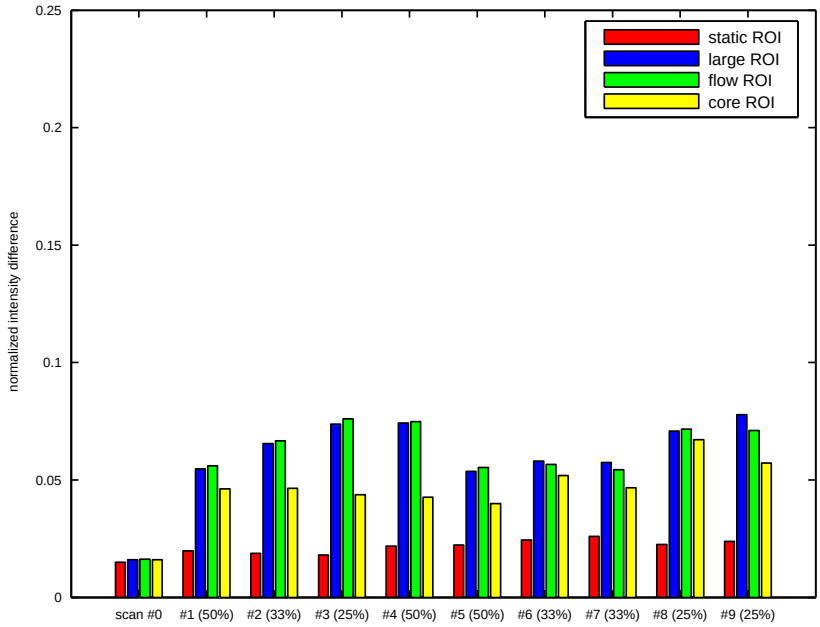

Figure 5.8: The normalized intensity differences in different ROIs in the slice BB.

sampling ratio. For the ktVD scans, the values of D_i increased slightly as the sampling ratio decreased. The results from scan #4 were close to those from the three k-t BLAST scans. For the scans after scan #4, the values of D_i were larger, between 10% and 15% in the large or flow ROIs. This suggests at low sampling ratios in the slice AB intensity measurements from the ktVD scans were less accurate than those from the k-t BLAST scans. In the core ROI the values of D_i were close to those from the k-t BLAST scans. For each two ktVD scans with the same sampling ratio, the scan with more samples collected in central k-t space (scan #5, #7 or #9) produced slightly larger values of D_i than the other. This suggests sparser sampling in outer k-t space might lead to less accurate intensity measurements. For all the undersampled scans, the values of D_i in the flow ROI were larger than those in other ROIs, while the results in the core ROI were smaller than those in the flow or large ROIs. This suggests the intensity differences were larger near the artery walls, which could also be observed in the intensity difference images in the previous section.

The results in the slice BB show different patterns from those in the slice AB. The values of D_i from the three k-t BLAST scans were still close to each other, increasing slightly as the sampling ratio decreased. It suggests in this slice the intensity results from the k-t BLAST scans were slightly more sensitive to the changes of the sampling ratio than in the slice AB. The results from the ktVD scans were smaller or close to those from the k-t BLAST scans, mostly between 5% and 8% in the ROIs with arteries. This may suggest when the spatial structure of the image was simpler ktVD scans would produce more accurate intensity measurements and they did not change much with the changes of the sampling ratio. For all the undersampled scans, the results in the large ROI were very close to those in the flow ROI. The values of D_i in the core ROI were close to those in the flow ROI for most scans. This suggests in the ktVD scans with low sampling ratios the loss in spatial resolution was less serious than in the slice AB.

5.3.5 Intensity differences in different periods

Figure (5.9) shows the intensity differences in different periods of the cardiac cycle in the slice AB. Figure (5.10) shows the same type of results from the slice BB.

For both slices and most undersampled scans, the values of D_i were larger in the systolic period than those in the diastolic period. This suggests intensity measurements

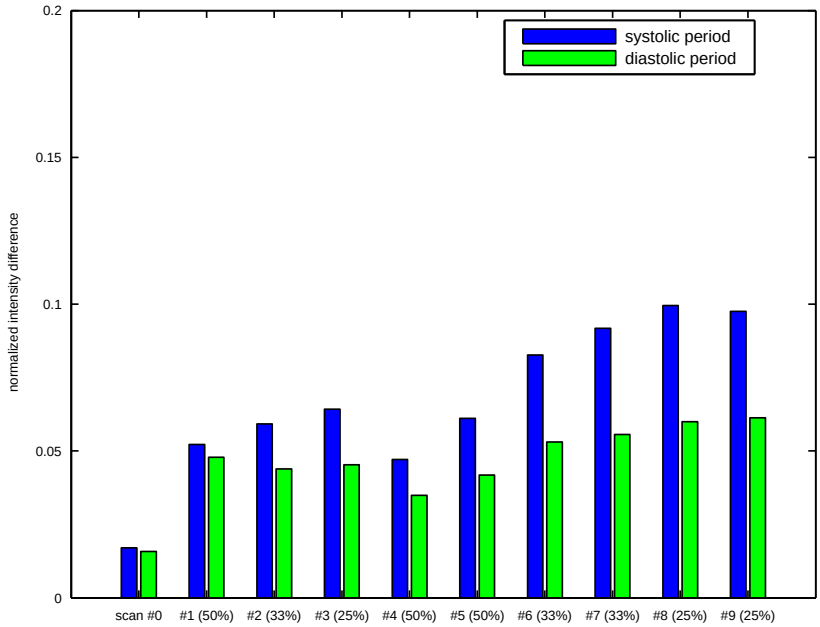

Figure 5.9: The normalized intensity differences over different periods of the cardiac cycle in the slice AB.

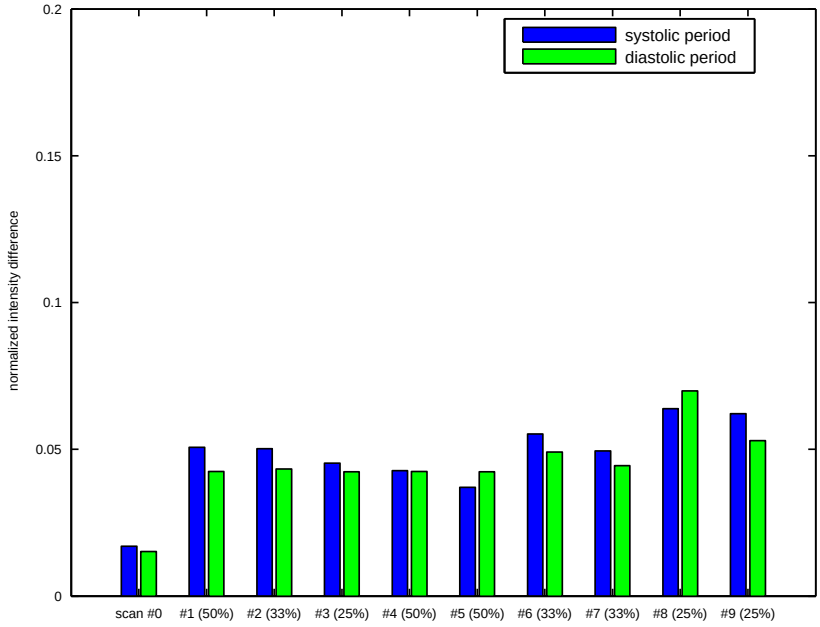

Figure 5.10: The normalized intensity differences over different periods of the cardiac cycle in the slice BB.

from the undersampled scans were less accurate when the blood flow was faster.

In the slice AB, for both the k-t BLAST scans and the ktVD scans, the differences between the results in the systolic period and those in the diastolic period increased as the sampling ratio decreased. This suggests lower sampling ratios might lead to larger intensity errors in dynamic area. At the sampling ratio of 33% or 25%, the values of D_i in the systolic period from the ktVD scans were larger than those from the k-t BLAST scan at the same sampling ratio. This suggests at low sampling ratios the intensity measurements in dynamic area from the ktVD scans were less accurate than those from the k-t BLAST scans.

In the slice BB, the results from all the undersampled scans were close to each other. In most cases the values of D_i in the systolic period were very close to those in the diastolic period. It suggests in this slice the intensity results from both the k-t BLAST scans and the ktVD scans were not sensitive to the dynamic properties of the flow.

5.3.6 Velocity differences in different regions

Figure (5.11) shows the velocity differences in the flow ROI and the core ROI in the slice AB. Figure (5.12) shows the same type of results from the slice BB.

In both slices, the values of D_v from the fully sampled scan were small, between 1 and 2 cm/s. This suggests velocity differences caused by background noise were less than 2 cm/s. Most results from the undersampled scans were less than or close to 5 cm/s. They were about two or three times as large as the results from the fully sampled scan. Since the peak velocity in the arteries was about 80 cm/s, in average the velocity differences were not large. For most undersampled scans the values of D_v were smaller in the core ROI than those in the flow ROI. This suggests near the artery walls the velocity measurements were less accurate.

In the slice AB, the values of D_v from all the undersampled scans were close to each other. At the high sampling ratio of 50%, the results from the ktVD scans were slightly smaller. This suggests velocity measurements in the slice AB did not change much with the sampling patterns. The differences between the results from each two ktVD scans at the same sampling ratio were less than 1 cm/s. This suggests the average velocity differences in the slice AB were not sensitive to the changes of sampling density variations in k-t space.

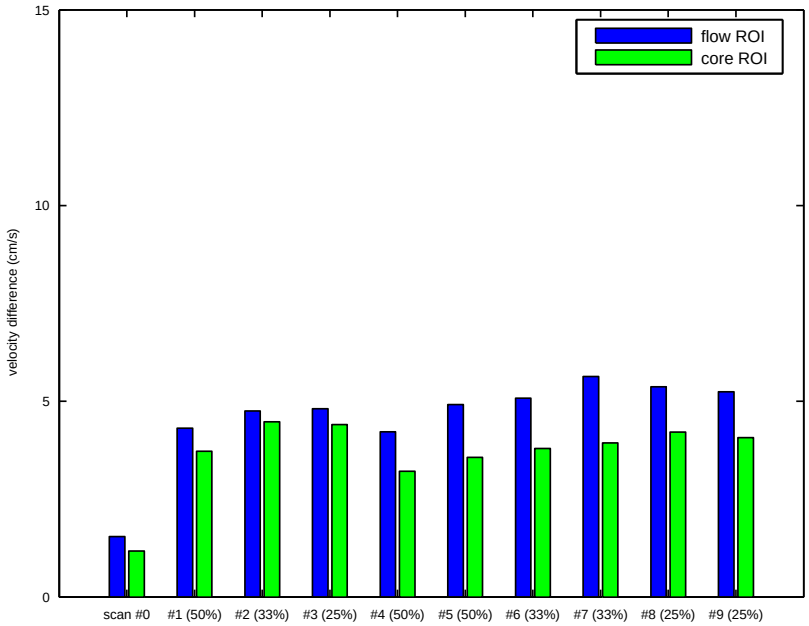

Figure 5.11: The velocity differences in the flow ROI and the core ROI in the slice AB.

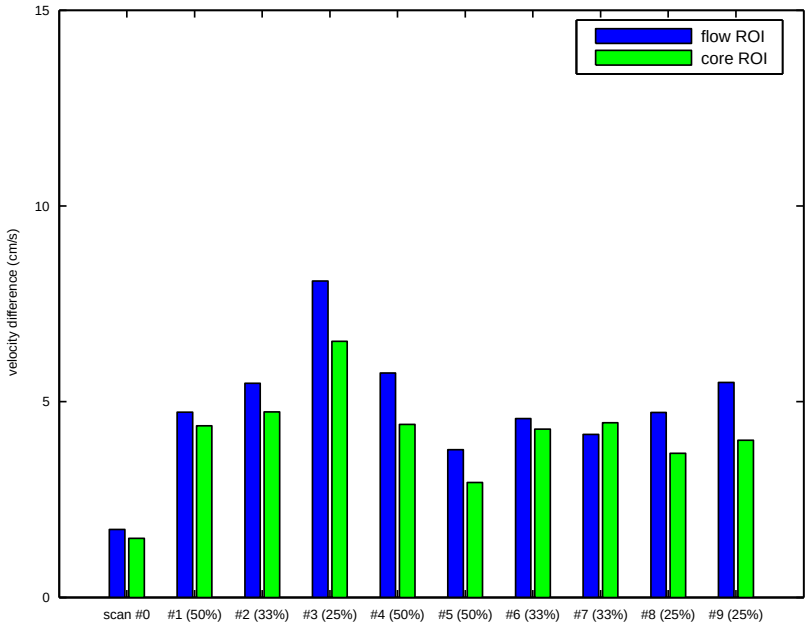

Figure 5.12: The velocity differences in the flow ROI and the core ROI in the slice BB.

In the slice BB, the values of D_v from all the k-t BLAST scans increased as the sampling ratio decreased. At the sampling ratio of 25%, the results from scan #3, around 7 cm/s, were about 2-3 cm/s larger than those from other scans. This suggests the velocity measurements in the RCCA with the k-t BLAST method were less accurate at this low sampling ratio. The values of D_v from most ktVD scans were slightly less than or close to 5 cm/s. At the same sampling ratio they were smaller than or close to those from the k-t BLAST scan. This suggests the velocity measurements from the ktVD scans did not change much with the sampling ratio, and they were similar to or more accurate than the results from the k-t BLAST scans at the same sampling ratio. At the sampling ratio of 50%, the values of D_v from scan #4 were about 2 cm/s larger than those from scan #5. At the sampling ratio of 33% or 25%, the results were close between the two ktVD scans at the same sampling ratio. This may suggest for ktVD scans velocity results were less sensitive to sampling density variation in k-t space at lower sampling ratios, and at high sampling ratios sparser sampling in outer k-t space might lead to less accurate velocity measurements.

5.3.7 Velocity differences in different periods

Figure (5.13) shows the velocity differences over different periods of the cardiac cycle in the slice AB. Figure (5.14) shows the same type of results from the slice BB.

In both slices and all the scans, the values of D_v in the systolic period were larger than those in the diastolic period. This suggests undersampling caused larger velocity errors when the blood flow was faster. The results from the fully sampled scan suggest background noise is greater in the systolic period.

In the slice AB, the values of D_v in the systolic period increased slightly as the sampling ratio decreased for both the k-t BLAST scans and the ktVD scans, while the results in the diastolic period did not change as much. This suggests for the slice AB measurements of faster blood flow were more likely to be affected by the changes of the sampling ratio. It also suggests at the tested sampling ratios, the temporal fidelity of the velocity results was not sensitive to the changes of the sampling ratio. The differences between the results in the systolic period and those in the diastolic period from the two ktVD scans at the same sampling ratio were close to each other. This suggests in the slice AB the loss in temporal resolution was not sensitive to the changes of sampling density variation in k-t space.

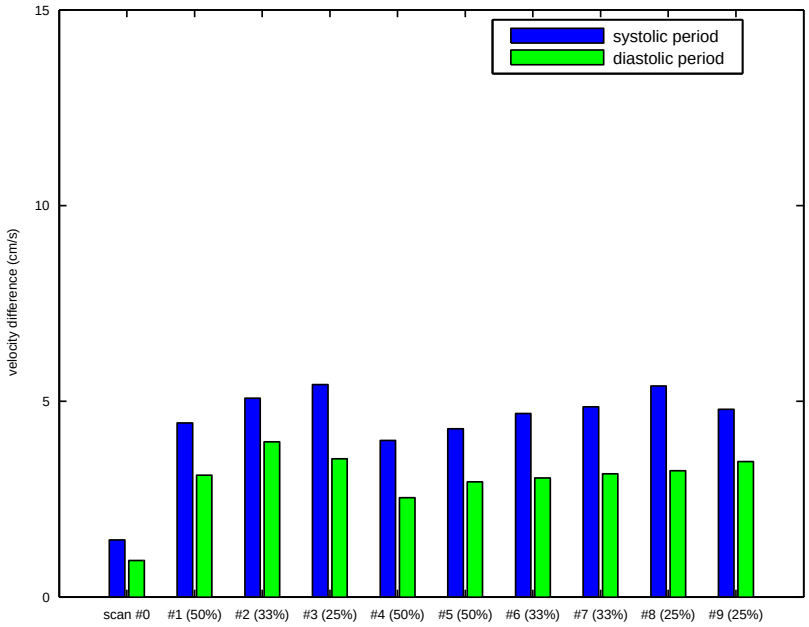

Figure 5.13: The velocity differences over different periods of the cardiac cycle in the slice AB.

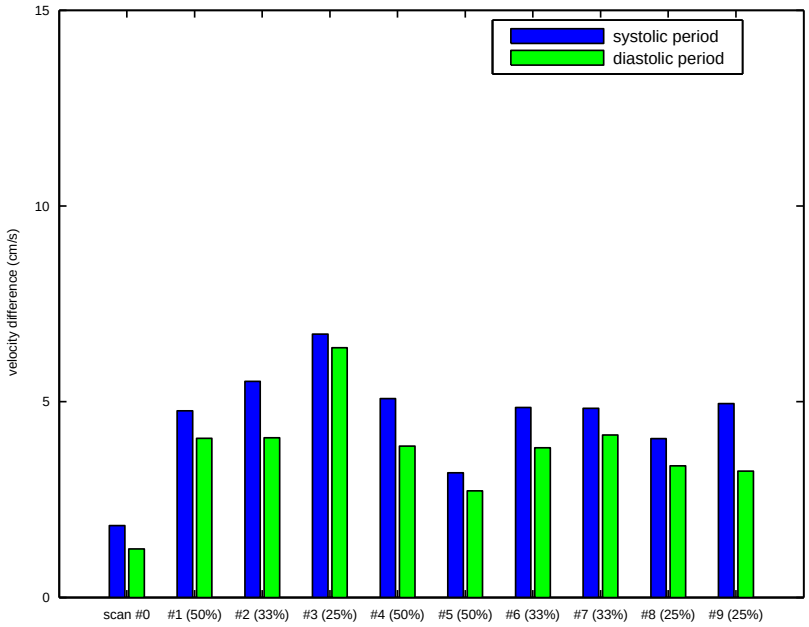

Figure 5.14: The velocity differences over different periods of the cardiac cycle in the slice BB.

In the slice BB, for the k-t BLAST scans the results in the systolic period increased as the sampling ratio decreased, suggesting again measurements of higher velocities were more sensitive to the changes of sampling patterns. At the sampling ratio of 25%, the value of D_v in the diastolic period was close to that in the systolic period, about 2-3 cm/s larger than the results from other k-t BLAST scans. This suggests for the slice BB at low sampling ratios the k-t BLAST measurements of both fast and slow flow were affected similarly by the changes of the sampling ratio. The results in the systolic period from the ktVD scans were close to each other, smaller than or similar to those from the k-t BLAST scan at the sampling ratio of 50%. This suggests for the RCCA the ktVD scans gave more accurate measurements of fast flow than the k-t BLAST scans at low sampling ratios. It also suggests the loss of temporal resolution as the sampling ratio decreased was less serious in the ktVD scans than in the k-t BLAST scans. The difference between the results in the two periods from scan #4 was larger than that from scan #5. For scan #8 the difference between the results in the two periods was smaller than that from scan #9. This suggests for the RCCA the loss of temporal resolution changed with sampling density variation in k-t space, and this change depended on the sampling ratio.

5.3.8 Velocity waveforms of single voxels

Figure (5.15) and (5.16) show the velocity waveforms of a selected voxel in RCCA from all the scans. In Figure (5.15) the results from the k-t BLAST scans and the ktVD scans were displayed separately. In Figure (5.16) the results from the undersampled scans with the same sampling ratio were grouped and displayed together. The results from the fully sampled scan (both NEX 1 and NEX 4) were always included as a reference. Figure (5.17), (5.18), (5.19), (5.20), (5.21) and (5.22) show the same type of results of other three selected voxels. As displayed, voxel #1 was close to the centre of the RCCA, voxel #4 was close to the wall of RCCA, and the other two voxels were between them.

For voxel #1, the waveforms from the k-t BLAST scans were closer to those from the fully sampled scans as the sampling ratio increased. At the sampling ratio of 25%, the waveform from the k-t BLAST scan showed different shape from those of the results from the fully sampled scan. The waveforms from the ktVD scans all had shapes very close to those of the results from the fully sampled scan. Most waveforms were

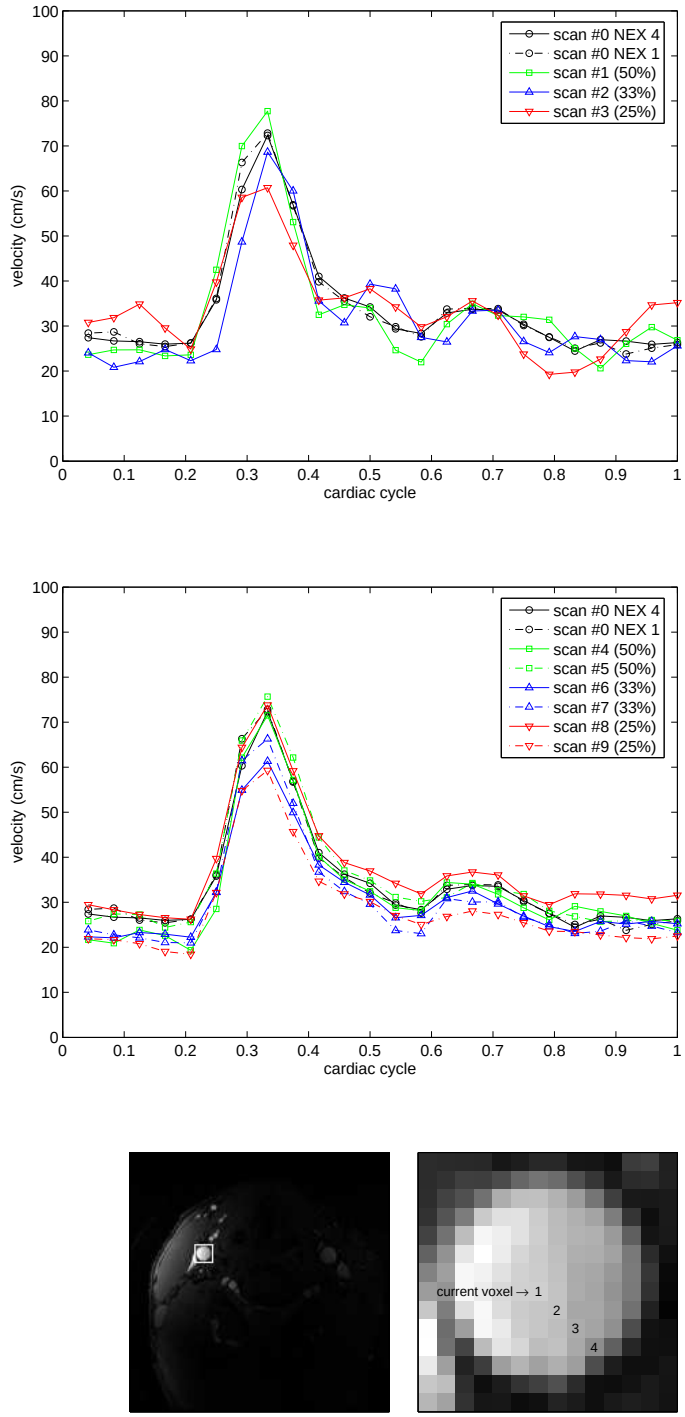

Figure 5.15: The velocity waveforms of a selected voxel in RCCA from all the scans. The results from the k-t BLAST scans and the ktVD scans are displayed separately. The position of the voxel is displayed in the bottom images.

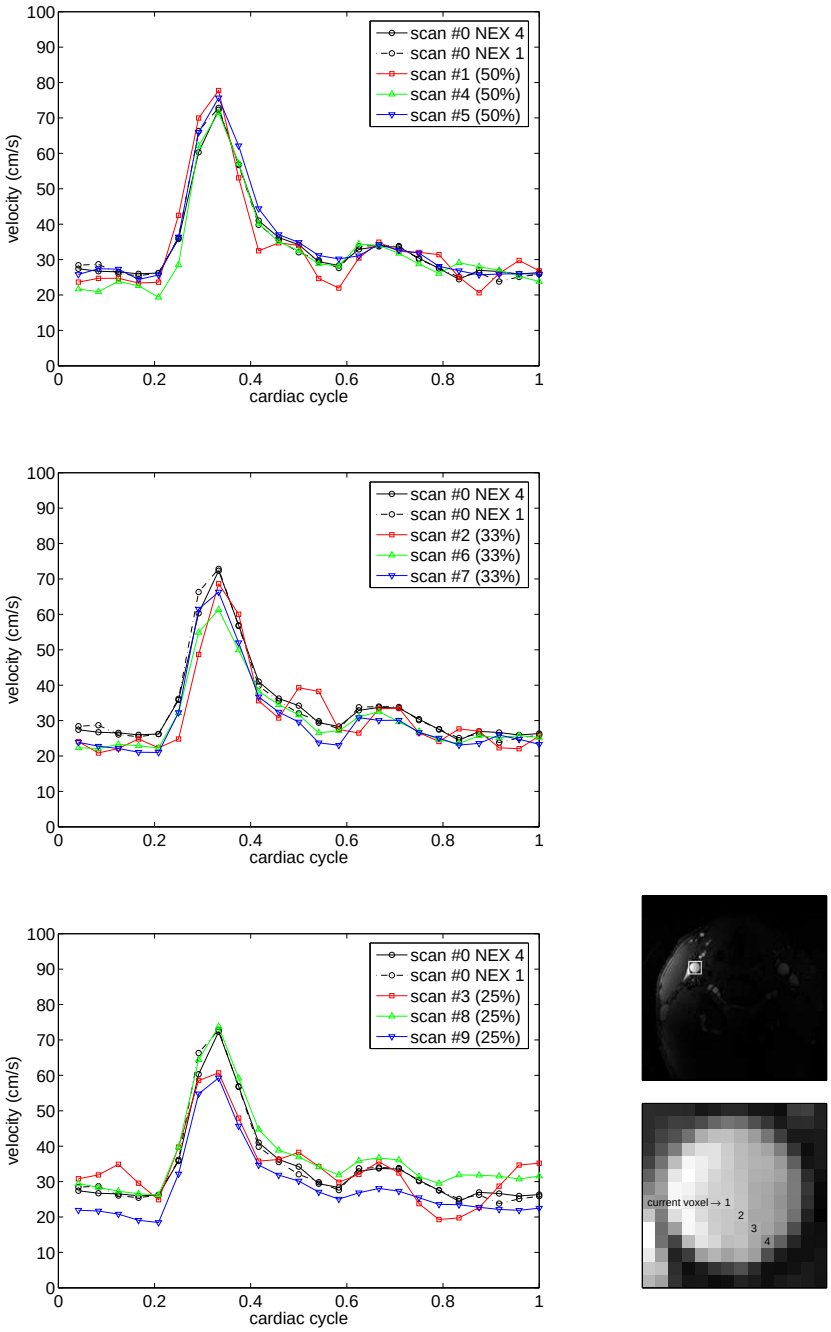

Figure 5.16: The velocity waveforms of a selected voxel in RCCA from all the scans. The results from the undersampled scans with the same sampling ratio are grouped and displayed together. The position of the voxel is displayed in the bottom right images.

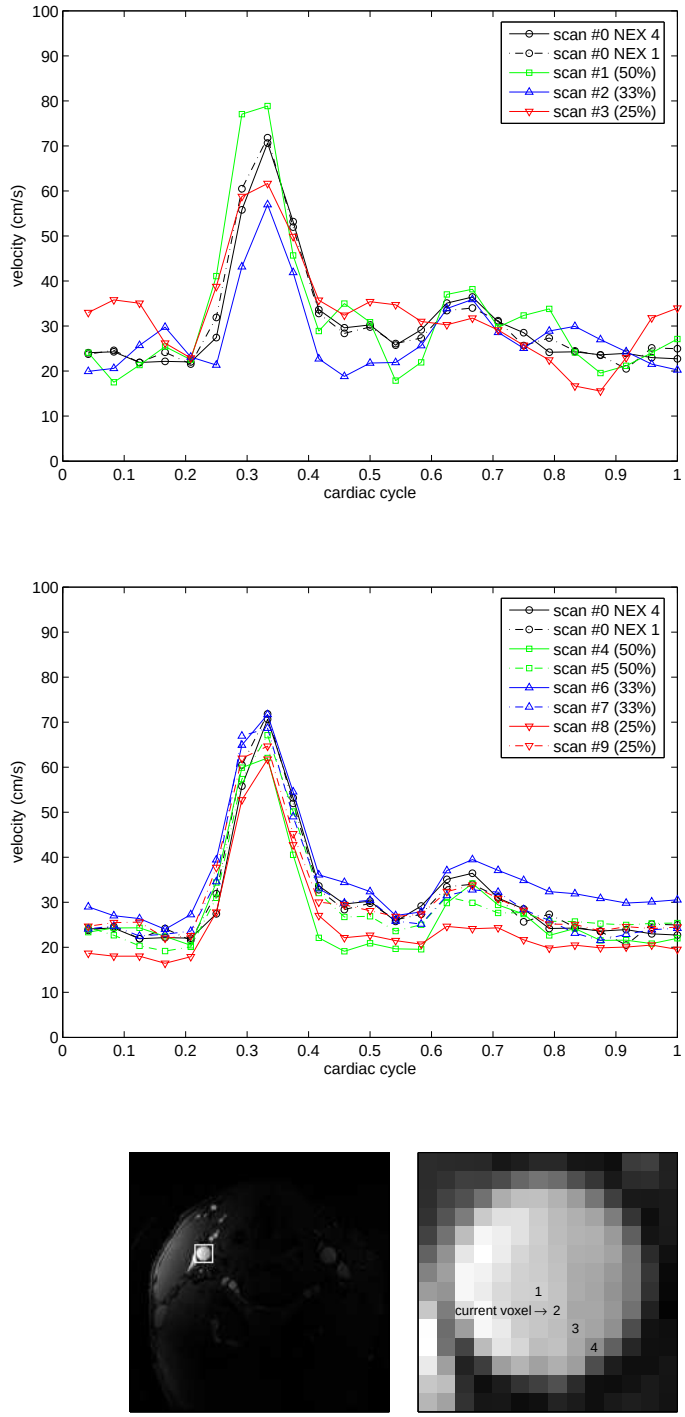

Figure 5.17: The velocity waveforms of a selected voxel in RCCA from all the scans. The results from the k-t BLAST scans and the ktVD scans are displayed separately. The position of the voxel is displayed in the bottom images.

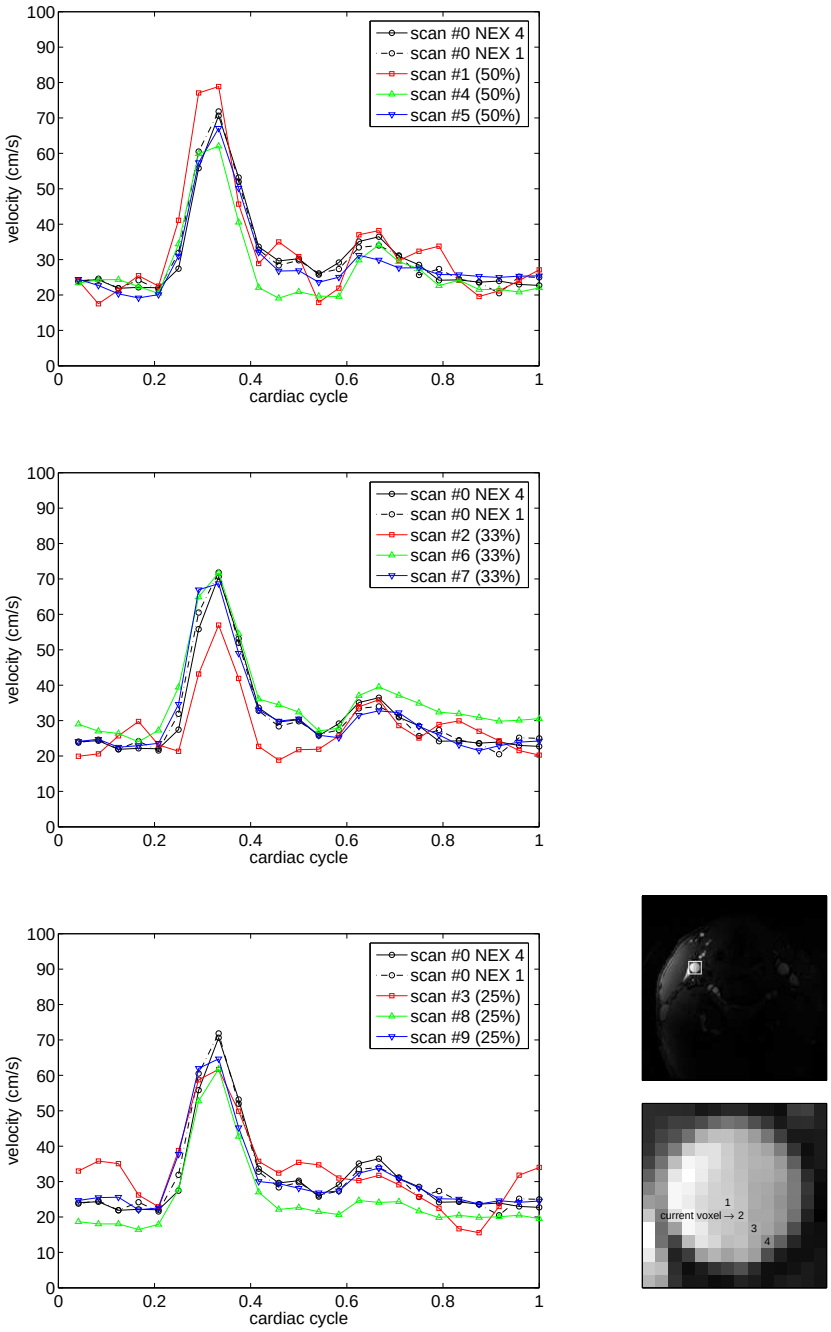

Figure 5.18: The velocity waveforms of a selected voxel in RCCA from all the scans. The results from the undersampled scans with the same sampling ratio are grouped and displayed together. The position of the voxel is displayed in the bottom right images.

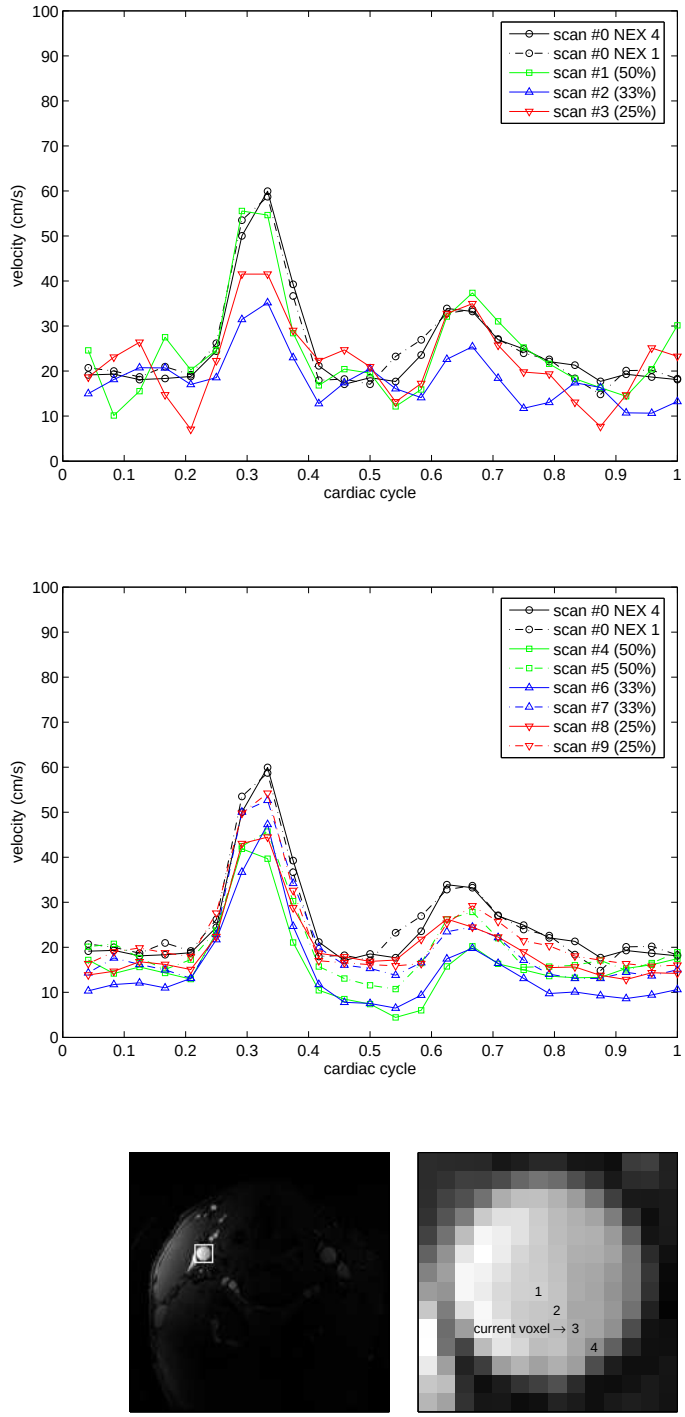

Figure 5.19: The velocity waveforms of a selected voxel in RCCA from all the scans. The results from the k-t BLAST scans and the ktVD scans are displayed separately. The position of the voxel is displayed in the bottom images.

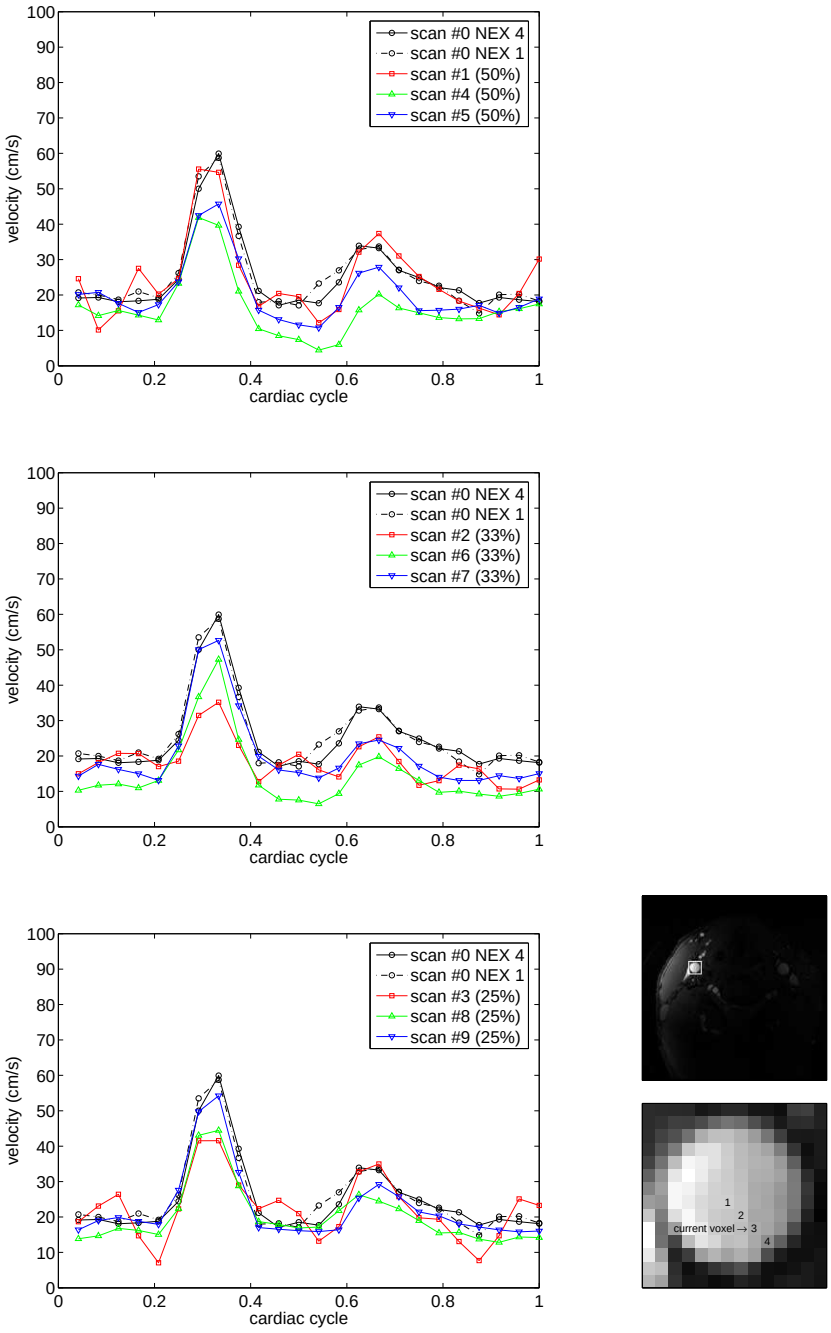

Figure 5.20: The velocity waveforms of a selected voxel in RCCA from all the scans. The results from the undersampled scans with the same sampling ratio are grouped and displayed together. The position of the voxel is displayed in the bottom right images.

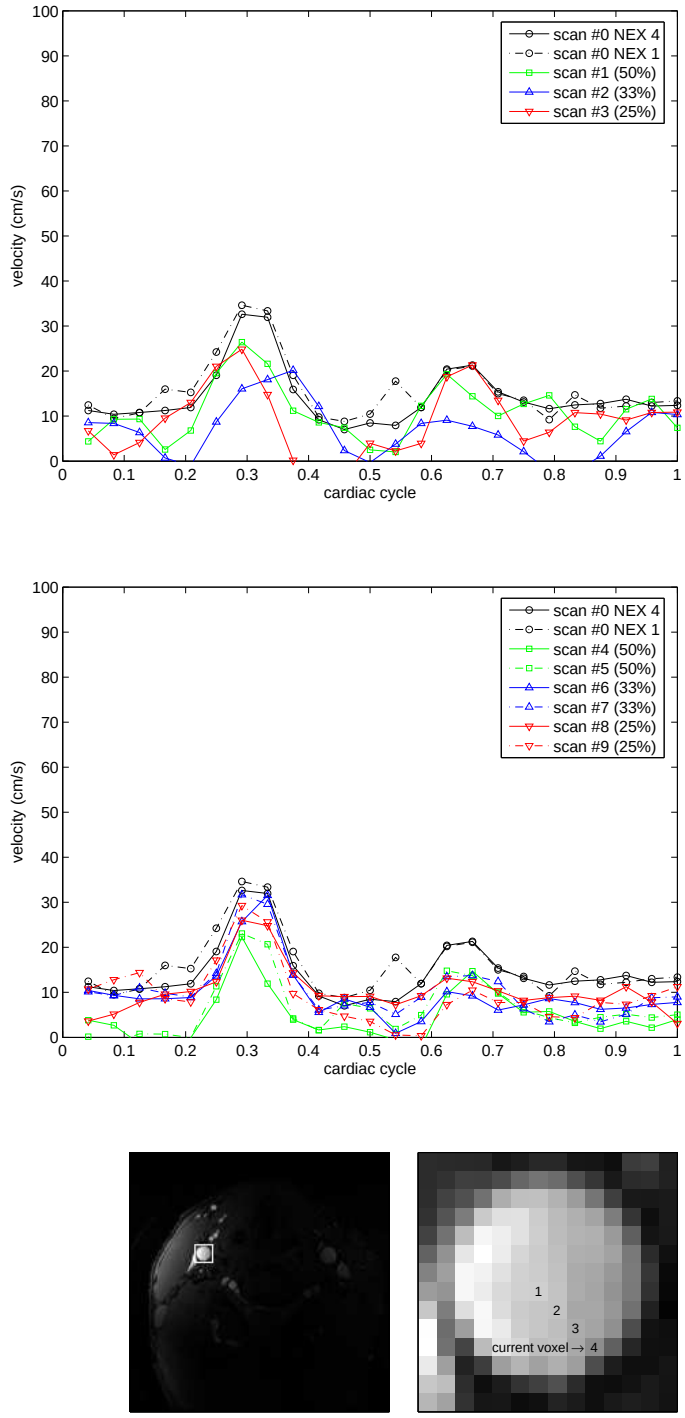

Figure 5.21: The velocity waveforms of a selected voxel in RCCA from all the scans. The results from the k-t BLAST scans and the ktVD scans are displayed separately. The position of the voxel is displayed in the bottom images.

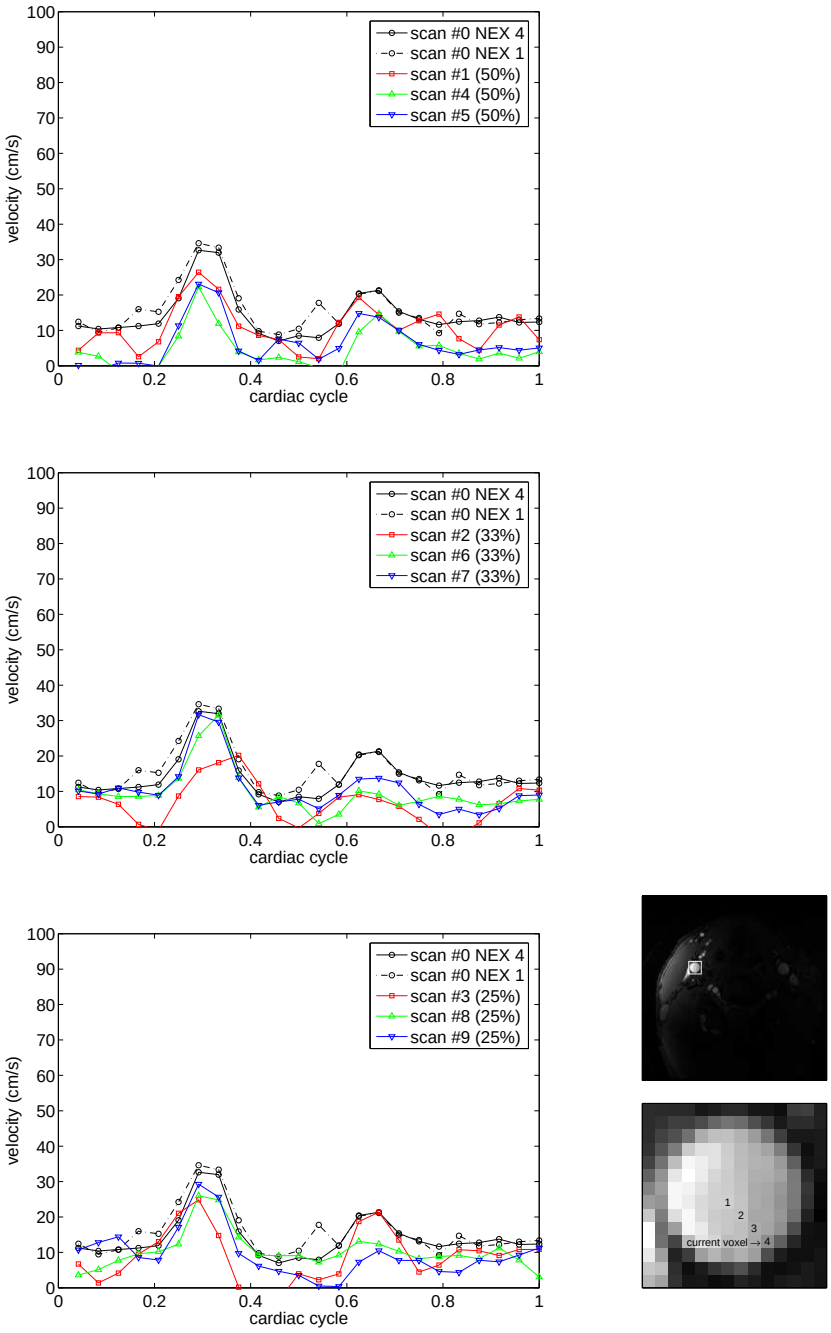

Figure 5.22: The velocity waveforms of a selected voxel in RCCA from all the scans. The results from the undersampled scans with the same sampling ratio are grouped and displayed together. The position of the voxel is displayed in the bottom right images.

also closer to those from the fully sampled scans as the sampling ratio increased. This suggests velocity measurements were more accurate as the sampling ratio increased, and the ktVD scans gave better temporal resolution than the k-t BLAST scans at the same sampling ratio. This can also be observed when the waveforms from the scans at the same sampling ratio were displayed together. The waveform from scan #6 was slightly smoother than that from scan #7. The waveform from scan #9 gave relatively lower velocities than those from scan #8 and underestimated velocities throughout the cardiac cycle. This suggests at low sampling ratios the changes of sampling density variation in k-t space might lead to changes in the velocity results, and these effects depended on the sampling ratio.

For voxel #2 the results showed similar pattern to that of the results from voxel #1. The results from the ktVD scans were more accurate than those from the k-t BLAST scans in the temporal dimension. It is also observed the waveforms from scan #5, #7, and #9 were closer to those from the fully sampled scan than those from scan #4, #6 and #8, respectively. This suggests at the same sampling ratio collecting more samples in central k-t space gave better velocity results.

For voxel #3 the ktVD scans also gave better results than those from the k-t BLAST scans. For each pair of ktVD scans at the same sampling ratio, denser sampling in central k-t space still gave better results. Most ktVD scans underestimated velocities at most phases of the cardiac cycle. The waveforms from scan #7 and #9 were closer to those from the fully sampled scan than those from other ktVD scans. As a result the ktVD scans at the sampling ratio of 50% no longer gave best results.

For voxel #4 the differences between the two waveforms from the fully sampled scan were larger than those from other voxels. This suggests in the results from voxel #4 the noise level was higher. Since voxel #4 was close to the artery wall, this was expected. The waveforms from the undersampled scans were less similar to those from the fully sampled scan than in the results from other voxels. Overall the ktVD scan results were still better than those from the k-t BLAST scans. The differences between each pair of ktVD scans at the same sampling ratio were less obvious. Velocity underestimation in the ktVD results could still be observed.

5.3.9 Flow rates of carotid arteries

Figure (5.23) and (5.24) show the flow rates of the RCCA from all the scans. In Figure (5.23) the results from the k-t BLAST scans and the ktVD scans were displayed separately. In Figure (5.24) the results from the undersampled scans with the same sampling ratio were grouped and displayed together. The results from the fully sampled scan (both NEX 1 and NEX 4) were always included as a reference. Figure (5.25), (5.26), (5.27) and (5.28) show the same type of results of the RICA and the RECA.

The flow rate waveforms of the RCCA from the k-t BLAST scans showed less similarities to those from the fully sampled scans as the sampling ratio decreased. The waveform from scan #2 had a lower peak. The waveform from scan #3 showed large differences from those from the fully sampled scan at most phases of the cardiac cycle. This suggests the flow measurements from the k-t BLAST scans were less accurate at lower sampling ratios. The differences between the flow rate waveforms from the ktVD scans and those from the fully sampled scan were small. At most phases of the cardiac cycle there were no apparent differences between the results from any two of the ktVD scans. This suggests the flow measurements from the ktVD scans did not change much with the changes of the sampling patterns, and they were more accurate than those from the k-t BLAST scans at low sampling ratios.

The results of the RICA showed slower and less dynamic flow than those of the RCCA. The differences between the flow rate waveforms were also less obvious than those in the results of the RCCA. The waveforms from the k-t BLAST scans became smoother as the sampling ratio decreased. At the peak flow moment the differences between waveforms were large. After the peak at most phases of the cardiac cycle the flow was underestimated. This suggests in the k-t BLAST scans the loss of temporal resolution was more serious at lower sampling ratios. The flow rate waveforms from the ktVD scans were close to those from the fully sampled scan. The differences between the undersampled and fully sampled results were slightly larger as the sampling ratio decreased, mostly at the phases of the cardiac cycle after the peak flow moment. This suggests the flow measurements from the ktVD scans were less accurate at low sampling ratios, and the changes were not large. At the peak flow moment the differences from the fully sampled results were small. At low sampling ratios the shapes of the waveforms from the ktVD scans remained similar to those from the fully sampled scans. This suggests in the ktVD scans the loss of temporal resolution was less serious

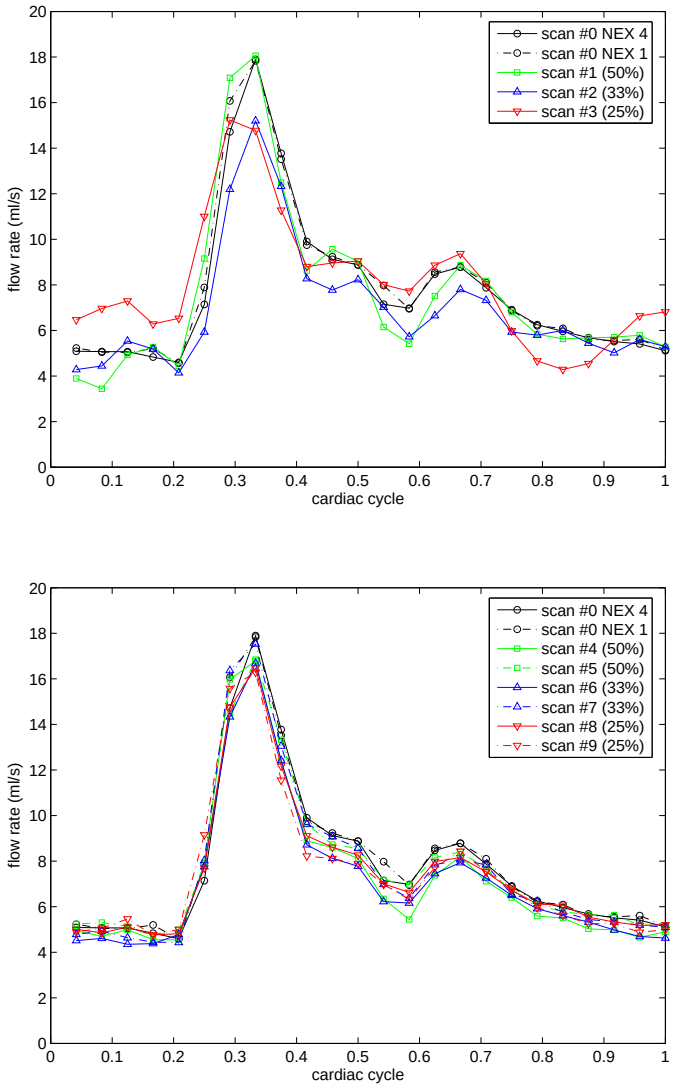

Figure 5.23: The flow rates of the RCCA from all the scans. The results from the k-t BLAST scans and the ktVD scans are displayed separately.

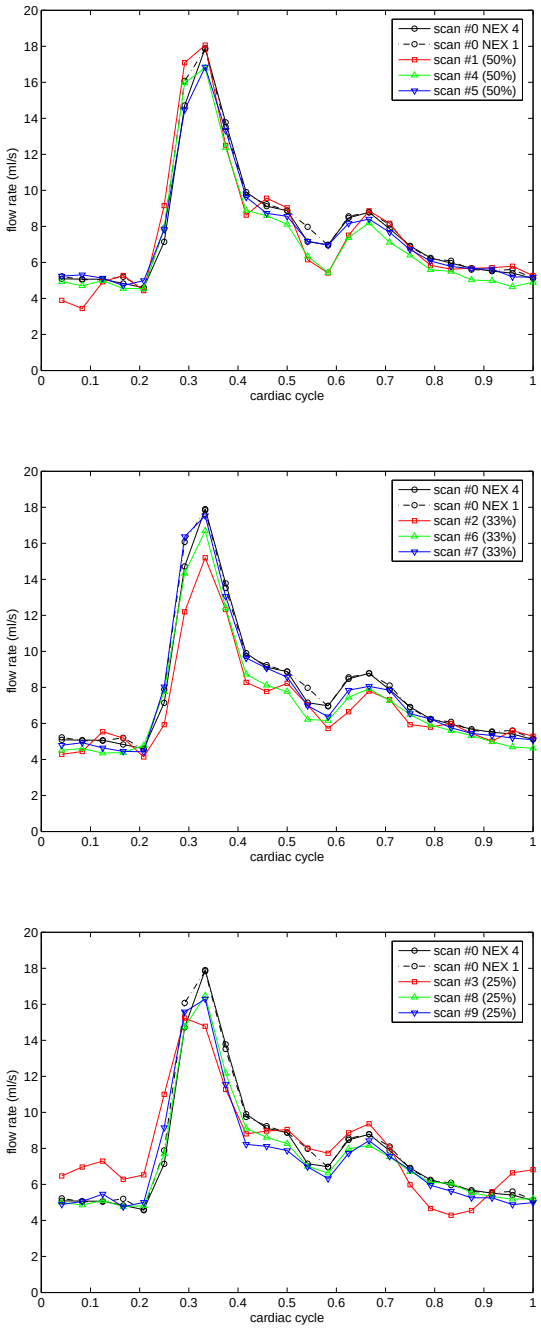

Figure 5.24: The flow rates of the RCCA from all the scans. The results from the undersampled scans with the same sampling ratio are grouped and displayed together.

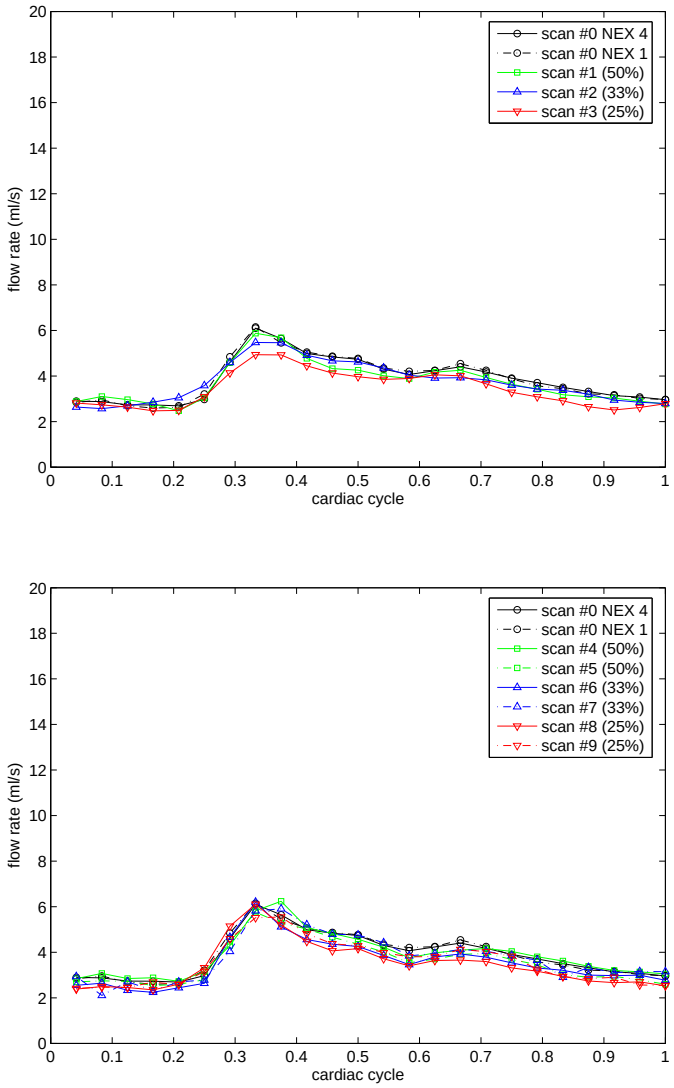

Figure 5.25: The flow rates of the RICA from all the scans. The results from the k-t BLAST scans and the ktVD scans are displayed separately.

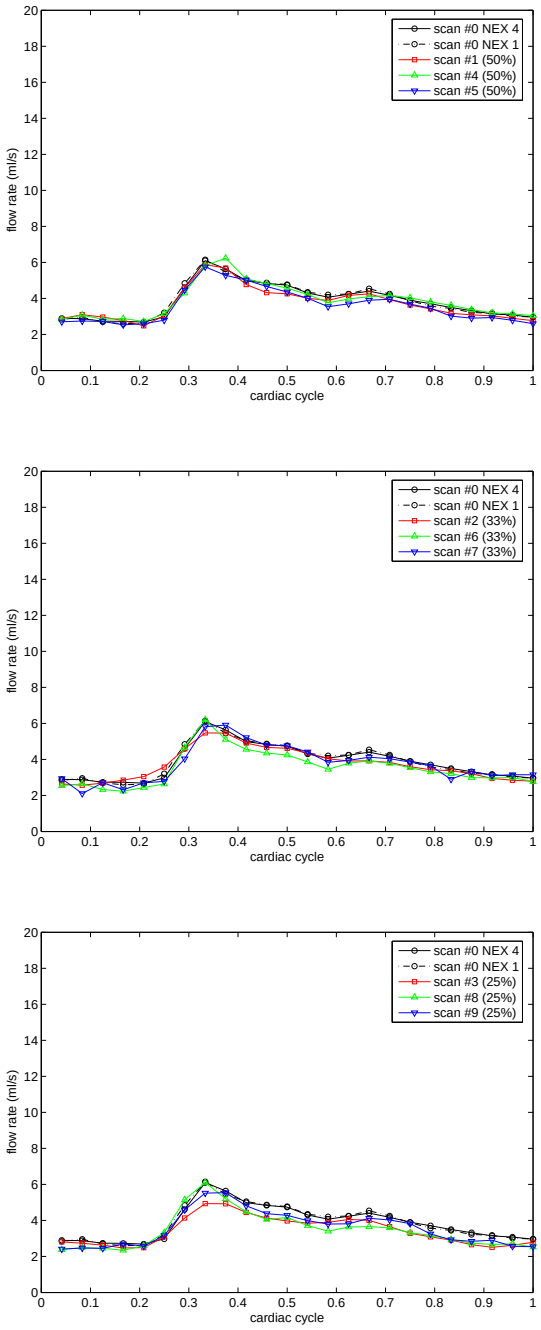

Figure 5.26: The flow rates of the RICA from all the scans. The results from the undersampled scans with the same sampling ratio are grouped and displayed together.

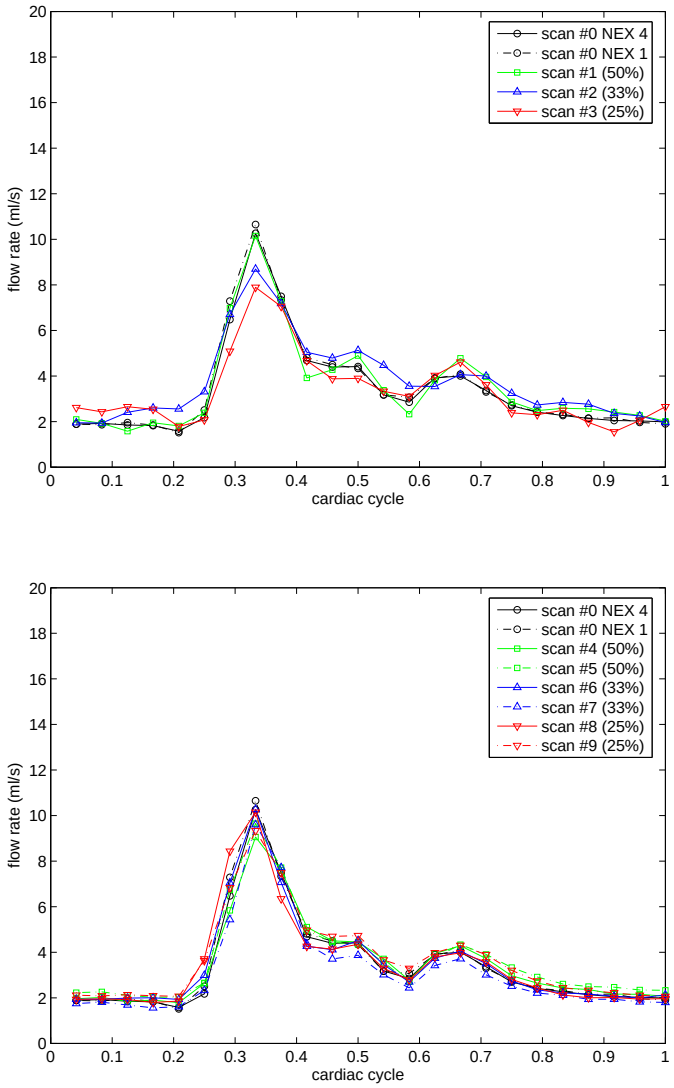

Figure 5.27: The flow rates of the RECA from all the scans. The results from the k-t BLAST scans and the ktVD scans are displayed separately.

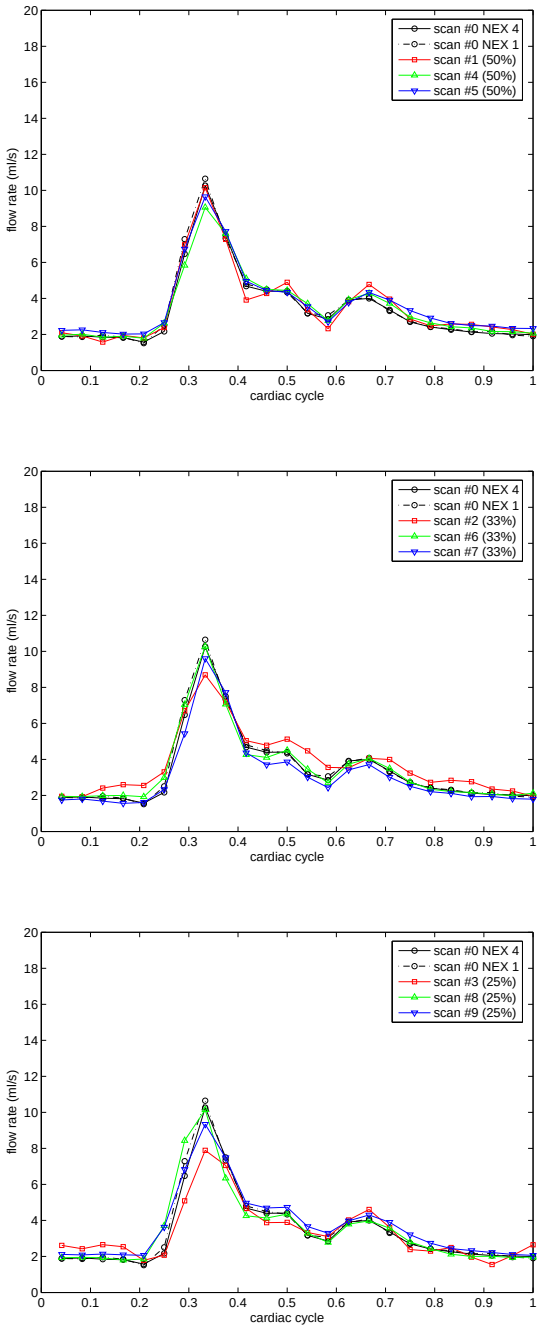

Figure 5.28: The flow rates of the RECA from all the scans. The results from the undersampled scans with the same sampling ratio are grouped and displayed together.

than in the k-t BLAST scans at the same sampling ratio. At the phases after the peak flow moment the flow was also underestimated in most ktVD scans. The underestimation was more serious in scan #6 and scan #8 than in scan #7 and scan #9, respectively. This suggests denser sampling in central k-t space might make the flow measurements from ktVD scans more accurate.

The flow in the RECA was also slower than that in the RCCA, but it was more dynamic than that in the RICA. The results from the undersampled scans showed a similar pattern to that in the results of the RCCA. For the k-t BLAST scans the loss of temporal resolution was more serious as the sampling ratio decreased. The results from the ktVD scans were more accurate than those from the k-t BLAST scans at the same sampling ratios. The flow measurements from the ktVD scans were not sensitive to the changes of sampling patterns. The flow rate waveforms from scan #7 and #9 were slightly smoother than those from scan #6 and #8, respectively. This suggests at low sampling ratios the loss of temporal resolution in the ktVD scans was slightly more serious when more samples were collected in central k-t space.

5.4 Discussion

Ideally the in vivo test presented in this chapter should provide more realistic results than those obtained from the simulations in the previous chapter. However, the implementation limits of in vivo experiments might lead to uncertainties in the comparisons between scans. Although the same settings except different sampling patterns were used for the scans in comparison, the underlying true signal of different scans could be different. In the comparisons it was difficult to separate the inherent scan-to-scan differences from those caused by the changes of the undersampling pattern. Many factors could contribute to scan-to-scan differences. Background noise could be different from scan to scan. The properties of the carotid blood flow could also change over time. Although measures had been taken to reduce time between scans, it should be noted in the comparisons the scan-to-scan differences could always contributed to any observed differences.

Due to the long scan time and the requirement of suppressing involuntary motion like swallowing for more than twenty minutes, only three volunteers had been scanned with the same protocol. The results presented in this chapter were all acquired from

one of them. The data of this subject was selected because it did not show any serious motion artefacts or apparent signs of displacements between scans. To test the reproducibility of the results, more volunteers could be recruited and more tests could be repeated on each volunteer. This could be included in future work.

Since a volunteer scan could not be too long, only limited sampling patterns and sampling ratios were tested. The results obtained from these comparisons might not fully reflect the relationship between the accuracy of the measurements and the undersampling method applied. A possible solution to this problem is to increase the number of tests while reducing the number of scans in each test. For example, a minimum test can have only three scans, a fully sampled scan and two undersampled scans with different sampling patterns. Scan-to-scan differences may also be reduced in this way but to compare several different sampling patterns a very large number of tests have to be conducted.

Only two slices were scanned in each test because of long scan time. It was observed in the intensity differences and the velocity differences the performance of each sampling method was different in different slices. This suggests signal content is also an important parameter in the comparisons of undersampling methods, like the sampling pattern or the sampling ratio. If more slices were scanned, more details of the relationship between the signal content and undersampling performance could be examined. In future work more tests should be carried out separately for different slices.

The scan settings could also have influence on the comparison results. The undersampling performance of the k-t BLAST method and the ktVD method was affected by the SNR level, and the SNR of the signal was affected by the scan parameters (T_R, T_E, acquisition bandwidth, voxel size, and others). With the limit of total scan time it was difficult to test different scan settings in a single test. More tests are necessary for the study of these effects. Another solution is to compare results acquired with different coils in the same scan, which have different SNR levels.

In the segmentation of the arteries some voxels near the artery wall were difficult to classify. In the temporal averaged images there might be tissue producing high intensity next to and out of the artery wall, which would be difficult to separate from the arteries also showing high intensities. In the complex difference images small phase differences due to slow flow near the artery wall might produce low intensities inside arteries. As a result the cross-section area of an artery often appeared smaller in the complex difference images than in the temporal averaged images. A possible

solution to this problem is to use additional high resolution TOF scans with the same slice position and in-plane position of the gated scans. However this will cost scan time. Ideally segmentation can be carried out without additional information other than that acquired in the gated scans. With the applied segmentation method, some voxels inside and close to the artery wall would probably be labelled as out of the artery wall. For the comparisons this would lead to underestimated flow rate results, especially when the flow near the artery wall was fast. Since the same set of ROIs was used for all the scans in each slice, incorrect segmentation of small number of voxels would not affect the comparison results substantially.

The intensity difference images from both undersampling methods showed spatial resolution loss. The intensity differences could be scan-to-scan differences, undersampling errors, or both. It is not clear what the main reason was for the large intensity differences near the artery wall, which could lead to errors in segmentation. The results showed spatial resolution loss in the ktVD images was more serious than that in the k-t BLAST images. If most of the large intensity differences were scan-to-scan differences, changing the order of the scans in the scanning protocol might produce different results. For example, if the ktVD scans were carried out before the k-t BLAST scans and immediately after the fully sampled scans, the ktVD images would probably show less intensity differences than the k-t BLAST images. The order of the scans using the same undersampling method could also be changed. The sampling patterns of low sampling ratios could be tested before those of high ratios to examine the contributions of scan-to-scan differences to the small increase in intensity difference as the sampling ratio decreased. For more accurate comparisons of the intensity differences caused by undersampling errors it is still necessary to reduce scan-to-scan differences.

According to the intensity difference images and the averaged intensity differences in different regions, good intensity results should be similar to those obtained in scan #1 or scan #2, giving values of D_i less than 5% in the flow ROI. Some ktVD scans in the slice AB with low undersampling ratios gave values of D_i more than 10% in the flow ROI. Since in these scans the values of D_i in the core ROI were much less than those in the flow ROI, for the regions near the artery wall the values of D_i could be larger than 15%. If most of the intensity differences were undersampling errors, further comparisons of the velocity results from these scans might not be useful because the intensity errors were too large. It might be helpful to set 10% as the highest acceptable level of the values of D_i in the flow ROI when intensity results were evaluated.

Only the timeframes corresponding to the peak flow moment were shown in the intensity difference images. As shown in the comparisons of the intensity differences over different periods, the values of D_i in the core ROI of the slice BB did not change much over the cardiac cycle, but in the slice AB as the sampling ratio decreased the differences between the values of D_i in different periods became much larger. In either slice the intensity differences at the peak flow moment were probably larger than or close to those at other phases of the cardiac cycle. So the intensity difference images have shown the most serious spatial resolution loss in the cardiac cycle. For the scans in the slice AB, the values of D_i in the diastolic period were close to 5% and in the systolic period they were 2-5% larger. As previously described the values of D_i at the level of 5% were relatively good intensity results. In the diastolic period the intensity difference images from most scans were probably similar to those from scan #1 or scan #2. This suggests only in the systolic period in the slice AB the k-t BLAST scans produced better intensity results than the ktVD scans.

The evaluation of the velocity results is more difficult than that of the intensity results because in addition to undersampling errors and scan-to-scan differences intensity errors could cause velocity errors. Intensity results could also have little influence on velocity results. Since in the slice AB the intensity differences from the ktVD scans were large, the corresponding velocity results were probably less useful than those from the slice BB in the comparisons of undersampling methods. Nevertheless, the velocity differences from the ktVD scans in the slice AB were close to those from the k-t BLAST scans. This suggests in the slice AB without the velocity errors caused by possible intensity errors the velocity differences from the ktVD scans could be smaller than or similar to those from the k-t BLAST scans. In the slice BB the velocity differences showed similar pattern to that of the intensity differences. It suggests the influence from the intensity results on the velocity results was greater in this slice than in the slice AB. Since the intensity differences in the slice BB were not large, the similarity was probably caused by scan-to-scan differences or undersampling errors.

Most results shown in the comparisons of the velocity waveforms of single voxels were consistent with those in the comparisons of the velocity differences in the slice BB. It should also be noted there were some differences between the results from these two types of comparisons. Both types of comparisons showed the velocity measurements from the k-t BLAST scans became less accurate as the sampling ratio decreased, and it was most serious at the sampling ratio of 25%. Only the comparisons of the ve-

locity waveforms showed at the sampling ratio of 50% the shapes of the waveforms from the k-t BLAST scans were different from those from the fully sampled scans. If velocity results of most voxels in the arteries were similar to those examined in the comparisons of the velocity waveforms, the k-t BLAST scans at the sampling ratio of 50% should probably be regarded as failed. This suggests the values of D_v were not sufficient for absolute evaluations of the velocity results. It may be helpful to use correlation to compare the shapes of the velocity waveforms from the undersampled scans and those from the fully sampled scans. For the ktVD scans, both types of comparisons showed the velocity results at different sampling ratios were close to those from the fully sampled scans. Only the comparisons of the velocity waveforms showed there were often velocity underestimations, and for some voxels the velocity measurements were less accurate as the sampling ratio decreased. For each pair of ktVD sampling patterns of the same sampling ratio and different sampling density variations over k-t space, both types of comparisons showed the effects of sampling density variations changed with the sampling ratio. Only the comparisons of the velocity waveforms showed for some voxels denser sampling in central k-t space gave better velocity results. For the k-t BLAST scan and the ktVD scans at the same sampling ratio, both types of comparisons showed the ktVD scans gave more accurate velocity measurements at low sampling ratios, but the comparisons of the velocity differences did not show how inaccurate the k-t BLAST results were, and the comparisons of velocity waveforms showed at the sampling ratio of 50% the velocity results from the ktVD scans were also better. Overall, the comparisons of the velocity waveforms appeared more useful for the evaluations of the undersampling results.

Since only four voxels have been examined in the comparisons of the velocity waveforms, they did not necessarily represent all the voxels in the arteries. The flow rate waveforms averaged in the flow ROI are more general measures of the velocity results. In the RCCA, the results from the comparisons of the flow rate waveforms were similar to those from the comparisons of the velocity differences in the slice AB. In the RICA and RECA, the results were similar to those from the comparisons of the velocity waveforms of single voxels. It should be noted the flow rate waveforms of the RICA and RECA were calculated in the slice AB. Since the intensity differences in the slice AB from some ktVD scans were large, the corresponding flow rate results were probably affected by intensity errors.

In summary, according to the acquired data, the k-t BLAST scans produced good

intensity images but the velocity results became less accurate as the sampling ratio decreased. At low sampling ratios serious temporal resolution loss in velocity results was observed and for some voxels it was also seen at high sampling ratio. The intensity images of the slice AB from the ktVD scans showed large differences from those fully sampled, especially in the regions near the artery wall. Most velocity results were close to those fully sampled although some velocities were underestimated. Averaged velocity differences between the measurements from the ktVD scans and those from the fully sampled scans were less than or close to 5 cm/s. The velocity results from the ktVD scans did not change much with the sampling ratio or with the sampling density variation in k-t space. Velocity waveforms from some voxels showed better results when more samples were collected in central k-t space and the sampling ratio remained unchanged. At the same sampling ratio the ktVD scans generally produced better velocity results than the k-t BLAST scans. Velocities measured for the voxel close to the artery wall from all the undersampled scans showed large differences from the measurements from the fully sampled scans. All the comparisons between scans were subject to possible influence of scan-to-scan differences and the velocity results could be inaccurate when there were large intensity differences between the undersampled and the fully sampled scans.

Chapter 6

In vivo test of undersampling in three dimensions of k-t space

6.1 Introduction

So far all the tests were carried out in 2D scans and the signals were undersampled in only two dimensions of k-t space. In 3D scans, where phase encoding is used in two spatial dimensions, the signals can be undersampled in three dimensions of k-t space. The extra spatial dimension available for undersampling may allow further scan time reduction compared with what can be achieved with undersampling in only two dimensions of k-t space. On the other hand, 3D scans also need more scan time reduction than 2D scans. For example, on the scanner used in this work, a 2D PC scan can be set to acquire one slice while the minimum number of slices for the 3D PC sequence is 16. The minimum scan time of a 3D PC scan will be much longer than that of a 2D PC scan at the same temporal and in-plane resolution.

The signals of the 3D scans can also be undersampled in the same fashion as in the 2D scans. The same undersampling pattern can be used for all the slice encoding steps. In this way the data is undersampled in two of the four dimensions of k-t space. It can be compared with data undersampled in three dimensions to evaluate the differences.

In practice, 3D scans are sometimes more favourable than 2D scans. Since the RF pulses are not limited to a single slice, slices in 3D scans can be thinner than those allowed in 2D scans. This improves spatial resolution. T_R can also be shorter in 3D scans. This improves temporal resolution or reduces total scan time. So it will be

very desirable if undersampling in three dimensions of k-t space can save more scan time or produce more accurate measurements for 3D scans than undersampling in two dimensions.

In this chapter different ktVD undersampling patterns were tested *in vivo* using the 3D PC sequence. Results from data undersampled in different numbers of dimensions of k-t space and at different sampling ratios were compared with results from a fully sampled scan.

6.2 Method

6.2.1 Undersampling in three dimensions of k-t space

The design of the variable-density sampling patterns in three dimensions is similar to the design of the sampling patterns undersampling in two dimensions of k-t space. In the temporal dimension the sampling rate for each k-space position does not change. As a k-space position goes further away from the centre of k-space the number of samples collected at this position decreases. In 3D scans this change of sampling density can happen along both phase encoding dimensions, including the slice encoding dimension. Theoretically this allows many possible designs of how fast the sampling density changes along the two phase encoding dimensions. In this work a simple approach was adopted to build the sampling patterns in three dimensions. In the 3D PC sequence the slice encoding steps are executed sequentially, so the sampling pattern in three dimensions can be divided into many sampling patterns in two dimensions, each for a slice encoding step. For each slice encoding step the acquisition covers two spatial encoding dimensions and the temporal dimension, the same scan matrix as in a 2D scan of a single slice. The actual design of the sampling patterns started from the sampling patterns in two dimensions. These sampling patterns were applied to the slice encoding steps and formed the sampling patterns in three dimensions. As described previously, all the slice encoding steps can use the same sampling pattern so the sampling density remains constant along the slice encoding dimension. Otherwise, sparser sampling patterns can be applied to slice encoding positions closer to the edge of k-space. This makes the sampling density change as desired along two dimensions of k-space.

The sampling ratio of a sampling pattern in three dimensions is calculated in the

same way as for the sampling patterns in two dimensions. It is defined as the ratio of the number of samples collected in all the slice encoding steps of an undersampled scan to the number of samples collected in a scan of the same scan matrix and fully sampled. It is also the ratio of the scan time of the undersampled scan to the scan time of the fully sampled scan.

6.2.2 The scanning protocol

Only a limited number of scans can be included in the protocol because the minimum scan time of a 3D scan is long. The time of each scan is determined by the T_R, the number of flow encoding directions, the scan matrix, and the sampling ratio of the applied sampling pattern. The minimum number of slice encoding steps allowed by the 3D PC sequence is 16. The total scan time increases in proportion to the number of slice encoding steps. The selected scan matrix was $192 \times 192 \times 16$ in the three spatial dimensions and 24 in the temporal dimension. T_R was 15 ms. Flow encoding was applied only in the superior/inferior direction so each sample prescribed in the sampling patterns will be sampled twice, with and without flow encoding. For a fully sampled scan the scan time was about 37 minutes. To compare undersampling in two dimensions with undersampling in three dimensions, two scans were carried out for the same sampling ratio. Three different sampling ratios were tested (33%, 25% and 17%). The total scan time of the fully sampled scan and the six undersampled scans was about 92 minutes. This is extremely long for a volunteer so no additional scans were included in the protocol. It would be desirable to have two more scans testing the sampling ratio of 50%, but this would add an additional 37 minutes to the already long scan time.

The scanning protocol consisted of eight scans. The first was a localizer. The second was fully sampled and from this all the following scans used similar settings except the sampling pattern. The fully sampled scan was immediately followed by three pairs of undersampled scans. In each pair the two scans had the same overall sampling ratio. In the first of the two scans k-t space was undersampled in two dimensions, while in the second scan three dimensions were undersampled. The sampling ratios and the scan time of the scans are listed in Table (6.1).

Seven scans were retrospectively gated. Before the seven scans a 2D TOF scan of 28 slices was prescribed as a localizer. This TOF scan (scan #1) took about 2 minutes.

scan	sequence	number of dimensions undersampled	sampling ratio	scan time (min)
#1	2D TOF			2
#2	3D PC		100%	37
#3	3D PC	2	33%	12
#4	3D PC	3	33%	12
#5	3D PC	2	25%	9
#6	3D PC	3	25%	9
#7	3D PC	2	17%	6
#8	3D PC	3	17%	6

Table 6.1: The scanning protocol

For the gated scans, from scan #2 to #8, the sampling patterns in two dimensions used for individual slice encoding steps are shown in Figure (6.1). In total, six different sampling patterns in two dimensions were used as elements to build the seven sampling patterns in three dimensions for the seven scans. The sampling ratios of the sampling patterns in two dimensions were 100%, 50%, 33%, 25%, 17% and 13%. For the fully sampled scan (scan #2) and the three scans undersampled in only two dimensions of k-t space (scan #3, #5 and #7), all the slice encoding steps of each scan used the same sampling pattern. The overall sampling ratios of these scans (scan #2, #3, #5 and #7) equalled the sampling ratios of the sampling patterns in two dimensions. The other three scans (scan #4, #6 and #8) undersampled the k-t space in three dimensions by changing sampling patterns for different slice encoding steps. For example, the overall sampling ratio of scan #4 was 33%. The central four slice encoding steps (7th to 10th) used the sampling pattern with a sampling ratio of 50%. For the four steps (5th, 6th, 11th and 12th) next to the central steps the sampling ratios were all 33%. For the other eight steps (1st to 4th and 13th to 16th), the sampling ratios of the applied sampling patterns in two dimensions were all 25%. The total number of samples collected in scan #4 equalled the number of samples collected in scan #3, but in scan #4 more samples were collected at the positions close to the centre of k-space than in scan #3. The distributions of samples along the two phase encoding dimensions for the three scans (scan #4, #6 and #8) are displayed in Figure (6.2). The sampling ratio of scan #6 was 25% and the ratio of scan #8 was 17%.

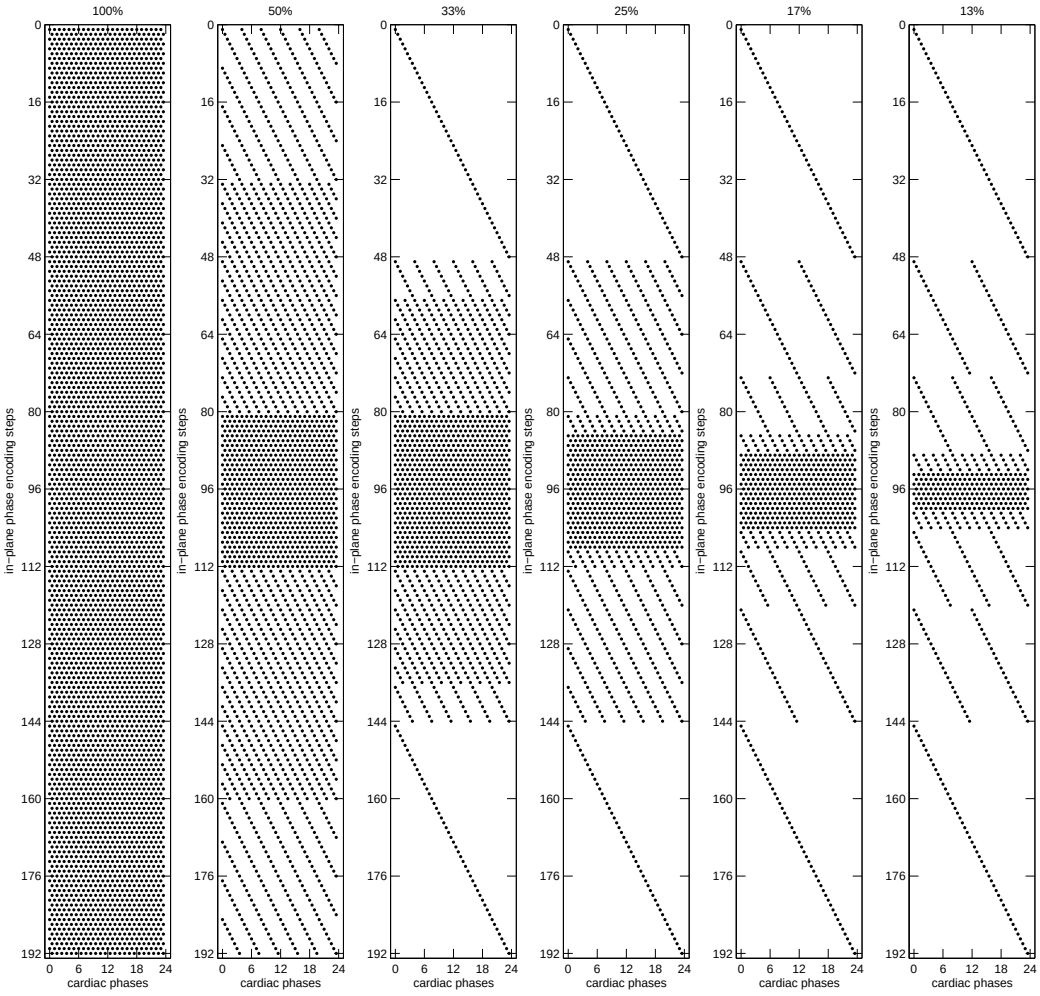

Figure 6.1: The sampling patterns in two dimensions used for individual slice encoding steps. Each black dot in the sampling patterns represents a k-space line.

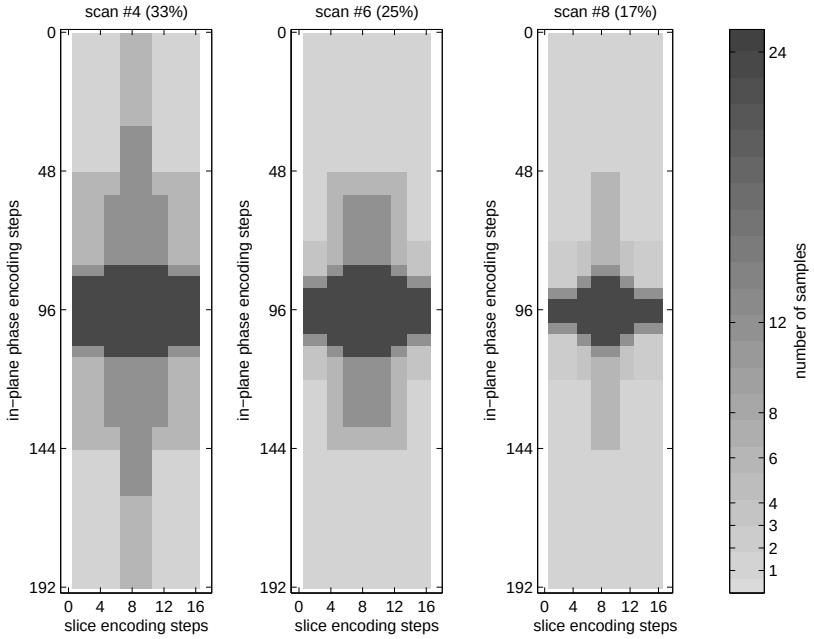

Figure 6.2: The distributions of samples along the two phase encoding dimensions for the three scans undersampled in three dimensions of k-t space.

6.2.3 Other scan parameters

The scanned subject was a male healthy volunteer. The study was approved by a local ethics committee, and informed consent was obtained from the volunteer. The subject lay supine throughout the scans. Frequency encoding was in the anterior/posterior direction. A 4-element phased-array carotid surface coil was used for signal reception. All the channels of the coil were used in the scan.

For the 2D TOF scan, the FOV was 12 cm and the in-plane resolution was 192×192. Although the FOV and the in-plane resolution of this scan were the same as those of other scans, the left/right and anterior/posterior position of the FOV was different from other scans. 28 slices were scanned and the slice thickness was 2 mm. Spacing between slices was also set to 2 mm so the 28 slices covered 56 mm along the superior/inferior direction. The T_E was 4.2 ms, the T_R was 21 ms, and the Flip Angle was 50°.

For the fully sampled and undersampled 3D PC scans, the FOV was 12 cm and voxel size was $0.625 \times 0.625\ mm^2$. 12 slices were prescribed and the slice thickness was 3.0 mm. In the acquisition, 16 slice encoding steps were executed during each

scan and images of 16 slices could be reconstructed from the signal. The images of the outmost four slices, two on each side, had to be discarded because the slice excitation profile was different from the ideal rectangular window function near the edge of the slab, and each of these four images had signal contributions from multiple slices due to phase wrap in slice direction. This was also one of the reasons the slice thickness was not set to the allowed minimum. The closer to the edge of the slab a slice was, the more likely the imperfect slice encoding profile would affect it. Another reason for using thick slices was to increase the scan range along the superior/inferior direction so both CCA and ICA could be covered by several slices. The scan matrix was $192 \times 192 \times 16$ in the spatial dimensions and 24 in the temporal dimension. At the full temporal resolution 24 samples were collected from each k-space position and 24 time frames could be reconstructed for each slice in each scan. The average heart rate of the volunteer was around 56 beat/min. Flow encoding was only applied in the superior/inferior direction so in each scan for each slice the reconstruction results consisted of 24 time frames with flow encoding and 24 time frames without flow encoding. The V_{ENC} was 100cm/s, the T_R was set to the minimum value of 15 ms, the T_E was 4.7 ms under the setting of the T_R, the acquisition bandwidth was 15.63 kHz, and the Flip Angle was 30°. In the 3D PC sequence raw signals were set to be saved to files directly without any post-processing to allow offline reconstruction.

6.2.4 Reconstruction

For the 2D TOF scan the image reconstruction was completed immediately after the scan with the standard software installed on the scanner. The images of the 28 slices were saved to files in DICOM format.

For the seven gated scans, the timing of each sample was reconstructed from the gating records. The k-space position of each sample was determined according to the sampling patterns. Gridding was applied to the raw signals at each k-space position separately to get the signals in k-t space for 24 phases of the cardiac cycle. The output from the gridding operations had six dimensions, including the three spatial dimensions, the temporal dimension, the flow encoding dimension and the coil dimension. 3D inverse Fourier transform was applied to the three spatial dimensions to convert the signals into images.

6.2.5 Methods for comparisons between scans

The results were compared in the same way as in Chapter 5. The comparisons were carried out for each of the two selected slices separately. The intensity and velocity differences were also averaged over all slices and compared with those from single slices.

6.2.6 Displacement correction

The positions of the ROIs were slightly adjusted for each undersampled scan separately before the calculation of the intensity or velocity differences. The 3D scans were about ten times longer than 2D scans. Small movements of the subject during the scans were more likely to happen than in 2D scans. These movements could result in small displacements of the FOV of a scan. If the displacements were not corrected the voxel-wise differences would be differences between measurements from different locations, which would not be ideal for the comparisons.

Since the subject movements were small, the problem was simplified by assuming the possible displacements were only in the left/right and the anterior/posterior directions. The same corrections were applied to all the slices. It was also assumed the displacements only happened between scans so the FOV of each scan only needed to be corrected once.

The corrections for each scan included following steps. From the fully sampled scan, the intensity images of all the time frames of a slice without flow encoding were averaged to generate a high SNR image. Two ROIs were selected where the coils had high sensitivities. The ROIs included both high signal area and empty background so there was a high contrast edge line in each ROI. The two edge lines of the two ROIs were in different directions. The edge lines could be easily extracted from the images by setting a threshold in intensity. An example of the positions of the ROIs and the edge lines is shown in Figure (6.3). These ROIs were also used as the static ROI in the comparisons between scans. The positions of the ROIs were copied to the images from the undersampled scan and edge lines were also extracted from those images. By comparing the two sets of edge lines it was possible to determine how the FOV of the undersampled scan had moved relative to FOV of the fully sampled scan. Figure (6.3) shows examples of such edge line comparisons.

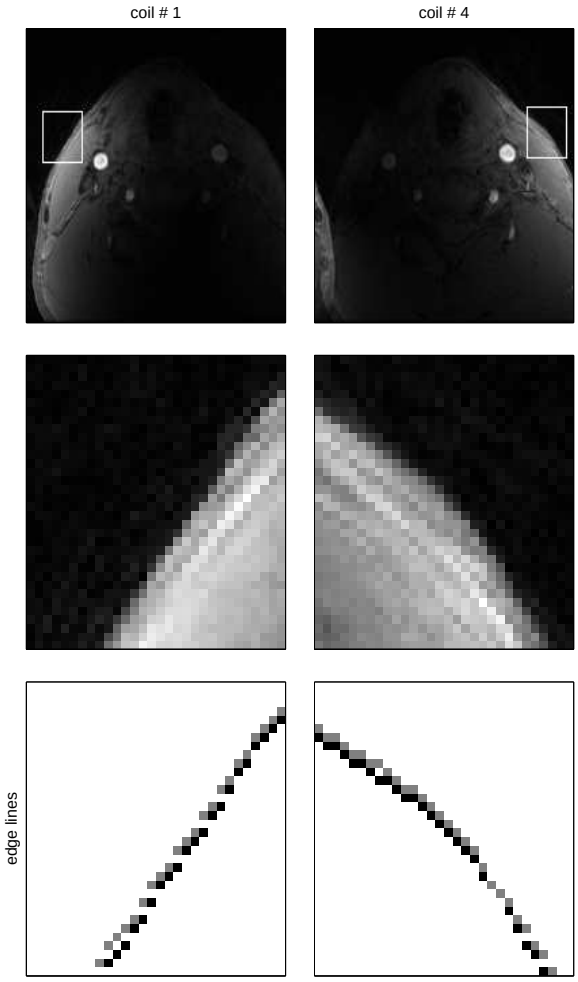

Figure 6.3: An example of the positions of the ROIs and the edge lines used for displacement correction. In the graphs in the bottom row, the black dots show the positions of the edge lines from the fully sampled scan and the grey dots show the positions of the edge lines from the undersampled scan. The ROI in the image from coil #4 was also used as the static ROI for the comparisons between scans.

6.2.7 Segmentation

The segmentation was carried out in the same way as in Chapter 5.

6.3 Results

6.3.1 Slice positions

Figure (6.4) shows the positions of the twelve slices prescribed for the seven gated scans. The 3D structure of the arteries was obtained from the 28 images collected in the 2D TOF scan. Most comparisons will focus on one slice below the bifurcations and one slice above the bifurcations. The two slices were referred to as the slice BB and the slice AB.

6.3.2 Coil selection

Figure (6.5) shows images of the slice BB and the slice AB from all coils. The images were the temporal averages of the images without flow encoding from the fully sampled scan. Coil #4 was selected for the comparisons between scans. It had high sensitivity coverage of the left carotid arteries. The left carotid arteries also appeared slightly wider in the images than the arteries on the right side.

6.3.3 Displacement correction

Table (6.2) lists the adjustments of the positions of the ROIs for all the undersampled scans in order to correct subject movement between scans. All the detected displacements were small, not more than one voxel in both directions.

Figure (6.6) shows the intensity difference images before and after displacement corrections for all the undersampled scans (scan #3 to scan #8). The images were obtained by calculating the absolute values of the intensity differences between the images from the fully sampled scan and the images from the undersampled scan. The original images from the fully sampled scan are also displayed. All the images correspond to the peak flow time.

Overall the effects of correction were more obvious in the images from scan #3, #4 and #5. After correction there were still apparent intensity differences at the positions

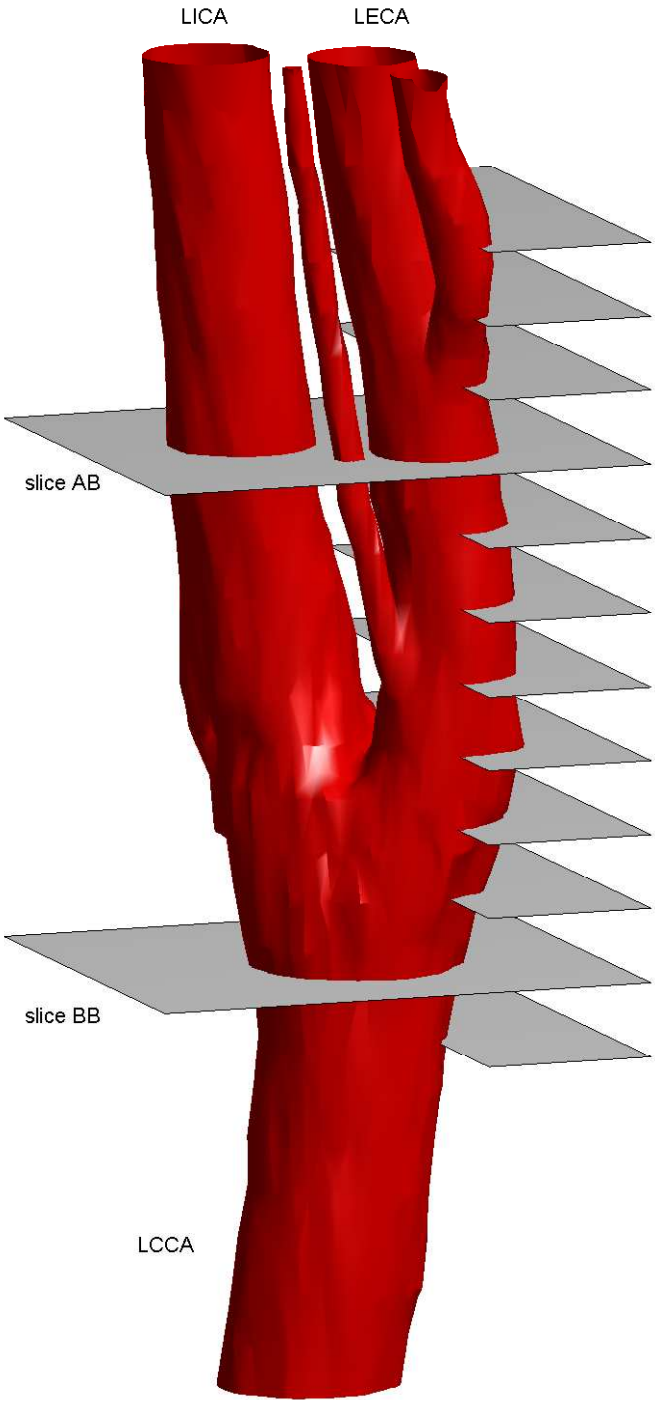

Figure 6.4: The positions of the twelve slices prescribed for the seven gated scans shown with the left carotid ateries rendered from the TOF iamges. The slice BB and the slice AB are highlighted.

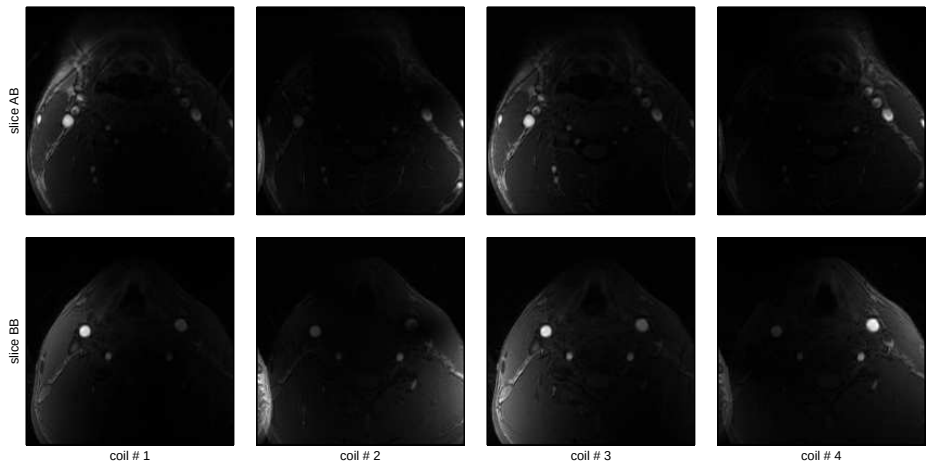

Figure 6.5: The images of the slice BB and the slice AB from all coils. The images were the temporal averages of the images without flow encoding from the fully sampled scan.

scan	adjustments (voxel)	
	posterior	right
#3	1	
#4	1	1
#5		1
#6		1
#7		1
#8		1

Table 6.2: The adjustments made to the positions of the ROIs for all the undersampled scans for displacement correction

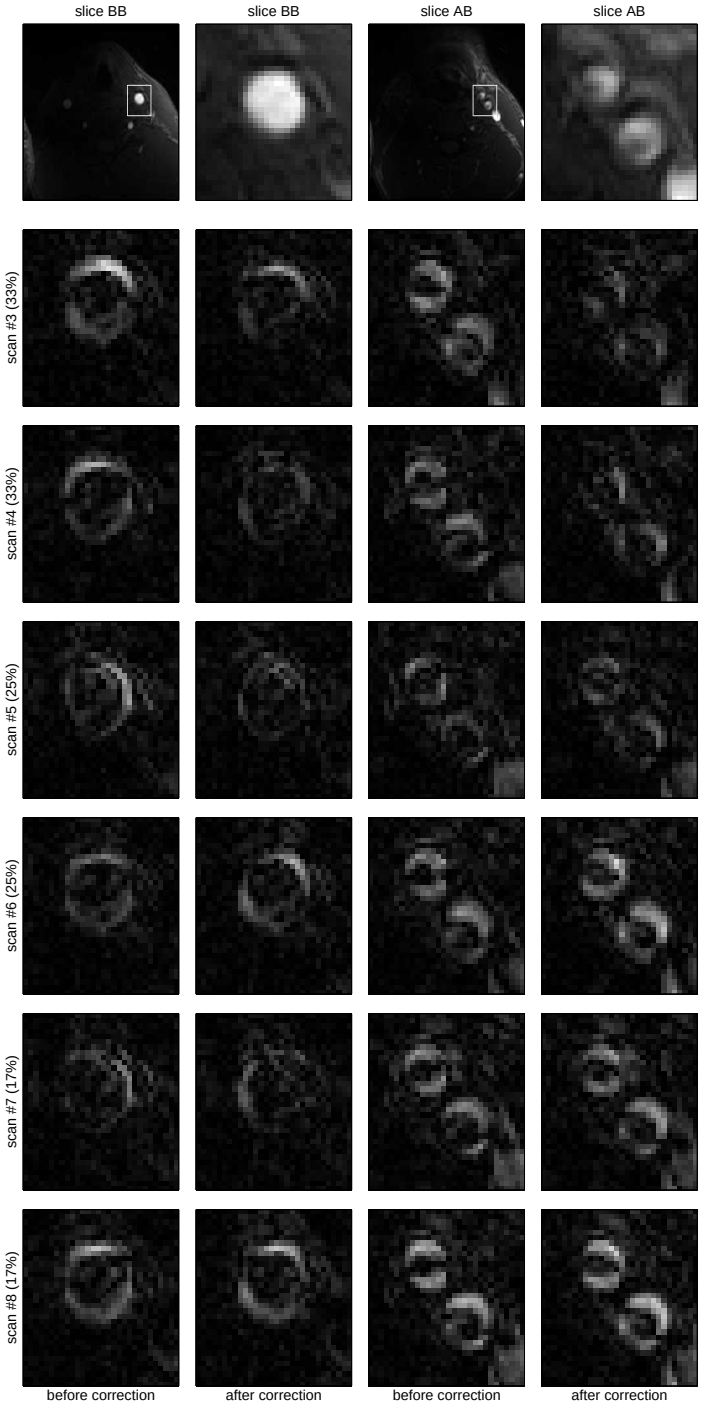

Figure 6.6: The intensity difference images before and after the displacement corrections for all the undersampled scans.

near the vessel walls in the images from scan #6, #7 and #8. It can be expected the intensity differences from the later three scans may be larger than those from the first three undersampled scans.

6.3.4 Intensity differences in different regions

Figure (6.7) shows the intensity differences in different ROIs in the slice BB. Figure (6.8) and Figure (6.9) show the same type of results from the slice AB and results averaged over all slices.

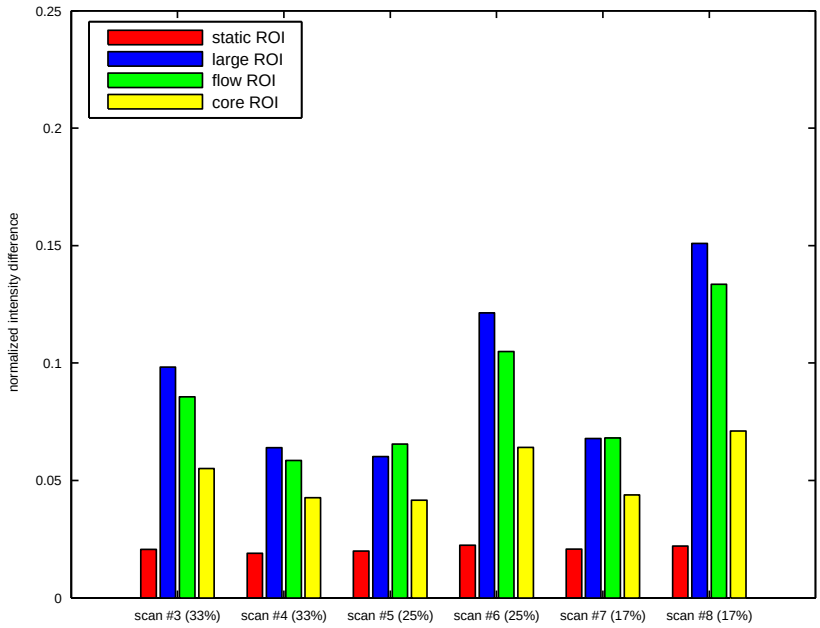

Figure 6.7: The normalized intensity differences in different ROIs in the slice BB.

In the static ROI, the values of D_i from all scans were close to each other, around 2%. This suggests after displacement correction the intensity differences at the positions without dynamic signal content were at the same level for all the scans.

In the slice BB, at the sampling ratio of 33%, the values of D_i from scan #3 were larger than those from scan #4. At other sampling ratios, the values of D_i in the large and flow ROIs from scan #6 and #8 were about 5-8% larger than those from scan #5 and #7. The results from the slice AB and all the slices showed a similar trend but the differences between different undersampled scans were smaller than those in the slice

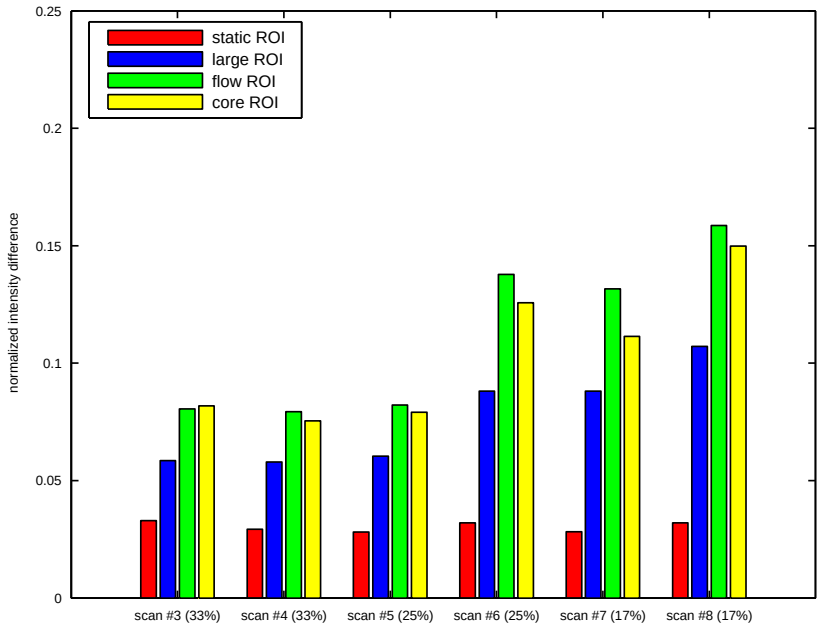

Figure 6.8: The normalized intensity differences in different ROIs in the slice AB.

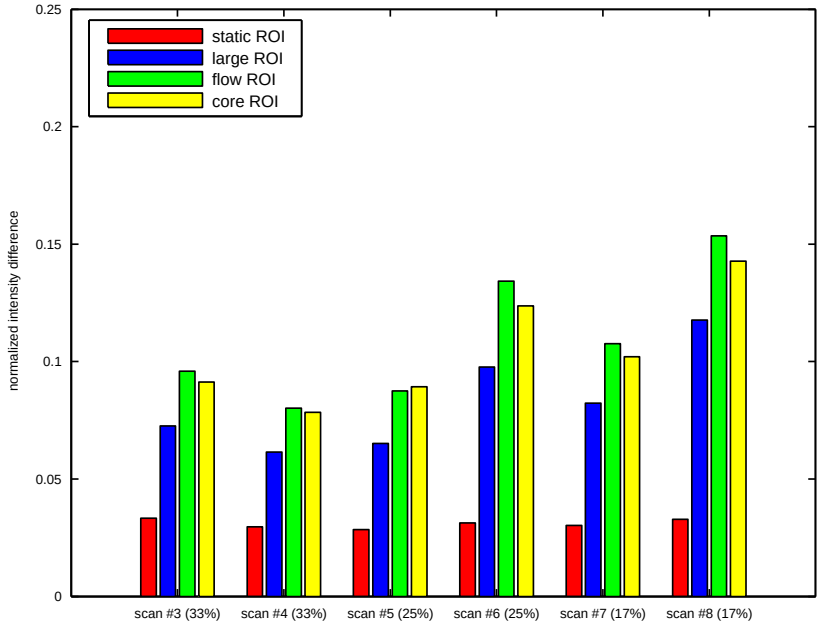

Figure 6.9: The normalized intensity differences in different ROIs averaged over all slices.

BB. This suggests the scans undersampled in three dimensions of k-t space gave better intensity results than the scans undersampled in two dimensions at high sampling ratio but the latter showed better performance at low sampling ratios.

For most scans the values of D_i from the large ROI and the flow ROI were larger than those from the core ROI in the slice BB. In the slice AB and averaged across all the slices, the values of D_i from the large ROI were smaller than those from the flow ROI and the core ROI. This suggests in the slice BB the voxels near the artery walls contribute more intensity differences than the voxels in the central area of the arteries, and in the slice AB or most slices, the intensity differences were larger inside than outside.

6.3.5 Intensity differences in different periods

Figure (6.10) shows the intensity differences over different periods of the cardiac cycle in the slice BB. Figure (6.11) and Figure (6.12) show the same type of results from the slice AB and results averaged over all slices.

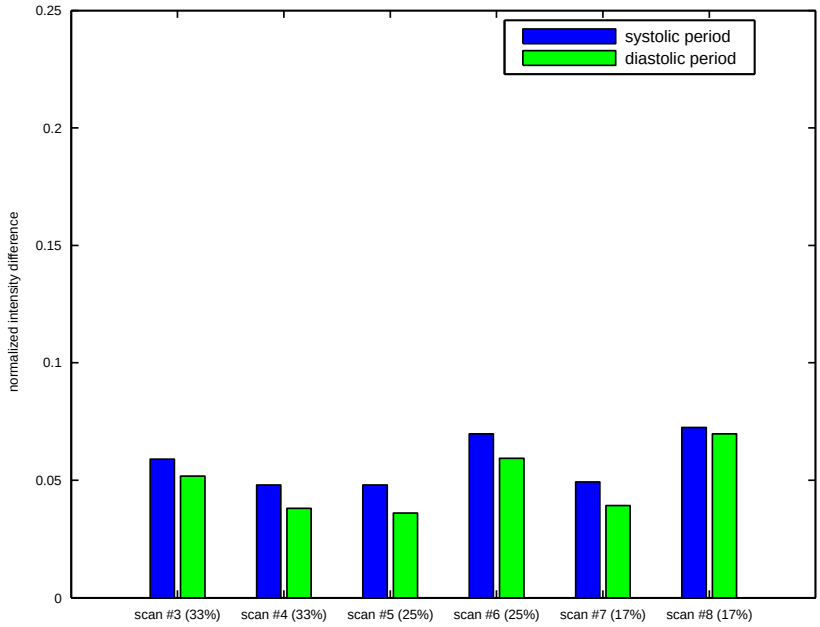

Figure 6.10: The normalized intensity differences over different periods of the cardiac cycle in the slice BB.

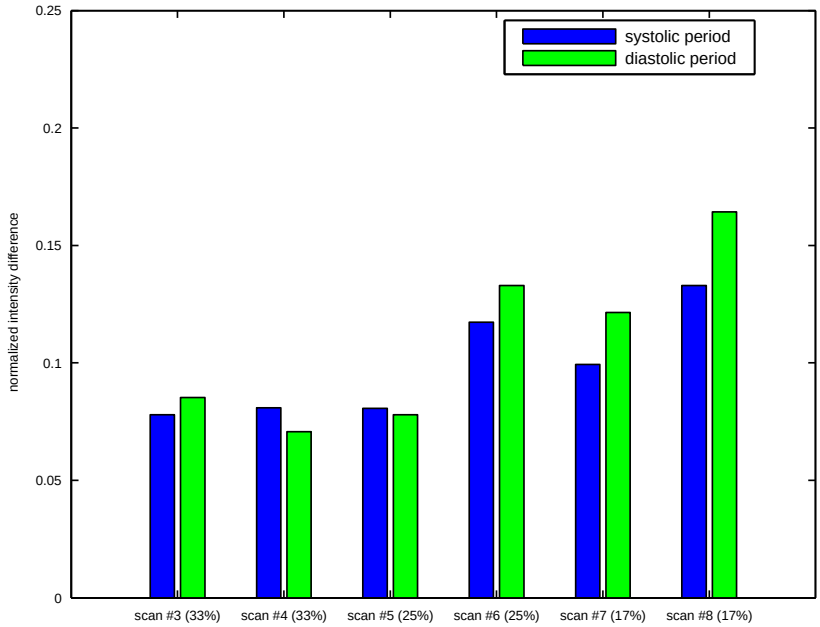

Figure 6.11: The normalized intensity differences over different periods of the cardiac cycle in the slice AB.

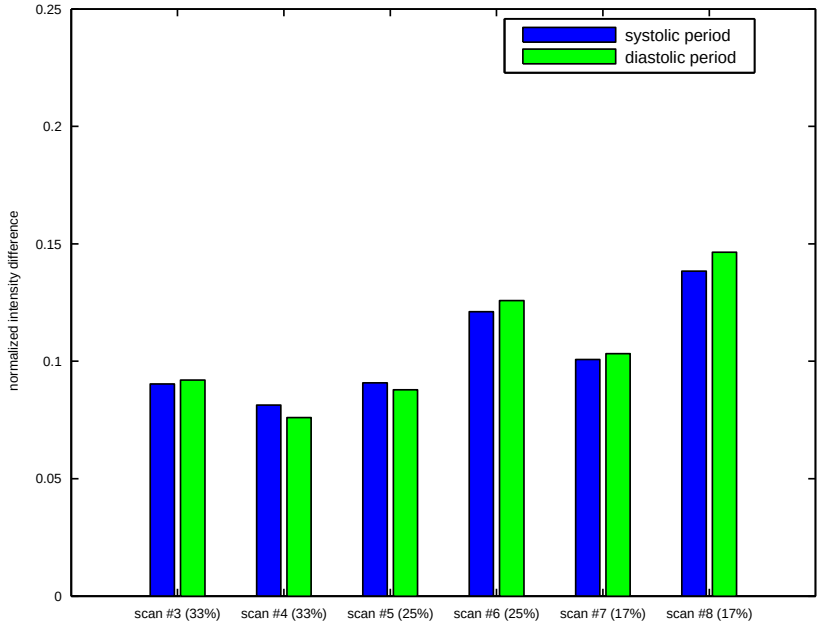

Figure 6.12: The normalized intensity differences over different periods of the cardiac cycle averaged over all slices.

In the slice BB results for each scan the values of D_i from the systolic period were larger than those from the diastolic period. In the results of the slice AB and the results averaged over all slices, for the same scan the values of D_i over the two periods were close to each other. When the intensity differences were large, such as in the results from scan #7, #8 and #9 in the slice AB, the values of D_i from the systolic period were smaller than those from the diastolic period. This suggests for most slices when the intensity differences were not large the values of D_i from the systolic period were slightly larger than or close to those from the diastolic period.

6.3.6 Velocity differences in different regions

Figure (6.13) shows the velocity differences in the flow ROI and the core ROI in the slice BB. Figure (6.14) and Figure (6.15) show the same type of results from the slice AB and results averaged over all slices.

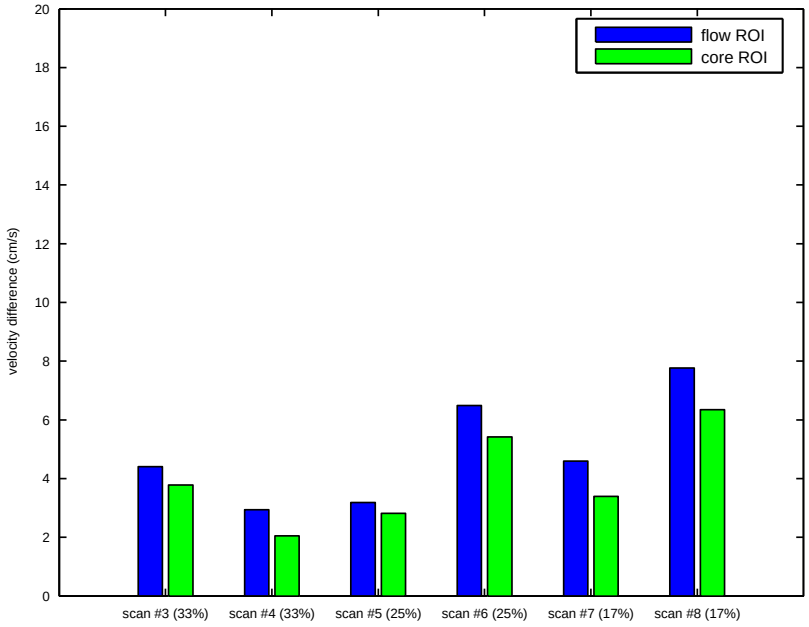

Figure 6.13: The velocity differences in the flow ROI and the core ROI in the slice BB.

In the results of the two slices and the results averaged over all slices, scan #4 gave larger values of D_v than those from scan #3. Scan #5 and #7 produced smaller velocity differences than Scan #6 and #8. This suggests the scans undersampled in

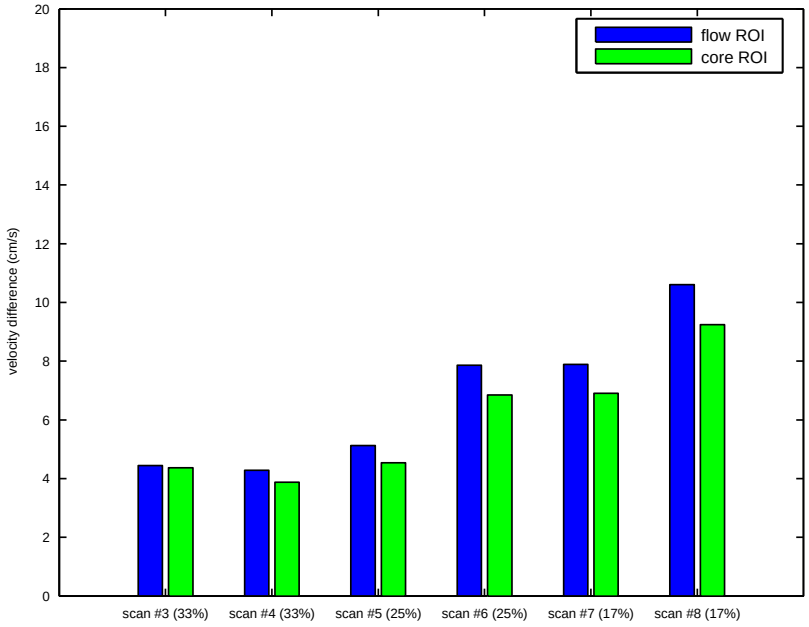

Figure 6.14: The velocity differences in the flow ROI and the core ROI in the slice AB.

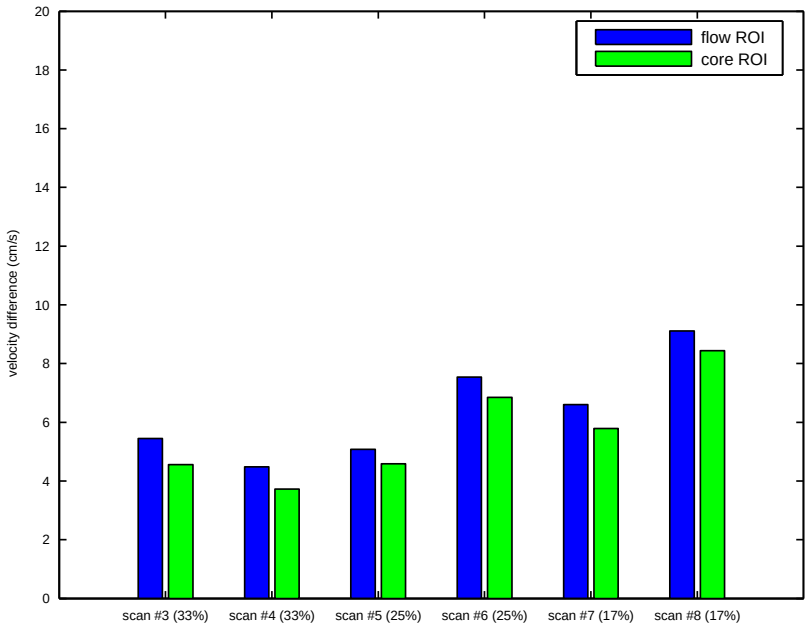

Figure 6.15: The velocity differences in the flow ROI and the core ROI averaged over all slices.

three dimensions of k-t space gave better velocity results than the scans undersampled in two dimensions at high sampling ratio but the latter showed better performance at low sampling ratios.

From scan #3, #4 and #5, the values of D_v in the core ROI were at the level of 4 cm/s. The other scans produced values of D_v close to 7 cm/s. This suggests the velocity measurements from scan #6, #7 and #8 might have large errors.

From scan #3, #4 and #5, the values of D_v in the core ROI were at the level of 4 cm/s. The other scans produced values of D_v close to 7 cm/s. These are averaged results. For individual voxels, velocity differences from scan #6, #7 and #8 might be larger. This suggests at some positions in the lumen the velocity errors obtained from scan #6, #7 and #8 might be larger than 7 cm/s.

For all the scans the values of D_v from the flow ROI were larger than those from the core ROI. This suggests velocity measurements were less accurate near the artery walls.

The values of D_v from the slice BB were smaller than or close to those from the slice AB or the results averaged over all slices. This suggests velocity measurements were more accurate in the slice BB or in the CCA than in most slices.

6.3.7 Velocity differences in different periods

Figure (6.16) shows the velocity differences over different periods of the cardiac cycle in the slice BB. Figure (6.17) and Figure (6.18) show the same type of results from the slice AB and results averaged over all slices.

In the results from both slices and those averaged over all slices, the values of D_v were about 1-3 cm/s larger in the systolic period than in the diastolic period. This suggests the undersampled velocity measurements were less accurate when the blood flow was more dynamic.

6.3.8 Velocity waveforms of single voxels

Figure (6.19) shows the velocity waveforms of a selected voxel from the fully sampled scan and all the undersampled scans. Figure (6.20), Figure (6.21) and Figure (6.22) show the same type of results of other selected voxels.

Overall for the same voxel the differences between the waveforms increased as the

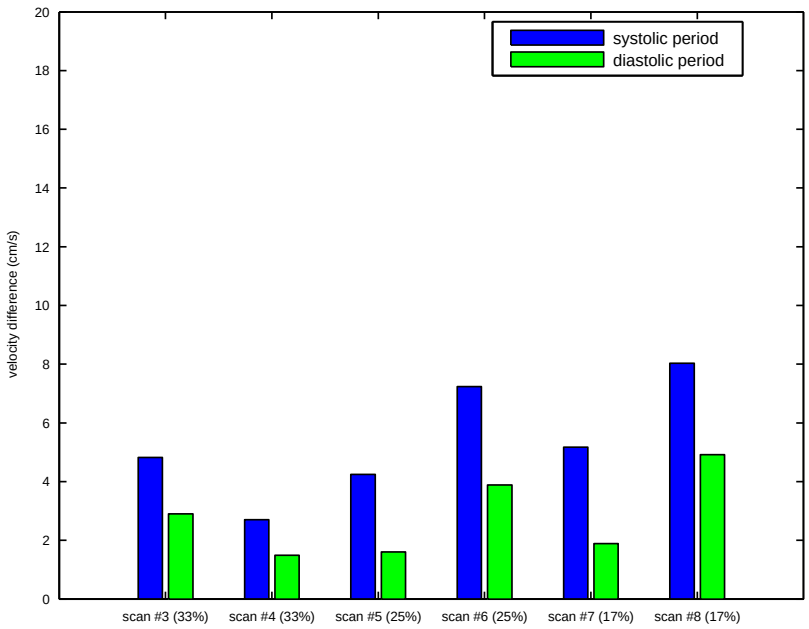

Figure 6.16: The velocity differences over different periods of the cardiac cycle in the slice BB.

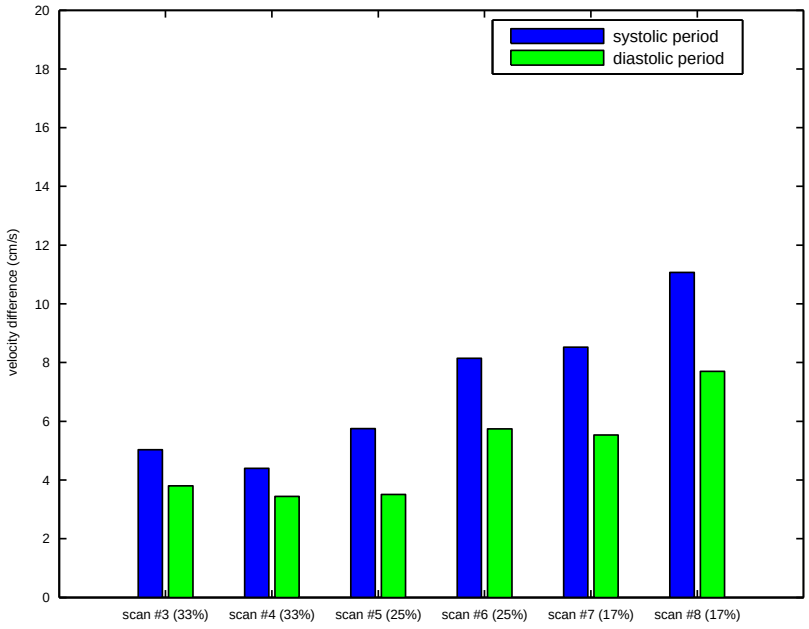

Figure 6.17: The velocity differences over different periods of the cardiac cycle in the slice AB.

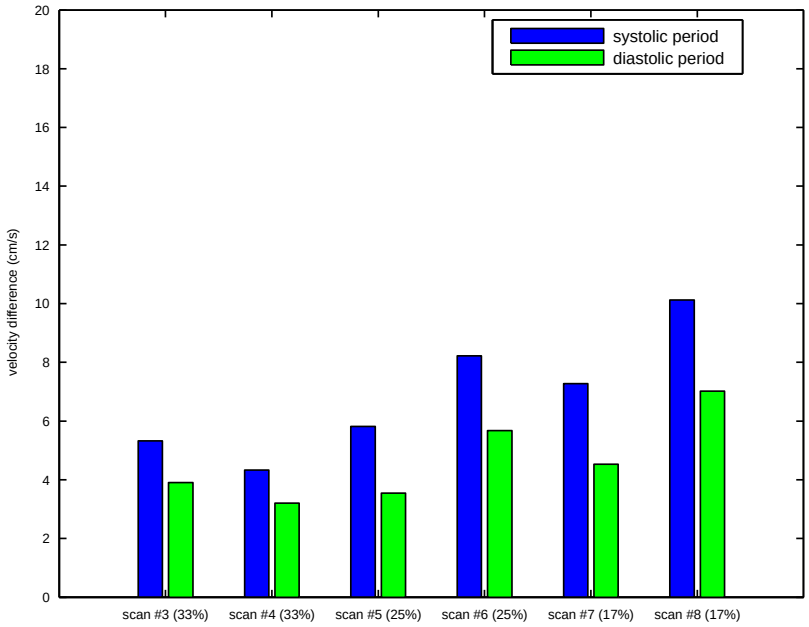

Figure 6.18: The velocity differences over different periods of the cardiac cycle averaged over all slices.

distance between the voxel and the centre of the artery increased. For voxel #3 and #4, the velocity differences between the waveforms from the scans at low sampling ratios could be larger than 10 cm/s in most cardiac phases. This suggests the sampling ratio might be too low for this subject at this resolution.

For most voxels the waveforms from scan #4 were closer than those from scan #3 to the waveforms from the fully sampled scan. The waveforms from scan #5 and #6 were close to each other for all the voxels. For most voxels the waveforms from scan #7 were smoother than those from scan #8. This suggests at the same sampling ratio the scans undersampled in three dimensions of k-t space gave better temporal resolution than those undersampling in two dimensions.

6.3.9 Flow rates of carotid arteries

Figure (6.23) shows the flow rates of the LCCA from the fully sampled scan and all the undersampled scans. Figure (6.24) and Figure (6.25) show the same type of results for the LICA and LECA. The flow ROI of the slice BB was used for the calculation of the results for the LCCA. The flow rates of the LICA and LECA were calculated in the

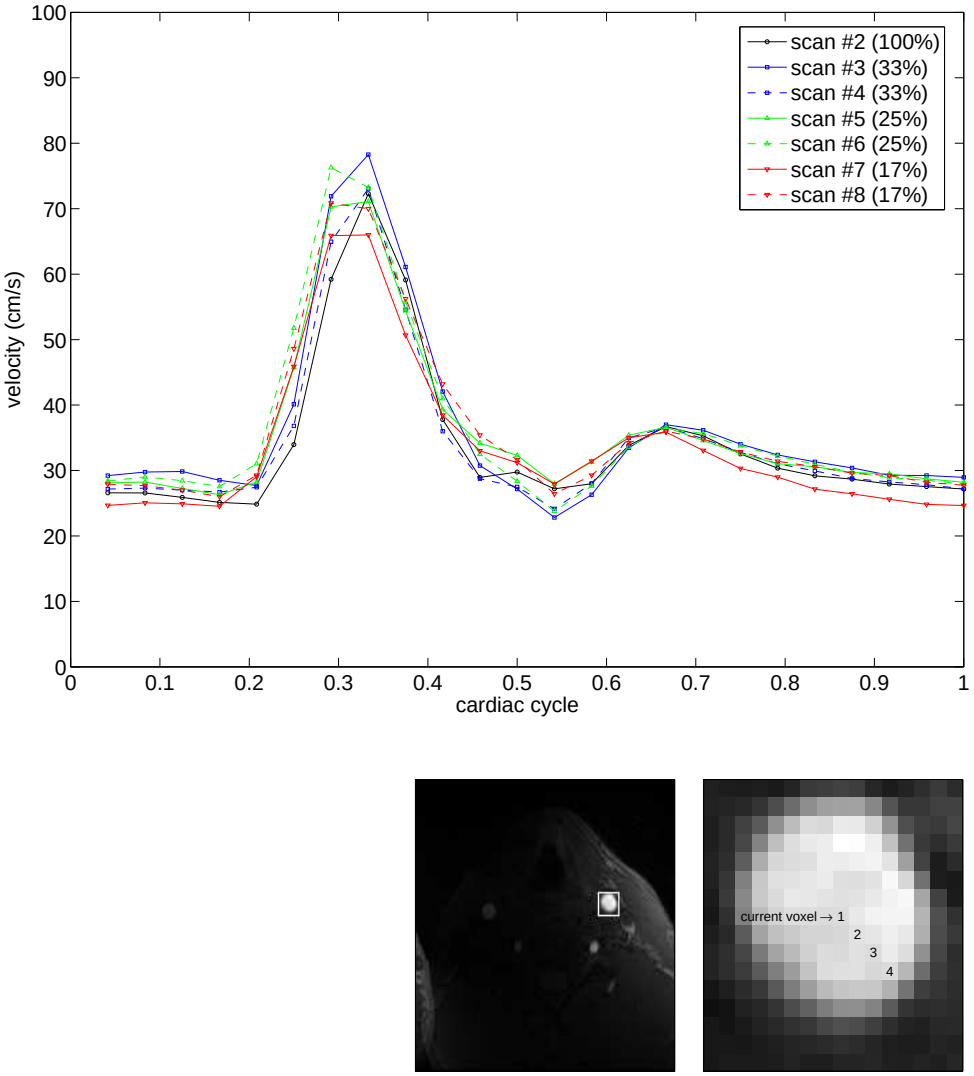

Figure 6.19: The velocity waveforms of a selected voxel from the fully sampled scan and all the undersampled scans. The position of the voxel is displayed in the bottom image.

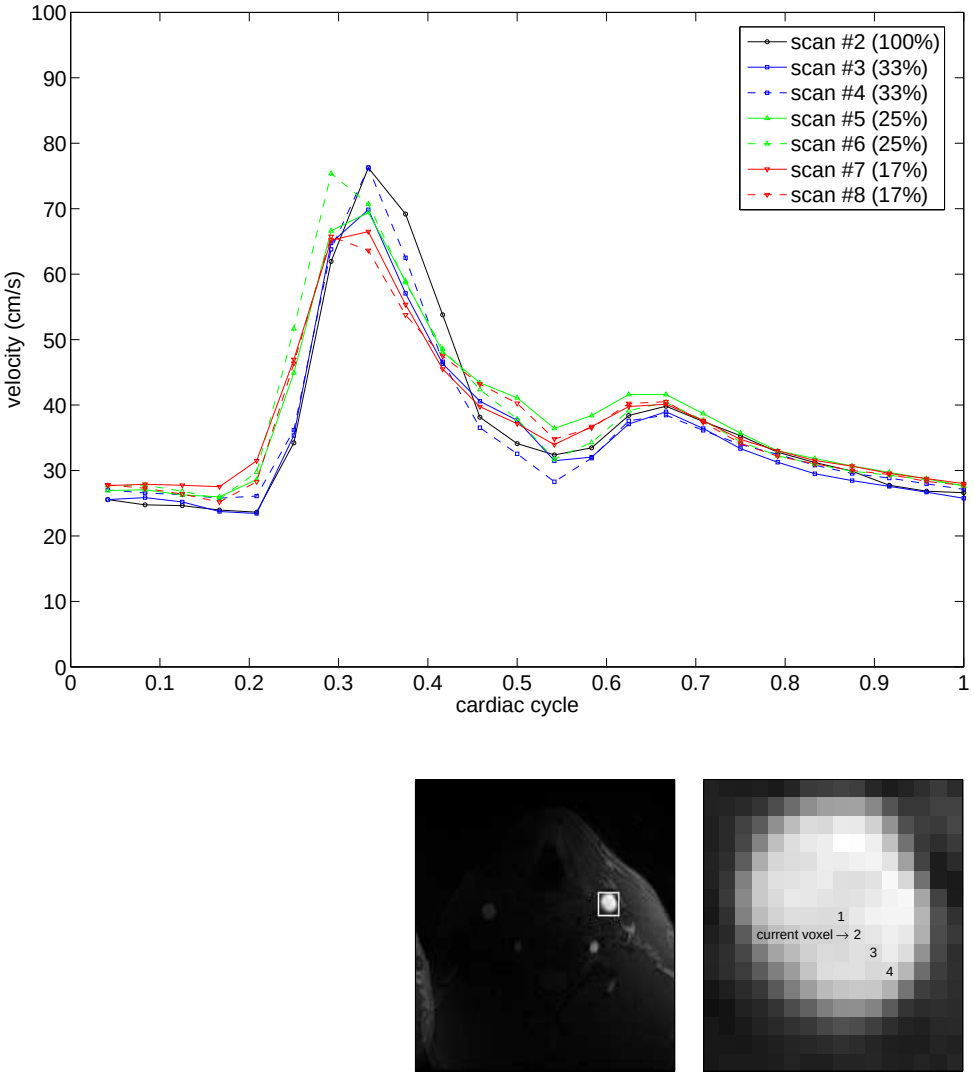

Figure 6.20: The velocity waveforms of a selected voxel from the fully sampled scan and all the undersampled scans. The position of the voxel is displayed in the bottom image.

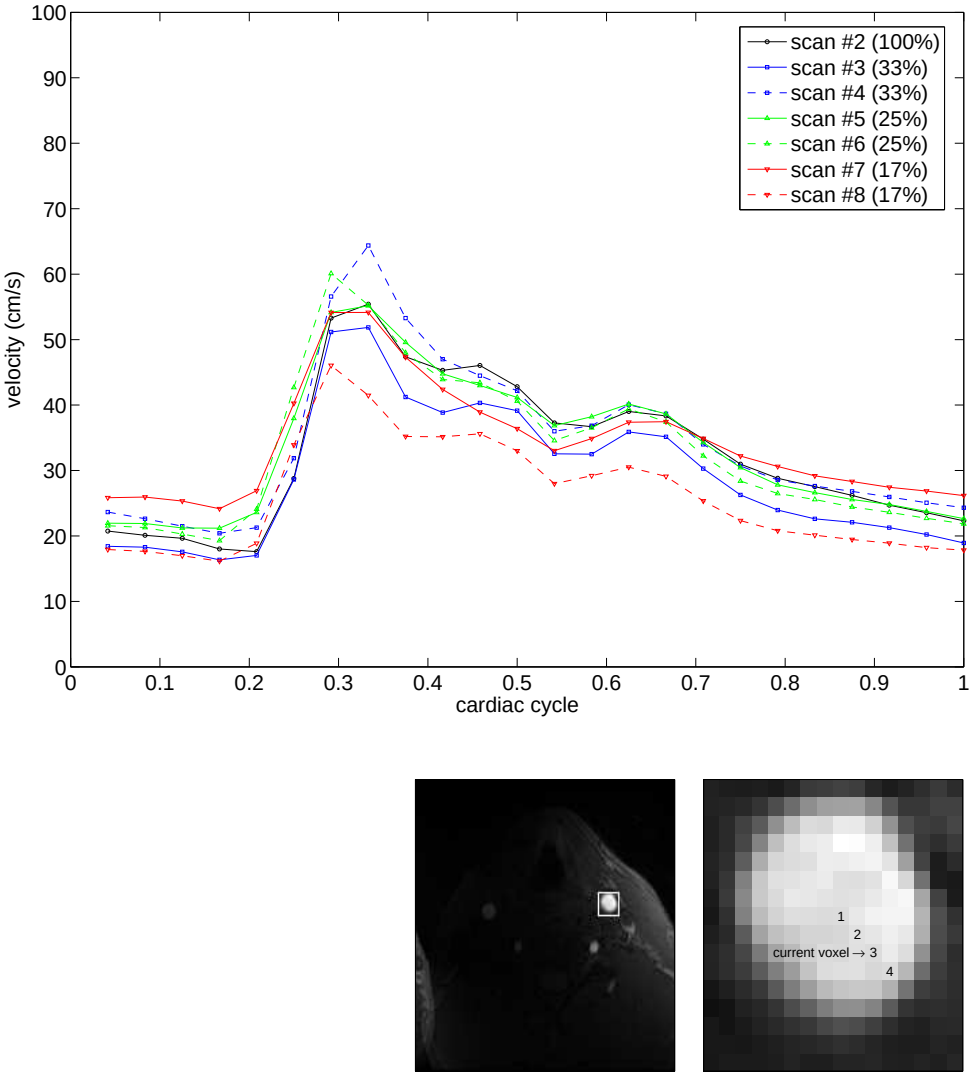

Figure 6.21: The velocity waveforms of a selected voxel from the fully sampled scan and all the undersampled scans. The position of the voxel is displayed in the bottom image.

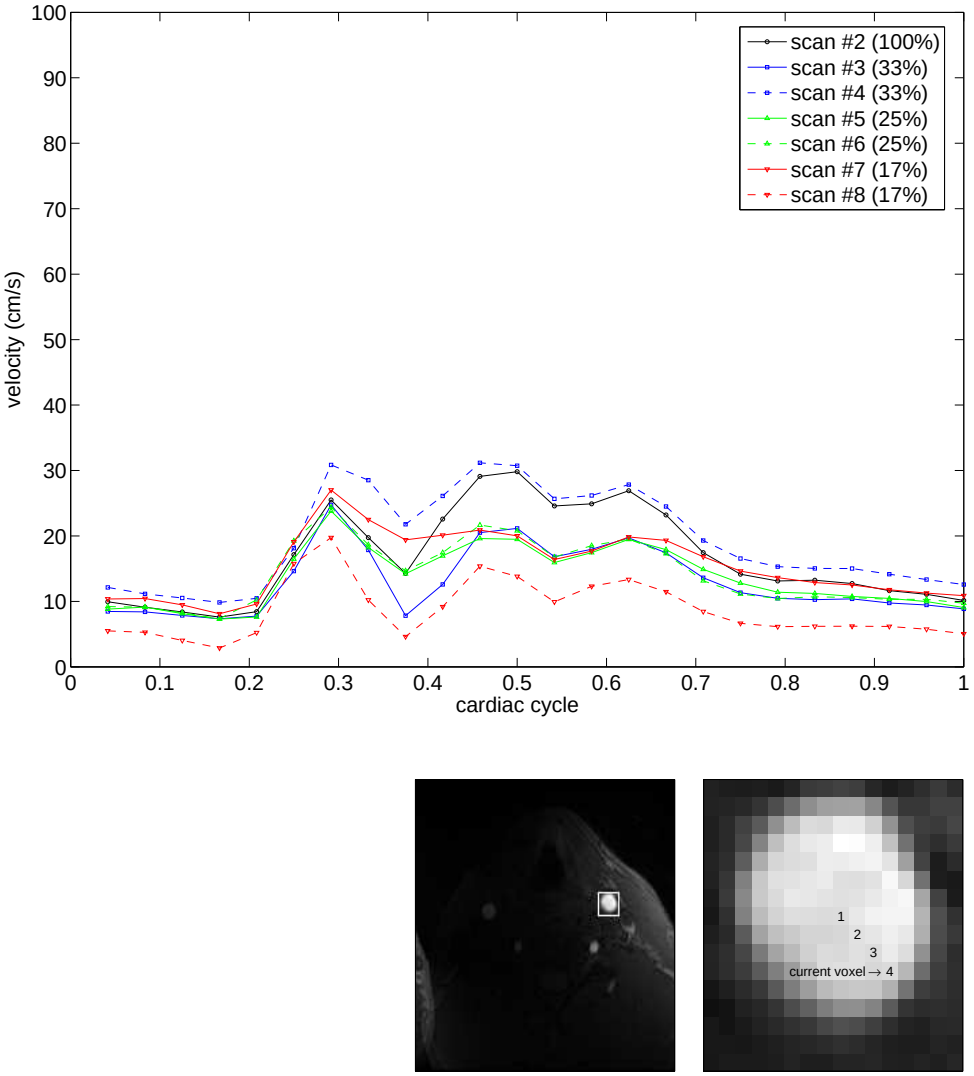

Figure 6.22: The velocity waveforms of a selected voxel from the fully sampled scan and all the undersampled scans. The position of the voxel is displayed in the bottom image.

flow ROI of the slice AB.

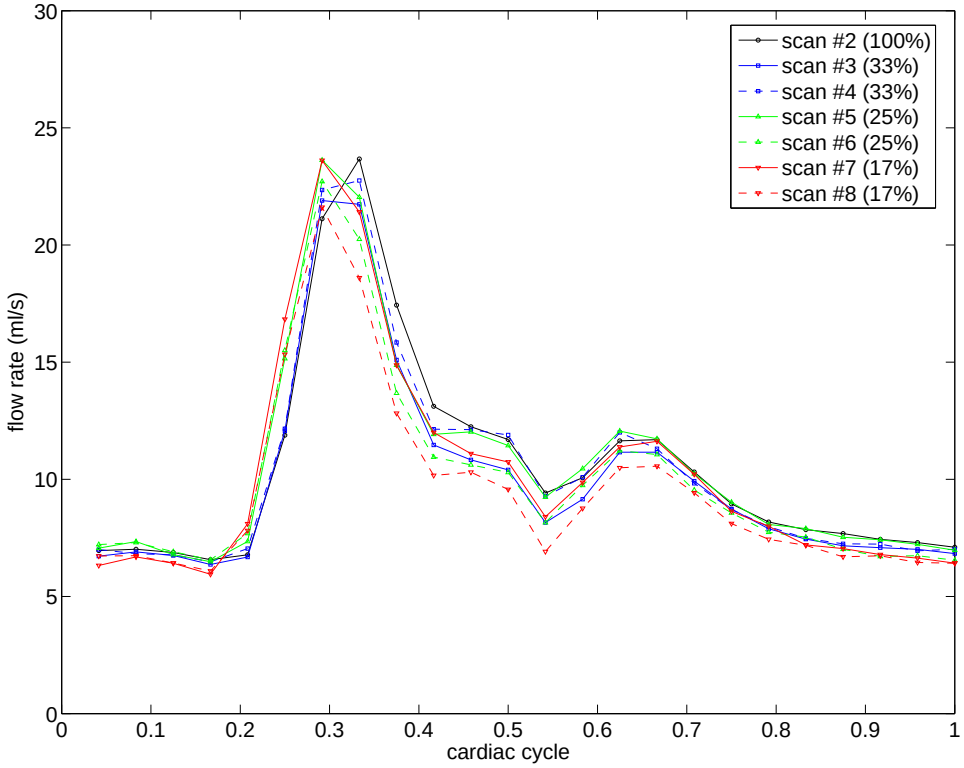

Figure 6.23: The flow rates of the LCCA from the fully sampled scan and all the undersampled scans.

For the LCCA, the flow rate waveform from scan #4 was slightly better than the results from other undersampled scans. The flow rate waveforms from other scans were close to from each other. For the LICA, all the undersampled scans produced underestimated flow rates. The underestimation of flow rate was more serious as the sampling ratio decreased. For the LECA, the flow rate waveforms from scan #3, #4, #5 and #6 were close to the waveform from the fully sampled scan. The flow rate waveforms from scan #7 and #8 were smoother than those from other scans but the differences were not large.

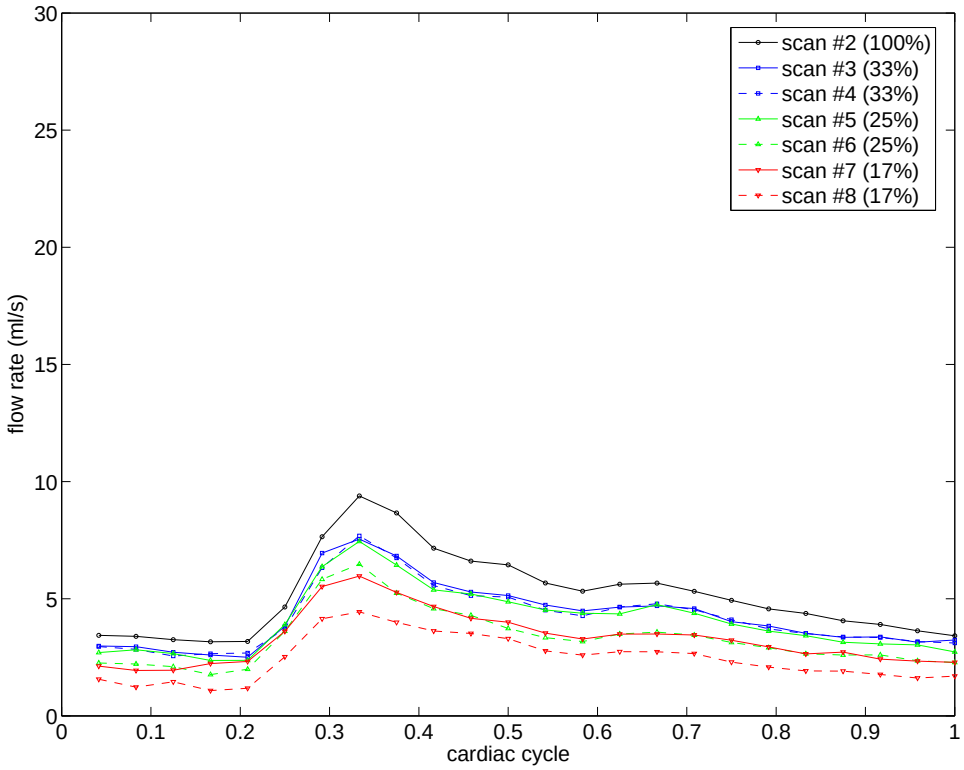

Figure 6.24: The flow rates of the LICA from the fully sampled scan and all the undersampled scans.

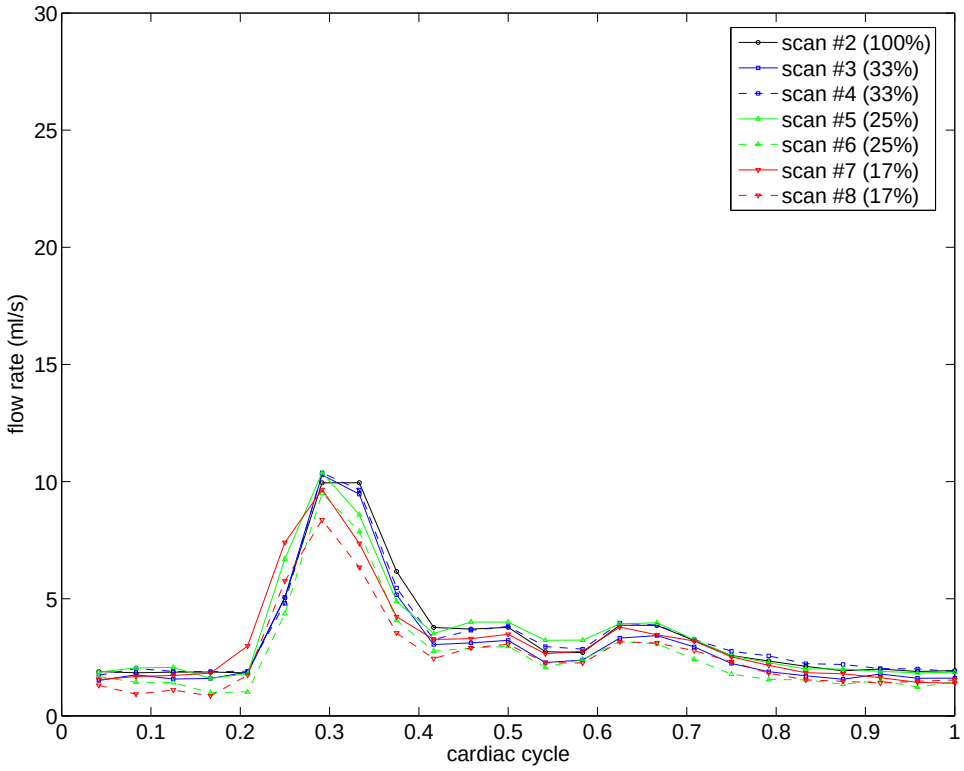

Figure 6.25: The flow rates of the LECA from the fully sampled scan and all the undersampled scans.

6.4 Discussion

Unlike in Chapter 4 and Chapter 5, the sampling patterns for 3D scans were not tested in simulations but directly tested *in vivo* in this chapter. One of the reasons is that, in 3D scans much longer than 2D scans, the differences between the timing of the *in vivo* undersampled acquisitions and that of the fully sampled scan, which could provide source data in simulated undersampling, might be much larger than the timing differences in 2D scans. This could make the simulation results substantially different from the *in vivo* results. If the simulation results are similar to the *in vivo* results, they will support the conclusions obtained from the *in vivo* results. If the simulation results are different, the *in vivo* results will still be regarded more realistic for the evaluation of the ktVD method. Another reason is that for the ktVD method it is not necessary to test a large number of different settings of the control parameters. In future work, 3D simulations can be used to test more designs of the sampling pattern.

The k-t BLAST method can also be used for undersampling in three dimensions in a similar way as in this chapter. For different slice encoding steps different sampling patterns can be used to change sampling density along the slice encoding dimension. Since in the comparisons of the undersampling results from the 2D scans the ktVD method showed better performance than the k-t BLAST method, and only a limited number of 3D scans were allowed in the *in vivo* scanning protocol due to long scan time, the k-t BLAST method was not tested *in vivo* in 3D scans. The reconstruction time of the k-t BLAST method is also a concern. In 3D scans the reconstruction for each slice encoding step is similar to that of a 2D scan. For example, if sixteen slices need to be reconstructed, the computation time will be sixteen times the time for a 2D scan of a single slice. It could take more than a day for the k-t BLAST method to reconstruct images for a single 3D scan.

In the displacement correction, since the displacements were small, it was assumed that the displacements were only in two directions, all slices had the same displacements as those in the slice BB, and displacements only happened between scans. This significantly simplified the displacement correction. The real situation might be different from these assumptions. There could be displacements in the superior/inferior direction, into/out of the slices; the subject might have angular movements during the test; the displacements could happen in the middle of a scan. As a result the effects of the displacement correction might be different for different slices and different scans.

In the slice BB the displacement correction should have the best effects. In those slices far away from the slice BB, such as the slice AB, it could be less accurate if the displacements were different in different slices. This might be one of the reasons why the intensity differences observed in the slice AB were larger than those in the slice BB for some scans. If there were angular movements, displacements in the superior/inferior direction, or displacements in the middle of a scan, they were not corrected. The uncorrected displacements could lead to differences between scans in the comparisons and make it difficult to assess the undersampling errors. To address this problem more comprehensive correction methods can be applied in future studies. The correction can be carried out for each slice separately. Sagittal or coronal images can be examined to correct displacements in the superior/inferior direction. For rotational movements, more than three edge lines in different directions can be extracted from each image to determine the position changes. Many post-processing methods for motion correction can also be used to correct displacements [237, 238, 239, 240, 241, 242, 243, 244, 245]. It would be the best if subject movements could be suppressed in the first place. For this reason the scanned subject in this study had been asked to keep static during the test and suppress swallowing during each scan. Due to long scan time it was very difficult for the subject to remain completely static throughout the test, so the displacement correction was still necessary. In this work the comparisons of the edge lines were carried out manually, because the edge lines only needed to be compared once for each scan and the total number of comparisons was small. If a large number of images need to be corrected separately, automated corrections will be necessary.

In addition to the displacements, scan-to-scan differences could also contribute to the differences observed in the comparisons between scans. In the slice AB, the undersampled scans later in the scanning protocol generally produced larger intensity and velocity differences than those earlier in the protocol. This might be caused by scan-to-scan differences, but the changes of the sampling ratio could also be a possible reason. In future work the order of the scans can be changed to compare these two contributing factors. The scans at low sampling ratios can be carried out early in the protocol, close to the fully sampled scan, and the scans at high ratios can be placed near the end of the test. If the pattern of the changes of the intensity and velocity differences with the sampling ratio does not change much, scan-to-scan differences may not be the major contributing factor of the differences.

It has been observed that larger intensity differences often led to larger velocity

differences. For example, in the slice BB, the intensity differences from scan #6 and scan #8 were larger than those from scan #5 and scan #7, and the velocity differences followed a similar pattern. This suggests intensity errors could be one of the contributing factors of velocity errors. The velocity results might be less accurate if the intensity differences were larger.

In summary, the velocity differences increased as the sampling ratio decreased. According to the results averaged over all slices, at the sampling ratio of 33%, the velocity differences were between 4 and 6 cm/s; at the sampling ratio of 25%, they were between 5 and 8 cm/s; at the sampling ratio of 17%, they were between 6 and 10 cm/s. The velocity differences were larger near the arterial wall and close to the peak flow moment. According to the comparisons of velocity waveforms of single voxels, for the voxels near the LCCA wall, the velocity differences between the waveforms obtained at the sampling ratio of 17% and those from the fully sampled scan were larger than 10 cm/s in most cardiac phases; for the voxels near the centre of the LCCA lumen, the velocity waveforms obtained at all sampling ratios were close to those from the fully sampled scan. According to the comparisons of flow rate waveforms, at the sampling ratio of 33% or 25%, the waveforms were close to those from the fully sampled scan; at the sampling ratio of 17%, the differences between the waveforms from the undersampled scans and those from the fully sampled scan were larger, especially in the LICA. If undersampling errors contributed to most of the differences observed in the comparisons, undersampling in an extra dimension of k-t space improved the accuracy of the measurements in both intensity and velocity at the sampling ratio of 33%, and it caused more errors at the sampling ratios of 25% and 17%. If most of the differences observed in the comparisons were caused by subject movements or scan-to-scan differences, they are not suited for the evaluation of undersampling performance.

Chapter 7

In vitro test of undersampling in three dimensions of k-t space

7.1 Introduction

In the last chapter it was difficult to evaluate the performance of the undersampling methods at low sampling ratios due to possible interference from small subject motions. The number of slices was also limited by total scan time so the degree of signal redundancy in the slice encoding dimension was relatively lower than in normal 3D scans. Flow encoding was only applied in one direction to save scan time and the complete velocity field could not be compared between scans. To address these problems present in the *in vivo* test, a carotid phantom with pulsatile flow was used to test the undersampling methods.

For comparisons and validations, the use of a phantom has advantages and disadvantages. The scans of the phantom can be longer than the scans of a volunteer. The phantom does not move during a long scan. The dynamic properties of the signal from the controlled phantom are more stable over a long period than that from a volunteer. On the other hand, the structure of the phantom is relatively simple. Its signal has much more spatial redundancy than the signal from a volunteer. The dynamic variations of the signal from the phantom are more regular than those *in vivo*. The coil loading and the magnetic field inhomogeneities in a phantom scan are different from those in a volunteer scan so the noise level and the signal quality can be different. These differences mean the results from phantom tests are not guaranteed to be observed in the *in vivo*

scans.

In this chapter a flow phantom is used to test undersampling methods for high resolution 3D scans and velocity measurements in three directions. Results from the scans undersampled in three dimensions are compared with those from a fully sampled scan in the same way as in the *in vivo* tests. Velocity patterns are also compared.

7.2 Methods

7.2.1 The carotid phantom

Figure (7.1) shows the phantom (Shelley Medical Imaging Technologies, London, Ontario, Canada). The tubes inside the phantom were shaped similar to a realistic carotid bifurcation. In the carotid bulb region the phantom had an axisymmetric 30% diameter (50% area) stenosis. The fluid (Shelley) flowing through the phantom during the scans was a green liquid mimicking the fluid dynamic properties of real blood. The T1/T2 of the mimicking fluid was 1300/185 ms at 1.5 Tesla, the density of the fluid was 1030 kg/m^3, and the viscosity of the fluid was 0.0041 $Pa \cdot s$. The inlet and outlets of the phantom were connected to an MRI-compatible flow pump (Shelley) to form a closed loop. The pump driving the flow could be programmed to produce different types of input flow waveforms to the phantom, such as constant flow or pusatile carotid flow. The driving flow waveform (provided with the pump) used in the tests is displayed in Figure (7.2). At the start of each cycle of the waveform the pump could send out a TTL pulse through its TTL port. These pulses could be recorded for gating purposes. This setup was similar to an *in vivo* scan. The phantom took the place of the carotid arteries of a volunteer. The flow inside the phantom had similar waveforms to those of real blood flow. The pulses from the pump signalled the starts of the cycles of the flow in the same way as the pulses from an oximeter provided the timing information of *in vivo* cardiac cycles. For convenience, the cycles of the pusatile flow driven by the pump are also referred to as cardiac cycles. The length of the simulated cardiac cycle was 1.12 s.

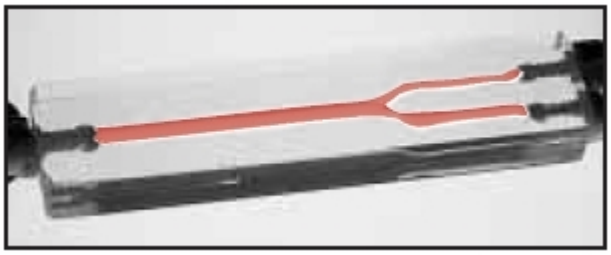

Figure 7.1: The carotid phantom.

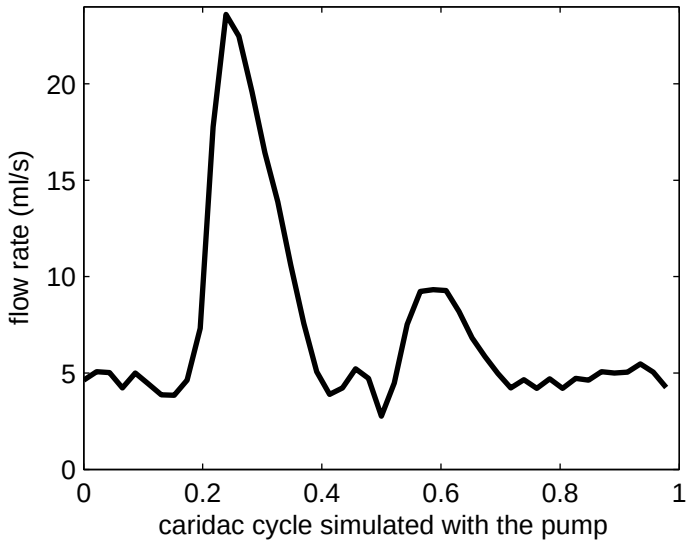

Figure 7.2: The driving flow waveform from the pump.

7.2.2 The scanning protocol

Five scans were included in the scanning protocol. The first (scan #1) was a 2D TOF scan of 28 slices serving as a localizer for later scans. The following four scans were all retrospectively gated and used the same settings except the applied sampling patterns. The second scan (scan #2) was fully sampled, followed by three undersampled scans (scan #3, #4 and #5). The signals were undersampled in three dimensions of k-t space in all three undersampled scans. The sampling ratios of scan #3, #4 and #5 were 13%, 17%, and 25%, respectively.

Since the phantom did not move and the dynamic changes of the signals from the phantom were stable over a long period of time, the total scan time was allowed to be much longer than in the *in vivo* tests. The scan matrix was set to $192 \times 192 \times 32$ in the three spatial dimensions and 24 in the temporal dimension. T_R was 13 ms. Flow encoding was applied in all three spatial directions so each sample prescribed in the sampling patterns was sampled four times, including the acquisition without flow encoding. The scan time for the fully sampled scan was about two hours and seven minutes. The total scan time of the four gated scans was about three hours and seventeen minutes. The sampling ratios and the scan time of the scans are listed in Table (7.1).

scan	sequence	number of dimensions undersampled	sampling ratio	scan time (min)
#1	2D TOF			2
#2	3D PC		100%	128
#3	3D PC	3	13%	16
#4	3D PC	3	17%	21
#5	3D PC	3	25%	32

Table 7.1: The scanning protocol

It would be desirable to include scans undersampled in two dimensions of k-t space for comparisons with the scans undersampled in three dimensions. The total scan time would be about four and a half hours with these scans. This was not implemented because booking such a long time slot on the scanner was difficult.

Five different sampling patterns in two dimensions were used as elements to build the four sampling patterns in three dimensions for the four gated scans (scan #2, #3, #4

and #5). The sampling patterns in two dimensions used for individual slice encoding steps are shown in Figure (7.3). The sampling ratios of these sampling patterns were 100%, 33%, 25%, 17% and 4%. The sampling pattern with a sampling ratio of 100% was used for all slice encoding steps of the fully sampled scan. The other three scans (scan #3, #4 and #5) undersampled the k-t space in three dimensions by changing sampling patterns for different slice encoding steps. Each sampling pattern in three dimensions consisted of three sampling patterns in two dimensions. The distributions of samples along the two phase encoding dimensions for the three undersampled scans (scan #3, #4 and #5) are displayed in Figure (7.4).

7.2.3 Other scan parameters

The phantom was placed to make the three tubes at the same anterior/posterior or horizontal level. The tube corresponding to the CCA (tube CCA) was parallel to the superior/inferior axis, in the inferior end. The two tubes corresponding to the ICA and ECA (tube ICA and tube ECA) were in the superior end, with the tube ICA on patient left. The waveform of the input flow from the pump has been shown in Figure (7.2). The peak flow rate was 23.6 ml/s, the temporal mean flow rate was 7.234 ml/s, and the period of the flow was 1196 ms. A fluid bag filled with 0.9% sodium chloride solution was placed under the phantom to load the coils. Frequency encoding was in the anterior/posterior direction. A 4-element phased-array carotid surface coil was used for receiving signal. All the channels of the coil were used in the scans.

For the 2D TOF scan, the FOV was 9 cm and the in-plane resolution was 192×192. Although the FOV and the in-plane resolution of this scan were the same as those of other scans, the left/right and anterior/posterior position of the FOV was different from other scans. 28 slices were scanned and slice thickness was 2 mm. Spacing between slices was also set to 2 mm so the 28 slices covered 56 mm along the superior/inferior direction. The T_E was 4.2 ms, the T_R was 21 ms, and the Flip Angle was 50°.

For the fully sampled scan and the undersampled scans, the FOV was 9 cm and voxel size was $0.47 \times 0.47\ mm^2$. 28 slices were prescribed and the slice thickness was 2.0 mm. In acquisition 32 slice encoding steps were executed during each scan under this setting and images of 32 slices could be reconstructed from the signal. The images of the outmost four slices, two at each end, had to be discarded because of the imperfect slab excitation profile. Images of additional four slices in the superior end

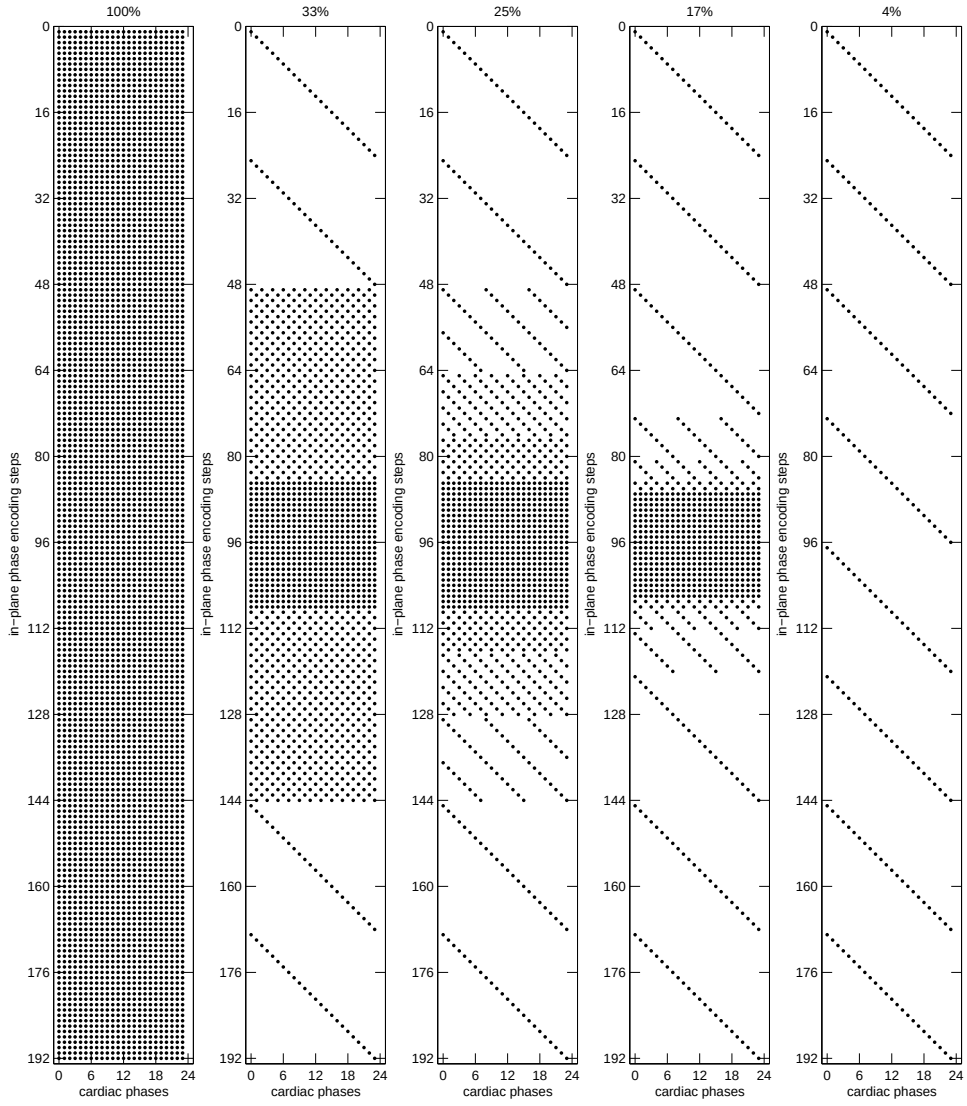

Figure 7.3: The sampling patterns in two dimensions used for individual slice encoding steps. Each black dot in the sampling patterns represents a k-space line.

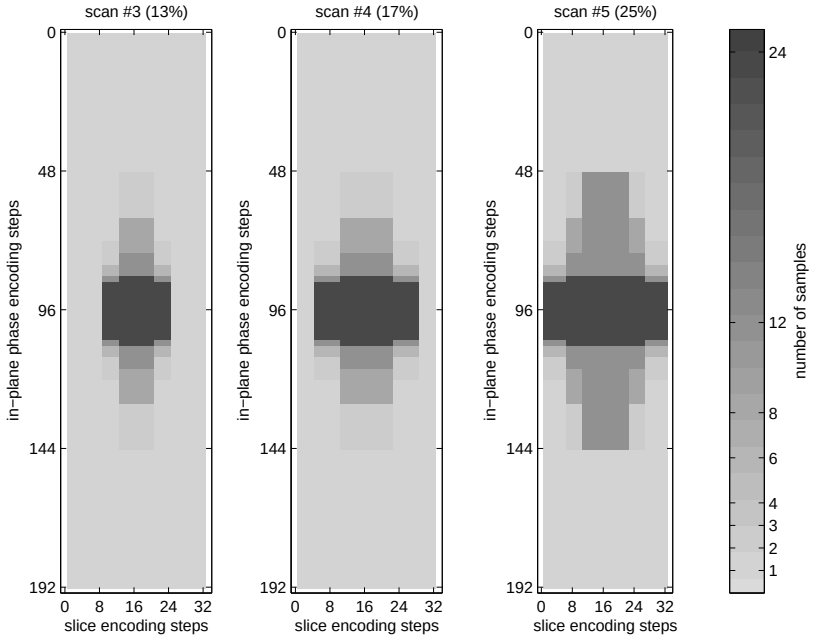

Figure 7.4: The distributions of samples along the two phase encoding dimensions for the three scans undersampled in three dimensions of k-t space.

were also discarded because these slices were in the region where the low sensitivities of the coils resulted in low SNR. The scan matrix was only larger in the slice encoding dimension than the matrix used in the *in vivo* tests. If the matrix had also been enlarged in other dimensions the total scan time would be too long. Another limit was the size of the collected data. Each 3D PC scan produced a single raw signal file, and the software on the scanner did not allow any file larger than two Gigabyte. At the full temporal resolution, 24 samples were collected from each k-space position and 24 time frames could be reconstructed for each slice in each scan. Flow encoding was applied in all three directions so in each scan for each slice the reconstruction results consisted of four sets of 24 time frames, each of a different type of flow encoding. The VENC was 100cm/s, the T_R was 13 ms, the T_E was 4.0 ms under the setting of the T_R, the acquisition bandwidth was 31.25 kHz, and the Flip Angle was 30°. In the 3D PC sequence raw signals were set to be saved to files directly without any post-processing to allow offline reconstruction.

7.2.4 Reconstruction

For the 2D TOF scan the image reconstruction was completed immediately after the scan with the standard software installed on the scanner. The images were used to set the position of the FOV of the following scans. These images were also saved to files in DICOM format.

For the four gated scans, timing of each sample was reconstructed from the gating records. The k-space position of each sample was determined according to the sampling patterns. Gridding was applied to the raw signals at each k-space position separately to get the signals in k-t space for 24 phases of the cardiac cycle. The output from the gridding operations had six dimensions, including the three spatial dimensions, the temporal dimension, the flow encoding dimension and the coil dimension. A 3D inverse Fourier transform was applied to the three spatial dimensions to convert the signals into images.

7.2.5 Methods for comparisons between scans

The intensity and velocity differences between the undersampled scans and the fully sampled scan were compared in a similar way as in Chapter 6. When the D_v was compared in different regions or different periods, only the velocities in the superior/inferior direction were compared. When the D_v was compared in different directions of the flow, it was averaged in the core ROI and over all cardiac phases. Comparisons in two selected slices were presented. The differences were also averaged over all slices for comparisons.

In the comparisons of the velocity waveforms of single pixels and the flow rate waveforms of the tubes in the selected slices, only the velocities in the superior/inferior direction were used.

In order to compare velocity field measured in each scan, two midline planes, one axial and one coronal, were selected and the velocity vectors of all the voxels with flow in the selected plane were presented. The positions of the planes are shown in Figure (7.5).

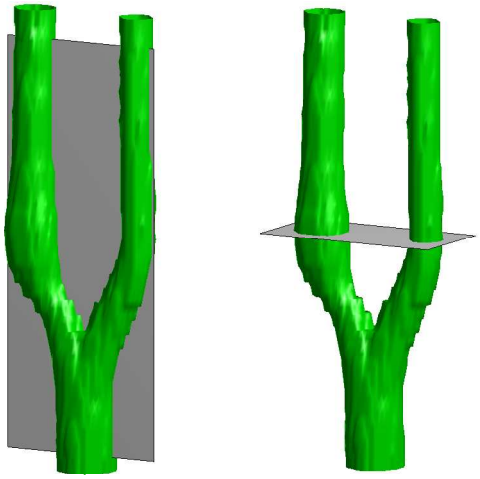

Figure 7.5: The positions of the midline coronal plane (left) and the axial plane (right) used to evaluate the velocity patterns.

7.2.6 Segmentation

The placement of the flow ROI required distinguishing the voxels with flow from those without. This can be achieved by inspecting the phase difference waveforms of single voxels measured from the fully sampled scan. The phase difference waveforms were obtained by calculating the complex phase differences between the images from the data without flow encoding and the data with flow encoding in the superior/inferior direction. In the images the tubes were always surrounded by empty background. The voxels without flow produced phase difference waveforms changing randomly over the cardiac cycle. The waveforms from the voxels with flow were generally smoother. Figure (7.6) shows examples of waveforms from both types of voxels. The segmentation was carried out manually.

7.3 Results

7.3.1 Slice positions

Figure (7.7) shows the positions of the 24 slices where images where used in the comparisons. The 3D structure of the tubes was obtained from the 28 images collected in the 2D TOF scan. Most comparisons will focus on one slice below the bifurcation and

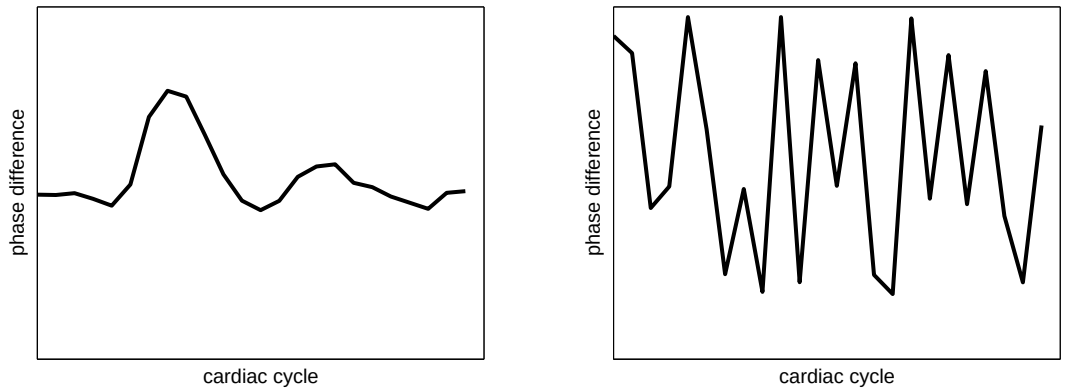

Figure 7.6: Examples of phase difference waveforms of a voxel inside the tube (left) and a voxel in empty background (right).

one slice crossing the carotid bulb. The two slices were referred to as the slice BB and the slice AB.

7.3.2 Coil selection

Figure (7.8) shows images of the slice BB and the slice AB from all coils. The images were the temporal averages of the images without flow encoding from the fully sampled scan. Coil #1 was selected for the comparisons between scans because the SNR of the images from this coil was higher than those from other coils.

7.3.3 The regions of interest

Figure (7.9) shows the positions of the selected ROIs of the slice BB and the slice AB. In other slices the ROIs were placed in a similar way. In all the slices the static ROIs were at the same position.

7.3.4 The intensity difference images

Figure (7.10) shows the intensity difference images of the slice BB and the slice AB from the three undersampled scans. The images were obtained by calculating the absolute values of the intensity differences between the images from the fully sampled scan and the images from the undersampled scan. The images from the fully sampled

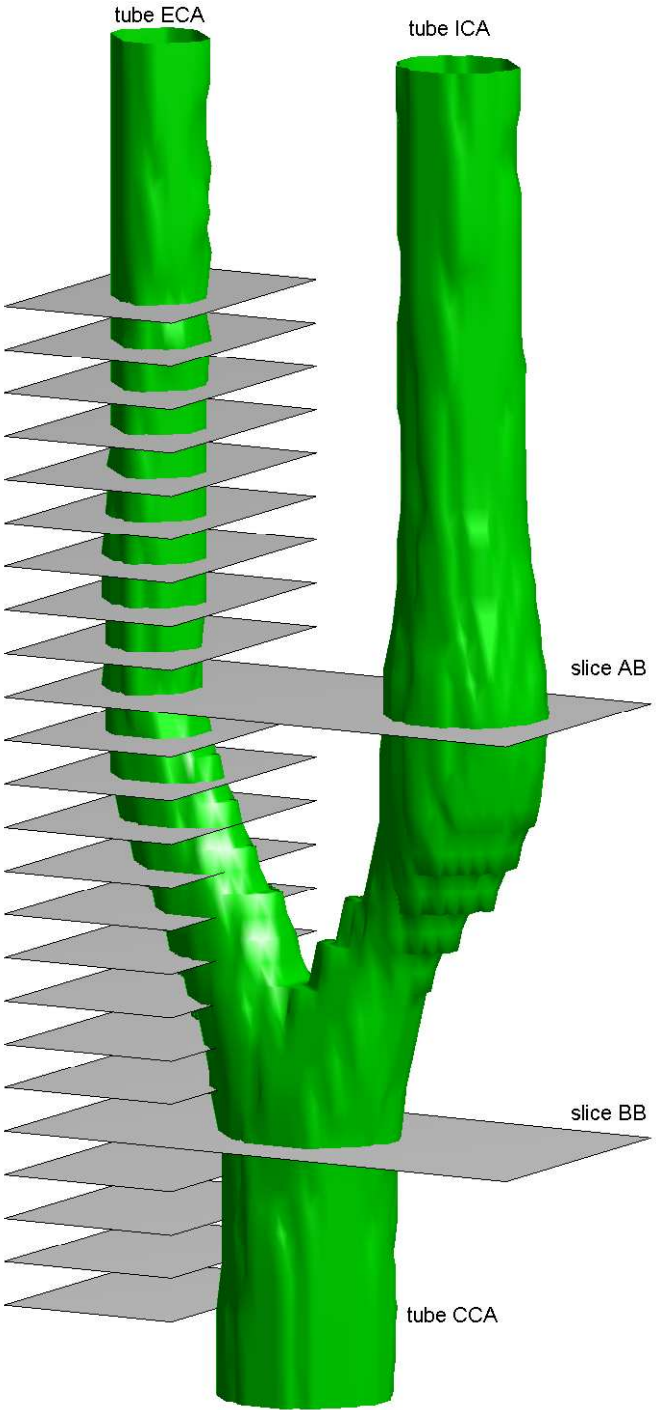

Figure 7.7: The positions of the 24 slices where images were used in the comparisons. The slice BB and the slice AB are highlighted.

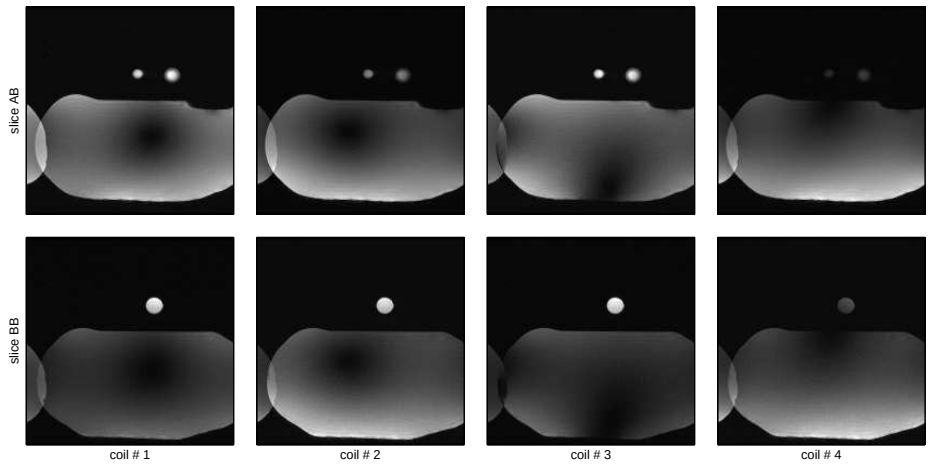

Figure 7.8: The images of the slice BB and the slice AB from all coils. The images were the temporal averages of the images without flow encoding from the fully sampled scan.

scan are also displayed. All the images correspond to the peak flow moment. Flow encoding was applied in the superior/inferior direction.

In the slice BB the intensity differences were slightly larger in the tube than the background noise outside the tube. In the slice AB near the walls of the tubes the intensity differences were apparently larger than the background noise. The images from the undersampled scans were similar to each other regarding the locations of high intensity differences. This suggests the intensity differences caused by undersampling from different undersampled scans were close to the same level.

7.3.5 Intensity differences in different regions

Figure (7.11) shows the intensity differences in different ROIs in the slice BB. Figure (7.12) and Figure (7.13) show the same type of results from the slice AB and results averaged over all slices.

The results from both selected slices and the results averaged over all slices show the values of D_i in the same region from different scans were close to each other. This suggests the intensities were not sensitive to the changes of the undersampling patterns or the changes of the sampling ratio.

In the slice BB, the values of D_i increased as the ROIs included less area. This

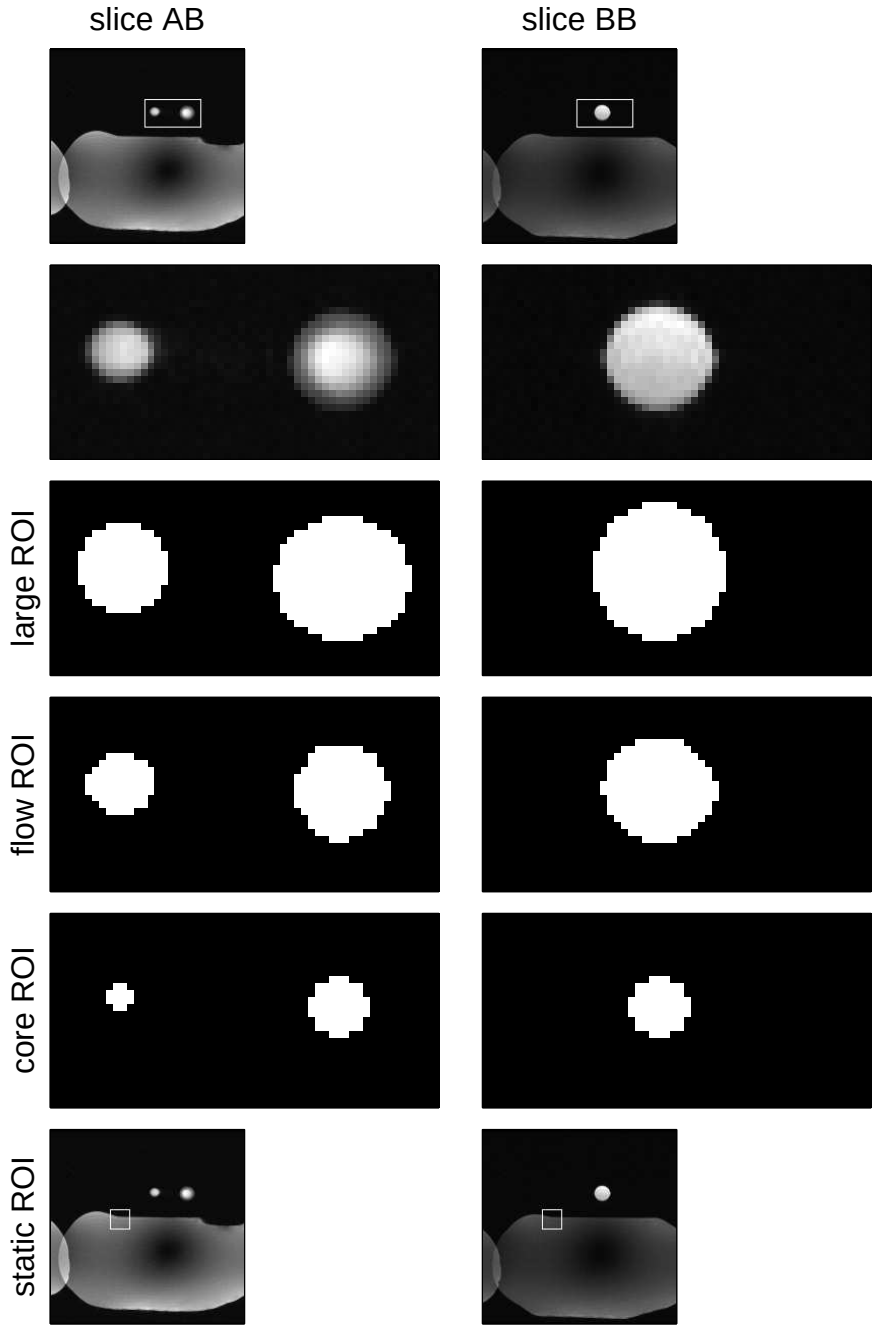

Figure 7.9: The positions of the static ROI, the large ROI, the flow ROI and the core ROI in the slice BB and the slice AB.

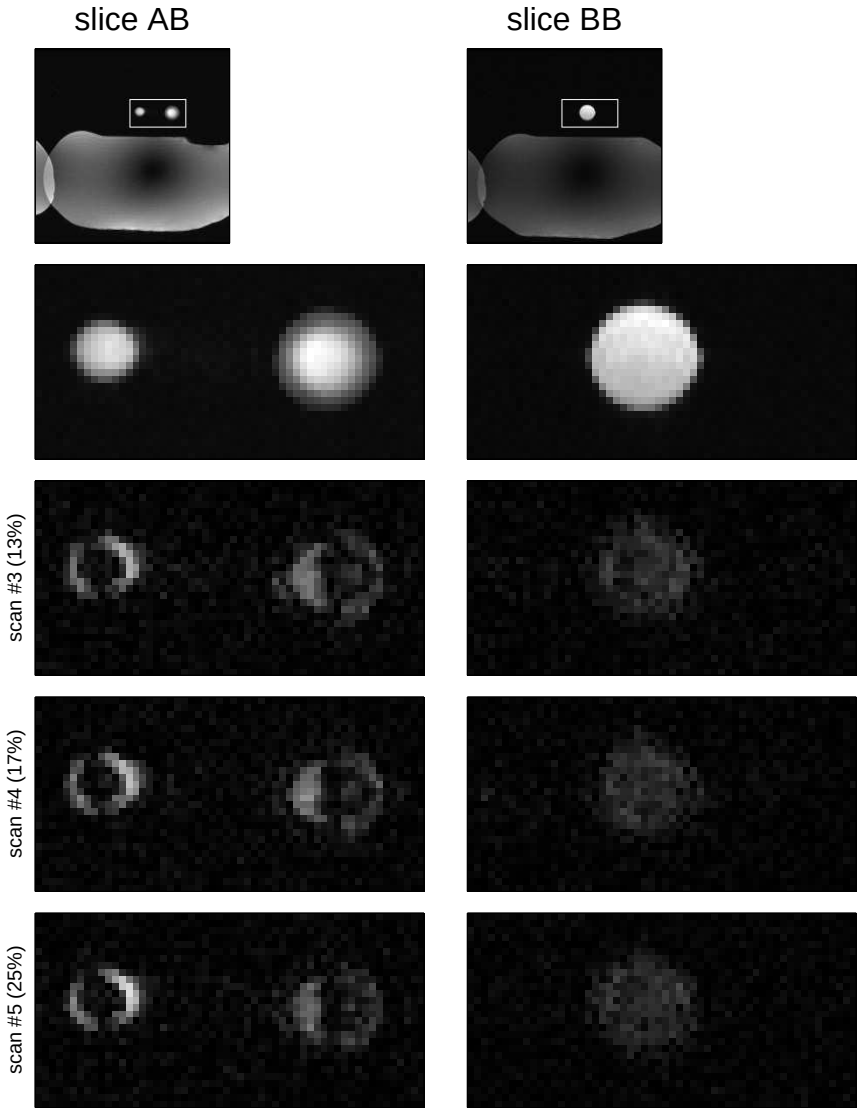

Figure 7.10: The intensity difference images at the peak flow moment without flow encoding from all undersampled scans with regard to the fully sampled scan.

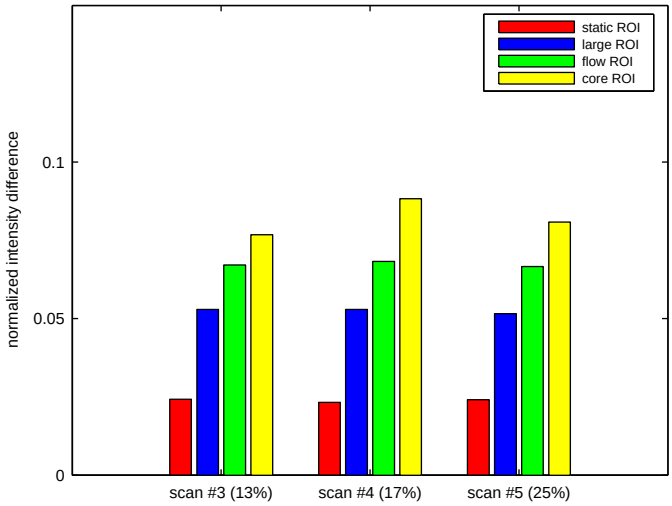

Figure 7.11: The normalized intensity differences in different ROIs in the slice BB.

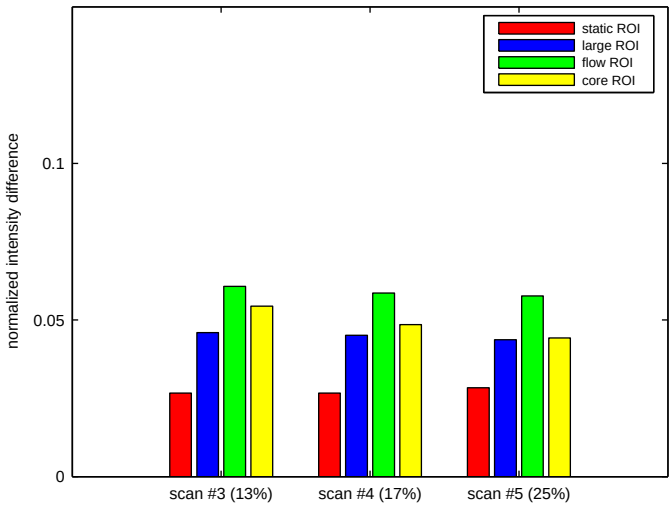

Figure 7.12: The normalized intensity differences in different ROIs in the slice AB.

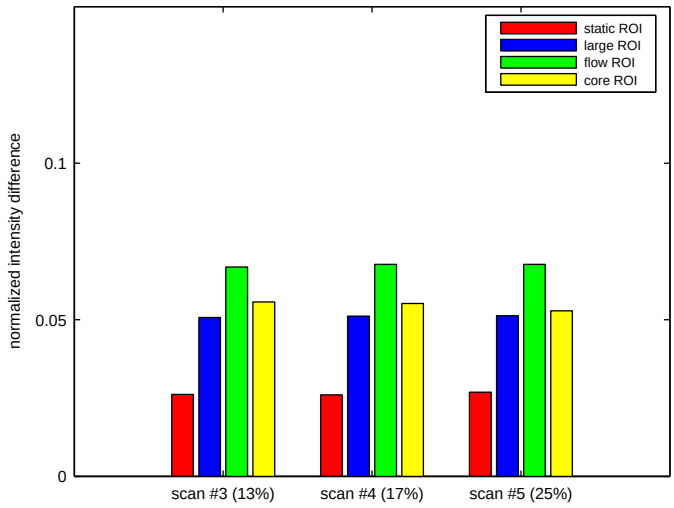

Figure 7.13: The normalized intensity differences in different ROIs averaged over all slices.

indicates in the slice BB the intensity differences were larger in the core ROI than in other ROIs. In the results from the slice AB and results averaged over all slices, the flow ROI gave the largest intensity differences. This suggests for most slices the intensity differences were larger in the regions inside the tube and close to the wall than in other regions.

In different slices, the values of D_i from the large ROI and the flow ROI did not change much. For the core ROI, the results averaged in all slices suggest in most slices the intensity differences were close to those in the slice AB.

7.3.6 Intensity differences in different periods

Figure (7.14) shows the intensity differences over different periods of the cardiac cycle in the slice BB. Figure (7.15) and Figure (7.16) show the same type of results from the slice AB and results averaged over all slices.

In all results the values of D_i of the systolic period were larger than those of the diastolic period. In the slice AB the values of D_i of the systolic period were about twice as large as those of the diastolic period. In the results from the slice BB and the results averaged over all slices the differences between the two periods were not as large as in the slice AB. This suggests in the slice AB where the flow pattern was more

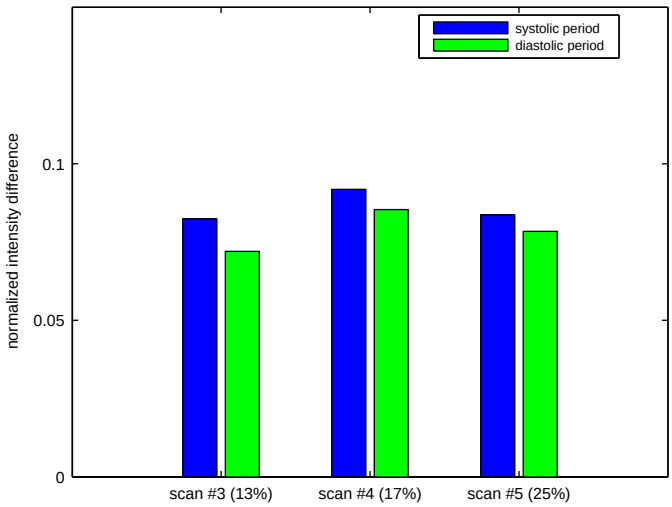

Figure 7.14: The normalized intensity differences over different periods of the cardiac cycle in the slice BB.

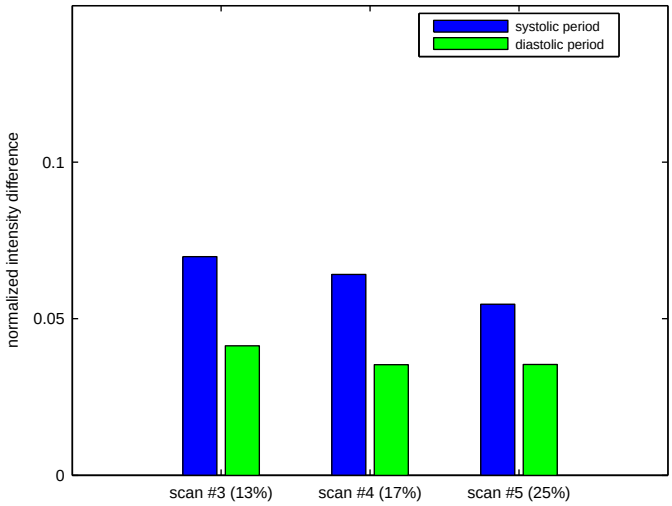

Figure 7.15: The normalized intensity differences over different periods of the cardiac cycle in the slice AB.

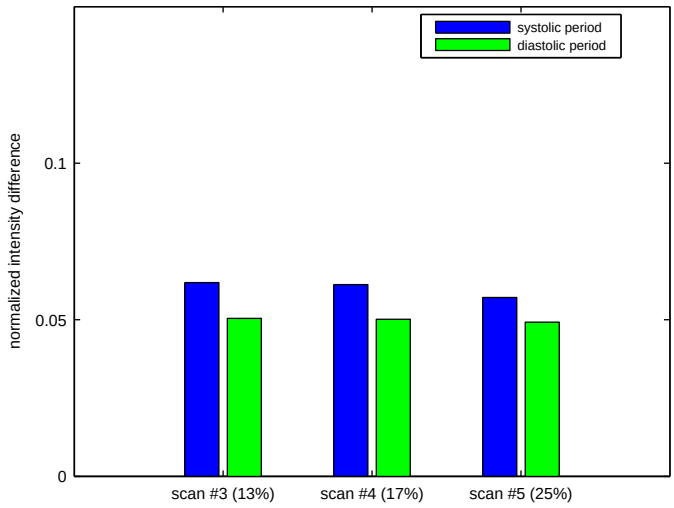

Figure 7.16: The normalized intensity differences over different periods of the cardiac cycle averaged over all slices.

complex the undersampling may cause more intensity errors in the systolic period than in the diastolic period.

7.3.7 Velocity differences in different regions

Figure (7.17) shows the velocity differences in the flow ROI and the core ROI in the slice BB. Figure (7.18) and Figure (7.19) show the same type of results from the slice AB and results averaged over all slices.

Overall the values of D_v were small compared to the peak velocity of 100 cm/s. In the same region, the values of D_v from any two of the undersampled scans were close to each other, slightly smaller (less than or close to 1 cm/s) as the sampling rate increased. This suggests the averaged velocity errors did not change much with the sampling ratio in these scans. The results averaged in all slices indicate the averaged velocity errors were about 5 cm/s.

In all results the values of D_v of the flow ROI were larger than those of the core ROI. This suggests velocity measurements were less accurate near the walls than those in the central regions.

In the slice BB the values of D_v were much smaller than those in the slice AB. In the slice AB the differences between the results of the two ROIs were also larger than

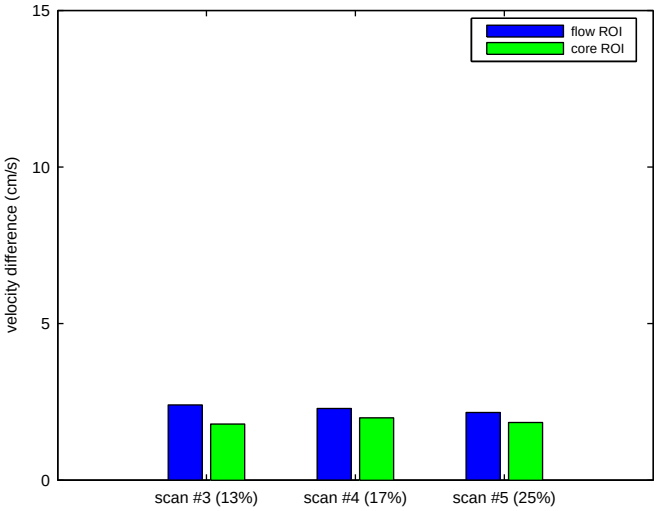

Figure 7.17: The velocity differences in the flow ROI and the core ROI in the slice BB.

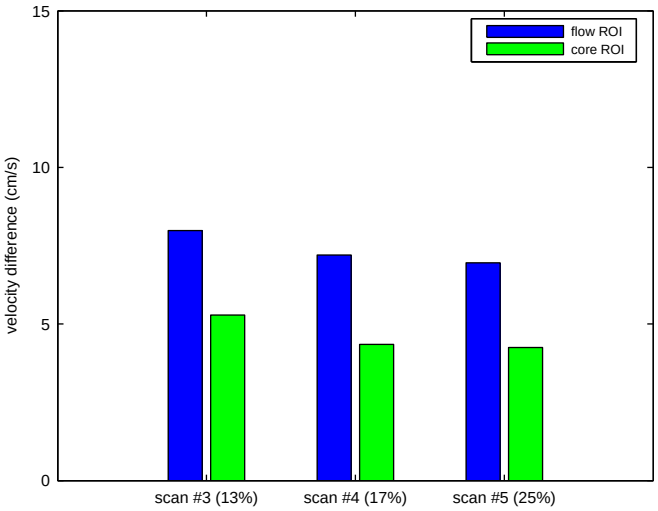

Figure 7.18: The velocity differences in the flow ROI and the core ROI in the slice AB.

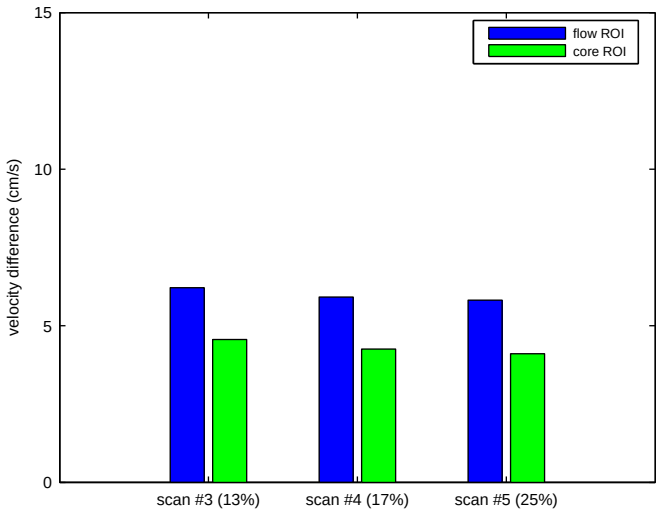

Figure 7.19: The velocity differences in the flow ROI and the core ROI averaged over all slices.

those in the slice BB. This suggests in the slice AB where the flow pattern was more complex the undersampling may cause more velocity errors and the errors were mainly in the regions near the walls.

7.3.8 Velocity differences in different periods

Figure (7.20) shows the velocity differences over different periods of the cardiac cycle in the slice BB. Figure (7.21) and Figure (7.22) show the same type of results from the slice AB and results averaged over all slices.

In all results the values of D_v of the systolic period were close or larger than those of the diastolic period. The differences between the results of the two periods were not large. This suggests the velocity measurements near the peak flow moment were slightly less accurate than those in other phases of the cardiac cycle.

7.3.9 Velocity differences in different directions of the flow

Figure (7.23) shows the velocity differences in three directions of the flow in the slice BB. Figure (7.24) and Figure (7.25) show the same type of results from the slice AB and results averaged over all slices.

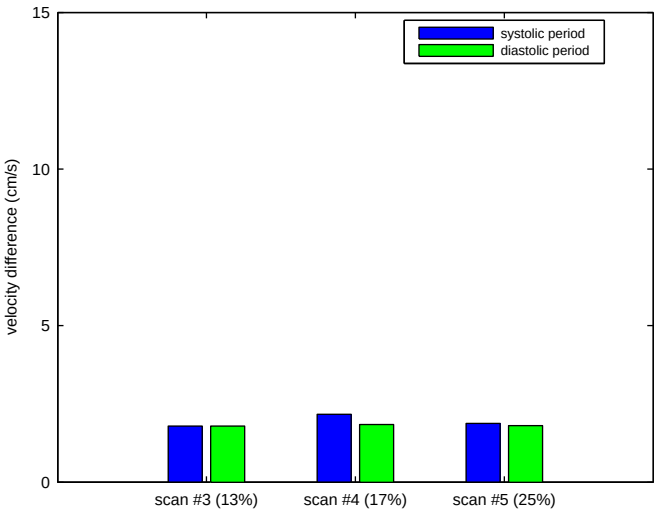

Figure 7.20: The velocity differences over different periods of the cardiac cycle in the slice BB.

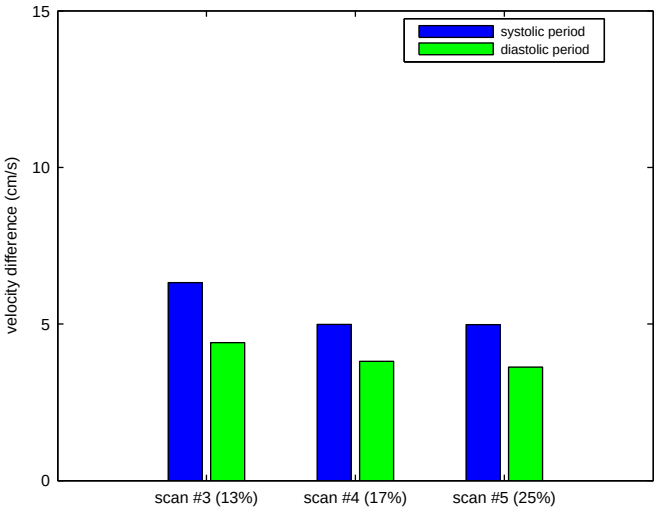

Figure 7.21: The velocity differences over different periods of the cardiac cycle in the slice AB.

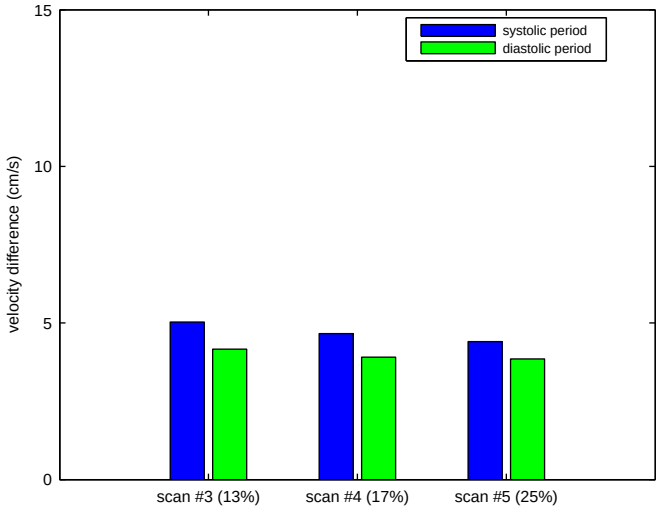

Figure 7.22: The velocity differences over different periods of the cardiac cycle averaged over all slices.

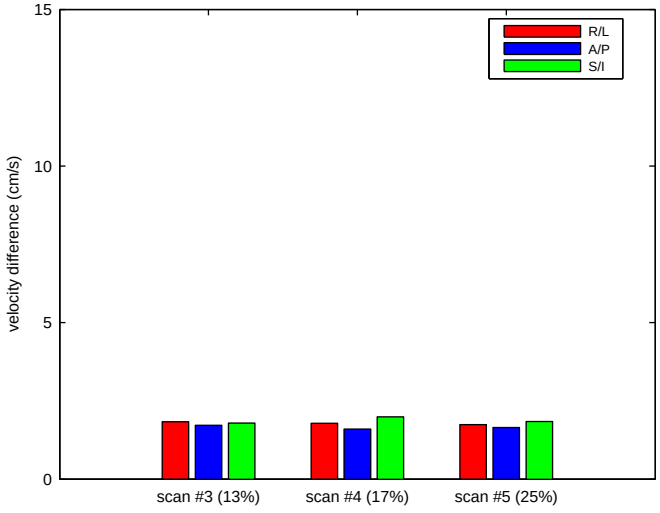

Figure 7.23: The velocity differences in three directions of the flow in the slice BB.

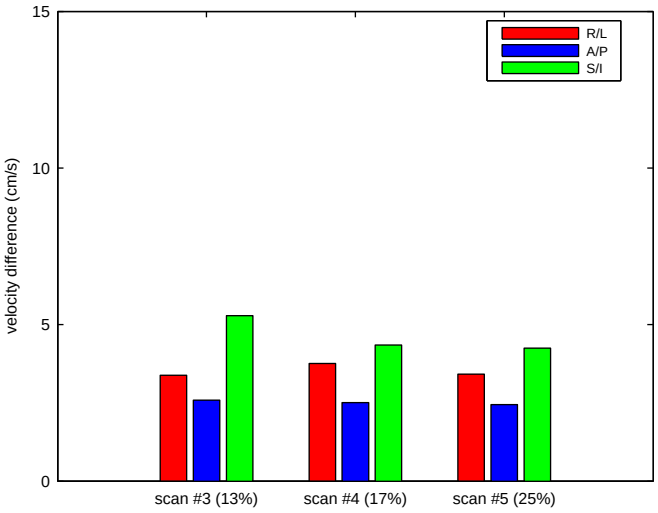

Figure 7.24: The velocity differences in three directions of the flow in the slice AB.

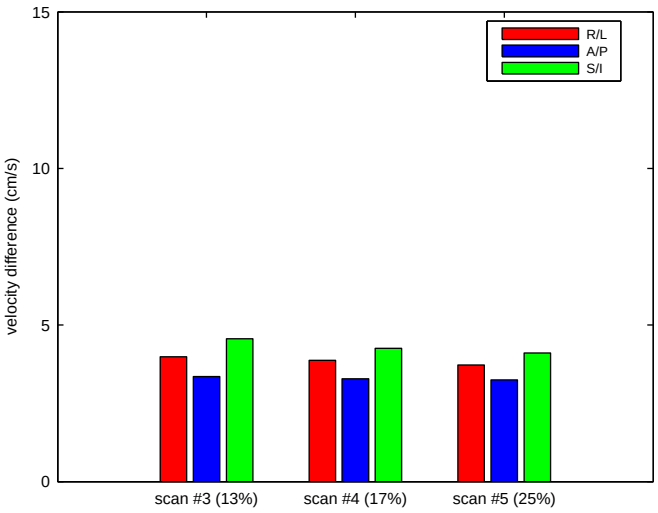

Figure 7.25: The velocity differences in three directions of the flow averaged over all slices.

In all the results the values of D_v in the anterior/posterior direction were smaller than those in other directions. The results averaged over all slices show the values of D_v in different directions were close to each other. This suggests the velocity errors were at the same level in all three directions.

7.3.10 Velocity waveforms of single voxels

Figure (7.26) shows the velocity waveforms of a selected voxel from the fully sampled scan and all the undersampled scans. Figure (7.27), Figure (7.28) and Figure (7.29) show the same type of results of other selected voxels.

Overall the waveforms from the undersampled scans were close to those from the fully sampled scan. For the voxels #1, #2 and #3, the differences between the waveforms were smaller than those for the voxel #4. For voxel #4, the waveform from scan #5 was closer to the waveform from the fully sampled scan than those from scan #3 and #4. This suggests in the regions near the wall scans with a higher sampling ratio may give more accurate measurements and in the central area this improvement is not apparent.

7.3.11 Velocity patterns in the midline coronal and axial planes

Figure (7.30) shows the velocity patterns at the peak flow moment of the midline coronal plane. Figure (7.31) shows the patterns of the axial plane. Velocity vectors of all the voxels in the flow ROI in the planes are displayed. The differences between the patterns from the undersampled scans and the pattern from the fully sampled scan are also displayed. The positions of the planes have been shown in Figure (7.5).

In the midline coronal plane, the velocity patterns from the undersampled scans were similar to the pattern from the fully sampled scan. At several positions near the walls of the tubes there were velocity vectors apparently not consistent with the flow. This might be caused by partial volume effect or the low SNR near the walls. In the patterns of the velocity differences between the undersampled scans and the fully sampled scan, most positions with large differences were near the walls or in the region corresponding to the carotid bulb where the flow was complex or turbulent. The differences between the pattern from scan #3 and the pattern from #2 were apparently larger than the differences between the pattern from scan #4 or #5 and the pattern

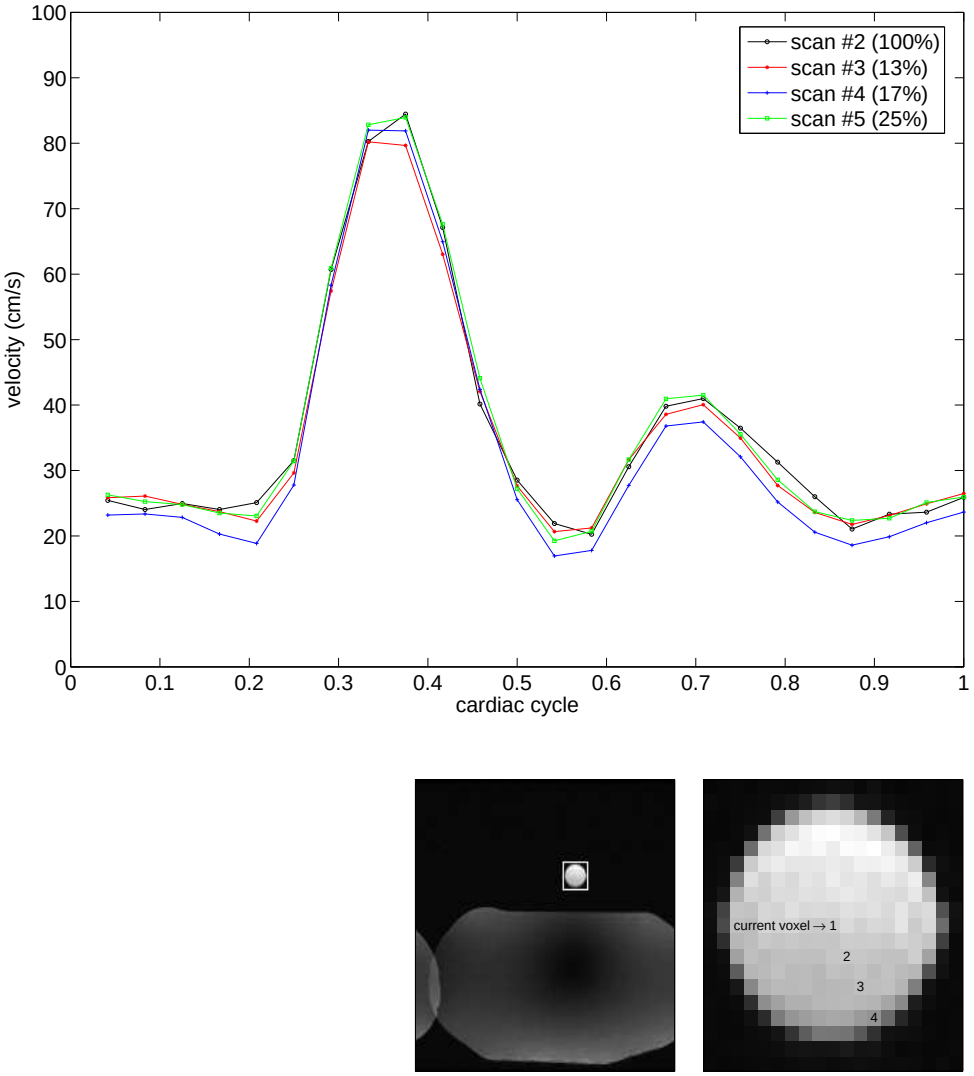

Figure 7.26: The velocity waveforms of a selected voxel from the fully sampled scan and all the undersampled scans. The position of the voxel is displayed in the bottom image.

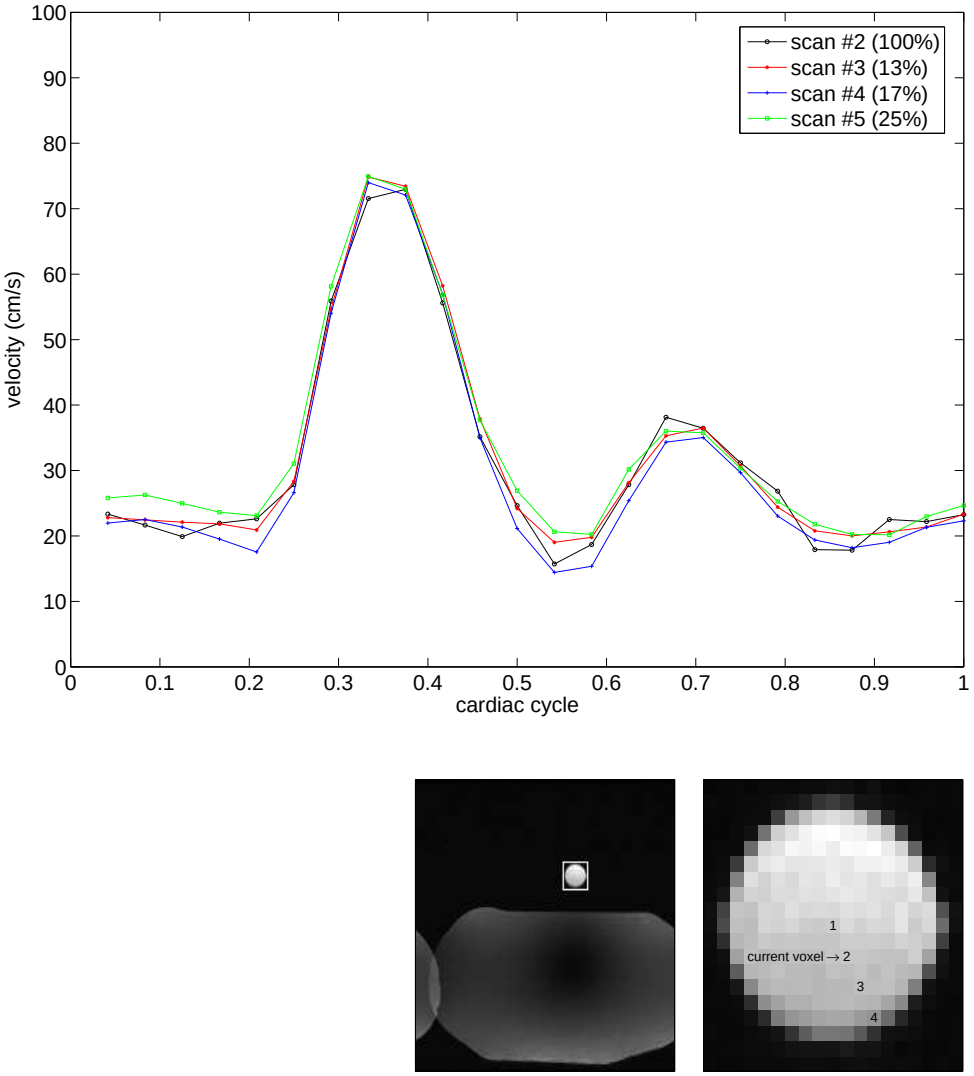

Figure 7.27: The velocity waveforms of a selected voxel from the fully sampled scan and all the undersampled scans. The position of the voxel is displayed in the bottom image.

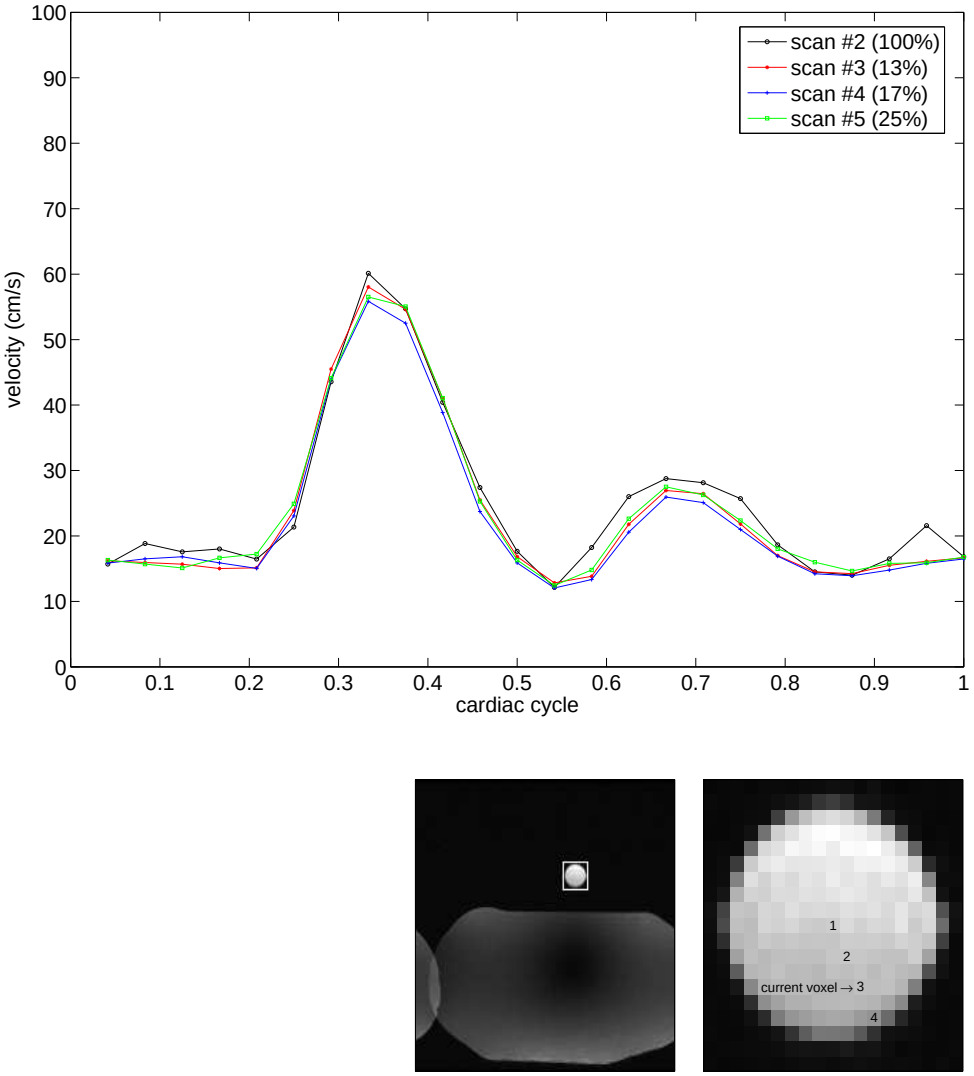

Figure 7.28: The velocity waveforms of a selected voxel from the fully sampled scan and all the undersampled scans. The position of the voxel is displayed in the bottom image.

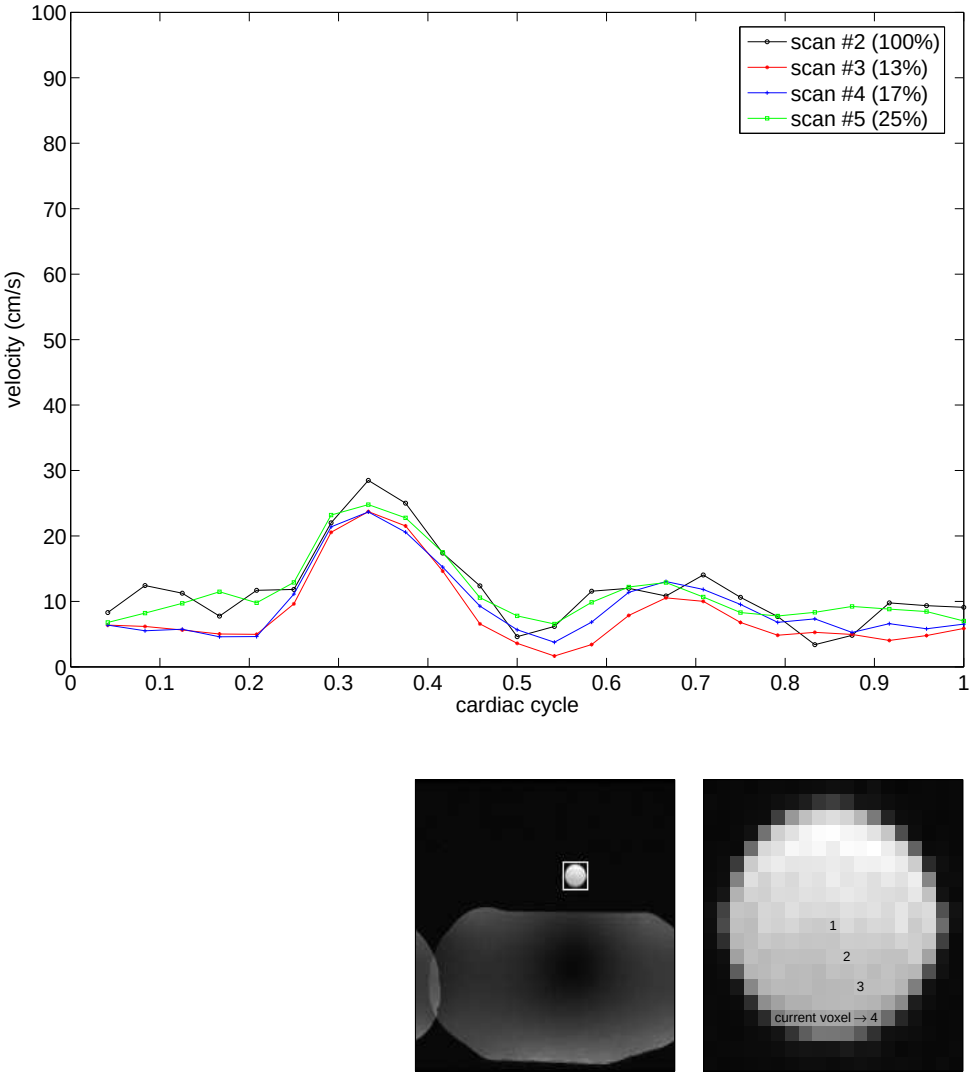

Figure 7.29: The velocity waveforms of a selected voxel from the fully sampled scan and all the undersampled scans. The position of the voxel is displayed in the bottom image.

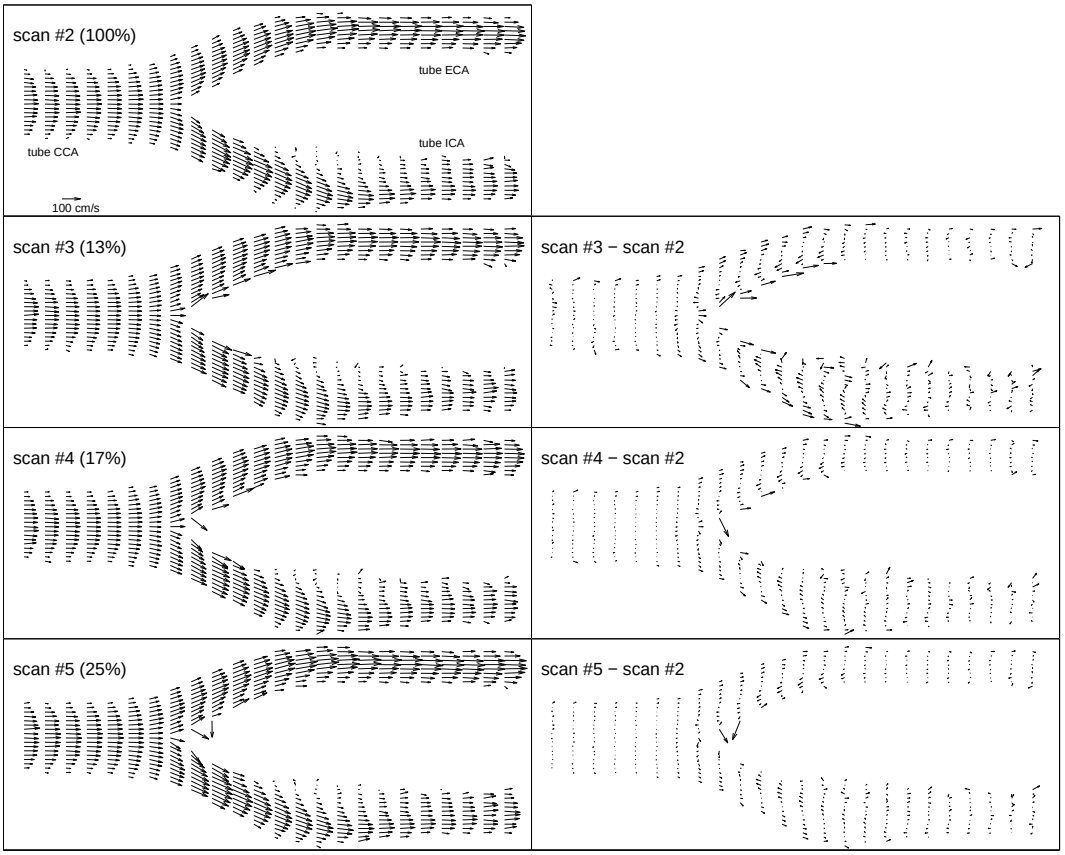

Figure 7.30: The velocity patterns at the peak flow moment of the midline coronal plane. The vectors represents the projection of the 3D velocity vectors in the coronal plane. The differences between the patterns from the undersampled scans and the pattern from the fully sampled scan are displayed on the right.

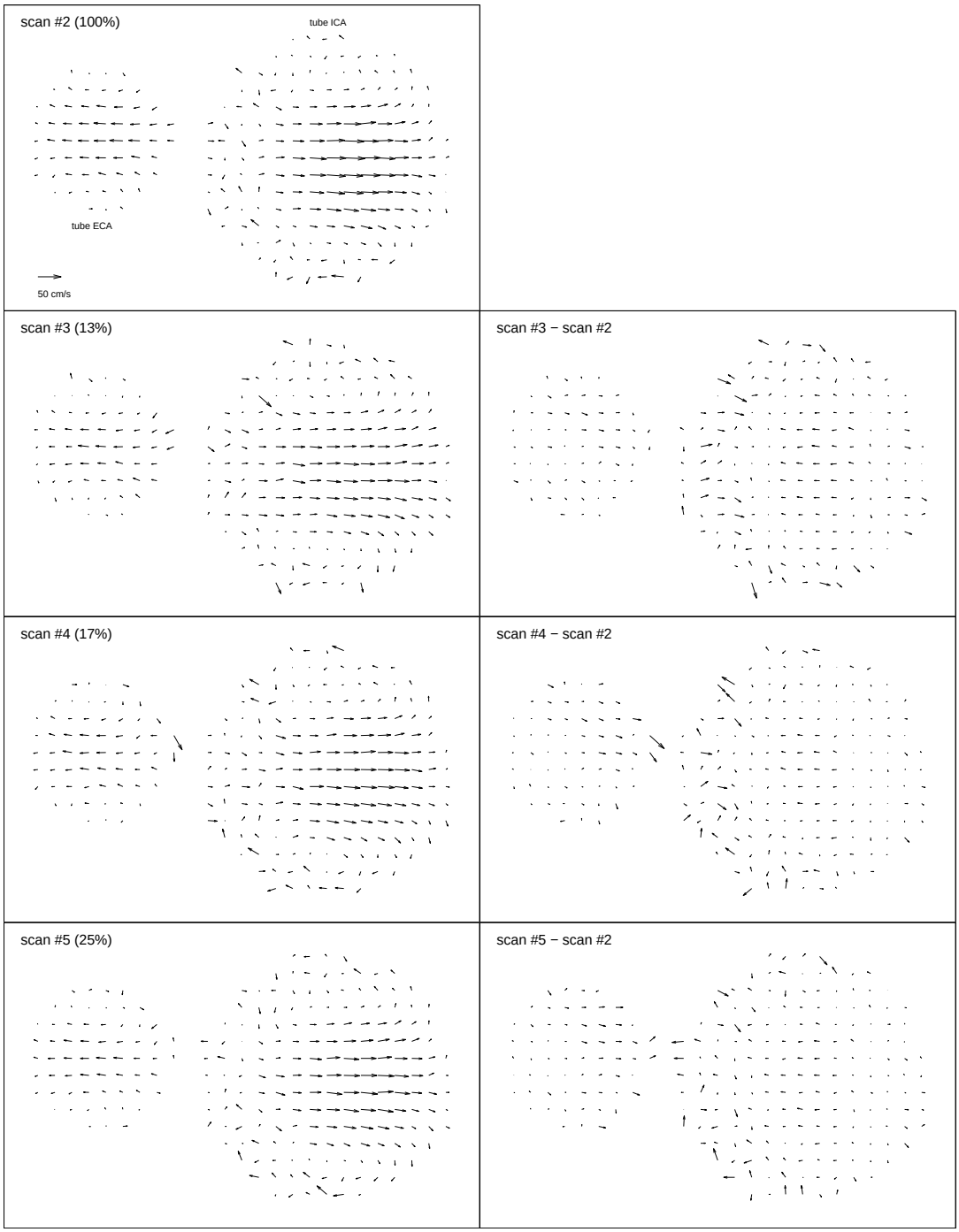

Figure 7.31: The velocity patterns at the peak flow moment of the axial plane. The vectors represents the projection of the 3D velocity vectors in the axial plane. The differences between the patterns from the undersampled scans and the pattern from the fully sampled scan are displayed on the right.

from #2. This suggests the measurements of the velocity field are more accurate at a sampling ratio higher than 13%.

In the axial plane the velocity patterns from different scans were close to each other. The patterns of the velocity differences were also similar to each other. This indicates the accuracy of the measurements of the velocities in the axial plane did not change much with the sampling ratio. It might also be possible the patterns of differences were similar because the differences were all large when the flow in the axial plane was slow and complex.

7.3.12 Flow rates of different tubes

Figure (7.32) shows the flow rates of the tube CCA from the fully sampled scan and all the undersampled scans. Figure (7.33) and Figure (7.34) show the same type of results of the tubes ICA and ECA. The flow rates were calculated in the slice BB and the slice AB.

For the tube CCA, the flow rate waveforms from the undersampled scans were almost the same as the waveform from the fully sampled scan. For the tubes ICA and ECA, the waveforms from the undersampled scans were closer to the waveforms from the fully sampled scan when the sampling ratio was larger. For the tube ECA, the waveform from scan #3 was smoother than those from other scans. This may suggest the sampling ratio of 13% is too low for the signal.

7.4 Discussion

With 32 slices scanned and the velocities measured in three directions, the scans were longer than those in Chapter 6. At the sampling ratio of 25%, the scan time was reduced to 32 minutes, but it was still too long for human subjects. Unless the results obtained at lower sampling ratios can be proved accurate, velocity measurements with the same scan setting as that selected for the phantom test are not fast enough for clinical applications.

In the phantom test the order of the scans in the scanning protocol was different from those in the *in vivo* tests in Chapter 5 and Chapter 6. The scans at lower sampling ratios were placed closer to the fully sampled scan. Since the phantom could not move, only the undersampling errors and the scan-to-scan differences were the major

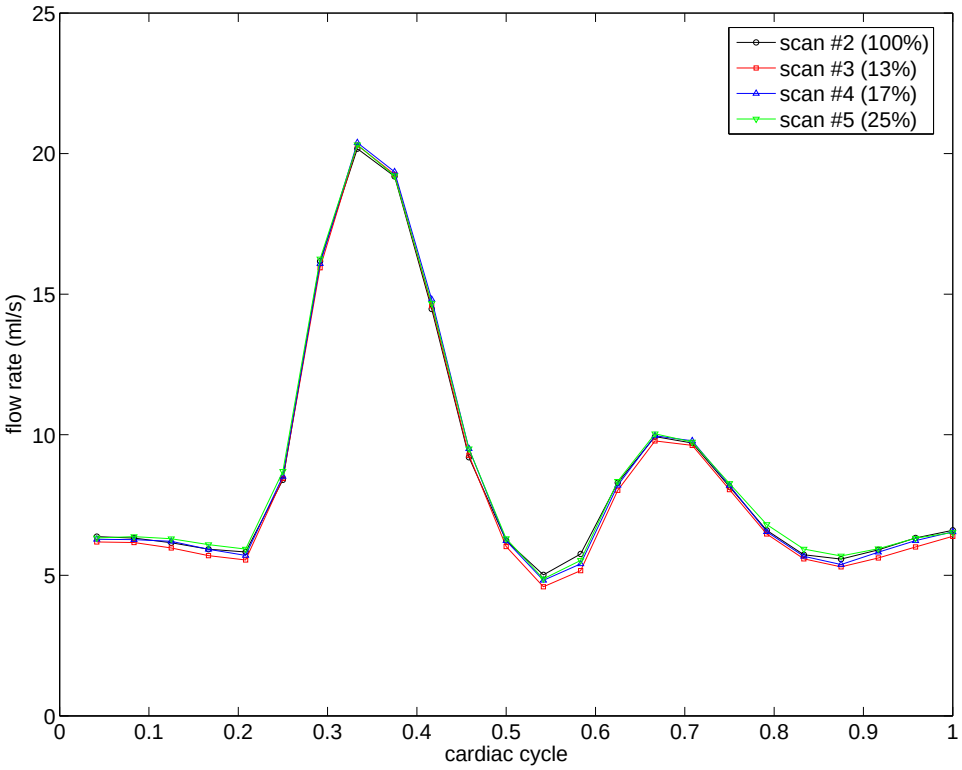

Figure 7.32: The flow rates of tube CCA from the fully sampled scan and all the undersampled scans.

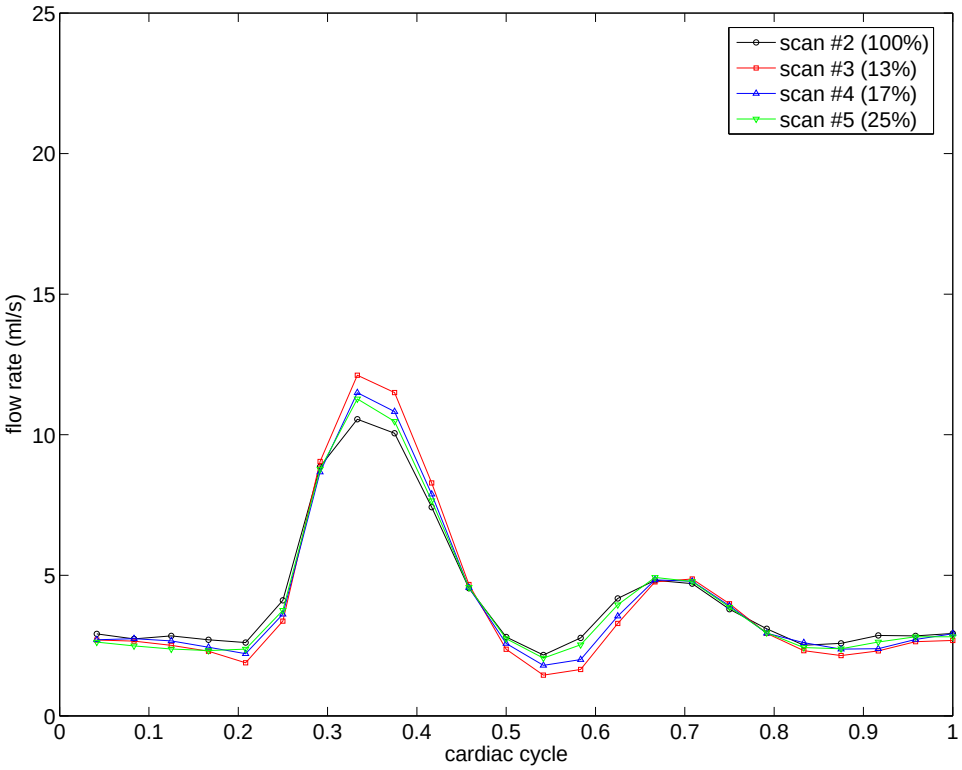

Figure 7.33: The flow rates of tube ICA from the fully sampled scan and all the undersampled scans.

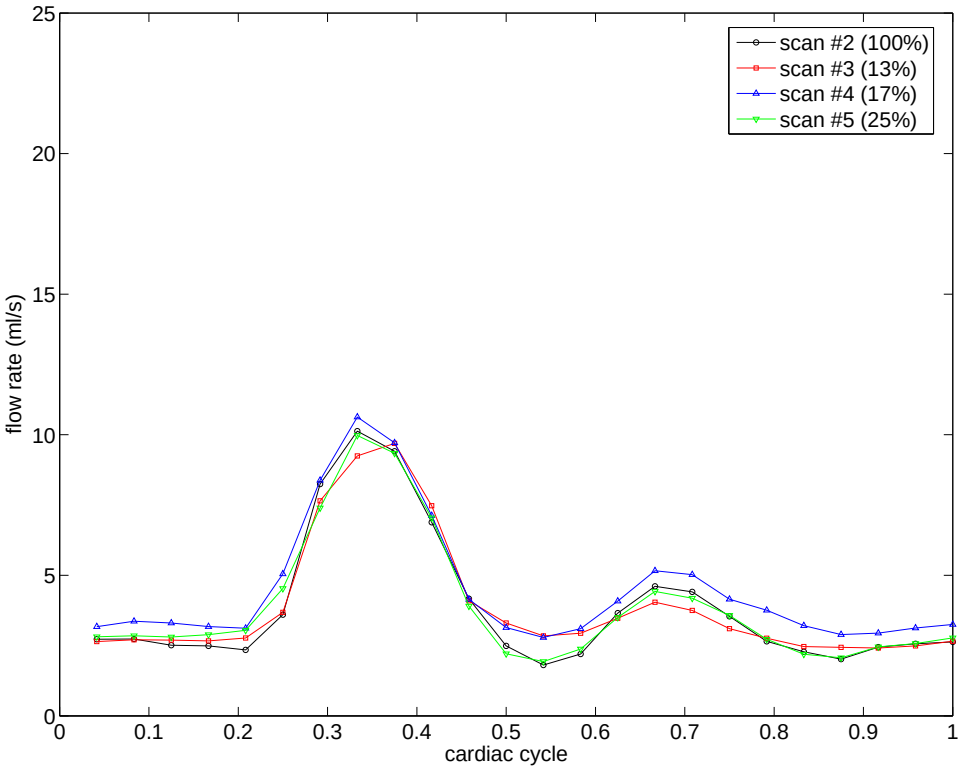

Figure 7.34: The flow rates of tube ECA from the fully sampled scan and all the undersampled scans.

contributors to the differences observed in the comparisons between scans. As discussed previously in Chapter 6, the results from the scans closer to the fully sampled scan were likely to contain smaller scan-to-scan differences. With this scan order, if the results obtained at lower sampling ratios showed larger differences from the full sampled results than those at higher sampling ratios, the corresponding undersampling errors should also be larger because the scan-to-scan differences were most likely to be smaller. This would make it easier to evaluate the undersampling errors at low sampling ratios.

The comparisons of intensity and velocity differences showed that the differences were not sensitive to changes in the sampling ratio. When averaged over all slices, the intensity differences obtained at different sampling ratios were almost identical to each other; the differences between the velocity differences in the same region at different sampling ratios were smaller than 0.5 cm/s.. This seems to suggest the measurements obtained at the sampling ratio of 13% were as accurate as those at the sampling ratio of 25%. However, the comparisons of the velocity patterns in the midline coronal plane showed that the results obtained at the sampling ratio of 13% were less accurate. This suggests in the phantom test the results averaged over all slices were not the best measures of undersampling errors. One of the reasons might be that large velocity differences were limited in small regions near the tube wall and in the bulb of the tube ICA, as shown in the comparisons of the velocity patterns in the midline coronal plane. Another reason could be that large velocity differences were limited in a short period close to the peak flow moment. As shown in the comparisons of the velocity differences over different periods, in the slice AB, the differences between the velocity differences at the same sampling ratio in different periods were around 2 cm/s, larger than those in the slice BB, which were smaller than 0.5 cm/s. The comparisons of the velocity differences in different regions showed a similar pattern. If it is necessary to select an optimal sampling ratio, the results of the comparisons of the velocity patterns should be used as the principal criteria. As to the phantom test presented in this chapter, according to the comparisons of velocity patterns and the comparisons of flow rate waveforms, the optimal sampling ratio should not be lower than 17%. In future work, the velocity differences can be averaged in a more localized region and over a shorter period for better assessments of undersampling errors.

Most comparisons showed that the results obtained in the phantom test were more accurate than those of the *in vivo* test in Chapter 6, especially in the comparisons of

velocity waveforms of single voxels and the comparisons of flow rate waveforms. In the *in vivo* test the sampling ratio of 17% was regarded too low, but in the phantom test at the same ratio the results were acceptable. It is possible that the absence of subject displacements and the relatively simple spatial structure of the phantom contributed to the good performance of the undersampled scans in the phantom test. It is more likely that the larger scan matrix selected in the phantom test led to more signal redundancy, which allows further undersampling. In future work, the effects of subject displacements can be studied by using phantoms able to simulate subject movements during scans; realistic phantoms with complex spatial structures can be used to test the effects of the changes in structure complexity; the phantom can be scanned with different scan matrices to investigate the correlation with undersampling performance.

The comparisons of velocity differences in different directions of the flow showed that the velocity differences of the velocities in the axial plane were close to those of the velocities in the superior/inferior direction. As shown in the velocity patterns, the velocities in the superior/inferior direction could be more than 100 cm/s at the peak flow moment; those in the left/right direction were less than 50 cm/s; in the anterior/posterior direction, the flow was much slower. The small differences between the velocity differences and the large differences between the scales of the velocities in different directions of the flow may suggest that in average the measurements were similarly accurate in all directions. It may also suggest that in the axial plane the undersampling errors in velocity were relatively large compared with the scales of the velocities. As shown in the velocity patterns in the axial plane, in the tube ICA the differences between the velocities obtained from the undersampled scan and those from the fully sampled scan were large, especially in the regions where the flow were complex. The measurements were not accurate enough for the reconstruction of the 3D velocity field, even at the highest sampling ratio. It should be noted that due to the turbulent and complex nature of the flow the measurements obtained in the fully sampled scan might also be inaccurate in some regions in the bulb of the tube ICA. It is difficult to evaluate the undersampling performance in these regions.

In summary, the velocity differences averaged over all slices did not change much with the sampling ratio. They were close to 5 cm/s. In the slice BB, the velocity differences were very small, about 2 or 3 cm/s. In the slice AB, they were larger, between 4 and 8 cm/s. The velocity measurements were less accurate near the edge of the lumen than in the central region of the tube, and the velocity differences were

always larger when the flow was faster. The velocity differences of the velocities in the axial plane were smaller than those in the superior/inferior direction, but they were at a similar level. The comparisons of the velocity waveforms of single voxels in the tube CCA suggest the results had good temporal resolution. Only those results of the voxel close to the edge of the lumen obtained at the sampling ratios of 13% and 17% showed slightly larger differences from the fully sampled results. The velocity patterns suggest most large velocity differences were at the positions close to the wall of the tube ICA and tube ECA or in the regions where the flow was slow and complex. At the sampling ratio of 13%, the differences between the undersampled pattern and the fully sampled pattern were apparently larger than those obtained at other sampling ratios. This may suggest the sampling ratio of 13% was too low. Most flow rate waveforms were close to the fully sampled results. Only in the tube ECA at the sampling ratio of 13% the flow rate waveform was apparently smoother. Slightly larger differences in flow rate were often observed close to the flow peak.

Chapter 8

Conclusions

8.1 Introduction

The aim of this work was to implement and evaluate two undersampling methods, the k-t BLAST and the ktVD method (Chapter 3), for time-resolved MR velocity measurement of carotid blood flow in order to reduce scan time for such scans. In this chapter the results obtained in the preceding chapters are summarized. General conclusions are drawn from these results and suggestions of future work are made.

8.2 Simulations of undersampling in two dimensions of k-t space

The two methods were first tested in numerical simulations in Chapter 4. Realistic data sets collected in a fully sampled 2D time-resolved scan were used as source data sets for simulated undersampling. Two dimensions of k-t space were undersampled. Different settings of the control parameters of each undersampling method were tested. The differences between the reconstruction results obtained from the undersampled data and the source data sets were used to evaluate undersampling errors. Optimal settings of the control parameters were selected accordingly. Nine sets of simulation results corresponding to nine different sampling patterns of three sampling ratios were compared under the selected setting of the control parameters. The sampling ratios were 50%, 33% and 25%. At each sampling ratio, one k-t BLAST sampling pattern

and two ktVD sampling patterns were tested. The results obtained with different undersampling methods and different sampling patterns were compared with those from the source data sets.

As presented in the simulation results, at the sampling ratio of 50% the intensity and velocity errors from both methods were small. The normalized intensity differences were less than or close to 5%, and the velocity differences were less than 2.5 cm/s. At lower sampling ratios the intensity errors obtained with the ktVD method became larger, and the velocity differences obtained with the k-t BLAST method became larger, between 5 and 5.5 cm/s at the sampling ratio of 25%. The intensity results were slightly less accurate in the lumen than outside, and the velocity errors were larger when the blood flow was more dynamic. In general the results were more accurate at higher sampling ratios. At the sampling ratios of 33% and 25%, the velocity differences obtained with the ktVD method, about 3 cm/s, were very close to those obtained with the k-t BLAST method at the sampling ratio of 33%.

For the k-t BLAST method, a smaller value of the noise regularization weight or a lower noise level led to better results, and the undersampling errors were not sensitive to the changes of the number of training k-space lines. For the ktVD method, the results did not change much with the changes of the noise level or the sampling density variation of the sampling pattern at the same sampling ratio.

The intensity results from the k-t BLAST simulations were close to or slightly better than those from the ktVD simulations. At high sampling ratios the velocity and flow rate results from the k-t BLAST simulations were similar to those from the ktVD simulations. At the sampling ratio of 25% the ktVD method produced velocity and flow rate results more accurate than those obtained with the k-t BLAST method.

8.3 *In vivo* test of undersampling in two dimensions of k-t space

The sampling patterns tested in the simulations in Chapter 4 were applied *in vivo* in Chapter 5. Nine undersampled 2D scans were carried out immediately after a fully sampled scan. All these scans were retrospectively gated, and the same scan setting except the sampling patterns was used for all of them. The results obtained with different undersampling methods and different sampling patterns were compared with those

from the fully sampled scan.

All comparisons between scans were subject to possible influence of scan-to-scan differences and the velocity results could be inaccurate when there were large intensity differences between the undersampled and the fully sampled results.

The k-t BLAST scans produced good intensity images but the velocity results became less accurate as the sampling ratio decreased. At the sampling ratio of 25% serious temporal resolution loss in velocity was observed and for some voxels it was also seen at the sampling ratio of 33%.

The intensity images of the slice AB from the ktVD scans showed large differences from those fully sampled, especially in the regions near arterial wall. Most velocity results were close to those fully sampled although some velocities were underestimated. Velocity differences between the measurements from the ktVD scans and those from the fully sampled scans were less than or close to 5 cm/s. The velocity results from the ktVD scans did not change much with the sampling ratio or with the sampling density variation in k-t space. Velocity waveforms from some voxels showed better results when more samples were collected in central k-t space and the sampling ratio remained unchanged.

At the same sampling ratio the ktVD scans generally produced better velocity results than the k-t BLAST scans. Velocities measured for the voxel close to arterial wall from all the undersampled scans showed large differences from the measurements from the fully sampled scans.

8.4 *In vivo* test of undersampling in three dimensions of k-t space

In 3D scans k-t space can be undersampled in either two or three dimensions. In Chapter 6 six undersampling patterns of the ktVD method at three sampling ratios were tested *in vivo* in 3D scans. The sampling ratios were 33%, 25% and 17%. At each sampling ratio k-t space was undersampled in two dimensions in one sampling pattern and undersampled in three dimensions in the other sampling pattern. The results from the scans undersampled in different number of dimensions of k-t space and at different sampling ratios were compared with those from a fully sampled scan.

The minimum scan time of the 3D scans was much longer than that of the 2D

scans. As a result the test of 3D scans was much longer than those of 2D scans. This limited the scan resolution and the number of scans in the test. During the long test the subject might have involuntary small movements and this could lead to differences in comparisons caused by subject displacement. Scan-to-scan differences could also affect comparison results.

Large intensity differences and velocity differences were often observed together in the results from the same scan. It is likely that the velocity differences were associated with velocity errors caused by intensity errors..

If undersampling errors contributed to most of the differences observed in the comparisons, undersampling in an extra dimension of k-t space improved accuracy of measurements in both intensity and velocity at the undersampling ratio of 33%, and it caused more errors at the undersampling ratios of 25% and 17%. If most of the differences observed in the comparisons were caused by subject movements or scan-to-scan differences, they are not suited for the evaluation of undersampling performance.

The differences between the fully sampled and the undersampled scans increased as the sampling ratio decreased. At the sampling ratio of 33%, the velocity differences averaged over all slices were between 4 and 6 cm/s; at the sampling ratio of 25%, they were between 5 and 8 cm/s; at the sampling ratio of 17%, they were between 6 and 10 cm/s.

At the sampling ratios of 25% and 17%, the differences between the velocity waveforms of single voxels from the undersampled scans and those from the fully sampled scan were larger for the voxels near the LCCA wall. Flow rate underestimation in the LICA was also more serious at these sampling ratios.

8.5 *In vitro* test of undersampling in three dimensions of k-t space

In order to test undersampling in three dimensions in high resolution 3D scans and measure velocity in three dimensions, a flow phantom was scanned with different sampling patterns of the ktVD method in Chapter 7. Three different undersampling patterns were tested. The sampling ratios were 13%, 17% and 25%. The results from the undersampled scans were compared with those from a fully sampled scan.

The normalized intensity differences averaged over all slices did not change much

with the sampling ratio. They were between 5% and 7%. The velocity differences averaged over all slices were close to 5 cm/s. They were not sensitive to the changes of the sampling pattern. In the slice BB, the velocity differences were very small, about 2 or 3 cm/s. In the slice AB, they were larger, between 4 and 8 cm/s.

The comparisons of velocity differences in different regions suggest measured velocities were less accurate near the edge of the lumen than in the central region of the tube. When they were averaged over all slices, the differences between the velocity differences averaged in the flow ROI and those averaged in the core ROI were about 2 cm/s. The velocity differences were always larger when the flow was faster. When they were averaged over all slices, the differences between the velocity differences averaged in the systolic period and those averaged in the diastolic period were not large, less than 1 cm/s. The comparisons of velocity differences in different directions of the flow suggest the velocity differences were larger in the direction along which the flow was faster. For the relatively slow anterior/posterior flow, the velocity differences could be close to those of the fast superior/inferior flow.

The comparisons of the velocity waveforms of single voxels in the tube CCA suggest the results had good temporal resolution. Only those results of the voxel close to the edge of the lumen obtained at the sampling ratios of 13% and 17% showed slightly larger differences from the fully sampled results.

The velocity patterns suggest most large velocity differences were at the positions close to the wall of the tube ICA and tube ECA or in the regions where the flow was slow and complex. At the sampling ratio of 13%, the differences between the undersampled pattern and the fully sampled pattern were apparently larger than those obtained at other sampling ratios. This may suggest the sampling ratio of 13% was too low.

Most flow rate waveforms were close to the fully sampled results. Only in the tube ECA at the sampling ratio of 13% the flow rate waveform was apparently smoother. Slightly larger differences in flow rate were often observed close to the flow peak.

8.6 Conclusions

The results obtained in this work have demonstrated that the k-t BLAST method and the proposed ktVD method could be applied on a clinical scanner to make *in vivo*

time-resolved MR velocity measurement in carotid arteries two or three times faster while retaining an accuracy in velocity within 10 cm/s and an in-plane resolution of 0.625 mm. The results also demonstrated that the performance of the undersampling methods was affected by many factors, such as the degree of signal redundancy or the noise level. In undersampling simulations with fully sampled 2D data, the observed averaged velocity differences between the undersampled and fully sampled results at the sampling ratio of 25% were about 5 cm/s for the k-t BLAST method, and 3 cm/s for the ktVD method. For *in vivo* 2D retrospectively gated carotid velocity measurement using the k-t BLAST method, the observed averaged velocity differences were about 5 cm/s at the sampling ratio of 33%, and 8 cm/s at the sampling ratio of 25%. For the ktVD method, the observed averaged velocity differences were about 5 cm/s at the sampling ratio of 33% or 25%. At the same sampling ratio the velocity results obtained with the ktVD method were close to or more accurate than those obtained with the k-t BLAST method, and the image reconstruction using the ktVD method was much faster than that of the k-t BLAST method. Flow rate waveforms and velocity waveforms of individual voxels showed at the sampling ratio of 25% there were losses of temporal resolution in k-t BLAST results. In 3D *in vivo* experiments, three dimensions of k-t space were undersampled with the ktVD method and at the sampling ratio of 17% the observed averaged velocity differences were about 8 cm/s. In high-resolution 3D phantom experiments, the observed averaged velocity differences obtained with the ktVD method were about 5 cm/s at the sampling ratio of 13%, and the velocity patterns showed large velocity differences close to vessel wall within the carotid bulb.

8.7 Future work

As discussed previously, a lot more experiments need to be carried out to test the reproducibility and accuracy of the results presented in this work. More volunteers need to be scanned to make statistical comparisons between different undersampling methods. The signal structures need to be studied with statistical nonlinear models. The effects of scan parameters also need to be investigated.

In this study all ktVD reconstructions used linear temporal interpolations. Recovering skipped signal in k-t space is a general inverse problem and many other methods can be used. For example, the k-t BLAST reconstruction method can be applied to the

data acquired with a ktVD sampling pattern, and the ktVD reconstruction method can also be used for the data from a k-t BLAST scan. Advanced methods, such as compressed sensing [219, 220, 221, 222], may be applied to improve the reconstruction of the data from an undersampled scan.

A promising method for further scan acceleration is to use coil sensitivity information in reconstruction. This provides an extra dimension of the data for undersampling in addition to those of k-t space. In this work the reconstruction methods were applied to each coil separately. The comparisons used the data from only one selected coil. If the spatial map of the sensitivity of the coils is available, the data from all coils can be used together in reconstruction. This is similar to the situation where a higher sampling ratio is applied. The extra data can either be used to improve signal quality or reduce scan time. It would be even better if a method can work without the prior knowledge of the sensitivity map. In reconstruction the coil sensitivity information may be derived from the undersampled data.

The ktVD method proposed in this study may also be applied to other time-resolved applications such as cardiac or functional studies. The performance of the method in these new areas remains to be investigated.

Appendix A

Relevant source code

A.1 Temporal gridding

```
function result = tmpgrid(n_in,n_out,t_in,sample)
% Temporal gridding by linear interpolation ...
%     of two nearest neighbours
%
% presented in Matlab syntax
% exception handling omitted
% [input]: n_in, number of samples over the cardiac cycle
% [input]: n_out, number of values to be interpolated ...
%     over the cardiac cycle
% [input]: t_in[n_in], temporal positions of the samples ...
%     in the cardiac cycle
%              values in (0,1]
% [input]: sample[n_in], samples
%              timing corresponding to t_in[n_in]
% [output]: result[n_out], gridding results
%              timing corresponding to: 1/n_out, 2/n_out,...,1

% only one sample, copy the value to all entries of result[n_in]
if n_in == 1
  result = sample * ones(n_out,1);
```

```
end

% more than one sample, interpolate from two nearest neighbours
if n_in > 2
  % temporal positions of the gridding points
  t_out = (1:1:n_out) / n_out;
  % loop for all the grid points
  for tt = 1:n_out
    t_grid = t_out(tt);
    % find the two nearest neighbours of t_grid ...
    %      in t_in[n_in], t_a and t_b;
    % t_a <= t_grid <= t_b;
    ...;
    t_a = t_in(idx_a);
    t_b = t_in(idx_b);
    t_ba = t_b - t_a;
    % if t_a is very close t_b, copy the average to result(tt)
    if t_ba <= 0.001
      result(tt) = (sample(idx_a) + sample(idx_b))/2;
    end
    % otherwise, linear interpolation
    if t_ba > 0.001
      result(tt) = sample(idx_a) * (t_b - t_grid)/t_ba ...
                     + sample(idx_b) * (t_grid - t_a)/t_ba;
    end
  end
end
```

A.2 k-t BLAST reconstruction

```
function result = reconktb(nt,nk,ns,tlog,klog,...
                                sample,sample_tr,sigma,w_regu)
% k-t BLAST reconstruction
```

```
%
% 2D k-t data at a single frequency encoding position is processed
% presented in Matlab syntax
% exception handling omitted
% [input]: nt, full resolution in t
% [input]: nk, full resolution in k
% [input]: ns, number of samples collected, ns <= nk*nt
% [input]: tlog[ns], timing record of the samples
%              values in (0,1]
% [input]: klog[ns], sampling pattern
%              list of k positions in acquisition order
%              values in 1,2,...,nk
% [input]: sample[ns], samples in k-t space
%              in k corresponding to klog(ns)
%              in t corresponding to tlog(ns)
% [input]: sample_tr[nk,nt], training data in k-t space
%              filtered and gridded
%              in t corresponding to 1/nt, 2/nt,...,1
% [input]: sigma, scalar, noise covariance
% [input]: w_regu, scalar, weight for noise regularization
% [output]: result[nk,nt], reconstructed full data in k-t space
%              in t corresponding to 1/nt, 2/nt,...,1


% build 2D Fourier transform operator OP_F[nk*nt,nk*nt]
%     for any matrix m[ny,nt], ...
%       reshape(m, nk*nt,1) = OP_F * reshape(ifft2(m), nk*nt,1)
for ii = 1:nk*nt
  v_temp = zeros(nk*nt,1);
  v_temp(ii) = 1;
  OP_F(ii,:) = reshape(fft2(reshape(v_temp,nk,nt)),1, nk*nt);
end

% build k-t undersampling operator OP_U[ns,nk*nt]...
```

```
%       from klog[ns], tlog[ns]
%     OP_U * reshape(result, nk*nt,1) = sample
%     each sample is linear interpolated from ...
%       two entries in result[nk,nt]
%     no more than two nonzero entries ...
%       in each row of OP_U[ns,nk*nt]
OP_U = zeros(ns,nk*nt);
% for each sample, find two nearest grid points in t and same k
for ss = 1:ns
  k_now = klog(ss);
  t_now = tlog(ss);
  % find the two grid points in t nearest to t_now
  % t_a <= t_now <= t_b;
  ...;
  t_a = idxa/nt;
  t_b = idxb/nt;
  t_ba = t_b - t_a;
  % save linear interpolation weight values into OP_U[ns,nk*nt]
  OP_U(ss,(k_now-1)*nt+idxa) = (t_b - t_now)/t_ba;
  OP_U(ss,(k_now-1)*nt+idxb) = (t_now - t_a)/t_ba;
end

% calculate temporal baseline data
%     samplebase[nk] in k-space, sample averaged in t
samplebase = zeros(nk,1);
samplecount = zeros(nk,1);
for ss = 1:ns
  samplebase(klog(ss)) += sample(ss);
  samplecount(klog(ss)) += 1;
end
samplebase = samplebase./samplecount;

% calculate samplediff[ns] in k-t space, ...
%        sample[ns] without temporal baseline
```

```
for ss = 1:ns
  samplediff(ss) = sample(ss) - samplebase(klog(ss));
end

% build training operator OP_M[nk*nt,nk*nt]
% inverse Fourier transform training data into x-f space
tr_xf = ifft2(sample_tr);
% remove baseline from training data
tr_xf(:,1) = zeros(nk,1);
% set diagnal entries of OP_M[nk*nt,nk*nt]
OP_M = zeros(nk*nt,nk*nt);
tr_xf_tmp = reshape(tr_xf, nk*nt,1)
for ii = 1:nk*nt
  OP_M(ii,ii) = abs(tr_xf_tmp(ii))^2;
end

% build noise regulation operator OP_SIG[ns,ns]
%     set diagnal entries as w_regu*sigma*sigma
OP_SIG = w_regu*sigma*sigma*eyes(ns,ns);

% build linear equation operator OP_A[ns,ns]
OP_A = OP_U * OP_F * OP_M * OP_F' * OP_U' + OP_SIG;

% solve linear equation OP_A * solution = samplediff
%     solution[ns,1]
solution = inv(OP_A) * samplediff;

% calculate result_xf in x-f space
result_xf = OP_M * OP_F' * OP_U' * solution;

% Fourier transform to k-t space
result_kt = OP_F * result_xf;

% add temporal baseline data
```

```
result = reshape(result_kt,nk,nt) + samplebase * ones(1,nt);
```

A.3 ktVD sampling patterns

```
function n_smp = lssmpktvd(nk,nk_fs,ns)
% print all possible ktVD sampling patterns ...
%     given limits
%
% fixed t resolution (nt): 24 (cardiac phases)
% sampling pattern is always symmetric in k
% k-t space is divided into bands
% in each band the number of samples must be multiples of 24
% presented in Matlab syntax
% exception handling omitted
% [input]: nk, full resolution in k
%              must be a even number
% [input]: nk_fs, number of central k positions fully sampled in t
%              must be a even number
% [input]: ns, number of samples collected
%              ns <= nk*nt
%              ns/24 must be a even number
% [output]: n_smp, total number of possible sampling patterns

nt = 24;
% possible number of samples at each k position
ns_perk = [1, 2, 3, 4, 6, 8, 12, 24];
% reduction factors corresponding to ns_perk
f_redu = nt./ns_perk;
% available number of cardiac cycles in half k-t space
nc_free = (ns/nt - nk_fs)/2;

% loop for all posibilities
n_smp = 0;
```

```
for nc1 = 0:nc_free
  for nc2 = 0:nc_free
    for nc3 = 0:nc_free
      for nc4 = 0:nc_free
        for nc5 = 0:nc_free
          for nc6 = 0:nc_free
            for nc7 = 0:nc_free
              nc_try = [nc1,nc2,nc3,nc4,nc5,nc6,nc7, nk_fs/2];
              nk_try = nc_try .* f_redu;
              % check if total number of samples is correct
              if sum(nc_try) == (ns/nt)/2
                % check if total number of k lines is correct
                if sum(nk_try) == nk/2
                  % a new sampling pattern found
                  n_smp += 1;
                  % calculate a weight for later sorting
                  % weight is total number of k lines ...
                  %     with 6/8/12 samples
                  wt = 2* nc_try(5:7) .* f_redu(5:7).';
                  % save sampling pattern temporarily
                  smp_tmp(n_smp,:) = [nc_try, wt];
                end
              end
            end
          end
        end
      end
    end
  end
end

% sort all sampling patterns in decending order by nc7 and wt
smp_all = sortrows(smp_tmp,[-7 -9]);
```

```
% print all sampling patterns
fprintf(...);
```

A.4 ktVD reconstruction

```
function result = reconktvd(nt,nk,ns,tlog,klog,sample)
% ktVD reconstruction
%
% 2D k-t data at a single frequency encoding position is processed
% presented in Matlab syntax
% exception handling omitted
% [input]: nt, full resolution in t
% [input]: nk, full resolution in k
% [input]: ns, number of samples collected, ns <= nk*nt
% [input]: tlog[ns], timing record of the samples
%              values in (0,1]
% [input]: klog[ns], sampling pattern
%              list of k positions in acquisition order
%              values in 1,2,...,nk
% [input]: sample[ns], samples in k-t space
%              in k corresponding to klog(ns)
%              in t corresponding to tlog(ns)
% [output]: result[nk,nt], reconstructed full data in k-t space
%              in t corresponding to 1/nt, 2/nt,...,1

% loop for each k
for kk = 1:nk
  % find all data corresponding to kk
  samplecount = 0;
  for ss = 1:ns
    if klog(ss) == kk
      samplecount += 1;
      sample_grid(samplecount) = sample(ss);
```

```
      tlog_grid(samplecount) = tlog(ss);
    end
  end
  % temporal gridding
  result(kk,:) = tmpgrid(samplecount,nt,tlog_grid,sample_grid);
  % clean up
  clear sample_grid, tlog_grid;
end
```

Bibliography

[1] GA Donnan, M Fisher, M Macleod, and SM Davis. Stroke. *The Lancet*, 371(9624):1612–1623, 2008.

[2] V Fuster, RA O'Rourke, R Walsh, and P Poole-Wilson. *Hurst's the Heart*. McGraw-Hill, 2008.

[3] RA O'Rourke, V Fuster, RW Alexander, R Roberts, SB King, I Nash, and EN Prystowsky. *Hurst's the Heart Manual of Cardiology*. McGraw-Hill, 2005.

[4] F. Hansen, P. Mangell, B. Sonesson, and T. Lanne. Diameter and compliance in the human common carotid artery–variations with age and sex. *Ultrasound in medicine & biology*, 21(1):1, 1995.

[5] J.B. Thomas, L. Antiga, S.L. Che, J.S. Milner, D.A. Hangan Steinman, J.D. Spence, B.K. Rutt, and D.A. Steinman. Variation in the Carotid Bifurcation Geometry of Young Versus Older Adults Implications for Geometric Risk of Atherosclerosis. *Stroke*, 36(11):2450–2456, 2005.

[6] JAG Rhodin. Architecture of the vessel wall. *Handbook of Physiology*, 2:1–31, 1979.

[7] JD Humphrey and S. Na. Elastodynamics and arterial wall stress. *Annals of biomedical engineering*, 30(4):509, 2002.

[8] GS Berenson, SR Srinivasan, W. Bao, WP Newman, RE Tracy, and WA Wattigney. Association between multiple cardiovascular risk factors and atherosclerosis in children and young adults: The Bogalusa Heart Study. *The New England Journal of Medicine*, 338(23):1650–1656, 1998.

[9] G Howard, LE Wagenknecht, GL Burke, A Diez-Roux, GW Evans, P McGovern, FJ Nieto, and GS Tell. Cigarette smoking and progression of atherosclerosis: The Atherosclerosis Risk in Communities (ARIC) Study. *Journal of the American Medical Association*, 279(2):119–124, 1998.

[10] D Waters, L Higginson, P Gladstone, SJ Boccuzzi, T Cook, and J Lesperance. Effects of Cholesterol Lowering on the Progression of Coronary Atherosclerosis in Women: A Canadian Coronary Atherosclerosis Intervention Trial (CCAIT) Substudy. *Circulation*, 92(9):2404–2410, 1995.

[11] EJ Mayer-Davis, R D'Agostino Jr, AJ Karter, SM Haffner, MJ Rewers, M Saad, and RN Bergman. Intensity and amount of physical activity in relation to insulin sensitivity: the Insulin Resistance Atherosclerosis Study. *Journal of the American Medical Association*, 279(9):669–674, 1998.

[12] J Lynch, N Krause, GA Kaplan, R Salonen, and JT Salonen. Workplace demands, economic reward, and progression of carotid atherosclerosis. *Circulation*, 96(1):302–307, 1997.

[13] AC Nicholson and DP Hajjar. Herpesviruses in Atherosclerosis and Thrombosis Etiologic Agents or Ubiquitous Bystanders? *Arteriosclerosis, Thrombosis, and Vascular Biology*, 18(3):339–348, 1998.

[14] A Laurila, A Bloigu, S Nayha, J Hassi, M Leinonen, and P Saikku. Chronic Chlamydia pneumoniae Infection Is Associated With a Serum Lipid Profile Known to Be a Risk Factor for Atherosclerosis. *Arteriosclerosis, Thrombosis, and Vascular Biology*, 17(11):2910–2913, 1997.

[15] S Glagov, C Zarins, DP Giddens, and DN Ku. Hemodynamics and atherosclerosis. Insights and perspectives gained from studies of human arteries. *Archives of Pathology & Laboratory Medicine*, 112(10):1018–1031, 1988.

[16] DP Giddens, CK Zarins, and S Glagov. The Role of Fluid Mechanics in the Localization and Detection of Atherosclerosis. *Journal of Biomechanical Engineering*, 115:588, 1993.

[17] AM Malek, SL Alper, and S Izumo. Hemodynamic shear stress and its role in atherosclerosis. *Journal of the American Medical Association*, 282(21):2035–2042, 1999.

[18] KS Cunningham and AI Gotlieb. The role of shear stress in the pathogenesis of atherosclerosis. *Laboratory Investigation*, 85(1):9–23, 2005.

[19] Y Fung. *Biomechanics: Circulation*. Springer, 1997.

[20] DN Ku. Blood flow in arteries. *Annual review of fluid mechanics*, 29:399–434, 1997.

[21] CK Zarins, DP Giddens, BK Bharadvaj, VS Sottiurai, RF Mabon, and S Glagov. Carotid bifurcation atherosclerosis. Quantitative correlation of plaque localization with flow velocity profiles and wall shear stress. *Circulation Research*, 53(4):502–514, 1983.

[22] DN Ku, DP Giddens, CK Zarins, and S Glagov. Pulsatile flow and atherosclerosis in the human carotid bifurcation. Positive correlation between plaque location and low oscillating shear stress. *Arteriosclerosis, Thrombosis, and Vascular Biology*, 5(3):293–302, 1985.

[23] DL FRY. Certain histological and chemical responses of the vascular interface to acutely induced mechanical stress in the aorta of the dog. *Circulation Research*, 24(1):93–108, 1969.

[24] CG Caro, JM Fitz-Gerald, and RC Schroter. Atheroma and arterial wall shear. Observation, correlation and proposal of a shear dependent mass transfer mechanism for atherogenesis. *Proceedings of the Royal Society of London*, 177(1046):109–133, 1971.

[25] BK Bharadvaj, RF Mabon, and DP Giddens. Steady flow in a model of the human carotid bifurcation. Part I: flow visualization. *Journal of Biomechanics*, 15(5):349–362, 1982.

[26] MJ Levesque and RM Nerem. The elongation and orientation of cultured endothelial cells in response to shear stress. *Journal of biomechanical engineering*, 107:341, 1985.

[27] MJ Levesque, D. Liepsch, S. Moravec, and RM Nerem. Correlation of endothelial cell shape and wall shear stress in a stenosed dog aorta. *Arteriosclerosis, Thrombosis, and Vascular Biology*, 6(2):220–229, 1986.

[28] M. Okano and Y. Yoshida. Junction complexes of endothelial cells in atherosclerosis prone and atherosclerosis resistant regions on flow dividers of brachiocephalic bifurcations in the rabbit aorta. *Biorheology(Oxford)*, 31(2):155–161, 1994.

[29] B.J. Ballermann, A. Dardik, E. Eng, and A. Liu. Shear stress and the endothelium. *Kidney International*, 54:S100–S108, 1998.

[30] O. Traub and B.C. Berk. Laminar shear stress mechanisms by which endothelial cells transduce an atheroprotective force. *Arteriosclerosis, thrombosis, and vascular biology*, 18(5):677–685, 1998.

[31] JB Sharefkin, SL Diamond, SG Eskin, LV McIntire, and CW Dieffenbach. Fluid flow decreases preproendothelin mRNA levels and suppresses endothelin-1 peptide release in cultured human endothelial cells. *Journal of vascular surgery*, 14(1):1, 1991.

[32] D.C. Chappell, S.E. Varner, R.M. Nerem, R.M. Medford, and R.W. Alexander. Oscillatory shear stress stimulates adhesion molecule expression in cultured human endothelium. *Circulation research*, 82(5):532–539, 1998.

[33] W.R. Milnor. *Hemodynamics*. Williams & Wilkins Baltimore, 1989.

[34] Z. Lou, W.J. Yang, and P.D. Stein. Errors in the estimation of arterial wall shear rates that result from curve fitting of velocity profiles. *Journal of biomechanics*, 26(4-5):383–390, 1993.

[35] J.N. Osinnski, D.N. Ku, S. Mukundan Jr, F. Loth, and R.I. Pettigrew. Determination of wall shear stress in the aorta with the use of MR phase velocity mapping. *Journal of Magnetic Resonance Imaging*, 5(6), 1995.

[36] A.M. Shaaban and A.J. Duerinckx. Wall Shear Stress and Early Atherosclerosis A Review. *American Journal of Roentgenology*, 174(6):1657–1665, 2000.

[37] D.S. Long, M.L. Smith, A.R. Pries, K. Ley, and E.R. Damiano. Microviscometry reveals reduced blood viscosity and altered shear rate and shear stress profiles in microvessels after hemodilution. *Proceedings of the National Academy of Sciences*, 101(27):10060–10065, 2004.

[38] R. Fahrig, AJ Fox, S. Lownie, and DW Holdsworth. Use of a C-arm system to generate true three-dimensional computed rotational angiograms: preliminary in vitro and in vivo results. *American Journal of Neuroradiology*, 18(8):1507–1514, 1997.

[39] S.D. Shpilfoygel, R.A. Close, D.J. Valentino, and G.R. Duckwiler. X-Ray videodensitometric methods for blood flow and velocity measurement: A critical review of literature. *Medical Physics*, 27:2008, 2000.

[40] I. Waechter, J. Bredno, R. Hermans, J. Weese, D.C. Barratt, and D.J. Hawkes. Model-based blood flow quantification from rotational angiography. *Medical Image Analysis*, 12(5):586–602, 2008.

[41] W. Rutishauser, G. Noseda, W.D. Bussmann, and B. Preter. Blood flow measurement through single coronary arteries by roentgen densitometry: part II. Right coronary artery flow in conscious man. *American Journal of Roentgenology*, 109(1):21–24, 1970.

[42] H. Schmitt, M. Grass, R. Suurmond, T. Kohler, V. Rasche, S. Hahnel, and S. Heiland. Reconstruction of blood propagation in three-dimensional rotational X-ray angiography (3D-RA). *Computerized Medical Imaging and Graphics*, 29(7):507–520, 2005.

[43] H. Bogunovic and S. Loncaric. Blood Flow and Velocity Estimation Based on Vessel Transit Time by Combining 2D and 3D X-ray Angiography. In *MMIC-CAI*, volume 4191, page 117. Springer, 2006.

[44] ACF Colchester, DJ Hawkes, JNH Brunt, GH Du Boulay, and A. Wallis. Pulsatile blood flow measurements with the aid of 3-D reconstruction from dynamic angiographic recordings. In *Information Processing in Medical Imaging*, volume 6, pages 247–265, 1986.

[45] KS Rhode, T. Lambrou, DJ Hawkes, and AM Seifalian. Novel approaches to the measurement of arterial blood flow from dynamic digital X-ray images. *IEEE transactions on medical imaging*, 24(4):500–513, 2005.

[46] U. Efron, RR Price, CW Smith, and AB Brill. A method to determine the instantaneous blood-flow using cine-or video-densitometric data. In *Proc. SPIE*, volume 143, pages 154–161, 1978.

[47] J.M. Fitzpatrick. A method for calculating velocity in time dependent images based on the continuity equation. In *Proc. IEEE Computer Vision and Pattern Recognition*, pages 78–81, 1985.

[48] K. Rhode, G. Ennew, T. Lambrou, D. Hawkes, and A. Seifalian. The Measurement of Blood Flow from Dynamic Digital X-Ray Images Using a Weighted Optical Flow Algorithm: Validation in a Moving-Vessel Flow Phantom. In *Proc. Medical Image Understanding and Analysis: Cardiovascular Image Analysis*, 2001.

[49] S.P. Huan, B.E. Chapman, J.B. Muhlestein, D.D. Blatter, and D.L. Parker. Computer Simulation of Convection and Diffusion Effects on Velocity Estimations from X-Ray Contrast Density Time Curves. In *Proc. Information Processing in Medical Imaging*, volume 1230, pages 453–458, 1997.

[50] JA Moore, B.K. Rutt, S.J. Karlik, K. Yin, and C. Ross Ethier. Computational blood flow modeling based on in vivo measurements. *Annals of biomedical engineering*, 27(5):627–640, 1999.

[51] JG Myers, JA Moore, M. Ojha, KW Johnston, and CR Ethier. Factors influencing blood flow patterns in the human right coronary artery. *Annals of biomedical engineering*, 29(2):109–120, 2001.

[52] P. Bergeron, R. Carrier, D. Roy, N. Blais, and J. Raymond. Radiation doses to patients in neurointerventional procedures. *American Journal of Neuroradiology*, 15(10):1809–1812, 1994.

[53] G.A. Holloway and D.W. Watkins. Laser Doppler measurement of cutaneous blood flow. *Journal of Investigative Dermatology*, 69(3):306–309, 1977.

[54] LE Drain. *The laser Doppler techniques*. Wiley-Interscience, Chichester, England, 1980.

[55] V. Rajan, B. Varghese, T.G. van Leeuwen, and W. Steenbergen. Review of methodological developments in laser Doppler flowmetry. *Lasers in Medical Science*, 24(2):269–283, 2009.

[56] JCA Doppler. On the coloured light of the double stars and certain other stars of the heavens. *Presentation at the Royal Bohemian Society of Sciences*, 1842.

[57] J.D. Briers. Laser Doppler, speckle and related techniques for blood perfusion mapping and imaging. *Physiological Measurement*, 22(4):35, 2001.

[58] DN Ku and DP Giddens. Laser Doppler anemometer measurements of pulsatile flow in a model carotid bifurcation. *Journal of biomechanics*, 20(4):407–421, 1987.

[59] P.N.T. Wells. *Physical principles of ultrasonic diagnosis*. Academic Press New York, 1969.

[60] PNT Wells. Ultrasonic colour flow imaging. *Physics in Medicine and Biology*, 39:2113–2145, 1994.

[61] DB Reid, M. Douglas, and EB Diethrich. The clinical value of three-dimensional intravascular ultrasound imaging. *Journal of endovascular surgery: the official journal of the International Society for Endovascular Surgery*, 2(4):356–364, 1995.

[62] DB Reid, EB Diethrich, P. Marx, and R. Wrasper. Intravascular ultrasound assessment in carotid interventions. *Journal of endovascular surgery: the official journal of the International Society for Endovascular Surgery*, 3(2):203, 1996.

[63] BB Goldberg. Ultrasound contrast agents. *Clinics in diagnostic ultrasound*, 28:35, 1993.

[64] V. Sboros, CM Moran, SD Pye, and WN McDicken. The behaviour of individual contrast agent microbubbles. *Ultrasound in medicine & biology*, 29(5):687, 2003.

[65] P.L.P. Allan and P.A. Dubbins. *Clinical Doppler Ultrasound*. Churchill Livingstone, 2006.

[66] P. Atkinson. A fundamental interpretation of ultrasonic doppler velocimeters. *Ultrasound in medicine & biology*, 2(2):107, 1976.

[67] RW Gill. Measurement of blood flow by ultrasound: accuracy and sources of error. *Ultrasound in medicine & biology*, 11(4):625–641, 1985.

[68] PM Embree and WD O'Brien Jr. The accurate ultrasonic measurement of the volume flow of blood by time domain correlation. In *IEEE 1985 Ultrasonics Symposium*, pages 963–966, 1985.

[69] O. Bonnefous and P. Pesqué. Time domain formulation of pulse-Doppler ultrasound and blood velocity estimation by cross correlation. *Ultrasonic imaging*, 8(2):73, 1986.

[70] GE Trahey, SM Hubbard, and OT Von Ramm. Angle independent ultrasonic blood flow detection by frame-to-frame correlation of B-mode images. *Ultrasonics*, 26(5):271–276, 1988.

[71] LN Bohs, BJ Geiman, ME Anderson, SC Gebhart, and GE Trahey. Speckle tracking for multi-dimensional flow estimation. *Ultrasonics*, 38(1-8):369–375, 2000.

[72] A. Gnasso, C. Carallo, C. Irace, V. Spagnuolo, G. De Novara, P.L. Mattioli, and A. Pujia. Association between intima-media thickness and wall shear stress in common carotid arteries in healthy male subjects. *Circulation*, 94(12):3257–3262, 1996.

[73] A. Gnasso, C. Irace, C. Carallo, M.S. De Franceschi, C. Motti, P.L. Mattioli, and A. Pujia. In vivo association between low wall shear stress and plaque in subjects with asymmetrical carotid atherosclerosis. *Stroke*, 28(5):993–998, 1997.

[74] A.P.G. Hoeks, S.K. Samijo, P.J. Brands, and R.S. Reneman. Noninvasive determination of shear-rate distribution across the arterial lumen. *Hypertension*, 26(1):26–33, 1995.

[75] APG Hoeks, TGJ Arts, PJ Brands, and RS Reneman. Comparison of the performance of the RF cross correlation and Doppler autocorrelation technique to estimate the mean velocity of simulated ultrasound signals. *Ultrasound in medicine & biology*, 19(9):727–740, 1993.

[76] PJ Brands, JM Willigers, LA Ledoux, RS Reneman, and AP Hoeks. A noninvasive method to estimate pulse wave velocity in arteries locally by means of ultrasound. *Ultrasound in medicine & biology*, 24(9):1325, 1998.

[77] J.E. Jorgensen, D.N. Campau, and D.W. Baker. Physical characteristics and mathematical modelling of the pulsed ultrasonic flowmeter. *Medical and Biological Engineering and Computing*, 11(4):404–421, 1973.

[78] DW Baker and RE Daigle. Noninvasive ultrasonic flowmetry. *Cardiovascular Flow Dynamics and Measurements*, pages 151–189, 1977.

[79] PE Hughes and TV How. Quantitative measurement of wall shear rate by pulsed Doppler ultrasound. *Journal of Medical Engineering and Technology*, 17(2):58–64, 1993.

[80] P. Flaud, A. Bensalah, and P. Peronneau. Deconvolution process in measurement of arterial velocity profiles via an ultrasonic pulsed Doppler velocimeter for evaluation of the wall shear rate. *Ultrasound in medicine & biology*, 23(3):425, 1997.

[81] T.R. Nelson and D.H. Pretorius. Three-dimensional ultrasound imaging. *Ultrasound in Medicine and Biology*, 24:1243–1270, 1998.

[82] CP Markou and DN Ku. Accuracy of velocity and shear rate measurements using pulsed Doppler ultrasound: a comparison of signal analysis techniques. *Ultrasound in Medicine & Biology*, 17(8):803–814, 1991.

[83] PR Hoskins. Accuracy of maximum velocity estimates made using Doppler ultrasound systems. *British journal of radiology*, 69(818):172–177, 1996.

[84] E.Y.L. Lui, A.H. Steinman, R.S.C. Cobbold, and K.W. Johnston. Human factors as a source of error in peak Doppler velocity measurement. *Journal of Vascular Surgery*, 42(5):972–972, 2005.

[85] PA Peronneau, JP Bournat, A. Bugnon, A. Barbet, and M. Xhaard. Theoretical and practical aspects of pulsed Doppler flowmetry: real-time application to the measure of instantaneous velocity profiles in vitro and in vivo. In *Cardiovascular Applications of Ultrasound*, page 66, 1974.

[86] RS Reneman, T. Arts, and AP Hoeks. Wall shear stress–an important determinant of endothelial cell function and structure–in the arterial system in vivo. Discrepancies with theory. *Journal of vascular research*, 43(3):251, 2006.

[87] SK Samijo, JM Willigers, PJ Brands, R. Barkhuysen, RS Reneman, PJ Kitslaar, and AP Hoeks. Reproducibility of shear rate and shear stress assessment by

means of ultrasound in the common carotid artery of young human males and females. *Ultrasound in medicine & biology*, 23(4):583, 1997.

[88] EM Haacke, RW Brown, MR Thompson, and R Venkatesan. *Magnetic Resonance Imaging: Physical Principles and Sequence Design*. John Wiley & Sons, 1999.

[89] P van Dijk. Direct Cardiac NMR Imaging of Heart Wall and Blood Flow Velocity. *Journal of Computer Assisted Tomography*, 8(3):429, 1984.

[90] DJ Bryant, JA Payne, DN Firmin, and DB Longmore. Measurement of Flow with NMR Imaging Using a Gradient Pulse and Phase Difference Technique. *Journal of Computer Assisted Tomography*, 8(4):588, 1984.

[91] P.D. Gatehouse, J. Keegan, L.A. Crowe, S. Masood, R.H. Mohiaddin, K.F. Kreitner, and D.N. Firmin. Applications of phase-contrast flow and velocity imaging in cardiovascular MRI. *European radiology*, 15(10):2172–2184, 2005.

[92] JG Strang, RJ Herfkens, and NJ Pelc. Voxel size effects on vascular shear measurement. In *Proceedings of 2nd meetings of the International Society of Magnetic Resonance in Medicine.*, volume 2, page 1002, 1994.

[93] R. Frayne and B.K. Rutt. Measurement of fluid-shear rate by Fourier-encoded velocity imaging. *Magnetic Resonance in Medicine*, 34(3), 1995.

[94] S. Oyre, S. Ringgaard, S. Kozerke, W.P. Paaske, M. Erlandsen, P. Boesiger, and E.M. Pedersen. Accurate noninvasive quantitation of blood flow, cross-sectional lumen vessel area and wall shear stress by three-dimensional paraboloid modeling of magnetic resonance imaging velocity data. *Journal of the American College of Cardiology*, 32(1):128–134, 1998.

[95] P. Turski, F. Korosec, and CM Anderson. *Clinical magnetic resonance angiography*. Raven Press New York, 1993.

[96] G.G. Berntson, J. Thomas Bigger, D.L. Eckberg, P. Grossman, P.G. Kaufmann, M. Malik, H.N. Nagaraja, S.W. Porges, J.P. Saul, P.H. Stone, et al. Heart rate variability: origins, methods, and interpretive caveats. *Psychophysiology*, 34(6):623–648, 1997.

[97] H. Sakuma, N. Kawada, H. Kubo, Y. Nishide, K. Takano, N. Kato, and K. Takeda. Effect of breath holding on blood flow measurement using fast velocity encoded cine MRI. *Magnetic Resonance in Medicine*, 45(2), 2001.

[98] R.J. van den Hout, H.J. Lamb, J.G. van den Aardweg, R. Schot, P. Steendijk, E.E. van der Wall, J.J. Bax, and A. de Roos. Real-Time MR Imaging of Aortic

Flow: Influence of Breathing on Left Ventricular Stroke Volume in Chronic Obstructive Pulmonary Disease 1. *Radiology*, 229(2):513–519, 2003.

[99] G.P. Chatzimavroudis, H. Zhang, S.S. Halliburton, J.R. Moore, O.P. Simonetti, P.R. Schvartzman, A.E. Stillman, and R.D. White. Clinical blood flow quantification with segmented k-space magnetic resonance phase velocity mapping. *Journal of Magnetic Resonance Imaging*, 17(1):65–71, 2003.

[100] E. Laffon, R. Lecesne, V. De Ledinghen, N. Valli, P. Couzigou, F. Laurent, J. Drouillard, D. Ducassou, and J.L. Barat. Segmented 5 Versus Nonsegmented Flow Quantitation: Comparison of Portal Vein Flow Measurements. *Investigative radiology*, 34(3):176, 1999.

[101] MW de Haan, M. Kouwenhoven, AG Kessels, and JM van Engelshoven. Renal artery blood flow: quantification with breath-hold or respiratory triggered phase-contrast MR imaging. *European radiology*, 10(7):1133, 2000.

[102] K.S. Nayak, B.A. Hargreaves, B.S. Hu, D.G. Nishimura, J.M. Pauly, and C.H. Meyer. Spiral balanced steady-state free precession cardiac imaging. *Magnetic Resonance in Medicine*, 53(6), 2005.

[103] C. Tang, D.D. Blatter, and D.L. Parker. Accuracy of phase-contrast flow measurements in the presence of partial-volume effects. *Journal of Magnetic Resonance Imaging*, 3(2), 1993.

[104] R. Frayne, D.A. Steinman, B.K. Rutt, and C.R. Ethier. Accuracy of MR phase contrast velocity measurements for unsteady flow. *Journal of Magnetic Resonance Imaging*, 5(4), 1995.

[105] D. Meier, S. Maier, and P. Bosiger. Quantitative flow measurements on phantoms and on blood vessels with MR. *Magnetic Resonance in Medicine*, 8(1), 1988.

[106] DN Firmin, GL Nayler, PJ Kilner, and DB Longmore. The application of phase shifts in NMR for flow measurement. *Magnetic resonance in medicine*, 14(2):230, 1990.

[107] CE Spritzer, NJ Pelc, JN Lee, AJ Evans, HD Sostman, and SJ Riederer. Rapid MR imaging of blood flow with a phase-sensitive, limited-flip-angle, gradient recalled pulse sequence: preliminary experience. *Radiology*, 176(1):255–262, 1990.

[108] DN Ku, CL Biancheri, RI Pettigrew, JW Peifer, CP Markou, and H. Engels. Evaluation of magnetic resonance velocimetry for steady flow. *Journal of biomechanical engineering*, 112(4):464, 1990.

[109] J.M. Siegel, J.N. Oshinski, R.I. Pettigrew, and D.N. Ku. The accuracy of magnetic resonance phase velocity measurements in stenotic flow. *Journal of biomechanics*, 29(12):1665–1672, 1996.

[110] Y. Papaharilaou, D.J. Doorly, and S.J. Sherwin. Assessing the accuracy of two-dimensional phase-contrast MRI measurements of complex unsteady flows. *Journal of Magnetic Resonance Imaging*, 14(6):714–723, 2001.

[111] G.P. Chatzimavroudis, J.N. Oshinski, R.H. Franch, P.G. Walker, A.P. Yoganathan, and R.I. Pettigrew. Evaluation of the precision of magnetic resonance phase velocity mapping for blood flow measurements. *Journal of Cardiovascular Magnetic Resonance*, 3(1):11–19, 2001.

[112] D.A. Steinman. Image-based computational fluid dynamics modeling in realistic arterial geometries. *Annals of biomedical Engineering*, 30(4):483–497, 2002.

[113] MH Friedman, OJ Deters, CB Bargeron, GM Hutchins, and FF Mark. Shear-dependent thickening of the human arterial intima. *Atherosclerosis*, 60(2):161, 1986.

[114] R. Krams, JJ Wentzel, JAF Oomen, R. Vinke, JCH Schuurbiers, PJ De Feyter, PW Serruys, and CJ Slager. Evaluation of Endothelial Shear Stress and 3D Geometry as Factors Determining the Development of Atherosclerosis and Remodeling in Human Coronary Arteries in Vivo Combining 3D Reconstruction from Angiography and IVUS (ANGUS) with Computational Fluid Dynamics. *Arteriosclerosis, thrombosis, and vascular biology*, 17(10):2061–2065, 1997.

[115] OJ Ilegbusi, Z. Hu, R. Nesto, S. Waxman, D. Cyganski, J. Kilian, PH Stone, and CL Feldman. Determination of blood flow and endothelial shear stress in human coronary artery in vivo. *The Journal of invasive cardiology*, 11(11):667, 1999.

[116] MR Kaazempur-Mofrad and CR Ethier. Mass transport in an anatomically realistic human right coronary artery. *Annals of Biomedical Engineering*, 29(2):121–127, 2001.

[117] JS Milner, JA Moore, BK Rutt, and DA Steinman. Hemodynamics of human carotid artery bifurcations: computational studies with models reconstructed from magnetic resonance imaging of normal subjects. *Journal of vascular surgery*, 28(1):143, 1998.

[118] D.A. Steinman, J.B. Thomas, H.M. Ladak, J.S. Milner, B.K. Rutt, and J.D. Spence. Reconstruction of carotid bifurcation hemodynamics and wall thickness using computational fluid dynamics and MRI. *Magnetic Resonance in Medicine*, 47(1), 2002.

[119] SZ Zhao, XY Xu, AD Hughes, SA Thom, AV Stanton, B. Ariff, and Q. Long. Blood flow and vessel mechanics in a physiologically realistic model of a human carotid arterial bifurcation. *Journal of Biomechanics*, 33(8):975–984, 2000.

[120] K. Perktold, M. Hofer, G. Rappitsch, M. Loew, BD Kuban, and MH Friedman. Validated computation of physiologic flow in a realistic coronary artery branch. *Journal of biomechanics*, 31(3):217–228, 1997.

[121] R. Botnar, G. Rappitsch, M. Beat Scheidegger, D. Liepsch, K. Perktold, and P. Boesiger. Hemodynamics in the carotid artery bifurcation: a comparison between numerical simulations and in vitro MRI measurements. *Journal of Biomechanics*, 33(2):137–144, 2000.

[122] Q. Long, X.Y. Xu, B. Ariff, S.A. Thom, A.D. Hughes, and A.V. Stanton. Reconstruction of blood flow patterns in a human carotid bifurcation: a combined CFD and MRI study. *Journal of Magnetic Resonance Imaging*, 11(3), 2000.

[123] Q. Long, XY Xu, M. Bourne, and TM Griffith. Numerical study of blood flow in an anatomically realistic aorto-iliac bifurcation generated from MRI data. *Magnetic resonance in medicine*, 43(4):565, 2000.

[124] J.A. Moore, D.A. Steinman, and C. Ross Ethier. Computational blood flow modelling Errors associated with reconstructing finite element models from magnetic resonance images. *Journal of Biomechanics*, 31(2):179–184, 1997.

[125] JA Moore, DA Steinman, DW Holdsworth, and CR Ethier. Accuracy of computational hemodynamics in complex arterial geometries reconstructed from magnetic resonance imaging. *Annals of biomedical engineering*, 27(1):32–41, 1999.

[126] S. Prakash and C.R. Ethier. Requirements for mesh resolution in 3D computational hemodynamics. *Journal of biomechanical engineering*, 123:134, 2001.

[127] J.R. Cebral, R. Lohner, O. Soto, and P.J. Yim. On the modeling of carotid artery blood flow from magnetic resonance images. In *Proceedings of ASME Bioengineering Conference*, volume 50, pages 619–620. ASME, 2001.

[128] S. Kozerke and J. Tsao. Reduced data acquisition methods in cardiac imaging. *Topics in Magnetic Resonance Imaging*, 15(3):161, 2004.

[129] J. Tsao, P. Boesiger, and K.P. Pruessmann. kt BLAST and kt SENSE: dynamic MRI with high frame rate exploiting spatiotemporal correlations. *Magnetic Resonance in Medicine*, 50(5):1031–1042, 2003.

[130] S. Kozerke, J. Tsao, R. Razavi, and P. Boesiger. Accelerating cardiac cine 3D imaging using kt BLAST. *Magnetic Resonance in Medicine*, 52(1), 2004.

[131] C. Baltes, S. Kozerke, M.S. Hansen, KP Pruessmann, J. Tsao, and P. Boesiger. Accelerating cine phase-contrast flow measurements using kt BLAST and kt SENSE. *Magn Reson Med*, 54(6):1430–1438, 2005.

[132] C. Jahnke, E. Nagel, R. Gebker, A. Bornstedt, B. Schnackenburg, S. Kozerke, E. Fleck, and I. Paetsch. Four-dimensional single breathhold magnetic resonance imaging using kt-BLAST enables reliable assessment of left-and right-ventricular volumes and mass. *Journal of Magnetic Resonance Imaging*, 25(4), 2007.

[133] S. Huber, R. Muthupillai, H. Mojibian, B. Cheong, M. Kouwenhoven, and S.D. Flamm. Rapid assessment of regional and global left ventricular function using three-dimensional kt BLAST imaging. *Magnetic Resonance Imaging*, 26(6):727–738, 2008.

[134] A. Stadlbauer, W. van der Riet, G. Crelier, and E. Salomonowitz. Accelerated time-resolved three-dimensional MR velocity mapping of blood flow patterns in the aorta using SENSE and kt BLAST. *European Journal of Radiology*, 2009.

[135] A. Stadlbauer, W. van der Riet, S. Globits, G. Crelier, and E. Salomonowitz. Accelerated phase-contrast MR imaging: Comparison of kt BLAST with SENSE and doppler ultrasound for velocity and flow measurements in the aorta. *Journal of Magnetic Resonance Imaging*, 29(4), 2009.

[136] I. Marshall. Feasibility of kt BLAST technique for measuring seven-dimensional fluid flow. *Journal of Magnetic Resonance Imaging*, 23(2), 2006.

[137] EM Purcell, HC Torrey, and RV Pound. Resonance Absorption by Nuclear Magnetic Moments in a Solid. *Physical Review*, 69(1-2):37–38, 1946.

[138] F Bloch, WW Hansen, and M Packard. Nuclear Induction. *Physical Review*, 70(7-8):460–474, 1946.

[139] PC Lauterbur. Image formation by induced local interactions: examples employing nuclear magnetic resonance. *Nature*, 242(5394):190–191, 1973.

[140] P Mansfield and PK Grannell. NMR diffraction in solids? *Journal of Physics C: Solid State Physics*, 6(22):422–426, 1973.

[141] A Abragam. *The Principles of Nuclear Magnetism*. Oxford University Press, 1961.

[142] TC Farrar and ED Becker. *Pulse and Fourier Transform NMR: Introduction to Theory and Methods*. Academic Press, 1971.

[143] PT Callaghan. *Principles of Nuclear Magnetic Resonance Microscopy*. Oxford University Press, 1993.

[144] Z Liang and PC Lauterbur. *principles of magnetic resonance imaging: a signal processing perspective*. IEEE Press, 1999.

[145] MA Brown and CS Richard. *MRI: Basic Principles and Applications*. Wiley-Liss, 1995.

[146] P. Mansfield. Imaging by nuclear magnetic resonance. *Journal of Physics E: Scientific Instruments*, 21:18, 1988.

[147] EL Hahn. Spin Echoes. *Physical Review*, 80(4):580–594, 1950.

[148] HY Carr and EM Purcell. Effects of Diffusion on Free Precession in Nuclear Magnetic Resonance Experiments. *Physical Review*, 94(3):630–638, 1954.

[149] S Ogawa, TM Lee, AR Kay, and DW Tank. Brain Magnetic Resonance Imaging with Contrast Dependent on Blood Oxygenation. *Proceedings of the National Academy of Sciences*, 87(24):9868–9872, 1990.

[150] D.W. McRobbie, E.A. Moore, M.J. Graves, and M.R. Prince. *MRI from Picture to Proton*. Cambridge University Press, 2003.

[151] D Matthaei, A Haase, J Frahm, H Bomsdorf, and W Vollmann. Multiple chemical shift selective (CHESS) MR imaging using stimulated echoes. *Radiology*, 160(3):791, 1986.

[152] J Frahm, KD Merboldt, and W Hanicke. Direct FLASH MR imaging of magnetic field inhomogeneities by gradient compensation. *Magnetic Resonance in Medicine*, 6(4):474–480, 1988.

[153] ZH Cho and YM Ro. Reduction of susceptibility artifact in gradient-echo imaging. *Magnetic Resonance in Medicine*, 23(1):193–200, 1992.

[154] TS Sumanaweera, GH Glover, TO Binford, and JR Adler. MR susceptibility misregistration correction. *IEEE Transactions on Medical Imaging*, 12(2):251–259, 1993.

[155] DA Yablonskiy and EM Haacke. Theory of NMR signal behavior in magnetically inhomogeneous tissues: the static dephasing regime. *Magnetic Resonance in Medicine*, 32(6):749–763, 1994.

[156] JM Peeters, C Bos, and CJ Bakker. Analysis and correction of gradient nonlinearity and B0 inhomogeneity related scaling errors in two-dimensional phase contrast flow measurements. *Magnetic Resonance in Medicine*, 53(1):126–133, 2005.

[157] P van der Meulen, JP Groen, and JJ Cuppen. Very fast MR imaging by field echoes and small angle excitation. *Magnetic Resonance Imaging*, 3(3):297–299, 1985.

[158] J Frahm, A Haase, and D Matthaei. Rapid NMR imaging of dynamic processes using the FLASH technique. *Magnetic Resonance in Medicine*, 3(2):321–327, 1986.

[159] K Sekihara. Steady-state magnetizations in rapid NMR imaging using small flip angles and short repetition intervals. *IEEE transactions on medical imaging*, 6(2):157–164, 1987.

[160] GW Lenz, EM Haacke, and RD White. Retrospective cardiac gating: a review of technical aspects and future directions. *Magnetic Resonance Imaging*, 7(5):445–455, 1989.

[161] R Ashman. The normal duration of the QT interval. *American Heart Journal*, 23:522–534, 1942.

[162] AM Katz. *Physiology of the Heart*. Raven Press, 1977.

[163] Y Tao and I Marshall. Test of two heart rate variation models for retrospectively gated carotid scan. In *Proceedings of the British Chapter of the ISMRM*, volume 14, page 38, 2008.

[164] JD O'sullivan. A fast sinc function gridding algorithm for Fourier inversion in computer tomography. *IEEE Transactions on Medical Imaging*, 4(4):200–207, 1985.

[165] DT Sandwell. Biharmonic spline interpolation of GEOS-3 and SEASAT altimeter data. *Geophysical Research Letters*, 14(2):139–142, 1987.

[166] H Schomberg and J Timmer. The gridding method for image reconstruction by Fourier transformation. *IEEE Transactions on Medical Imaging*, 14(3):596–607, 1995.

[167] CB Barber, DP Dobkin, and H Huhdanpaa. The quickhull algorithm for convex hulls. *ACM Transactions on Mathematical Software*, 22(4):469–483, 1996.

[168] JG Pipe and P Menon. Sampling density compensation in MRI: rationale and an iterative numerical solution. *Magnetic Resonance in Medicine*, 41(1):179–186, 1999.

[169] D Rosenfeld. New approach to gridding using regularization and estimation theory. *Magnetic resonance in medicine*, 48(1):193–202, 2002.

[170] DN Firmin, GL Nayler, PJ Kilner, and DB Longmore. The application of phase shifts in NMR for flow measurement. *Magnetic Resonance in Medicine*, 14(2):230–241, 1990.

[171] NJ Pelc, FG Sommer, KC Li, TJ Brosnan, RJ Herfkens, and DR Enzmann. Quantitative magnetic resonance flow imaging. *Magnetic Resonance Quarterly*, 10(3):125–147, 1994.

[172] EL Hahn. Detection of sea-water motion by nuclear precession. *Journal of Geophysical Research*, 65(2):776–777, 1960.

[173] EO Stejskal and JE Tanner. Spin Diffusion Measurements: Spin Echoes in the Presence of a Time-Dependent Field Gradient. *the Journal of Chemical Physics*, 42(1):288, 1965.

[174] T Grover and JR Singer. NMR Spin-Echo Flow Measurements. *Journal of Applied Physics*, 42, 1971.

[175] AN Garroway. Velocity measurements in flowing fluids by MNR. *Journal of Physics D: Applied Physics*, 7(14):159–163, 1974.

[176] PR Moran. A flow velocity zeugmatographic interlace for NMR imaging in humans. *Magnetic Resonance Imaging*, 1(4):197–203, 1982.

[177] TE Conturo and GD Smith. Signal-to-noise in phase angle reconstruction: dynamic range extension using phase reference offsets. *Magnetic Resonance in Medicine*, 15(3):420–437, 1990.

[178] NJ Pelc, MA Bernstein, A Shimakawa, and GH Glover. Encoding strategies for three-direction phase-contrast MR imaging of flow. *Journal of Magnetic Resonance Imaging*, 1(4):405–413, 1991.

[179] DA Feinberg, JD Hale, JC Watts, L Kaufman, and A Mark. Halving MR imaging time by conjugation: demonstration at 3. 5 kG. *Radiology*, 161(2):527–531, 1986.

[180] P Margosian, F Schmitt, and D Purdy. Faster MR imaging: Imaging with half the data. *Health Care Instrumentation*, 1(6):195–197, 1986.

[181] DC Noll, DG Nishimura, and A Macovski. Homodyne detection in magnetic resonance imaging. *IEEE Transactions on Medical Imaging*, 10(2):154–163, 1991.

[182] EM Haackea, ED Lindskogjb, and W Lin. A fast, iterative, partial-fourier technique capable of local phase recovery. *Journal of Magnetic Resonance*, 92(1):126–145, 1991.

[183] G McGibney, MR Smith, ST Nichols, and A Crawley. Quantitative evaluation of several partial Fourier reconstruction algorithms used in MRI. *Magnetic Resonance in Medicine*, 30(1):51–59, 1993.

[184] DM Spielman, JM Pauly, and CH Meyer. Magnetic resonance fluoroscopy using spirals with variable sampling densities. *Magnetic Resonance in Medicine*, 34(3):388–394, 1995.

[185] DC Peters, FR Korosec, TM Grist, WF Block, JE Holden, KK Vigen, and CA Mistretta. Undersampled Projection Reconstruction Applied to MR Angiography. *Magnetic Resonance in Medicine*, 43:91–101, 2000.

[186] JG Pipe. Reconstructing MR images from undersampled data: Data-weighting considerations. *Magnetic Resonance in Medicine*, 43(6):867–875, 2000.

[187] X Hu and T Parrish. Reduction of field of view for dynamic imaging. *Magnetic Resonance in Medicine*, 31(6):691–694, 1994.

[188] JO Fredrickson and NJ Pelc. Temporal resolution improvement in dynamic imaging. *Magnetic Resonance in Medicine*, 35(4):621–625, 1996.

[189] WE Kyriakos, LP Panych, GP Zientara, and FA Jolesz. Implementation of a reduced field-of-view method for dynamic MR imaging using navigator echoes. *Journal of Magnetic Resonance Imaging*, 7(2):376–81, 1997.

[190] K Scheffler and J Hennig. Reduced circular field-of-view imaging. *Magnetic Resonance in Medicine*, 40(3):474–80, 1998.

[191] ME Brummer, D Moratal-Perez, CY Hong, RI Pettigrew, J Millet-Roig, and WT Dixon. Noquist: Reduced Field-of-View Imaging by Direct Fourier Inversion. *Magnetic Resonance in Medicine*, 51(2):331–342, 2004.

[192] DK Sodickson and WJ Manning. Simultaneous acquisition of spatial harmonics (SMASH): fast imaging with radiofrequency coil arrays. *Magnetic Resonance in Medicine*, 38(4):591–603, 1997.

[193] KP Pruessmann, M Weiger, MB Scheidegger, and P Boesiger. SENSE: sensitivity encoding for fast MRI. *Magnetic Resonance in Medicine*, 42(5):952–962, 1999.

[194] JJ van Vaals, ME Brummer, WT Dixon, HH Tuithof, H Engels, RC Nelson, BM Gerety, JL Chezmar, and JA den Boer. "Keyhole" method for accelerating imaging of contrast agent uptake. *Journal of Magnetic Resonance Imaging*, 3(4):671–675, 1993.

[195] RA Jones, O Haraldseth, TB Muller, PA Rinck, and AN Oksendal. K-space substitution: a novel dynamic imaging technique. *Magnetic Resonance in Medicine*, 29(6):830–834, 1993.

[196] AG Webb, ZP Liang, RL Magin, and PC Lauterbur. Applications of reduced-encoding MR imaging with generalized-series reconstruction (RIGR). *Journal of Magnetic Resonance Imaging*, 3(6):925–928, 1993.

[197] ZP Liang and PC Lauterbur. An efficient method for dynamic magnetic resonance imaging. *IEEE Transactions on Medical Imaging*, 13(4):677–686, 1994.

[198] JM Hanson, ZP Liang, EC Wiener, and PC Lauterbur. Fast dynamic imaging using two reference images. *Magnetic Resonance in Medicine*, 36(1):172–175, 1996.

[199] TL Chenevert, MA Helvie, AM Aisen, IR Francis, DD Adler, MA Roubidoux, and FJ Londy. Dynamic three-dimensional imaging with partial k-space sampling: initial application for gadolinium-enhanced rate characterization of breast lesions. *Radiology*, 196(1):135–42, 1995.

[200] JL Duerk, JS Lewin, and DH Wu. Application of keyhole imaging to interventional MRI: a simulation study to predict sequence requirements. *Journal of Magnetic Resonance Imaging*, 6(6):918–24, 1996.

[201] X Hu. On the "keyhole" technique. *Journal of Magnetic Resonance Imaging*, 4(2):231, 1994.

[202] TB Parrish and X Hu. Hybrid technique for dynamic imaging. *Magnetic Resonance in Medicine*, 44(1):51–55, 2000.

[203] GP Zientara, LP Panych, and FA Jolesz. Dynamically adaptive MRI with encoding by singular value decomposition. *Magnetic Resonance in Medicine*, 32(2):268–274, 1994.

[204] LP Panych, C Oesterle, GP Zientara, and J Hennig. Implementation of a fast gradient-echo SVD encoding technique for dynamic imaging. *Magnetic Resonance in Medicine*, 35(4):554–562, 1996.

[205] Y Cao and DN Levin. Feature-recognizing MRI. *Magnetic Resonance in Medicine*, 30(3):305–317, 1993.

[206] Y Cao and DN Levin. Using prior knowledge of human anatomy to constrain MR image acquisition and reconstruction: half k-space and full k-space techniques. *Magnetic Resonance Imaging*, 15(6):669–677, 1997.

[207] RD Peters and ML Wood. Multilevel wavelet-transform encoding in MRI. *Journal of Magnetic Resonance Imaging*, 6(3):529–540, 1996.

[208] SJ Riederer, T Tasciyan, F Farzaneh, JN Lee, RC Wright, and RJ Herfkens. MR fluoroscopy: technical feasibility. *Magnetic Resonance in Medicine*, 8(1):1–15, 1988.

[209] B Madore, GH Glover, and NJ Pelc. Unaliasing by Fourier-Encoding the Overlaps Using the Temporal Dimension (UNFOLD), Applied to Cardiac Imaging and fMRI. *Magnetic Resonance in Medicine*, 42(5):813–828, 1999.

[210] J Tsao. On the UNFOLD method. *Magnetic Resonance in Medicine*, 47(1):202–207, 2002.

[211] J Tsao, P Boesiger, and KP Pruessmann. k-t BLAST and k-t SENSE: Dynamic MRI With High Frame Rate Exploiting Spatiotemporal Correlations. *Magnetic Resonance in Medicine*, 50(5):1031–1042, 2003.

[212] FR Korosec, R Frayne, TM Grist, and CA Mistretta. Time-resolved contrast-enhanced 3D MR angiography. *Magnetic Resonance in Medicine*, 36(3):345–351, 1996.

[213] CA Mistretta, TM Grist, FR Korosec, R Frayne, DC Peters, Y Mazaheri, and TJ Carrol. 3D time-resolved contrast-enhanced MR DSA: advantages and tradeoffs. *Magnetic Resonance in Medicine*, 40(4):571–581, 1998.

[214] M Doyle, EG Walsh, GG Blackwell, and GM Pohost. Block regional interpolation scheme for k-space (BRISK): a rapid cardiac imaging technique. *Magnetic Resonance in Medicine*, 33(2):163–170, 1995.

[215] M Doyle, EG Walsh, RE Foster, and GM Pohost. Rapid cardiac imaging with turbo BRISK. *Magnetic Resonance in Medicine*, 37(3):410–417, 1997.

[216] S Krishnan and TL Chenevert. Spatio-temporal bandwidth-based acquisition for dynamic contrast-enhanced magnetic resonance imaging. *Journal of Magnetic Resonance Imaging*, 20(1):129–137, 2004.

[217] T Parrish and X Hu. Continuous update with random encoding (CURE): a new strategy for dynamic imaging. *Magnetic Resonance in Medicine*, 33(3):326–336, 1995.

[218] G Adluru, SP Awate, T Tasdizen, RT Whitaker, and EV Dibella. Temporally constrained reconstruction of dynamic cardiac perfusion MRI. *Magnetic Resonance in Medicine*, 57(6):1027–1036, 2007.

[219] EJ Candes, J Romberg, and T Tao. Robust uncertainty principles: exact signal reconstruction from highly incomplete frequency information. *IEEE Transactions on Information Theory*, 52(2):489–509, 2006.

[220] DL Donoho. Compressed Sensing. *IEEE Transactions on Information Theory*, 52(4):1289–1306, 2006.

[221] M Lustig, D Donoho, and JM Pauly. Sparse MRI: The application of compressed sensing for rapid MR imaging. *Magnetic Resonance in Medicine*, 58(6):1182–1195, 2007.

[222] U Gamper, P Boesiger, and S Kozerke. Compressed sensing in dynamic MRI. *Magnetic Resonance in Medicine*, 59(2):365–373, 2008.

[223] S Kozerke, J Tsao, R Razavi, and P Boesiger. Accelerating cardiac cine 3D imaging using k-t BLAST. *Magnetic Resonance in Medicine*, 52(1):19–26, 2004.

[224] C Baltes, S Kozerke, MS Hansen, KP Pruessmann, J Tsao, and P Boesiger. Accelerating cine phase-contrast flow measurements using k-t BLAST and k-t SENSE. *Magnetic Resonance in Medicine*, 54(6):1430–1438, 2005.

[225] I Marshall. Feasibility of kt BLAST technique for measuring "seven-dimensional" fluid flow. *Journal of Magnetic Resonance Imaging*, 23(2):189–196, 2006.

[226] C Jahnke, I Paetsch, R Gebker, A Bornstedt, E Fleck, and E Nagel. Accelerated 4D dobutamine stress MR imaging with k-t BLAST: feasibility and diagnostic performance. *Radiology*, 241(3):718–728, 2006.

[227] R Gebker, C Jahnke, I Paetsch, B Schnackenburg, S Kozerke, A Bornstedt, E Fleck, and E Nagel. MR Myocardial Perfusion Imaging with k-Space and Time Broad-Use Linear Acquisition Speed-up Technique: Feasibility Study. *Radiology*, 245(3):863–871, 2007.

[228] C Jahnke, E Nagel, R Gebker, A Bornstedt, B Schnackenburg, S Kozerke, E Fleck, and I Paetsch. Four-dimensional single breathhold magnetic resonance imaging using kt-BLAST enables reliable assessment of left-and right-ventricular volumes and mass. *Journal of Magnetic Resonance Imaging*, 25(4):737–742, 2007.

[229] Y Tao and I Marshall. A k-t variable-density undersampling technique (ktV-DUST) for dynamic imaging. In *Joint Annual Meeting ISMRM-ESMRMB*, volume 16, 2007.

[230] J Tsao, KP Pruessmann, and P Boesiger. Feedback regularization for SENSE reconstruction. In *Proceedings ISMRM*, volume 10, page 739, 2002.

[231] MS Hansen, C Baltes, J Tsao, S Kozerke, KP Pruessmann, and H Eggers. k-t BLAST Reconstruction From Non-Cartesian k-t Space Sampling. *Magnetic Resonance in Medicine*, 55:85–91, 2006.

[232] J Tsao, S Kozerke, P Boesiger, and KP Pruessmann. Optimizing spatiotemporal sampling for k-t BLAST and k-t SENSE: application to high-resolution real-time cardiac steady-state free precession. *Magnetic Resonance in Medicine*, 53(6):1372–1382, 2005.

[233] MS Hansen, S Kozerke, KP Pruessmann, P Boesiger, EM Pedersen, and J Tsao. On the influence of training data quality in kt BLAST reconstruction. *Magnetic Resonance in Medicine*, 52(5):1175–1183, 2004.

[234] A Sigfridsson, M Andersson, L Wigstrom, JP Kvitting, and H Knutsson. Improving temporal fidelity in k-t BLAST MRI reconstruction. In *Medical Image Computing and Computer-Assisted Intervention*, volume 10(pt2), pages 385–392, 2007.

[235] E Anderson, Z Bai, C Bischof, S Blackford, J Demmel, J Dongarra, J Du Croz, A Greenbaum, S Hammarling, A McKenney, and D Sorensen. *LAPACK Users' Guide*. Society for Industrial and Applied Mathematics, 1999.

[236] M.D. Ford, N. Alperin, S.H. Lee, D.W. Holdsworth, and D.A. Steinman. Characterization of volumetric flow rate waveforms in the normal internal carotid and vertebral arteries. *Physiological Measurement*, 26(4):477–488, 2005.

[237] M Hedley, H. Yan, and D Rosenfeld. Motion artifact correction in MRI using generalized projections. *IEEE Transactions on Medical Imaging*, 10(1):40–46, 1991.

[238] RA Zoroofi, Y Sato, S Tamura, and H Naito. MRI artifact cancellation due to rigid motion in the imaging plane. *IEEE transactions on medical imaging*, 15(6):768–784, 1996.

[239] D Atkinson, DLG Hill, PNR Stoyle, PE Summers, SF Keevil, R Sci, G Hosp, and UK London. Automatic correction of motion artifacts in magnetic resonance images using an entropy focus criterion. *IEEE Transactions on Medical imaging*, 16(6):903–910, 1997.

[240] D Atkinson, DLG Hill, PNR Stoyle, PE Summers, S Clare, R Bowtell, and SF Keevil. Automatic compensation of motion artifacts in MRI. *Magnetic Resonance in Medicine*, 41:163–170, 1999.

[241] D Atkinson and DL Hill. Reconstruction after rotational motion. *Magnetic Resonance in Medicine*, 49(1):183–187, 2003.

[242] ME Bourgeois, FTAW Wajer, M Roth, A Briguet, M Decorps, D Ormondt, C Segebarth, and D Graveron-Demilly. Retrospective intra-scan motion correction. *Journal of Magnetic Resonance*, 163(2):277–287, 2003.

[243] PG Batchelor, D Atkinson, P Irarrazaval, DL Hill, J Hajnal, and D Larkman. Matrix description of general motion correction applied to multishot images. *Magnetic Resonance in Medicine*, 54(5):1273–1280, 2005.

[244] W Lin, FW Wehrli, and HK Song. Correcting bulk in-plane motion artifacts in MRI using the point spread function. *IEEE Transactions on Medical Imaging*, 24(9):1170–1176, 2005.

[245] W Lin and HK Song. Extrapolation and Correlation (EXTRACT): A New Method for Motion Compensation in MRI. *IEEE Transactions on Medical Imaging*, 28(1):82–93, 2009.